Wave Loads on Underwater Protection Covers

Jarle Havn

June 14, 2011

Preface

This Master Thesis has been carried out at the Department of Marine Technology at the Norwegian University of Science and Technology (NTNU) in Trondheim, Norway. The subject was proposed by the Naval Department of Subsea7 in Stavanger in collaboration with the Department of Marine Technology, NTNU. First of all I would like to take the opportunity to thank my supervisor professor Bjørnar Pettersen (Department of Marine Technology, NTNU) and co-supervisor Specialist Engineer Petter Moen (Naval Department, Subsea7). I am sincerely grateful for the continuous guidance and advices by Bjørnar Pettersen (NTNU) throughout the thesis. I am Also very grateful for the technical support and excellent guidance in the present subject by Petter Moen (Subsea7). The experimental part of the subject was performed in the Student Wave Tank at one of the test facilities of Norwegian Marine Technology Research Institute (MARINTEK) in Trondheim, Norway. A special thank to Torgeir Waal (MARINTEK, NTNU) for great technical guidance and assistance performing the experiments, and the technical personal at the engineering workshop at MARINTEK for the making of the experimental models. Also I would like to thank Subsea7 for the financial support of the performed experiments.

Finally I will like to thank my friend and classmate Per Christian Endresen for interesting discussions and useful advices during the thesis.

Trondheim, June 14, 2011.

Jarle Havn

Abstract

Submerged structures in shallow water can be exposed to large hydrodynamic wave- and current forces. An estimate of the total external loads will be important for the design and robustness of the structures. The aim will also be to achieve more correct estimates in accordance with the physical loads. In the present work, wave forces on submerged protection covers over offshore pipelines in shallow water have been investigated. Protection covers have usually a small dry weight. In some cases, it can last some time before stabilizing gravel is dumped on the covers and the covers will in the mean time be freely exposed to the hydrodynamic forces. In order to investigate the shallow water forces, two simplified protection covers were studied with both a numerical CFD analysis and performed experiments in a wave tank. A rectangular and a half circular geometry was chosen for the simplified covers.

A Numerical Wave Tank (NWT) modeled with Computational Fluid Dynamics (CFD), can be used to make similar analysis as performed experiments in a physical wave tank. The use of numerical analysis can reduce both cost and time in comparison with physical experiments. In the present work a two dimensional numerical wave tank was investigated with the numerical CFD software ANSYS CFX. Further the numerical wave tank was used to investigate the dynamic wave forces on the simplified protection covers. Numerical wave elevation and numerical forces was compared with a theoretical approach. A modeled numerical piston or flap wavemaker gave reasonable wave elevation and was found usable to produce numerical waves. A comparison with results by Silva et al. (2010) gave almost similar results. Time series of wave elevation was found to be in good agreement with both theory and experiments. Numerical wave forces on the simplified covers gave good results compared with linear theory. Theoretical horizontal added mass coefficient was found to $C_{a,1} = 1.53$ for the rectangular cover and $C_{a,2} = 1.145$ for the half circular cover. Similar in CFD the horizontal added mass coefficients was found to be $C_{a,1} = 1.4$ and $C_{a,2} = 1.18$ respectively. The vertical forces from CFD was a small value larger than the theoretical linear vertical Froude-Kriloff forces.

The experimental tests was performed in the student wave tank at MARINTEK in Trondheim. Wave elevation from two wave probes and vertical force from three force transducers was measured. The wave elevation was compared with both numerical and theoretical wave elevation. The damping along the tank length was found to be similar as in the CFD analysis of around $1\%/m$. Due to different experimental setup and numerical modeling the vertical forces was not comparable. Non dimensional vertical forces and overturning moment was found from the performed experiments. Largest forces was measured on the rectangular cover. Largest non dimensional forces and overturning moment was found for the half circular cover.

Conclusion

Numerical Wave Tank

A numerical wave tank can be a effective tool to reduce analysis time and costs compared to physical experiments. Two methods have been used, a velocity input method and a piston of flap wavemaker method. The Velocity input method in section 4.2 produced numerical waves, but a variation and large damping in the wave amplitude along the tank was observed. A static water pressure was chosen at the outlet, which affected the solution and will not be recommended in combination with a no slip bottom condition and large element size towards the bottom. A beach at the outlet is suggested instead of a static water pressure condition. The reasons for the deviations in wave elevation can be the boundary conditions, the mesh fineness and the sudden velocity increase at the inlet. No difference was seen between CFX 12.0 and CFX 13.0. From the performed time discretization study, $T/\Delta t >= 100$ is to be recommended.

In section 4.3 three different wavemakers was studied. A hinged flap, a bottom hinged flap and a piston. All three methods gave almost similar results and can be used to produce numerical waves with good accuracy.

In section 4.4 a validation case from Silva et al. (2010) was chosen and a similar setup was modeled in order to try to achieve similar results. Almost similar results was obtained. The results from the validation case gave a small value more steady results. The reason could be some unmentioned settings in the article by Silva et al. (2010) or a slower start of the flap wavemaker. A slower first cycle motion of the flap wavemaker will reduce unnatural sudden water accelerations in the start. A mesh normal to the free surface in the whole domain will be recommended. Time series showed good results compared with Stokes 2nd order wave theory.

In section 4.5 the student wave tank at MARINTEK in Trondheim was modeled with same two dimensional tank dimensions and wavemaker. Good results was obtained for the wave elevation compared with Stokes 2nd order wave theory. Horizontal water velocity under a wave crest, wave zero crossing and wave trough gave good results compared with Stokes 2nd order wave theory. Similar dynamic wave pressure also gave good agreement compared with Stokes 2nd order wave theory. The fact that the velocity and pressure showed good results states that the wavemaker method can be used to produce numerical waves with good accuracy.

Suggested values regarding a numerical wave tank mesh parameters and time step is given in table 1.

Parameter	Setting
Elements per wave length	$\lambda/\Delta x >= 100$
Elements per wave amplitude	$\zeta_A/\Delta x > 10$
Mesh aspect ratio	$\Delta x/\Delta z < 10$
Timestep per wave period	$T/\Delta t > 100$

Table 1: Summary of suggested values for a numerical wave tank

CFD Analysis on Protection Covers

The modeled numerical wave tank from section 4.5 was used to study wave forces on two different submerged protection covers. Horizontal and vertical forces was calculated from the isolated sides of the studied protection cover. Both the total force, pressure force and viscous force was found. The Viscous forces was obtained to be very small and was neglected. The horizontal force gave good results compared with the calculated theoretical force based on a Froude-Kriloff pressure force with a additional added mass contribution. In the theoretical approach, a horizontal added mass coefficient of $C_a = 1.53$ was used for the rectangular protection cover and $C_a = 1.145$ for the half circular cover. The CFD results gave a horizontal added mass coefficient of $C_a^{CFD} = 1.4$ for the rectangular protection cover and $C_a^{CFD} = 1.18$ for the half circular protection cover. The horizontal added mass coefficients from theory and CFD shows good agreement. Vertical forces was assumed to only be the Froude-Kriloff pressure force in the theoretical approach since the structure was assumed small compared with the wave length. The vertical forces from CFD was a small value larger than the theoretical Froude-Kriloff force for both the rectangular and half circular cover, indicating a influence from the structure on the surrounding water.

Experiments

A parameter study was done on both the rectangular and half circular protection cover models with variation in both wave period T and wave amplitude ζ_A. A direct comparison of the wave elevation between experiments and CFD gave good agreement. Similar damping along the tank was obtained in the physical wave tank as in the numerical wave tank. The experimental wave elevation gave also good agreement with Stokes 2nd order wave theory. The flap wavemaker gave similar wave parameters as the input parameters for low periods below $1.25s$. Above $H = 0.15m$ and $T = 1.0s$ the wavemaker produced higher waves than the input values.

The vertical forces was not comparable with the CFD computations. The reason will mostly be the difference in modeling and experimental setup. During the experiments the wave orbital motion was observed around the protection cover and also for the water inside the cover. The water motion inside the cover will give a dynamic contribution to the original static water pressure inside the cover. The dynamic pressure contribution can give cancellation effects to the measured vertical forces. Cancellation effects of the measured forces can also be due to affection of the tank walls. The selected wave periods was found to be around and close to the natural periods of the transverse wave system of the tank. The transverse waves was only observed after the longitudinal waves from the wavemaker was damped out, but the tank walls will have some influence on the force measurements. Other factors which can affect the vertical force measurements can be measurement errors in the force transducers and errors in the acquisition system. The rectangular cover gave a small value larger forces. For the non dimensional forces the half circular cover gave largest values. The non dimensional overturning moment was also largest for the the half circular cover.

Contents

Contents

List of Figures

List of Tables

Nomenclature

The most used symbols are presented in the following table. Symbols not mentioned are explained in the present when used.

m	Mass.	z_{crit}	Critical depth.
ρ	Density of water.	l	Cover length.
V	Volume.	d	Cover height.
$\vec{V}$,U	Velocity.	b	Cover breath.
u	Horizontal water velocity.	r	Cover radius.
w	Vertical water velocity.	l_p	Mud mat length.
t	Time.	$\vec{n}$	Normal vector.
F, f	Force.	C_M	Mass coefficient.
$\vec{a}$	Acceleration.	C_D	Drag coefficient.
g	Gravity.	C_a	Added mass coefficient.
t	Time.	μ	Dynamic viscosity.
p	Pressure.	ν	Kinematic viscosity.
L	Length.	H	Wave height.
T	Wave period and Temperature.	S	Wavemaker stroke length at surface.
ζ	Surface elevation.	ζ_A	Wave amplitude.
ω	Wave frequency.	h	Water depth.
λ	Wave length.	k	Wave number.

Chapter 1

Introduction

The development in the offshore oil and gas industry has led to a huge increase in subsea installations in the past decades. Many types of submerged structures are installed in order to process and transport the offshore produced oil and gas. From subsea templates, the produced fluids are transported into shore in long pipes. The bottom topography variates a lot, similar as outback terrain on shore. Routes has to be made and the pipes has to be stabilized with gravel piles along the route. Close to the template there will be valve terminals and umbilical control connections which has to be protected. Thermal expansion zones and heating zones will also require protection. The thermal expansion zone accounts for the expansion and contraction of the pipe due to temperature differences and the heating zone heats up the produced fluids in a cold start up. To protect the pipe, shell constructions has been developed. The shell covers can be made of different materials and some are made of reinforced glasfibre laminates, often abbreviated GRP covers. The shell protection covers are mounted over the transport pipe in areas where protection is needed. Reinforced glasfibre is a strong and light material, and due to the small weight the protection covers are stabilized with gravel on side panels (mud mats) located on both sides of the covers. Typical dimensional loads on the protection covers will be installation loads, trawl loads, loads from dropped objects and environmental loads from current and waves. In some cases it can take some time before gravel is dumped on the protection covers and the mud mats. With no extra stabilizing mass, the protection covers will be free and vulnerable to the external loads.

Some of the challenges for the industry will be deep water with huge pressure, shallow water with wave and current forces, large pipes over long distances and increased complexity of the installations. In combination with the increased complexity there has been more focus on analysis and to predict the different external loads which will act on the submerged installations in different sea states. Computational Fluid Dynamics (CFD) has in the last years become a widely used analysis tool also for marine operations and subsea installations. The advantage with CFD is that viscous effects can be modeled which can reduce some of the experimental laboratory tests and replace some of the widely used empirical data in many analysis tools. In combination with experimental validation, CFD can be a very good analysis tool which can reduce both time and analysis costs. In the present work a simplified protection cover over a submerged pipeline in shallow water has been studied. Wave forces in shallow water has been the studied external load. A numerical analysis tool has been evaluated to model numerical waves with the CFD software ANSYS CFX. The results have been compared with a theoretical simplified method and in addition performed experimental results. The experiments was done in the student wave tank at MAR-INTEK test facilities at the department of Marine Technology at NTNU in Trondheim. First a overview of the problem is given in chapter 2. In chapter 4 a numerical study of a two dimensional numerical wave tank has been performed with the CFD software ANSYS CFX. In chapter 5 a theoretical simplified method has been studied. In chapter 7 a experimental study of the two models of the studied protection cover has been performed

1

Chapter 2

Overview of Problem

The main topic can be divided in two parts. First a numerical method in order to establish a numerical wave tank has been studied. Secondly wave forces on simplified protection covers over submerged pipelines has been studied. In figure 2.1 a subsea template is shown with installed protection covers over the transport pipe. Different cover types are used in different zones dependent of the aim of protection. In figure 2.2 two shell cover design is shown. The protection covers will usually be made in sections and mounted together over a distance of the pipe. Typical dimensions can be a length of $15m$ along the pipe, height of $2m$ and a cross sectional width of $6m$. In order to have less factors affecting the fluid flow regarding the geometry, simplified covers with basis from the covers in figure 2.2, have been studied.
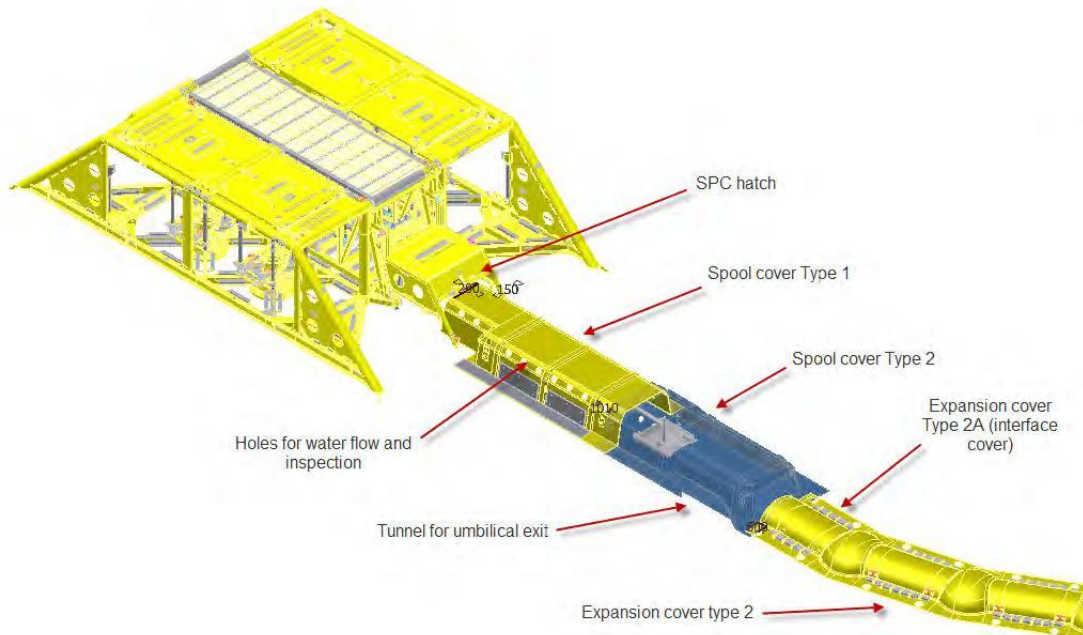
Figure 2.1: Template with different protection covers, (from Subsea7).

From the time of installation of the protection covers it can take some time before gravel are dumped on the mud mats. During this period the covers have no extra stabilizing mass and will lie on the bottom of its own weight. From the external current and wave loads the protection covers can be exposed to large forces in comparison with its mass. Especially in shallow water the wave forces can be large and can lead to movement of the protection covers and maybe also tip them over. The main focus was therefore to investigate the shallow water wave forces on similar protection covers. Wave loads can
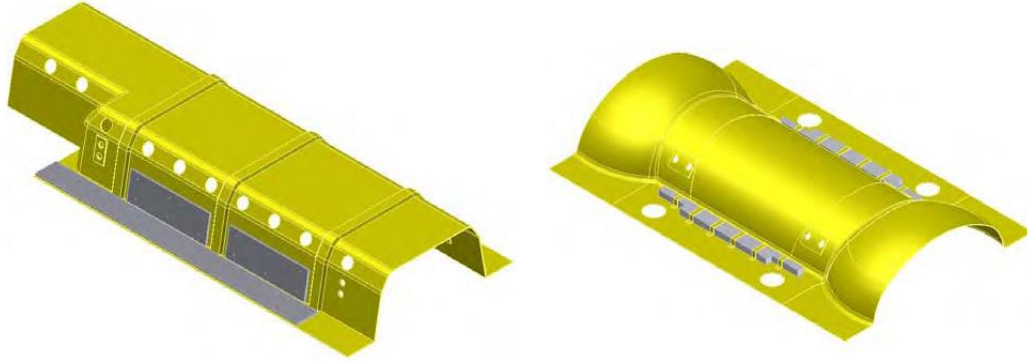
Figure 2.2: Examples of protection covers, (from Subsea7).

be estimated in different ways. In the present work a numerical approach has been studied based on Computational Fluid Dynamics (CFD) with the software ANSYS CFX. In order to investigate the wave forces with a CFD analysis a numerical wave tank had to be investigated and modeled. A numerical tank with similar dimensions as the student tank at MARINTEK was modeled. In addition to the numerical analysis a theoretical method and experimental tests have been performed. The theoretical method was based on potential linear wave theory. The experimental tests was performed in the student wave tank at MARINTEK and vertical forces was measured.

In order to compare results, simplified covers in model scale was studied in all three methods. A rectangular and a half circular cross sectional shape was selected for the simplified covers. With a scale factor of 20 the cross sectional height was chosen to $d = 0.1m$ and cross sectional width $l = 0.2m$ + 2 flat side panels chosen as $l_p = 0.05m$. In figure 2.3 the cross sectional dimensions are shown. Here Cover 1 represents the cover with rectangular cross section and Cover 2 represent the cover with half circular cross section. A two dimensional analysis has been studied with a unit length b a long the pipe direction. The dimensions and fluid parameters are listed in table 2.1.
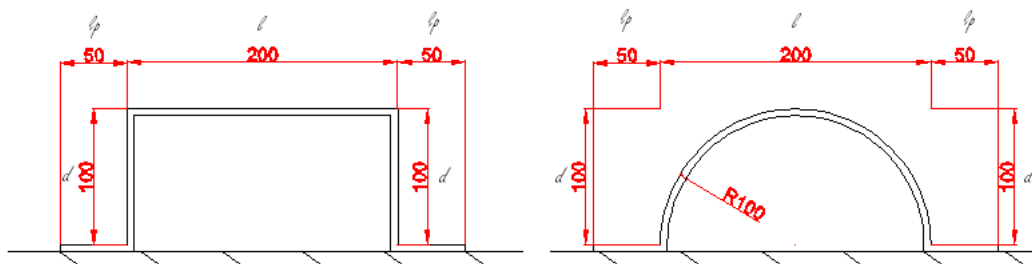
Figure 2.3: Cover 1 (rectangular) and Cover 2 (circular) with dimensions in [mm].

Model Parameters			
Cover c.s lenght	l	0.2	m
Mudmat lenght	l_p	0.05	m
Cover c.s height	d	0.1	m
Cover unit breadth	b	1	m
Cover radius	r	0.1	m
Water depth	h	1	m
density	ρ	1000	kg/m^3
Gravity	g	9.81	m/s^2

Table 2.1: Dimensions and Parameters for the simplified covers.

Chapter 3

Theory

3.1 CFD Theory

The fundamental equations used in todays CFD solvers are based on the famous theory of viscous fluids with its roots back to the fifteenth century. The famous multi talented Italian, Leonardo da Vinci, deduced in 1500 the conservation of mass for incompressible one-dimensional viscous flow. In 1687 Isaac Newton published his "Principia" where the linear viscous behavior for almost all common fluids, today called Newtonian fluids, was presented. Later on the master of calculus, Leonard Euler, derived the idealized frictionless equation of fluids. In the nineteenth century frictional resistance where added to the inviscid Euler equations by 5 different mathematicians: Navier (1827), Cauchy (1828), Poisson (1829), St. Venant (1843) and Stokes (1845). The resulting equations are today called the *Navier - Stokes relations*. Due to the fact that the equations are both non-linear and complex only few analytical particular solutions exists. With the invention of digital computer calculations in the latter half of the twentieth century a new era raised for computations of viscous flows. Combined with the development of different numerical methods the Navier - Stokes relations could be solved numerically by iterations. Simultaneous mathematicians and scientists have derived mathematical models for a more realistic fluid flow representation with boundary layers and turbulence approximations. Today, with the fast increase in computer power, the viscous equations can be used to solve large and complex systems by easy to use computer softwares. In the present chapter the main governing equations used in a CFD solver will be presented. The basic equations for viscous flows considered by White (2006) are the three laws of conservation:

1. *Conservation of Mass based on continuity*
2. *Conservation of Momentum based on Newton's second law*
3. *Conservation of Energy based on the first law of thermodynamics*

3.1.1 Conservation of Mass

The continuity equation in 3.1 states that the mass is constant in a given system. Meaning that the amount of mass into the system is equal to the mass out of the system. In equation 3.1 $\mathscr{V}$ represents the volume, ρ the density, m the mass, and t the time. By rewriting the total derivative, given in equation 3.2, and relate the rate of volume change to the normal-strain rate and further to the fluid velocity we get the more known continuity equation given in equation 3.3. In a numerical wave tank the fluid can be assumed incompressible, with constant density, and the continuity equation reduces to equation 3.4.

$$\frac{Dm}{Dt} = \frac{D(\rho\mathscr{V})}{Dt} = 0 \qquad (3.1)$$

$$\frac{D}{Dt} = \frac{\partial}{\partial t} + (\mathbf{V} \cdot \nabla) \tag{3.2}$$

$$\frac{\partial \rho}{\partial t} + \nabla(\rho \mathbf{V}) = 0 \tag{3.3}$$

$$\nabla(\mathbf{V}) = 0 \tag{3.4}$$

3.1.2 Conservation of Momentum

The conservation of momentum are often mentioned as the Navier Stokes equation in fluid mechanics. From Newton's second law, the total force is given as the rate of change of momentum. Momentum is often noted as mass times velocity, as shown in equation 3.5 with constant mass m outside of the total derivative. In a given system the conservation of momentum means that the momentum into the system equals the momentum out of the system. In practice this illustrates Newton's third law between fluid particles were a equal and opposite force will act on each particle in order to conserve the momentum. By dividing the fluid particle with its volume, the mass can be represented only with density, ρ. Further the sum of forces per volume can be divided into a body force and surface forces from external stresses as given in the stress - strain formulation of Navier Stokes in equation 3.6

$$\sum F = m\mathbf{a} = m\frac{D\mathbf{V}}{Dt} = \rho \mathcal{V} \frac{D\mathbf{V}}{Dt} \tag{3.5}$$

$$\rho \frac{D\mathbf{V}}{Dt} = \mathbf{f} + \nabla \cdot \sigma \tag{3.6}$$

The body force, $\mathbf{f}$ given in equation 3.7, represents the forces which is applied to the total mass of the fluid element, usually given as the gravity force per unit volume ρg . In a numerical wave tank the buoyancy force must also be taken into consideration together with the gravity force. A buoyancy force is in general a force due to difference in density. We have assumed constant density but due to the two phase flow between water and air in a wave tank we have to take the difference between the fluids into account. In CFX solver manual, ANSYS (2010), the buoyancy term is given as $(\rho$ - $\rho_{ref})$g and will replace the hydrostatic pressure gradient given as the gravity force per unit volume. The reference density is given as the density of air, ρ_{air}, with a reference location in the air phase well above the wave height.

$$\mathbf{f} = (\rho - \rho_{ref})\mathbf{g} \tag{3.7}$$

The surface forces can be related to the velocity by the stress - strain relationship for a Newtonian fluid given in equation 3.8 with tensor notation.

$$\sigma_{ij} = -p\delta_{ij} + \mu \left(\frac{\partial u_i}{\partial x_j} + \frac{\partial u_j}{\partial x_i} \right) + \delta_{ij}\lambda\nabla(\mathbf{V}) \tag{3.8}$$

δ is the Kronecker delta function and λ the bulk viscosity which will dissapear due to the incompressible assumption. The pressure is due to the fact that when the fluid is at rest the viscous stresses vanish and we are left with the hydrostatic pressure normal to the surface. With constant viscosity and density, the Navier Stokes equation can be written as equation in 3.9.

$$\rho \frac{D\mathbf{V}}{Dt} = (\rho - \rho_{ref})\mathbf{g} - \nabla p + \mu\nabla^2\mathbf{V} \tag{3.9}$$

3.1.3 Conservation of Energy

The conservation of energy, given in equation 3.10, states that heat added and work done on the system will increase the total energy of the system. In equation 3.10, h is the enthalpy, k is the thermal conductivity and Φ is the dissipation function. Refer to White (2006) for more details. The temperature is of minor importance in a numerical wave tank with isothermal conditions .

$$\rho \frac{Dh}{Dt} = \frac{D\rho}{Dt}\nabla(k\nabla\mathbf{T}) + \Phi \tag{3.10}$$

From the three equations, continuity-, momentum- and energy conservation, the three unknowns *pressure*, *velocity* and *temperature* can be found. These parameters are the main output parameters in a CFD analysis and are the basis for all the other results.

3.1.4 Discretization in ANSYS CFX

The discretization used in ANSYS CFX is based on a Finite-Volume Method (FVM). The discretized finite volumes is constructed from the modeled mesh and in each finite volume the mass, momentum and energy is conserved. The method is always three dimensional due to the finite volumes. A two dimensional analysis can be done by only using one element in the extruded third direction. The conservation equations are further integrated over each control volume. Volume integrals of divergence and gradient operators are converted to surface integrals by Gauss' Divergence Theorem. The conservation is exactly satisfied in each control volume, which indicate also exactly conservation of the total domain. The volume and surface integrals are further discretized in order to be solved numerically. For the advection terms the discretization used in ANSYS CFX is given in equation 3.11 taken from the user manual of ANSYS (2010).

$$\phi_i = \phi_u + \beta\Delta\phi\Delta\vec{r} \tag{3.11}$$

In equation 3.11, ϕ_u is the upwind discretized value and ϕ_i is the discretized value at the integration node. $\vec{r}$ is the vector from the upwind node to the integration node. β is the blend factor which is between 0 and 1. When $\beta = 0$ a pure upwind scheme is obtained, which is robust but can introduce diffusive discretization errors. The high resolution scheme use a variable β value chosen as high as possible. When $\beta = 1$ a second order accuracy in space is achieved. In the present work a high resolution scheme and a specified blend of $\beta = 1$ has been used.

Regarding the time discretization, a second order Backward Euler discretization scheme has been used and is given in equation 3.12 taken from the user manual of ANSYS (2010).

$$\frac{\partial}{\partial t}\int_V \rho\phi\mathrm{d}V \approx V\frac{1}{\Delta t}\left(\frac{2}{3}(\rho\phi) - 2(\rho\phi)^o + \frac{1}{2}(\rho\phi)^{oo}\right) \tag{3.12}$$

In equation 3.12, the sub script o indicate previous iteration, V is the volume, ρ is the density and ϕ is the discretization value. The second order Backward Euler Method is robust, implicit, conservative in time and have no time step limitation. The equation is not bounded and can give nonphysical oscillations. Refer t0 the user manual of ANSYS (2010) for further information regarding the discretization schemes.

3.1.5 Dimensionless Parameters

Some important dimensionless parameters regarding CFD computations are the Reynolds number, Froude number, CFL Number and $Y+$ value. The Reynolds number Re is the ratio between inertia forces and viscous forces, shown in equation 3.13.

$$R_e = \frac{Inertia forces}{Viscous forces} = \frac{\rho U^2 L^2}{\mu U L} = \frac{\rho U L}{\mu} \tag{3.13}$$

In equation 3.13 ρ is the fluid density, U fluid velocity, L characteristic length scale and μ the dynamic viscosity (kinematic viscosity $\nu = \mu/\rho$). The main importance of the Reynolds number is to categorize the fluid flow from laminar to turbulent. A low Reynolds number indicates slowly varying viscous effects where the fluid is ductile and categorized laminar. When the Reynolds number increases, the fluid becomes more fluctuating, viscous effects varies more rapidly and the fluid is categorizes as turbulent. Similarity in Reynolds number is often hard to achieve in experimental tests. In CFD the exact fluid properties can be modeled and similarity in Reynolds number achieved.

The Froude number, shown in equation 3.14, gives the ratio between inertial forces and gravitational forces. From comparing with model scale and full scale it is usually written as in equation 3.15. Free surface waves are gravity driven waves and similarity in Froude number is therefore important in order to achieve correct surface waves in model scale. In a numerical wave tank it is not a problem since the studied dimensions can be used in the modeling. Physically the Froude number gives the ratio between the mean fluid velocity and the speed of the gravity driven free surface wave, with a analogy to the Mach number. In a open duct channel flow as in a wave tank the depth based Froude number can be used to classify the fluid flow. If the Froude number is less than unity the flow is considered sub critical and the gravitational forces are dominant. If the Froude number is larger than unity the flow is considered supercritical and the inertial forces are dominant. In deep water flows the characteristic length, L, equals the wave length and the term $\sqrt{gL}$ represents the wave velocity. In a supercritical flow the fluid velocity is larger than the wave velocity and waves can not propagate upstream. In a sub critical flow $F_n < 1$, the waves can propagate in any directions. The Froude number is mostly used to predict resistance of a moving body in water.

$$\hat{F}_n = \frac{Inertia forces}{Gravity forces} = \frac{\rho U^2 L^2}{\rho g L^3} = \frac{U^2}{gL} \tag{3.14}$$

$$F_n = \sqrt{\hat{F}_n} = \frac{U}{\sqrt{gL}} \tag{3.15}$$

The Courant-Friedrich-Levy number, shown in equation 3.16 is important in transient analysis for convergence stability. The CFL number gives the ratio between traveled length of a fluid particle and the actual element size. The criteria states that the Courant number should be below 1. The practical meaning is that a fluid particle should not travel a distance larger than the element size during a time step. In connection with the mesh the time step for the calculation can be estimated by the CFL number. In a implicit solver, which is used in ANSYS CFX, the CFL number sensitivity will be reduced and a small CFL number is not required in order to have stability. This means that a higher Courant number can be used without convergence problems. In a transient run ANSYS CFX recommend a CFL number in order of unity to resolve transient details.

$$CFL = \frac{U \Delta t}{\Delta x} \tag{3.16}$$

In turbulent flows close to boundaries the Y^+ value can be important in order to resolve the boundary layer. Y^+ is the non dimensional wall distance shown in equation 3.17. In equation 3.17 U_* is the friction velocity shown in equation 3.18, y the smallest element height normal to the wall and ν is the kinematic viscosity. In equation 3.18 τ_w is the wall shear force. From the relations Y^+ is proportional to both the friction velocity and the smallest element height. High fluid velocity close to the wall will give a higher Y^+ value, which will indicate a finer mesh close to the wall in order to resolve the boundary layer. If a wall function is used the recommended y^+ value is between $20 - 150$, depending on the Reynolds number. The reason is to have the first elements inside the logarithmic layer where the wall function is enabled. Without a wall function the mesh must be able to represent the boundary layer, and the recommended Y^+ value is recommended smaller than 20.

$$y^+ = \frac{U_* y}{\nu} \tag{3.17}$$

$$U_* = \sqrt{\frac{\tau_w}{\rho}} \tag{3.18}$$

In addition in free surface flows with surface tension the *Weber number* and the *Marangoni number* can be mentioned. The weber number gives the ratio between the inertia forces and surface tension forces, $W = \frac{\rho U^2 L}{\sigma}$, where ρ is the fluid density, U is fluid velocity, L is a characteristic surface length and σ is the surface tension. The surface tension force is a tangential force per unit length of a free surface element, keeping the surface together, and will be important for bubbles and droplets. Surface tension is a thermodynamic property where the tension is dependent of the temperature. If the temperature varies along the tank a surface tension gradient will give a shear force which will force the fluid to move from the hot region to a colder region. The convection effect is called the Marangoni effect. The Marangoni number is given as $Ma = -\frac{\partial \sigma}{\partial T} \frac{\Delta T L}{\mu \kappa}$, where μ is the dynamic viscosity, ΔT the bulk temperature difference and κ the thermal diffusivity. The Marangoni number gives the importance of the convection effect. In a numerical wave tank with gravity waves, isothermal conditions is often assumed and the Marangoni effect vanish. Also the inertia forces will dominate and consequently the surface tension can be neglected.

3.1.6   Turbulence Models

In a wave tank with only non breaking regular waves the flow will follow the orbital motion and can be assumed laminar, in similar manner like a uniform current flow will be laminar. If no structure is disturbing the fluid flow no separation and turbulent mixing will occur. In a real water of fluid the flow around structures will in most cases be turbulent and a turbulence model must be set up. From Reynolds decomposition the velocity can be written as a mean velocity and a fluctuation velocity as in equation 3.19. The mean velocity will say a time averaging velocity. By adding a fluctuation velocity in all three directions and insert it into the Navier-Stokes equations we get the Reynolds Averaged Navier Stokes (RANS) equations given in equation 3.20.

$$u = \overline{u} + u' \tag{3.19}$$

$$\rho \frac{D\overline{\mathbf{V}}}{Dt} = (\rho - \rho_{ref})\mathbf{g} - \nabla \overline{p} + \nabla \left(\mu \left(\frac{\partial u_i}{\partial u_j} + \frac{\partial u_j}{\partial u_i} \right) - \rho \overline{u_i' u_j'} \right) \tag{3.20}$$

The last term in equation 3.20, $-\rho \overline{u_i' u_j'}$, is the apparent turbulent stresses which are unknown. The system will now have more unknowns than equations. A turbulence model will give the relation between

the extra unknown turbulent stresses and the mean flow variables. All turbulence models have some empirical relations and the choice of model will depend upon the problem to solve. The turbulence models can be divided into *Eddy viscosity models*, *Reynolds stress models* and *Eddy simulation models*. The eddy viscosity models use the Boussinesq hypothesis by using a eddy (or turbulence) viscosity, μ_t. The Reynolds stress models use transport equations for the Reynolds stresses and the Eddy simulation models (LES and DES) resolves the eddies without the RANS formulation. The most used models among engineers are the Eddy viscosity models and especially the $K - \epsilon$ model. In the present work a $K - \epsilon$ and a SST (Shear Stress Transport) model has been used.

Eddy viscosity models

The Boussinesq hypothesis, referred from White (2006) and Andersson (1988), links the turbulent, or Reynolds stresses to the mean rate of deformation as shown i equation 3.21. This only moves the turbulent unknown from the apparent stresses to a turbulent viscosity, μ_T. The $K - \epsilon$ model is a two-equation model which relates the unknown turbulent viscosity, μ_T to the turbulent kinetic energy, K, and the turbulent dissipation ϵ. The relation is given in equation 3.22. Here $C_\mu = 0.09$ for the $K - \epsilon$ model. Near walls the $K - \epsilon$ model use a wall function. A scalable wall function uses the logarithmic velocity profile approximated from the velocity close to the wall. The boundary layer can be divided into a sub layer with almost linear velocity profile, a logarithmic layer following the logarithmic profile and a buffer layer where the laminar and turbulence effects are of equal importance. A boundary layer is shown in figure 3.1. The logarithmic profile is often mentioned as the "log law of the wall". One important issue with a wall function is the lack of modeling separation in the boundary layer. When the flow separates the velocity gradient becomes zero at the wall and the velocity profile will turn over and become negative. A wall function based on the logarithmic profile will not be able to represent a zero velocity gradient or back flow. In waves the velocity profile oscillates with the wave period and follow the orbital motions with reduced radius towards the bottom. A wall function without capability of separation should therefore not be used overall in a numerical wave tank.

$$-\rho \overline{u_i' u_j'} = \mu_T \left(\frac{\partial u_i}{\partial u_j} + \frac{\partial u_j}{\partial u_i} \right) \tag{3.21}$$

$$\mu_T = \rho C_\mu \frac{K^2}{\epsilon} \tag{3.22}$$

The SST model of Menter (1994) is based on the two-equation $K - \omega$ model. Menter (1994) is the head of the turbulence program of ANSYS CFX. Here K still is the turbulent kinetic energy and ω is the turbulent frequency. Similar as the $K - \omega$ model the SST model gives a more accurate flow near walls with a automatic switch from a wall function to a low-Reynolds number method. For the low-Reynolds number method the mesh close to the walls is assumed fine enough to resolve the viscous part of the boundary layer. The SST model use in this way the best from both the $K - \epsilon$ model and the $K - \omega$ model with use of the $K - \omega$ model for near wall treatment and the $K - \epsilon$ model in the bulk flow. The SST model can therefore be used when the boundary layer not follows the logarithmic profile given in a wall function as long as the mesh is fine enough to resolve the turbulence. In equation 3.23 the turbulent viscosity is given for the SST model. Here $a_1 = 5/9$, S is the invariant measure of the strain rate and $F2$ is a blending function given in 3.24.

$$\mu_T = \rho \left(\frac{a_1 k}{max(a_1 \omega, S F_2)} \right) \tag{3.23}$$
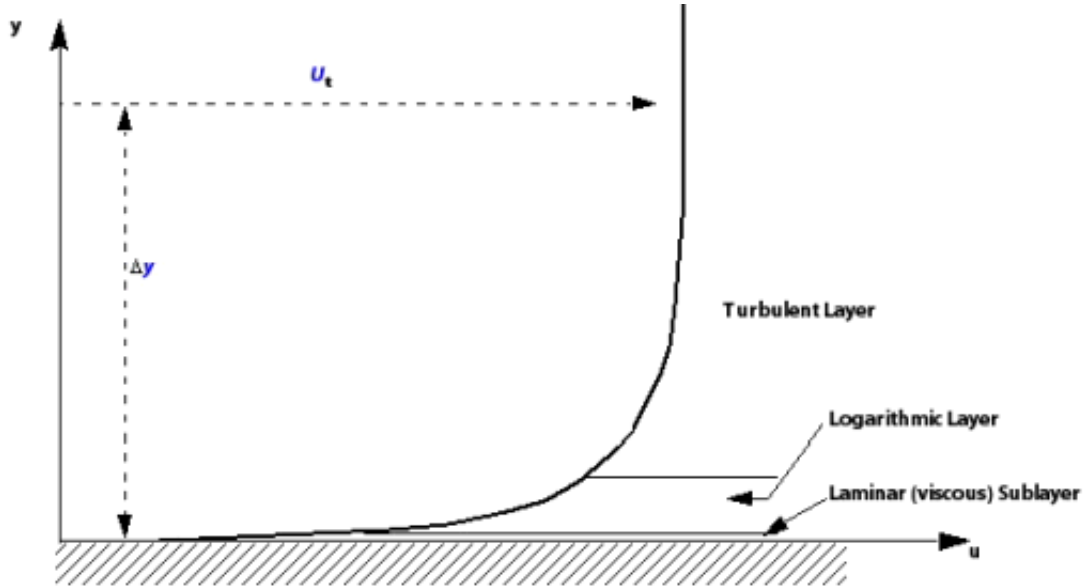
Figure 3.1: Boundary layer showing the sub layer, logarithmic layer and the buffer layer. From ANSYS (2010).

$$F_2 = tanh \left[\left[max \left(\frac{2\sqrt{k}}{\beta^* \omega y}, \frac{500\nu}{y^2 \omega} \right) \right]^2 \right] \qquad (3.24)$$

In a CFD analysis the characteristics of the chosen turbulence model must be specified. There are several alternatives. The turbulent kinetic energy K and the turbulent dissipation ϵ or the turbulent frequency ω can be specified. Alternatively a length scale or a eddy viscosity ratio can be specified instead of the ϵ or ω value. A third alternative is to specify the intensity of the turbulence instead of the kinetic energy. The intensity is given as the ratio between the turbulent fluctuation velocity and the mean velocity. In the present work medium turbulence is used when a turbulence model is selected. Medium intensity is given as 5% intensity and a eddy viscosity ratio equal 10. Medium turbulence is the recommended setting if you have no information regarding the turbulence, ANSYS (2010).

3.1.7   Free Surface

The first necessary condition to fulfill in order to model a numerical wave tank is the capability of modeling a free surface flow. Free surface flows are in general a special case of multiphase flows with one liquid and one gas phase, respectively water and air in this case. Also mentioned as a two phase flow. The free surface can be noted as a boundary which split the two phases. One of the major issue is that the free surface boundary are not rigid, but it is dynamically free. The actual position of the surface is only known at the initial time and will be part of the solution for later time steps. In order to be able to find the free surface position as function of both time and space, boundary conditions is necessary.

Free Surface Boundary Conditions

There exists two conditions defining the free surface:

1. *Kinematic boundary condition*
2. *Dynamic boundary condition*

The *kinematic boundary condition* requires that the water particles at the free surface stays at the free surface. This indicates no net fluid flow trough the free surface. The normal water velocity component located at the free surface has to be equal to the normal velocity component of the free surface boundary.

$$[(v - v_b)n]_{fs} = 0 \quad \dot{m}_{fs} = 0 \tag{3.25}$$

Here v is the water velocity, v_b the boundary velocity, $\dot{m}_{fs}$ the mass flux and fs indicates the free surface. The *dynamic boundary condition* require force equilibrium at the free surface. Normal forces on the surface has to be equal and opposite in direction and tangential forces equal and in the same direction. In gravity driven free surface flows the surface tension force and the viscous shear stress force at the surface can be neglected and we are left only with the pressure force. This gives water pressure equal to the air pressure at the free surface.

$$[p_{water} - p_{air}]_{fs} = 0 \tag{3.26}$$

Since the location of the free surface is unknown and becomes a part of the solution, one can only use one of the boundary conditions at the surface. The other boundary condition is needed to locate the surface position iteratively. There are several methods to define the surface position, and they can be classified into two main groups:

1. *Interface Tracking method*
2. *Interface Capturing method*

In the *interface tracking method* the free surface is defined as a sharp interface. The mesh is shaped according to the surface boundary which will follow the wave elevation. This requires a moving mesh which must be regenerated for each time step. The other method, *interface capturing method*, is used with a fixed mesh extended into the air. The volume cells will all be specified with a volume fraction of air and water. The free surface will then be located along the volume cells with a volume fraction of 0.5, which indicates equally filled with water and air. This method is also referred to as a *Volume tracking method* since it tracks cells with equally water and air fraction. The first capturing method was the *Marker and Cell method*, (MAC). Later on this method developed to the *Volume of Fluid method*, (VOF) which is used by many CFD solvers. Due to the fact that all cells would have a water and air fraction this method was time consuming earlier and the interface tracking method was preferred since it was faster. With increasing computer power the interface capturing method has become more popular. Also for reasons that the interface capturing method is more robust an can handle effects as flow spray and breaking waves. For the interface tracking method only simple wave profiles can be studied, were the mesh cells can follow the surface boundary. This limits the method from effects as breaking waves. In figure 3.2 volume cells with given water fraction is shown.
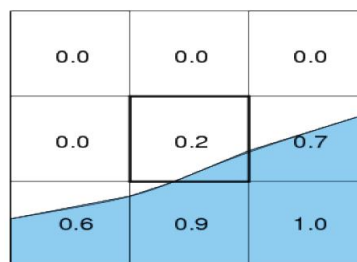
Figure 3.2: Water fraction

Ansys CFX use the *interface capturing method* to define the free surface. To get the free surface as thin as possible the mesh must be very fine with high density in the region covering the free surface. In the

practical computation the free surface will be smoothed over some grid cells. Adaptive mesh refinement is often used for unstructured meshes in steady state analysis were cells with water fraction of 0.5 will be refined. The solver then refines the area close to the free surface automatically. In a numerical wave tank a transient simulation is necessary. The mesh around the free surface are therefore refined uniformly around the initial location of the free surface. In my Project Thesis, Havn (2010) a validation case with a free surface flow was studied. A submerged hydrofoil with a given angle of attack in uniform current was studied and compared with published experimental results and a validation report from ANSYS CFX. The analysis showed that ANSYS CFX is capable of modeling free surface flows with good results.

3.1.8   Overview of Domain Boundary conditions

In a CFD analysis the problem to solve is bounded and modeled by a domain. The domain boundaries has to be specified in order to have a solution. The most used boundary conditions in a numerical wave tank are shortly listed in the following. Refer to the specific section for more information regarding the actual boundary conditions used in each analysis. Further details can also be found in the user manual of ANSYS (2010).

Inlet boundary condition

At a inlet boundary condition all fluid quantities has to be specified. At the boundary the velocity components can be specified in all three directions, the mass flow rate can be specified or the pressure can be specified. From the specified values the convective fluxes can be directly calculated. The gradient driven diffusive fluxes can be found from a approximation of the gradients. If the fluid conditions at the inlet not is known the inlet should be placed far from the studied part of the domain. In addition to the fluid specifications, the turbulence settings must be specified at the inlet.

Outlet boundary condition

Similar to the inlet condition, the outlet should be placed far away from the studied part of the domain since normally little information is known at the outlet. Most used outlet condition is to specify the pressure since the velocity profile usually not is known. In a numerical wave tank a static pressure can be used which will give a constant mean free surface level at the outlet. The static pressure condition is crucial to the dynamic wave elevation and will force the elevation to the mean surface level at the outlet. If the wave elevation could be prescribed at the outlet, a dynamic pressure condition could be used.

Opening

A opening boundary condition allows the fluid to flow both ways through the boundary. Here pressure with direction, velocity or entrainment can be specified. The entrainment option can be useful in situations where the flow direction is unknown. The turbulence settings also need to be specified. In flows where the flow oscillates or the fluid is free to move in or out a opening boundary is often used.

No slip and free slip wall

A impermeable wall is a physical boundary which limits the fluid to flow trough. The physical condition states that $U_i = U_{i,wall}$, indicating similar tangential fluid velocity on the wall as the wall velocity. The normal velocity on the wall is set to zero. With no fluid flow trough the wall the convective fluxes can be set to zero. If the wall is fixed also the tangential velocity on the wall is zero, indicating the no slip

condition. A moving wall can also have a no slip condition if the fluid has the same tangential velocity as the wall. In a piston or flap type wave maker a impermeable moving wall will force the fluid into motion. For a free slip wall the tangential fluid velocity are not affected by the wall and only the normal velocity on the wall is set to zero, $U_{n,wall} = 0$. On a free slip wall also the wall shear stress is set to zero, $\tau_w = 0$. In connection with turbulence the roughness can be specified. A wall can also be used as a thermal boundary with heat convection.

Symmetry plane

In steady flows symmetric solutions can be obtained. If the geometry and the flow field is assumed to be symmetric, a symmetry plane can be used. By only solving half the domain and introduce a symmetry plane in order to get the total solution, computation time can be reduced. On the symmetry plane all the convective fluxes is set to zero. The normal velocity is set to zero, but the velocity gradients normal to the plane can be non zero indicating that the normal stress is non zero. The tangential velocity on the symmetry plane can be non zero, but the normal gradients of the parallel, or tangential, velocity components are zero. The boundary condition requires no input. In a numerical wave tank the tank walls can be set as symmetry condition in order to perform a $2D$ analysis.

Domain Interface

Between sub domains, a connection interface condition has to be set up. A common interface connection is the General Grid Interface (GGI) condition which connect two different regions to each other. The GGI connection is a implicit and conservative connection which also can be used in cases where the grid on both sides does not match. A balance of the mass and momentum fluxes is achieved by evaluating the fluxes on each side of the interface.

3.2 Potential Wave Theory

The wave theory used in the present work is based on the potential theory. In the potential theory three well known assumptions can be summarized:

1. *Incompressible*
2. *Inviscid*
3. *Irrotational*

The incompressible assumption states that the density, ρ is constant. In a inviscid fluid the viscosity is equal zero. Irrotational flow means that the curl of the velocity is zero, or in other words the local angular velocity in a given point is zero. By these assumptions together with the given boundary conditions a velocity potential for regular waves can be expressed.

3.2.1 Linear wave theory (Airy theory)

A linear velocity potential is given in equation 3.27 valid for all water depths with linear assumptions for the wave parameters. The surface elevation for this potential is given in equation 3.28.

$$\phi = \frac{g\zeta_A}{\omega} \frac{cosh k(h+z)}{cosh kh} sin(kx - \omega t) \tag{3.27}$$

$$\zeta = \zeta_A cos(kx - \omega t) \tag{3.28}$$

From the derivatives of the velocity potential the wave velocities can be expressed, given in equation 3.29 and 3.30. The dynamic pressure is also evaluated from the velocity potential, given in equation 3.31.

$$u = \frac{\partial \phi}{\partial x} = \frac{kg\zeta_A}{\omega} \frac{coshk(h+z)}{coshkh} cos(kx - \omega t) \tag{3.29}$$

$$w = \frac{\partial \phi}{\partial z} = \frac{kg\zeta_A}{\omega} \frac{sinhk(h+z)}{coshkh} sin(kx - \omega t) \tag{3.30}$$

$$p_{dyn} = -\rho \frac{\partial \phi}{\partial t} = \rho g\zeta_A \frac{coshk(h+z)}{coshkh} cos(kx - \omega t) \tag{3.31}$$

The linear surface elevation and velocities will be used as input in the first modeled method of a numerical wave tank. In the theoretical approach the linear dynamic pressure will be integrated to find pressure forces. The surface elevation and velocities will also be used in comparison with numerical and experimental results.
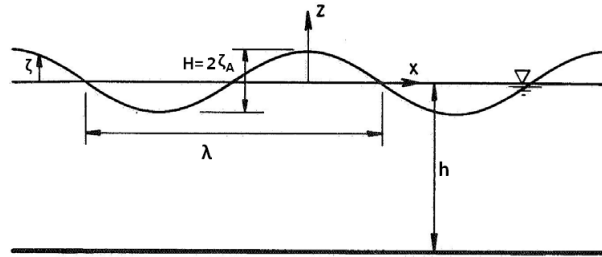
Figure 3.3: Wave characteristics

The linear assumption will limit these equations. From non dimensional wave parameters linearity criteria can be given. In linear wave theory the wave steepness is assumed small resulting in convective accelerations assumed small compared to the local acceleration. The assumed small ratio between the convective and local acceleration gives $k\zeta_A << 1$ which must hold in deep water. In shallow water both $kh << 1$ and $\zeta_A/h << 1$ must hold since we can not assume kh to be large. Refer to Myrhaug (2006) for more details. A common rule of thumb categorize deep water when $h > \lambda/2$. In deep water the linear wave theory is valid for $k\zeta_A << 1$. In the performed experiments in the student wave tank presented in chapter 7, the water depth is $h = 1m$. With the the wave number given as $k = \frac{2\pi}{\lambda}$, the linear criteria will be $\lambda >> 2\pi = 6.28m$ and $\zeta_A << 1m$ in shallow water. The Ursell number given in equation 3.32 can be used as a measure of the linearity assumption in shallow water. A Ursell number in order of unity will indicate strong non linearity Y.Wu (1981). A reduction in Ursell number will increase the linearity.

$$U_r = \frac{k\zeta_A}{(kh)^3} \tag{3.32}$$

Due to the water depth of $h = 1m$ in the student wave tank the wave height must be short and wave lenght long in order to achieve linear waves. With a variety of wave heights and wave lengths in the present work, some waves will definitely be non linear.

3.2.2 2nd order Stokes Wave Theory

A more realistic wave theory is given by the Stokes waves. Stokes waves are periodic waves represented by a series expansion with the wave steepness $k\zeta_A$ as parameter. The first series expansion term represents the linear wave theory. Stokes 5th order theory, which represents 5 series expansion terms, are frequently used in design of offshore structures. Here a Stokes 2nd wave theory will be outlined which represents the linear term and a second order term. The Stokes 2nd potential is given in equation 3.33. The Stokes 2nd surface elevation is given in equation 3.34.

$$
\begin{aligned}
\phi &= \phi_1 + \phi_2 \\
&= \frac{g\zeta_A}{\omega}\frac{coshk(h+z)}{coshkh}sin(kx-\omega t) \\
&\quad + \frac{3}{8}\zeta_A^2\omega\frac{cosh2k(h+z)}{sinh^4kh}sin2(kx-\omega t)
\end{aligned}
\tag{3.33}
$$

$$
\begin{aligned}
\zeta &= \zeta_A cos(kx-\omega t) \\
&\quad + \frac{1}{4}k\zeta_A^2\frac{coshk(h+z)}{sinh^3kh}(2+cosh2kh)cos2(kx-\omega t)
\end{aligned}
\tag{3.34}
$$

In similar way as for the linear wave velocity potential, velocities and dynamic pressure can be found from the derivatives of the Stokes 2nd potential. The 2nd order velocities and dynamic pressure first term is equal to the linear term. In addition a 2nd order term is added. The velocities is given in equation 3.35 and 3.36 and the dynamic pressure is given in equation 3.37.

$$
\begin{aligned}
u &= \frac{\partial\phi}{\partial x} = \frac{kg\zeta_A}{\omega}\frac{coshk(h+z)}{coshkh}cos(kx-\omega t) \\
&\quad + \frac{3}{4}\zeta_A^2\omega k\frac{cosh2k(h+z)}{sinh^4kh}cos2(kx-\omega t)
\end{aligned}
\tag{3.35}
$$

$$
\begin{aligned}
w &= \frac{\partial\phi}{\partial z} = \frac{kg\zeta_A}{\omega}\frac{sinhk(h+z)}{coshkh}sin(kx-\omega t) \\
&\quad + \frac{3}{4}\zeta_A^2\omega k\frac{sinh2k(h+z)}{sinh^4kh}sin2(kx-\omega t)
\end{aligned}
\tag{3.36}
$$

$$
\begin{aligned}
p_{dyn} &= -\rho\frac{\partial\phi}{\partial t} = \rho g\zeta_A\frac{coshk(h+z)}{coshkh}cos(kx-\omega t) \\
&\quad + \rho\frac{3}{4}\zeta_A^2\omega^2\frac{cosh2k(h+z)}{sinh^4kh}cos2(kx-\omega t)
\end{aligned}
\tag{3.37}
$$

The criteria regarding wave parameters in Stokes 2nd theory can be found from checking convergence by require the second order term to be smaller than the first linear term. In addition the criteria require a realistic surface with a single crested wave profile. From these two requirements it can be shown that the criteria for Stokes 2nd order waves are $Ur < \frac{1}{3}$ and $\frac{\zeta_A}{h} < 0.26$ Myrhaug (2006) and Dean & Dalrymple (1984).

A consequence of the second order wave velocity potential is that the wave crest and wave trough will not be similar as in linear theory. The total wave height, H, will in the other hand be similar as in linear theory and the surface profile will still be symmetric with respect to a vertical axis trough a wave crest or wave trough. The Stokes 2nd order amplitudes can be evaluated since the wave crest appears at $kx - \omega t = 0$ and the wave trough appears at $kx - \omega t = \pi$. The Stokes 2nd order crest and trough amplitudes is given in equation 3.38. By adding the wave crest amplitude and the wave trough amplitude the total wave height becomes similar as in linear theory. In 3.4 a comparison of the wave profiles is

given, showing the effect of the wave crest and wave trough. In addition the fluid particles will not move in closed orbital motions, but will drift in the propagation direction of the waves resulting in a net mass transport.

$$\frac{\zeta_C}{\zeta_A} = 1 + \frac{3}{4}\frac{k\zeta_A}{(kh)^3}$$

$$\frac{\zeta_T}{\zeta_A} = 1 - \frac{3}{4}\frac{k\zeta_A}{(kh)^3} \tag{3.38}$$

Figure 3.4: Comparison between Stokes and Linear wave profile (From Myrhaug (2006)).

3.3   Breaking wave

Another criteria which limits the waves is the breaking criteria. If the wave steepness, $S = \frac{H}{\lambda}$, becomes too large the wave will break. The wave theory will therefore not be valid with wave parameters when braking waves will occur. The critical value for the wave steepness is given as $S_{crit} = 1/7$ for regular waves in deep water. When the wave height become higher than $1/7$ wave length in deep water the wave will break. In an arbitrary water depth the breaking criteria can be found by the *Miche criterion* given in equation 3.39, Miche (1951).

$$\frac{H}{\lambda} = \frac{1}{7}tanh(5.5\frac{h}{\lambda}) \tag{3.39}$$

In deep water h becomes large and equation 3.39 gives the deep water steepness criteria. In shallow water when the water depth is small compared to the wave length, $tanh(5.5\frac{h}{\lambda}) \approx 5.5\frac{h}{\lambda}$, and the criteria becomes $H_{crit} = 0.78h$ (based on solitary wave theory).
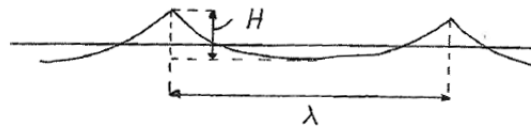
Figure 3.5: Definition of wave height and wave length (From Myrhaug (2006)).

3.4   Dimensionless parameters in Oscillatory flows

In addition to the already mentioned length scaled Reynolds number, the amplitude based Reynolds number and The Keulegan Carpenter number is of importance in a oscillatory flow. The Keulegan Carpenter

number, given in equation 3.40, can be used to classify the flow behavior.

$$KC = \frac{U_0 T}{D} \tag{3.40}$$

In equation 3.40 U_0 is the water particle velocity amplitude, T is the oscillation period and D is a characteristic length. In regular waves the oscillation period is defined as the wave period. The KC number gives the ratio between the particle orbital diameter and the structural diameter or length scale. When the particle velocity increase the Reynolds number will increase and the flow will be more turbulent. If the wave period is large the flow will stabilize during one period and give vortex shedding. When the wave period goes to infinity the flow goes towards a steady current flow. A high wave period indicate a high KC number and drag forces similar as in a steady current. On the other hand if the wave period is small enough the flow will not be stable before it turns in opposite direction. The oscillation will take place within the wake of the structure and in some cases give important drag forces dependent of the structure geometry. The KC parameter is therefore important when calculating wave forces which is dependent of the flow separation and vortex shedding on the structure.

The amplitude based Reynolds number, given in equation 3.41, can be used to relate turbulence in free surface waves.

$$Re_A = \frac{aV}{\nu} = \frac{a^2 \omega}{\nu} \tag{3.41}$$

In equation 3.41 a is the depth dependent wave amplitude, $V = \omega a$ is the orbital velocity and ν is the kinematic viscosity. The amplitude based Reynolds number was originally given as a hypothesis to relate the transition from laminar to turbulence for the wave orbital motion published by Babanin (2006). Normally free surface wave motion is assumed irrotational due to the assumptions from potential theory, with no shear stresses and indirectly no turbulence, given by Pleskachevsky et al. (2010). In a real fluid the the inviscid and irrotational assumption is not valid and shear stresses will be produced. Free surface waves has two length scales, the wave length λ and the wave amplitude $\zeta_A = a_0$. The wave amplitude will be more related to the water particle motion than the wave length since the wave amplitude equals the radius of the orbital motion in deep water. The wave amplitude will also decay from the free surface giving a depth dependence of the amplitude based Reynolds number. In the article published by Babanin (2006) experimental values of the amplitude based Reynolds number was performed in order to define the ocean's Mixed Layer Depth (MLD). An approximate critical value of $Re_{A,cr} = 3000$ for the transition between laminar and turbulence of the wave induced motion was confirmed. The critical value of the amplitude based Reynolds number can be used in a numerical approach of non breaking free surface waves to define turbulence in the wave particle motion. In the present work mostly shallow water has been studied. In shallow water the orbital path of the water particles will be elliptic instead of circular. In order to make a conservative relation to the amplitude based Reynolds number, the horizontal radius of the elliptic orbital path will be used for the depth dependent wave amplitude. The depth dependent horizontal water particle displacement from Dean & Dalrymple (1984) is given in equation 3.42 and the used amplitude based Reynolds number is given in equation 3.43. The critical depth z_{crit} will be the depth where the amplitude based Reynolds number will be below the critical value $Re_{A,cr} = 3000$.

$$a_x(z) = \zeta_A \frac{cosh k(h + z)}{sinh kh} \tag{3.42}$$

$$Re_A(z) = \frac{\left(\zeta_A \frac{cosh k(h+z)}{sinh kh}\right)^2 \omega}{\nu} \tag{3.43}$$

3.5   Wavemaker Theory

In all laboratory experiments with water waves the wavemaker is important to produce the wanted waves. The production of waves can be done by many different methods and are in fact a common result from any moving object in a free surface fluid. In the wavemaker theory a relation between the free surface motion and the wavemaker object must be set up to produce the wanted waves. One of the most easiest ways to produce waves is to move a piston , or a wall, normal to the free surface periodically. Dean & Dalrymple (1984) give a brief overview of the wavemaker theory for a piston and a flap. In figure 3.6 a simplified shallow water piston-type wavemaker theory is shown.
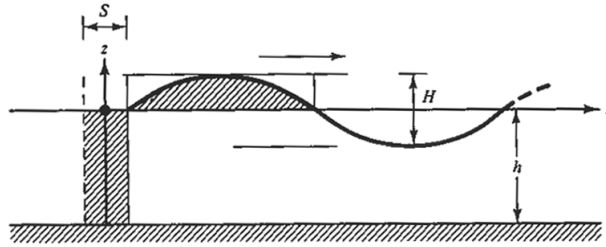
Figure 3.6: Simplified shallow water piston-type wavemaker theory of Galvin (from Dean & Dalrymple (1984)).

The principle is to relate the volume of water displaced by the piston over a whole stroke to the volume of water under a wave crest.The result from the water conservation given for simplified shallow water wave theory gives the relation in equation 3.44. For a bottom hinged flap the result becomes as given in equation 3.45. In equation 3.44 and 3.45 $H = 2\zeta_A$ is the wave height, $S = 2S_A$ the piston stroke, $k = 2\pi/\lambda$ the wave number and h the water depth.

$$\left(\frac{H}{S}\right)_{piston} = kh \tag{3.44}$$

$$\left(\frac{H}{S}\right)_{flap} = \frac{kh}{2} \tag{3.45}$$

The complete wavemaker theory is deduced from the same boundary value problem for two dimensional waves in potential theory. The kinematic and dynamic boundary conditions for the free surface and the no-slip condition for the bottom boundary are similar. Only difference is the lateral conditions which must take the piston, or flap, motion into account. The horizontal displacement is given in equation 3.46 and the stroke is given in equation 3.47 with z positive upwards and origin at the free surface. If the water depth is larger than the hinged flap the stroke motion of the flap will only be valid above the hinged point,h_h with no motion below.

$$x = \frac{S(z)}{2} sin\omega t \tag{3.46}$$

$$S(z) = \begin{cases} S, & \text{piston motion} \\ S\left(1 + \frac{z}{h_h}\right), & \text{flap hinged motion} \end{cases} \tag{3.47}$$

The final equations for the Stroke motion from solving the boundary value problem derived by Dean & Dalrymple (1984) is given in equation 3.48 for the piston and 3.49 for the bottom hinged flap. For the flap with a hinged point above the bottom the equation is derived in similar manner and shown in

equation 3.50 taken from Silva et al. (2010). In the equations 3.48, 3.49 and 3.50 k is the wave number for progressive waves, h the water depth and h_{flap} the height of the hinged flap.

$$\left(\frac{H}{S}\right)_{piston} = \frac{2(cosh(2kh-1)}{sinh(2kh)+2kh} \tag{3.48}$$

$$\left(\frac{H}{S}\right)_{flap} = 4\frac{sinh(kh)}{kh}\frac{khsinh(kh)-cosh(kh)+1}{sinh(2kh)+2kh} \tag{3.49}$$

$$\left(\frac{H}{S}\right)_{flap_h} = -\frac{2sinh(kh)}{kh_{flap}}\left(\frac{-cosh(-kh_{flap+kh})+cosh(kh)-sinh(kh)kh_{flap}}{cosh(kh)sinh(kh)+kh}\right) \tag{3.50}$$

In figure 3.7 the wave height to stroke ratio, H/S is shown for relative depths. In figure 3.7 the dotted lines represents the simplified wavemaker theory. The wavemaker theory is based on linear 1st order potential theory in shallow water with assumed small motions. The same limitations given for linear wave theory will limit the wavemaker theory. In laboratory wave basins the wavemaker theory are usually used to give the transfer function used as input for the physical wavemaker system. In similar manner the wavemaker theory can be used in a numerical wave tank to make numerical waves.
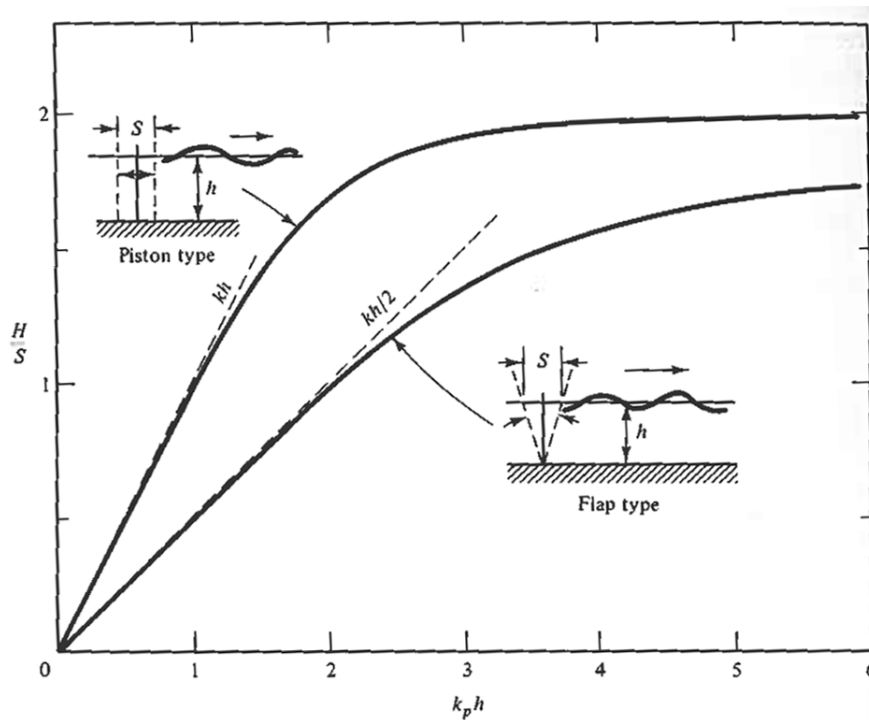
Figure 3.7: Wave height to stroke ratios versus relative depths from plane wavemaker theory (from Dean & Dalrymple (1984)).

Chapter 4

Numerical Wave Tank

In the latest years Computational Fluid Dynamics (CFD) has become a popular and common numerical analysis tool for engineers. In CFD a domain of interest is modeled by discretized elements. In each element a set of fundamental conservation equations is solved for each time step. The results in each element are then used as input for the next time step. From this method a time dependent dynamic analysis can be simulated. There are today a lot of different numerical schemes and numerical methods for fluid dynamics, both commercial softwares, open source codes and in house codes in the industry and at universities. For the commercial softwares it is often combined with a nice interface which makes it easier to perform analysis. For the open source and in house codes there might be more opportunities and easier to direct affect the solver equations but often not as easy to perform analysis due to limited interface. Therefore most commercial softwares has been used for engineers in a time limited and profit based industry.

In connection with increased computer power and fast development in numerical fluid dynamic solvers, CFD analysis has been used in many new areas in the last years. A Numerical wave tank (NWT) has been one of the new area with increasing activity, especially for marine engineers. With a numerical wave tank one can do almost similar analysis as many of the more expensive experiments performed in physical water basins. For many companies this will reduce both experimental costs and time performing analysis. Due to a lot of numerical parameters involved in a numerical setup, CFD analysis usually has to be validated with experimental data. In the present time, CFD is not capable of taking over performing physical experiments. CFD analysis can instead reduce experimental test conditions and perform parameter studies. In this way physical experiments and CFD analysis together can be a very effective tool and give faster and more accurate results. There are today several different commercial CFD softwares which are capable for wave modeling. In the present work ANSYS Workbench version 12.0 and 13.0 has been used to model a 2 dimensional numerical wave tank with ANSYS DesignModeler for geometry, ANSYS Meshing for meshing and ANSYS CFX for numerical setup and solver.

First in the present chapter, general settings used in ANSYS CFX is outlined. Next, four cases has been studied and given in table 4.1. Two different methods have been used to model numerical waves. First method in case 1 use a inlet velocity profile method. The velocity profile from linear wave theory and the linear wave elevation is given as input condition to the domain inlet. The second method in case 2, 3 and 4 use a piston or flap wavemaker method. The inlet wall is given a specified oscillation motion similar to a wavemaker in a physical wave tank.

	Studied Cases
1	Inlet Velocity Profile Method
2	Piston and Flap Wavemaker Method
3	Comparison with a Validation Case
4	Student Wave Tank

Table 4.1: Studied Cases.

4.1 General settings in ANSYS CFX

4.1.1 Domain and meshing

The CFD analysis is carried out using ANSYS Workbench. In the Workbench you get an overview of your project and can assemble the neseccary programs in boxes connected to each other as shown in figure 4.1. The domains used has been made in ANSYS DesignModeler. A domain was made by a set of two dimensional blocks and then equally extruded a small length. All the blocks was assembled into one part in order to make a continuously mesh. Further the mesh was made in ANSYS Meshing. Here a sweep method was used defined with only one element in the extruded direction in order to have a two dimensional analysis. On each block side, except for the extruded sides, a sizing method was used and number of divisions was set for each side. By this method a structural mesh was defined. In addition named sections was made in order to link the different boundaries with boundary conditions in CFX Pre. The number of elements and design of the mesh are important parts since it will directly influence the analysis time and solution. In the article given by Silva et al. (2010) some mesh size parameters are suggested for modeling numerical waves. The article suggest a aspect ratio of $\frac{\Delta z_{min}}{\Delta x} = 4.16$ with $\Delta x = 0.052$ and $\Delta z_{min} = 0.013$. In their case this gave 10 elements per wave height and 111 elements per wave length. In general free surface modeling is sensitive to the mesh, and especially the fineness around the free surface. A aspect ratio less then 10 and mesh normal to the free surface is suggested for free surface flows by Godderidge et al. (2008).
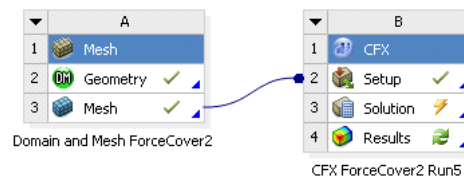
Figure 4.1: A project in Workbench.

4.1.2 Numerical settings in CFX Pre

In CFX Pre all the numerical settings are set. The domain in a numerical wave tank consist of two fluids, water and air. Density and viscosity used is given in table 4.2.

Fluid	Density $\rho \ [kg/m^3]$	Dynamic viscosity $\mu \ [kg/ms]$
Water	1025	$8.899e-4$
Air	1.185	$1.831e-5$

Table 4.2: Fluid specification.

In table 4.3 the general numerical settings is given. In all cases a transient analysis and a free surface model has been used. In order to have a pure 2nd order spatial discretization scheme the advection blend

factor was set equal 1 in all cases. A smaller blend factor will give lower accuracy and a blend factor of 0 indicate 1st order upwind spatial discretization. The robustness also increase for a lower blend factor. Alternatively the *high resolution* option can be used where the blend factor varies throughout the domain based on the local solution field. The 2nd order *Backward Euler Scheme* is an implicit time-stepping scheme recommended in general for transient runs and was used in all cases. The convergence criteria was set to a reasonable low value and number off coefficient loops was for most cases set to $3 - 6$ loops in each time step.

In a free surface flow the two phases are defined by use of a volume fraction for each phase as shown in equation 4.1 and 4.2. In equation 4.1 and 4.2 Z_{wl} is the mean water level, set equal to $0[m]$, and a built in step function is used. A water volume fraction value of 1 represents water and a value of 0 represents no water. The free surface will in this way be defined at a volume fraction of 0.5. The fluid model was defined as a homogeneous multiphase model with a interface compression level of 2. A homogeneous multiphase model means that the flow field is sheared for the two fluids. Only one set of momentum equations is needed since the velocity field will be identical for the two phases. The compression level sharpens the interface and gives faster convergence, but it also increase computation time. In the multiphase control a coupled volume fraction was selected. As a comment the homogeneous multiphase model is recommended for flows were the free surface is well defined. For flows were mixing occur, for example breaking waves, the inhomogeneous multiphase model should be used.

Parameter	Settings
Version	$CFX12.0$ and 13.0
Model	Transient
Turbulence	Laminar / $K - \epsilon$ / SST
Advection Scheme	High Resolution / Specified blend =1
Time Scheme	2nd order Backward Euler
Multiphase model	Homogeneous
Interphase compression	Level 2
Volume fraction	Coupled
Mean water level	$Z_{WL} = 0.0m$
Isothermal	$T = 20°C$

Table 4.3: General Numerical Settings.

$$AirFrac = step\left(\frac{z - Z_{wl}}{1.0[m]}\right) \tag{4.1}$$
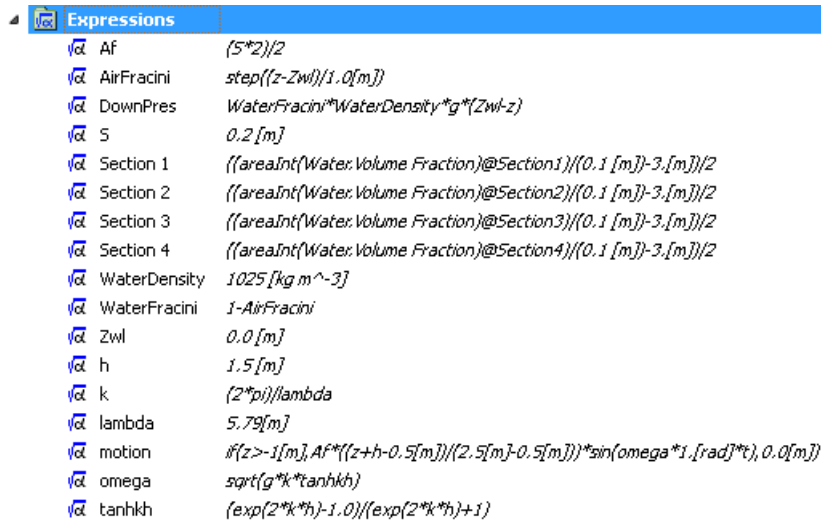
$$WaterFrac = 1 - AirFrac \tag{4.2}$$

Isothermal heat transfer and buoyancy is used in all cases. The buoyancy reference density is set equal to density of air, ρ_{air} and given a reference position at $z = 0.8m$ in order to be well above the water phase. In the solver control the advection discretization scheme, time discretization scheme, convergence criteria and number of convergence loops are set. The numerical settings are specified under each separate studied case.

Running in parallel will in many cases be suggested if available due to reduced computation time. In the present work the parallel environment was used in the first cases with 4 nodes. Due to some hard convergence in combination with the multiphase model, running in serial was selected. In the ANSYS solver manual ANSYS (2010) the convergence issue for free surface flows in parallel is noted and some advices given.

4.1.3 CFX Expression Language

The formulas used to set up a simulation in CFX Pre can be expressed with the built in CFX Expression Language (*CEL*). A example of the *CEL* expressions used for modeling a flap wavemaker is shown in figure 4.2. In CFX there are many built in functions which can be used and combined to make own functions and expressions. *CEL* gives the user opportunities to for example express new boundary conditions and fluid specifications which is useful when modeling specific cases. In a numerical wave tank the wave formulas can be expressed by *CEL* expressions. The surface elevation for example is defined by implementing the equations 4.1 and 4.2 in CFX Pre with *CEL* expressions . Refer to ANSYS CFX user manual ANSYS (2010) for more information regarding the *CEL* language and the built in functions available.

Figure 4.2: CEL expressions used for modeling a flap wavemaker

In order to capture the surface elevation at a given position as function of time, the *CEL* language was used. A cross sectional plane at the wanted position of the numerical wave gauge was made. From the definition of the volume fraction, which is defined 1 in the water phase, 0.5 at the free surface and 0 in the air phase, the vertical position of the free surface could be defined. The built in function *areaInt* was used to integrate the water volume fraction over the cross section. By dividing the area integral with the unit width of the tank and relocate the vertical position to the mean free surface position, the actual water height at the given time was found. In equation 4.3 the expression used in CFX is shown. In the solver a defined CEL expression can be monitored. In that way the surface elevation could be monitored during the analysis.

$$z(t) = \left(\frac{(areaInt(water.VolumeFraction)@section)}{b} \right) /2 - h \qquad (4.3)$$

In equation 4.3 the *areaInt* is a built in area integral function, *water.Volume Fraction* is the actual water volume fraction at a given z position, *section* is the studied cross sectional section and h is the water depth.

4.2 Case 1: Inlet Velocity Profile Method

The first method tried out to model a numerical two dimensional wave tank was based on specifying the water particle velocity and the wave elevation at the inlet. Linear wave theory for a general water depth

was used as input and regular waves was produced by specifying the wave elevation at the inlet by the volume fractions. In figure 4.3 the domain used is shown.
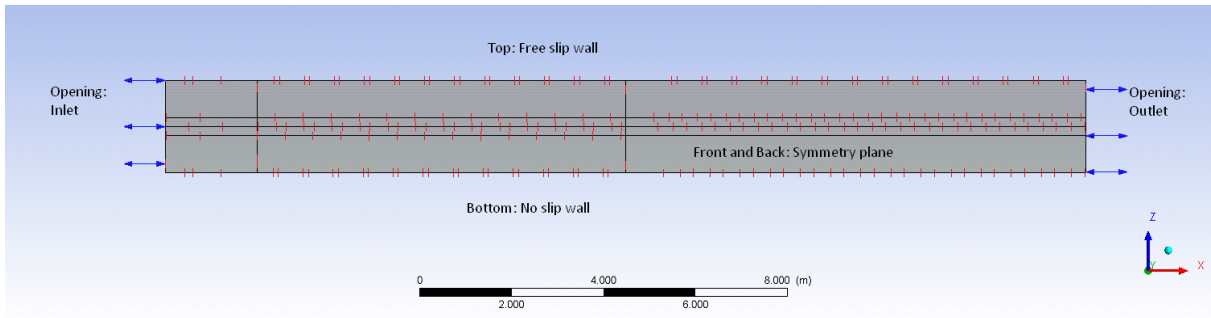
Figure 4.3: Domain Linear Velocity profile

The mesh was made from the suggested Δx and Δz values from the article published by Silva et al. (2010) given under section 4.1.1 in chapter 4. The specific used mesh values are given in table 4.4 and a close view of the mesh can be seen in figure 4.4. In table 4.4 Δx represents the horizontal element size in the domain, and Δz represents the vertical element size in the uniform area close to the free surface with $\pm 0.2m$ extension in the different phases. Air_z and $Water_z$ represents total number of elements vertically in the above air and below water phase respectively. The elements in the above and below phases are biased with coarser elements close to the top and bottom boundaries. In figure 4.5 the location of the mesh parameters is shown.

Parameter	Setting
Domain length	$20m$
Water depth	$0.8m + 0.2m$
Air height	$0.8m + 0.2m$
Extruded width	$0.01m$
Number of Elements	140000
Δx	0.02
Δz	0.0033
$\Delta x/\Delta z$	6.06
Air_z	10
$Water_z$	10

Table 4.4: Mesh details in linear velocity profile
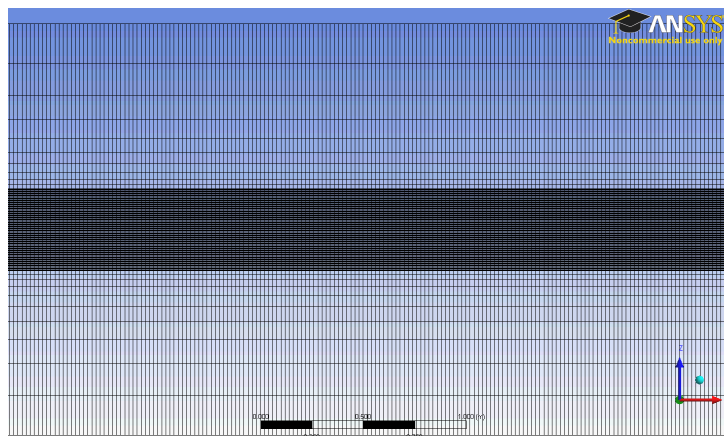
Figure 4.4: settings in Case 1 with a velocity profile input method.
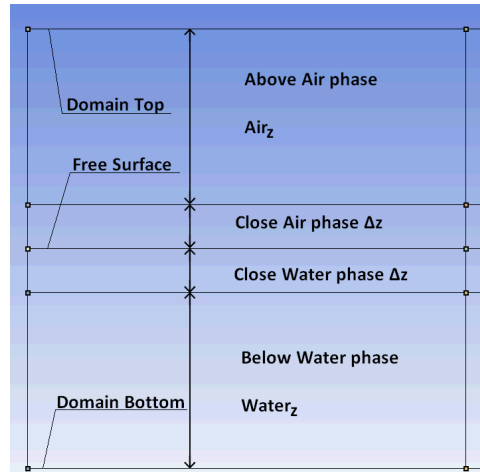
Figure 4.5: Placement of the mesh parameters.

4.2.1 Boundary Conditions and numerical settings

At the inlet a opening boundary condition was chosen with specified velocities in x and z direction. The velocities was given from the linear wave velocity potential specified in CFX with CEL formulas. At the top a free slip wall boundary was chosen. At the bottom a no slip wall condition was chosen. At the outlet a opening outlet was chosen with a specified static pressure. Here the pressure was taken as the static pressure at the mean free surface. The static pressure is given in equation 4.4 where f_w is the water volume fraction and z_{mwl} is the initial water level. This is a crucial boundary condition which prevent the free surface to move dynamically at the outlet. This will lead to reflections of the waves passing through. A static pressure condition can be used as a first option if the domain is large enough and simulation time shorter than the time used for the waves to reach the outlet. The domain sides was set as symmetry planes. In order to compare any difference the last run was performed with a beach at the domain end wall. The beach had slope $1 : 3$ and modeled as solid wall.

$$p_{static} = f_w \rho g (z_{mwl} - z) \tag{4.4}$$

In the first test runs the initial conditions was set to zero velocities and static pressure conditions with free surface at the Z_{wl} position. Due to some problems with convergence in the first iterations the initial conditions was modified. In order to achieve better convergence the linear wave theory was used as input to the velocities and surface elevation for the first two meters along the tank. To avoid sudden changes the initial condition was damped gradually out after the first two meters towards zero velocity and Z_{wl} position for the rest of the tank length. The initial surface elevation is shown in figure 4.6. The reason for the noncontinuous line in 4.6 is because of the initial discrete volume fraction values. The free surface, which is defined at a water volume fraction of 0.5, will in the solver be smoothed over 2-3 grid cells. The initial values, which in the *CEL* formulas are continuous, will therefore be noncontinuous in the first step. The same reason will sometimes give small unnatural steps at the initial free surface due to the discrete initial volume fractions. The numerical settings used is given in table 4.5. Regarding the turbulence settings *Laminar* means no turbulence fluctuation velocities. In a numerical wave tank with only free surface waves with small steepness a laminar turbulence model can be used. Run 1, 5 and 6 was performed with the $K - \epsilon$ model and there was not seen any difference between the two turbulence methods. Regarding the wave elevation, the convergence criteria will in most cases not be reached, resulting in always running maximum number of coefficient loops.

In table 4.6 wave- and numerical parameters are listed for all the performed runs. A time discretization study was performed in run $1 - 4$ with similar mesh and numerical settings but different time step Δt.
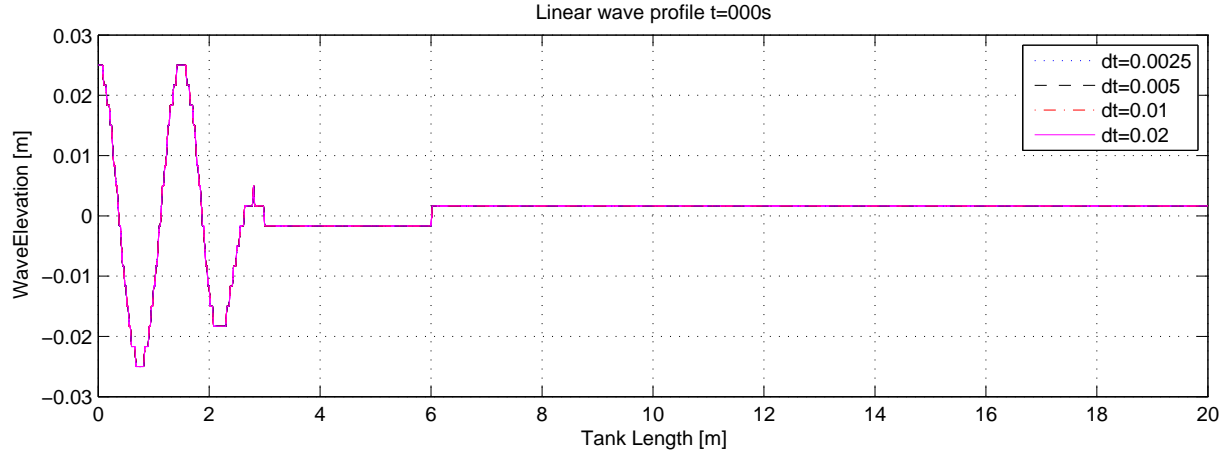
Figure 4.6: Initial condition free surface elevation at $t = 0.0s$

Parameter	Setting
Version	CFX 12.0 and CFX 13.0
Model	Transient
Turbulence	Laminar and $K - \epsilon$
Advection Discretization Scheme	Specified blend, blend factor =1
Time Discretization Scheme	Second order Backward Euler
Coefficient loops	$Min = 3 \, Max = 6$
Convergence criteria	$RMS < 1E - 5$
Prcision	Single
Total time	$25s$
Time step	$\Delta t = [0.0025 - 0.02]s$

Table 4.5: Numerical settings for Linear velocity profile

The time discretization study was performed in CFX 12.0. The next, run 5 and 6, was done with CFX 13.0. In run 6 a beach with slope 1:3 was used. From the choice of wave length and water depth, $1m > (1.5m/2)$, deep water can be assumed. With $\lambda = 1.5m$ the wave period will be $T = 0.98s$ according to linear wave theory. The wave steepness $H/\lambda = 1/30$, is well below the breaking criteria. The linearity criteria $k\zeta_A = 0.105 << 1$ can be discussable. The Ursell number, $Ur = \frac{k\zeta_A}{(kh)^2} = 0.0014$, is in the order of 10^{-3} indicating linear relations.

Run	Version	λ [m]	ζ_A [m]	Δt [s]	$T/\Delta t$	$Elements/\lambda$	$Elements/2\zeta_A$
1	CFX 12.0	1.5	0.025	0.02	49	75	15.1
2	CFX 12.0	1.5	0.025	0.01	98	75	15.1
3	CFX 12.0	1.5	0.025	0.005	196	75	15.1
4	CFX 12.0	1.5	0.025	0.0025	392	75	15.1
5	CFX 13.0	1.5	0.025	0.01	98	75	15.1
6	CFX 13.0	1.5	0.025	0.01	98	75	15.1

Table 4.6: Numerical settings specified for each run in comparison with validation case

In table 4.7 the critical depth z_{crit} and the depth based Froude number Fn is given. The critical depth is defined from where the amplitude based Reynolds number is equal or below the critical value $Re_{A,crit} = 3000$. The amplitude based Reynolds number given from Babanin (2006) indicate a turbulent mixing layer above the critical value of 3000. The depth where the amplitude based Reynolds number exceeds the critical value is indicated as the critical depth. Below the critical depth the mixing layer is assumed

laminar. The depth based Froude number Fn classifies the fluid flow. A Froude number less than unity indicate sub critical flow and larger than unity indicate supercritical fluid flow. In table 4.7 the critical depth is only $6cm$ below the surface indicating deep water and low wave steepness. The maximal Froude number indicate sub critical flow.

Critical depth: z_{crit} ($Re_A <= 3000$)	$-0.06m$
Maximal Froude number Fn	0.064

Table 4.7: Critical depth where the amplitude based Reynolds number is less og equal to the critical value 3000, and the depth based Froude number. Origo located at the free surface gives negative z values towards the bottom.

4.2.2 Results

In figure 4.7(a) a contour plot of the water volume fraction at the start of the domain after $t = 15s$ is shown. With correct aspect ratio the free surface becomes a thin line and the wave elevation seems reasonable. In figure 4.7(b) a close view of the free surface is shown. The surface is smoothed over approximately 3 elements. In relation to the initial values in figure 4.6 the surface will be defined on the element boarder and not smoothed as shown here in figure 4.7(b).
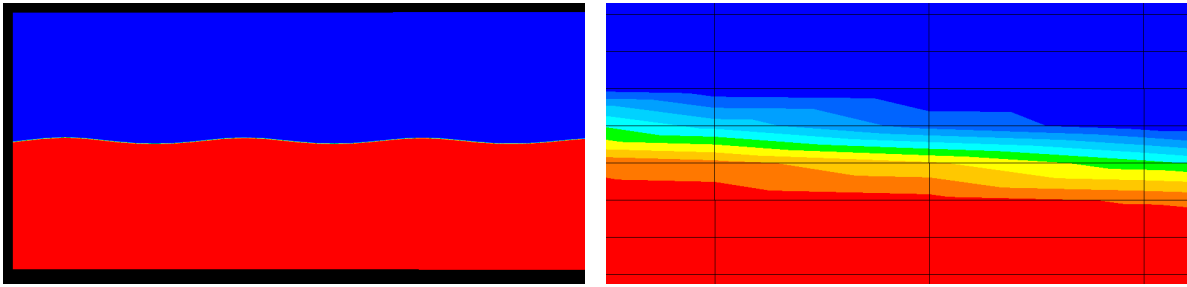
(a) Volume fraction at $t = 15s$ for the first part of the domain. Blue indicate air and red indicate water.

(b) A close view of the water volume fraction around the free surface. Shows the surface smoothing.

Figure 4.7: Contour plot of water volume fraction

Time discretization study

In figure 4.8 the surface elevation along the tank length is plotted for all four runs at $t = 20s$. With a group velocity of $c_g = 0.77m/s$ from linear wave theory, the waves have traveled $15.4m$ after $20s$. After $25s$ the waves would have traveled $19.25m$ which indicates a appropriate choice of simulation time with a tank length of $20m$. A overall tendency shows a damping of the wave amplitude along the tank length. Especially for $\Delta t = 0.02s$ the damping is large and also the wave length is reduced along the tank. For all four runs the wave trough have a shorter amplitude and also a larger damping than the wave crest. The reason for the difference between the wave crest and the wave trough can be due to the velocity input method, influence of the bottom boundary, influence of the outlet condition or the free surface method. Another factor which can explain the overall damping for all runs is the mesh fineness along the tank. The element size was set in accordance with the article by Silva et al. (2010), but they used much longer waves. A wave length of $1.5m$ gives 75 elements per wave length which is below the recommended value of 111 elements per wave length. Regarding the four runs with different time step size, dt, the wave elevation seems to converge with small changes in amplitude and wave length between the results with $\Delta t = 0.01s$, $\Delta t = 0.005s$ and $\Delta t = 0.0025s$. In the article by Silva et al. (2010) the time step was suggested to $T/\Delta t \geq 100$. In all runs the wave period $T = 0.98s$, with $\Delta t = 0.01$ the

ratio becomes $T/\Delta T = 98$. Regarding the CFL number the maximal value was between $1.5 - 2$ in run 4 with the highest time step. For the other runs with smaller time step the CFL number was lower. Refer to appendix C for more figures of the wave elevation along the tank length.
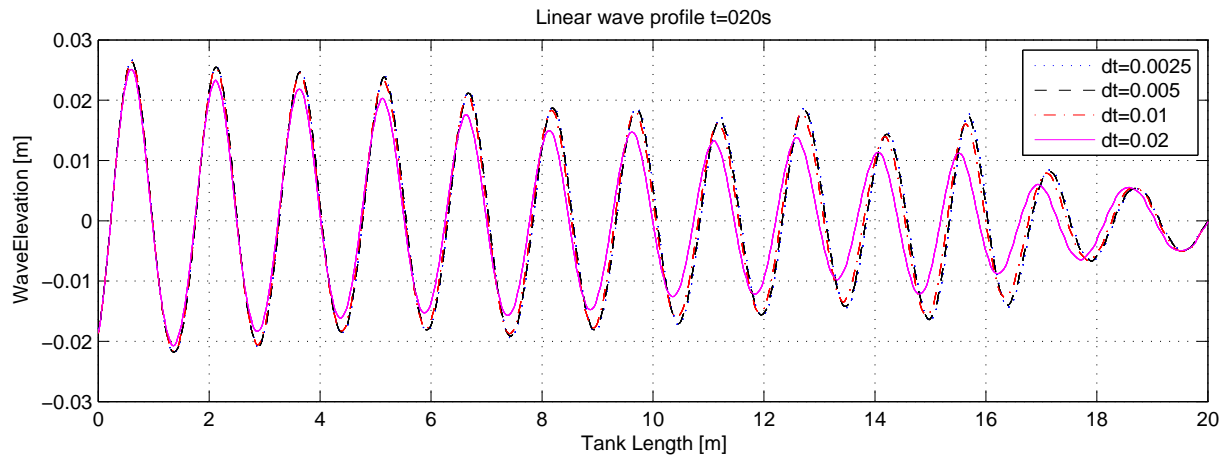
Figure 4.8: Surface elevation along the tank length for run $1 - 4$ at $t = 20s$.

In figure 4.9 the surface elevation as function of time is plotted at section $x = 2m$ and $x = 10m$ respectively. Due to the initial surface elevation from linear wave theory the elevation at $x = 2m$ shows a continuous wave profile. At $x = 2m$ there is small difference between the four runs during the analysis time but the same difference between the crest amplitude and the trough amplitude shown in figure 4.8 is also shown here. At $x = 10m$ the difference between the four runs are larger and the amplitudes are reduced similar as the reduction along the tank. From the time series of the wave elevation the wave amplitude shows a time dependent variation. It seems like a underlying slow frequency affecting the input wave frequency. The reasons can be the velocity input method, numerical reflections or the boundary conditions.
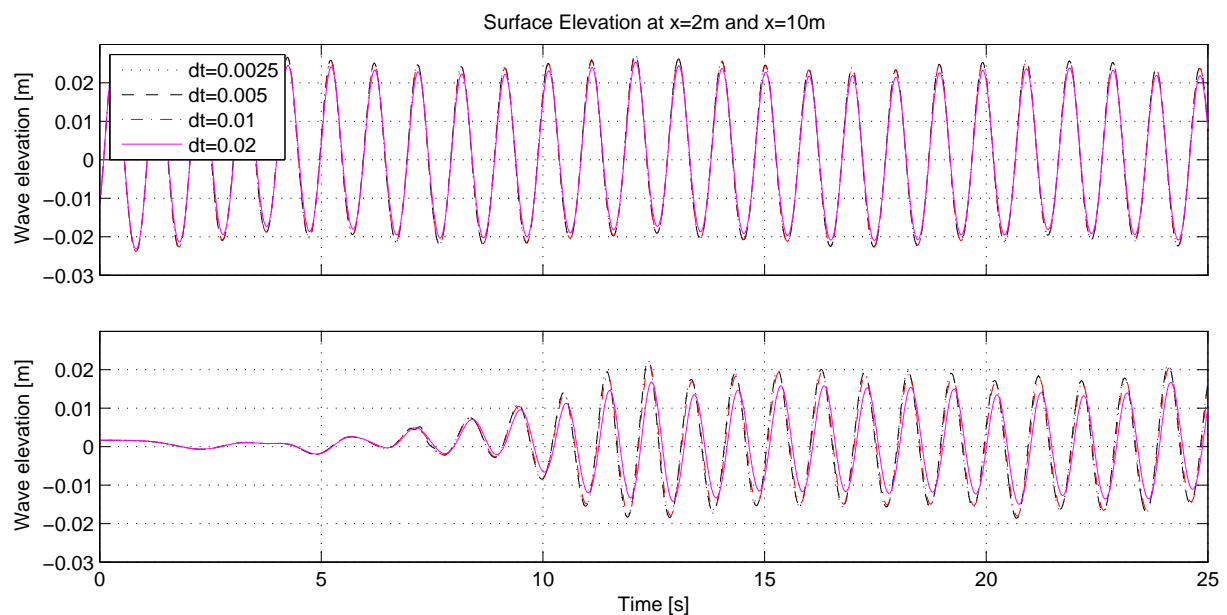
Figure 4.9: Surface elevation at section $x = 2m$ and $x = 10m$ for run $1 - 4$.

In figure 4.10 a contour plot of the superficial water velocity is shown at $t = 5s$. The maximal velocity is located at the wave crests as expected. Close to the bottom boundary the velocity are almost zero, indicating that the deep water assumption is reasonable. Notice the velocity increase at the outlet, which

not is natural after only $5s$. The velocity increase at the outlet can affect the solution further upstreams and be one of the reasons for the variation of the wave crest and wave trough. The reason for the velocity increase at the outlet can be the combination of a no-slip bottom wall condition with large elements towards the bottom and the fixed static outlet pressure condition. With a static water pressure outlet condition the pressure is defined to be the static water pressure in calm water without waves. A no slip condition combined with biased elements gives a large element with zero velocity at the bottom. The outlet will therefore be influenced of the restriction in velocity at the bottom and the wave motion at the free surface resulting in a increased velocity.

Figure 4.10: Contour plot of superficial water velocity at t=5s. Red indicate maximal velocity $[0.2m/s]$ and blue indicate zero velocity $[0m/s]$.

In figure 4.11(a) the measured mean period is plotted for the four runs with different time steps for a section at $x = 2m$. With decreasing time step the period seems to converge to a value just below the input wave period. In figure 4.11(b) the mean wave crest and mean wave trough value is plotted for the four runs at the same section $x = 2m$. The wave crest clearly converge to the correct input wave amplitude with $dt =< 0.01s$. The wave trough also converge, but to a lower value than the input wave amplitude. The reason for the difference between the wave crest and wave trough can be the damping along the tank after a half period. But also the same reasons as stated earlier, the velocity input method, influence of the bottom boundary, influence of the outlet condition or the free surface method which can have affected the wave trough.

(a) Mean period at $x = 2m$. (b) Crest and trough amplitude at $x = 2m$.
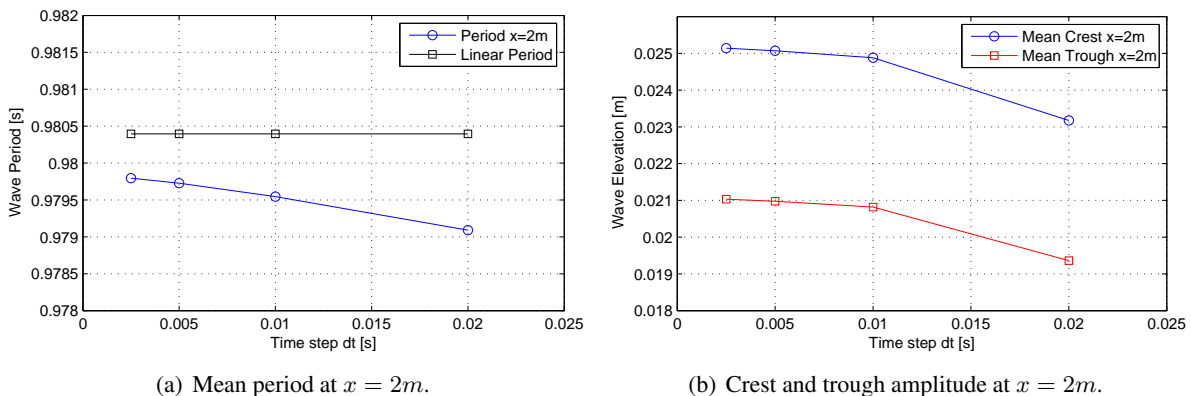
Figure 4.11: Mean period and amplitude at $x = 2m$. Notice the small scale on the vertical axis.

Compare CFX 12.0 **and CFX** 13.0

In the first analysis CFX 12.0 was used. When version 13.0 was available the newest version was chosen. In order to check for any differences regarding modeling numerical waves, the same mesh and analysis settings was used in CFX 13.0 for run 5 and 6. In addition in run 6 the outlet static pressure condition was replaced by a beach with slope $1 : 3$ modeled as a solid wall. In figure 4.12 the wave elevation along the tank for run 2, 5 and 6 are compared. All with similar mesh size and $\Delta t = 0.01s$. No difference is obtained from running CFX 13.0 compared with CFX 12.0. With a beach instead of the static pressure outlet the wave elevation is higher, but still with a small trough amplitude and a variation along the tank. Therefore the variation in amplitude along the tank length will not be due to the static boundary

condition at the outlet, but rather the velocity input method and the mesh fineness. Also the top free slip wall boundary condition can have influence on the wave elevation.
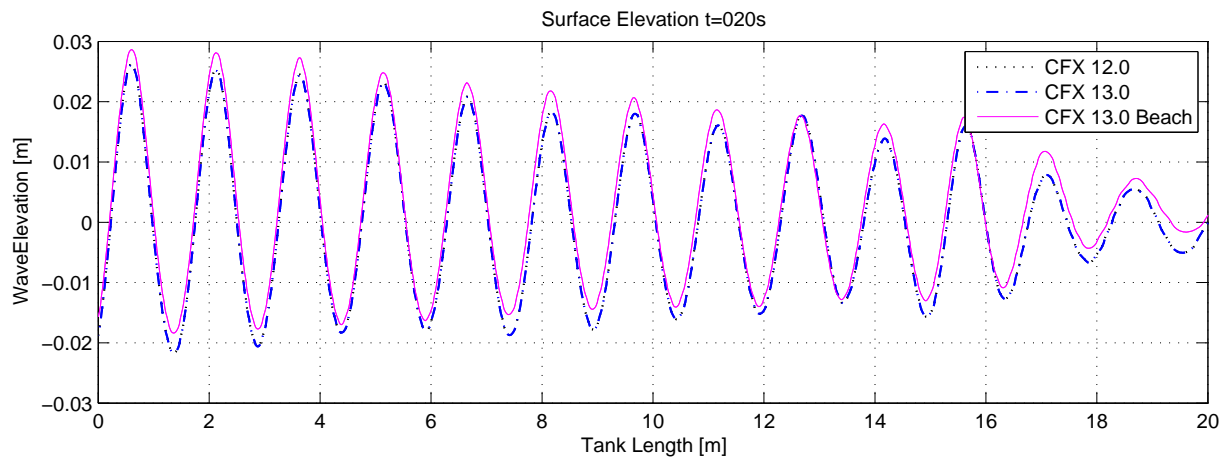
Figure 4.12: Surface elevation along the tank length for run 2, 5 and 6 at $t = 20s$

4.2.3   Conclusion

The linear potential wave theory can be used as input in a CFD analysis to produce deep water gravity waves. The specified input velocity method with a static water pressure at the outlet in combination with large elements close to the bottom wall, will not be a suggested method due to the forced mean water level at the outlet. A variation in amplitude was obtained in all cases with and without the static water pressure outlet boundary condition and for both $CFX12.0$ and $CFX13.0$. The reasons could be the boundary conditions, the mesh fineness or the sudden increase in velocity at the inlet. A slower start of the input velocity is suggested. The mesh fineness along the tank is suggested larger than 75 elements per wavelength to avoid numerical damping. Regarding the time step $T/\Delta t \geq 100$ suggested by Silva et al. (2010) will be recommended. The laminar turbulence setting can be used in a wave tank with only waves and no studied structure affecting the fluid flow. No difference was obtained between CFX 12.0 and CFX 13.0 modeling numerical waves. A beach at the domain end is recommended instead of a opening outlet condition with static wave pressure. A free slip wall at the top boundary can have affected the solution and a opening type boundary condition is suggested.

4.3   Case 2: Piston and Flap Wavemaker Method

A wavemaker can be made by several methods. In a physical wave basin a double flap or a multi flap wavemaker is often used in order to produce both regular and irregular sea. In a numerical sense similar wavemaker as in a physical wave basin can be modeled. In this section three simple wavemakers has been compared. A piston type wavemaker, a bottom hinged flap wavemaker and a general hinged flap wavemaker. Similar domain size and numerical settings as used by Silva et al. (2010) has been used. Only difference was the mesh settings and the dynamic motion of the wavemaker. The domain is shown in figure 4.13 and the general mesh parameters is given in table 4.8. The mesh used is shown in figure 4.14.
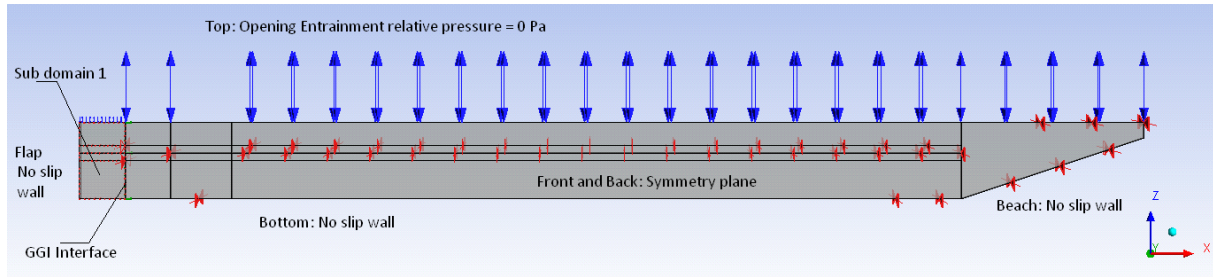
Figure 4.13: Domain used in comparison of wavemakers

Parameter	Setting
Domain length	$35m$
Water depth	$1.25m + 0.25m$
Air height	$0.75m + 0.25m$
Extruded width	$0.1m$
Number of Elements	107680
Δx	0.05
Δz	0.005
$\Delta x/\Delta z$	10
Air_z	20
$Water_z$	40

Table 4.8: Mesh details in Wavemaker study.

4.3.1 Boundary conditions and numerical settings

The domain was divided into two sub domains. The first sub domain located in the first $1.5m$ was set to a motion specified domain. In the motion specified sub domain the mesh on all boundaries was set as unspecified in order to aloud dynamic motion. The intersection between the two sub domains was set to a interface type boundary condition with a conservative mass and momentum flux. In the interface boundary condition the mesh in each sub domain will be linked together with a General Grid Interface *GGI* connection, with a conservative mass and momentum flux. The reason for using two sub domains was to limit the mesh motion to only a small part of the total domain. The top, bottom, front and back boundaries was set similar for the two sub domains. The bottom and the beach boundary was set to a no slip wall with $U_{wall} = 0$. The top boundary was set to a entrainment opening with zero static pressure in order to let the air flow in and out without any specific direction. The front and back boundaries was set to symmetry planes. The piston or flap wavemaker was set to a no slip wall with prescribed motion from the wavemaker theory.
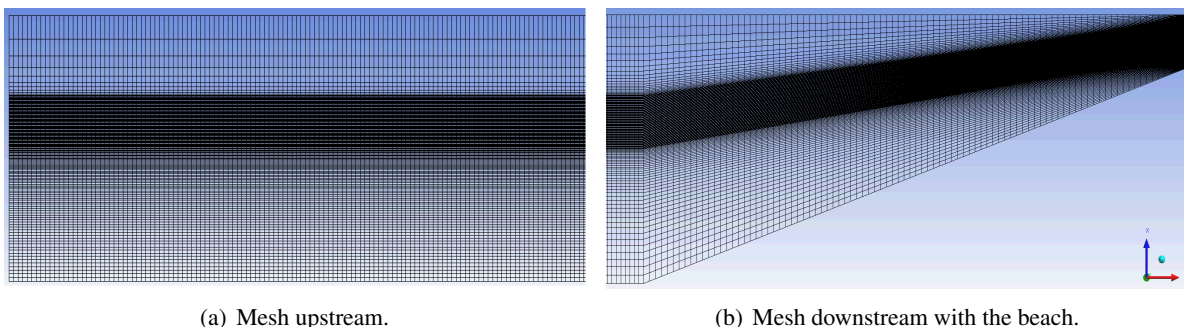
(a) Mesh upstream.

(b) Mesh downstream with the beach.

Figure 4.14: Mesh in case 2.
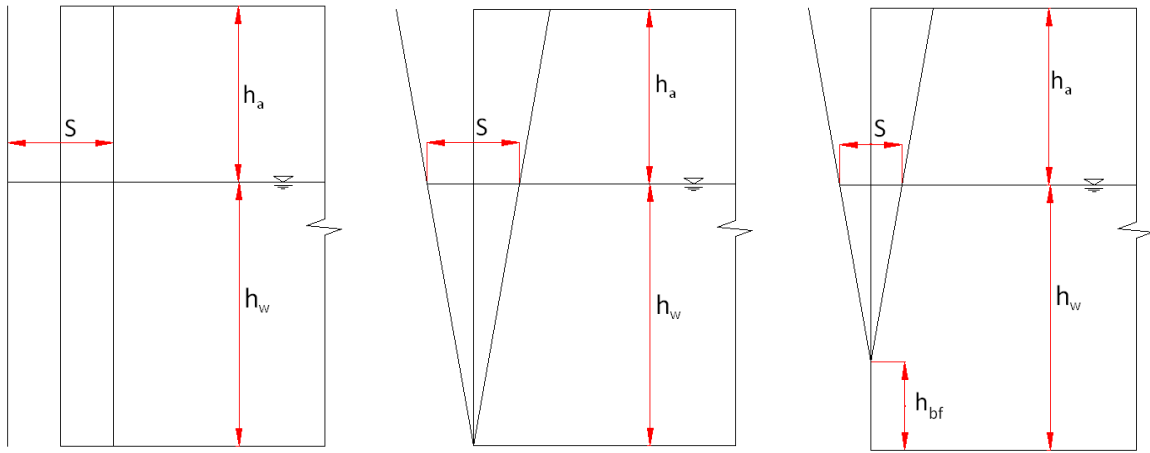
(a) Run 1. Piston type wavemaker.   (b) Run 2. Flap bottom hinged type (c) Run 3. Flap general hinged type
                                        wavemaker.   wavemaker.

Figure 4.15: Simple piston and flap type wavemakers. S =Piston stroke, h_w =Water depth, h_a =Air height and h_{bf} =Hinged height.

The numerical settings used is given in table 4.9. In table 4.10 the three runs is specified. From the wavemaker theory the chosen stroke length S gives similar wave amplitude $\zeta_A = 0.0645m$ for all three wavemakers. The specific wavemakers is shown in figure 4.15. In run 3 the height up to th hinged point was set to $h_{bf} = 0.5m$. Similar as in section 4.2 the Δx and Δz represents the element size in the uniform area close to the free surface. Air_z and $Water_z$ represents number of elements in the above air phase and the below water phase respectively. The non dimensional mesh parameters, $\lambda/\Delta x$, $\zeta_A/\Delta z$ and $T/\Delta t$ are in accordance with the suggested values given by Silva et al. (2010).

Parameter	*Setting*
Version	CFX 12.0
Model	Transient
Turbulence	Laminar
Advection Discretization Scheme	Specified blend, blend factor =1
Time Discretization Scheme	Second order Backward Euler
Convergence criteria	$RMS < 1E - 3$
Convergence loops	$1 - 3$
Precision	Single
Total time	$25s$
Time step	$\Delta t = 0.01s$

Table 4.9: Numerical settings for the Wavemaker study.

4.3.2 Results

In figure 4.16 the wave elevation along the tank length is compared for all three wavemakers. The difference is small between the different wavemakers indicating that the wavemaker theory gives stroke values in accordance with the wanted wave amplitude ζ_A. For all the three runs a transient start was obtained before steady waves was produced. A larger first wave can be seen in front of the wave train. Also some unsteady behaviour in amplitude values can be seen, especially after $t = 20s$. The reasons could be the mesh parameters, the sudden start of the wavemaker, the mesh over the beach and the

Run	Type	Stroke S [m]	Amplitude $\zeta_A[m]$	Period $T[s]$	Wave length λ [m]	$\Delta x/\lambda$	$\Delta z/\zeta_A$	$T/\Delta t$
1	$Piston$	0.2	0.0645	2.0	5.79	115.8	12.9	200
2	$Flap_{bottom}$	0.0149	0.0645	2.0	5.79	115.8	12.9	200
3	$Flap_{general}$	0.0874	0.0645	2.0	5.79	115.8	12.9	200

Table 4.10: Specific wavemaker input and numerical settings.

numerical settings used. A further investigation regarding the deviation from regular waves is discussed in section 4.4.

(a) Wave elevation along the tank at $t = 5s$.

(b) Wave elevation along the tank at $t = 10s$.

(c) Wave elevation along the tank at $t = 15s$.

(d) Wave elevation along the tank at $t = 20s$.
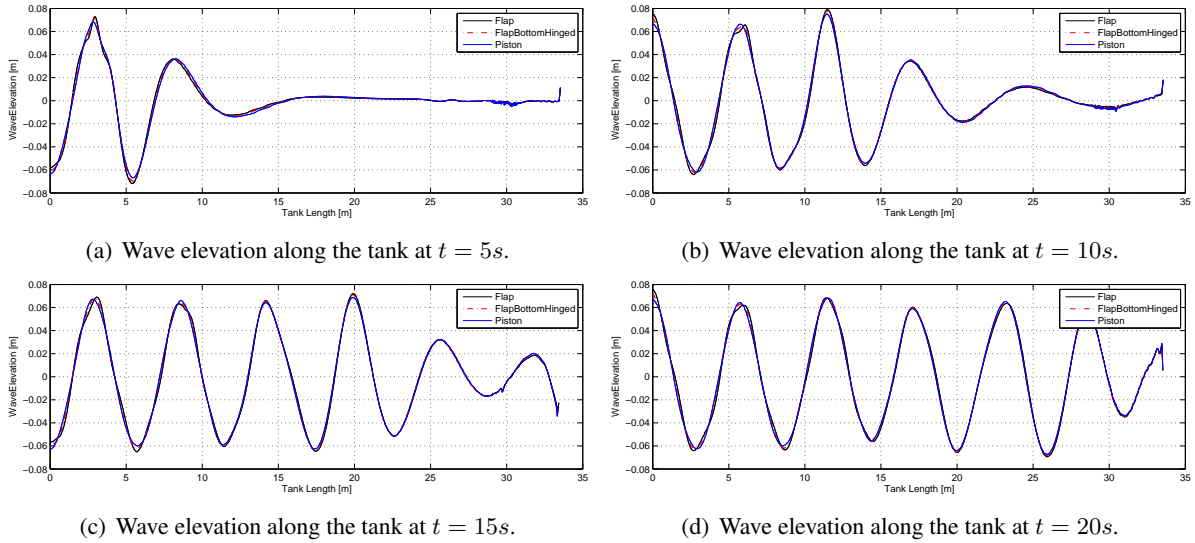
Figure 4.16: Comparison of wave elevation along the tank length for three different wavemakers. Piston indicate run 1, FlapBottomHinged indicates run 2 and Flap indicates run 3.

In figure 4.17 the time series at given sections in the tank is compared for all the three wavemakers. Small difference is obtained in the wave elevation and the different wavemakers can be used to make numerical waves.

In figure 4.18 the wave crest and wave trough from the time serie at section 1 is compared for the three wavemakers. Notice the small scale on the y-axis. From the wavemaker theory the wave amplitude was $\zeta_A = 0.0645m$. Shallow water is assumed. From Stokes 2nd order wave theory the crest amplitude is $\zeta_C = 0.0675m$ and the trough amplitude is $\zeta_T = -0.0615m$. The piston wavemaker gives values closest to the Stokes 2nd order wave amplitudes. The mean time between the maximal values showed very close values to the input period. Overall there is not large differences between the three wavemakers and all can be used to produce waves with reasonable wave amplitudes. After $t = 20s$ a deviation can be seen. The wave train will hit the domain end wall at approximately $t = 20s$ with a group velocity of $C_g = 1.69m/s$. The reflection from the beach will affect the wave elevation close to the beach and gradually further upstream. In a physical wave tank it is unlikely that the wave elevation at a section $x = 1.5m$ will be affected only seconds after the wave train hit the domain end. In a numerical wave tank this could happen and be one of the reasons for the small deviation in amplitude after $t = 20s$ shown in figure 4.18.
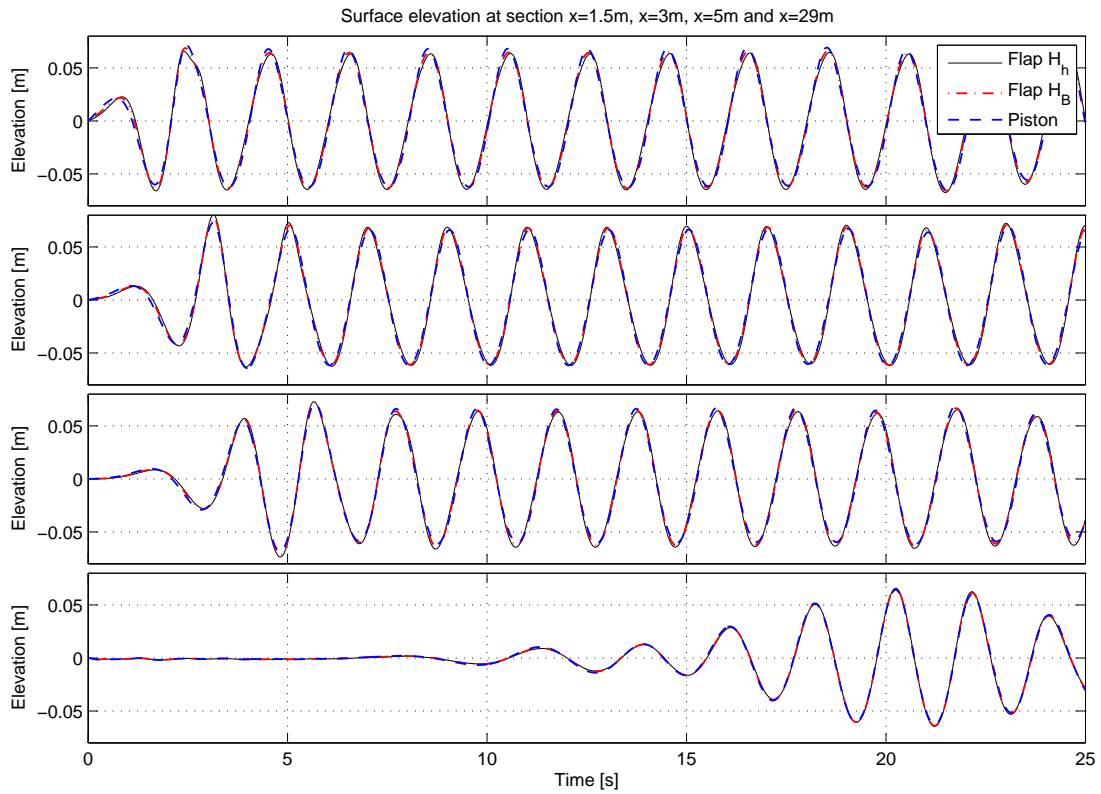
Figure 4.17: Comparison of time series of wave elevation at section $x = 1.5m,$, $x = 3m$, $x = 5m$ and $x = 29m$ for Piston run 1, FlapBottomHinged run 2 and Flap run 3.

(a) Comparison of Wave Crest.

(b) Comparison of Wave Trough.
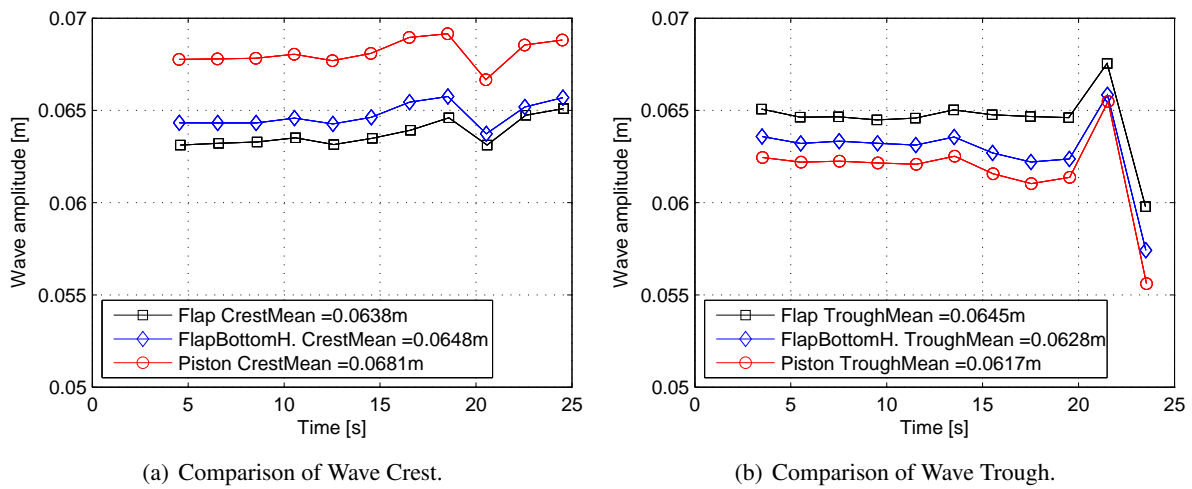
Figure 4.18: Comparison of Wave Crest and Wave Trough for piston, flap and bottom hinged flap wave-maker. Notice the close view scale of the vertical axis.
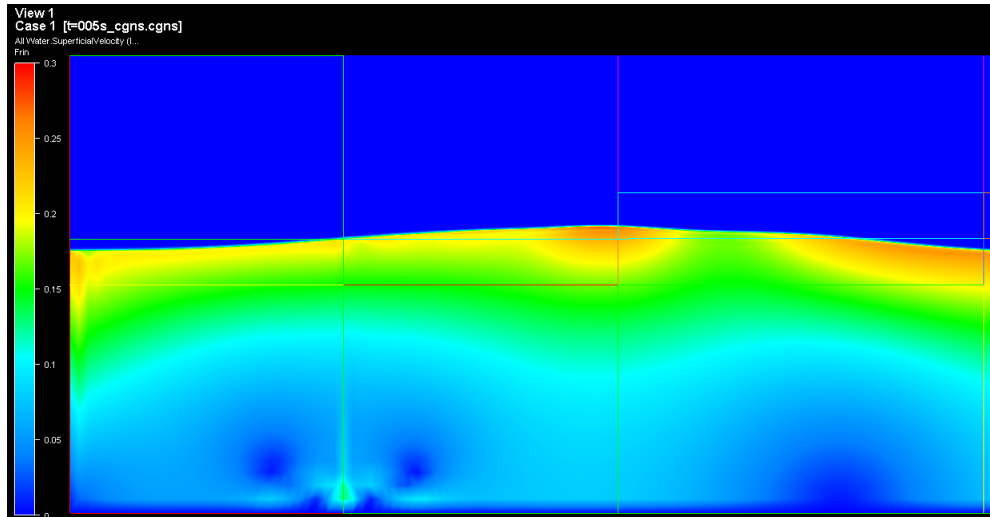
Figure 4.19: Contour plot of superficial water velocity around the domain intersection.

Figure 4.19 shows a close view of the superficial water velocity for the bottom hinged flap in run 2 at $t = 5s$. In order to restrict the mesh from moving in the whole domain, only the first $1.5m$ of the domain was modeled with a moving mesh. In figure 4.19 the interface type boundary conditions seems to affect the fluid velocities locally at the intersection. The wave elevation is not affected and gives reasonable values at the intersection. The water velocity downstream the intersection seems not affected by the intersection and gives values in accordance with the wave elevation. Sub domains can be used with the interface boundary condition but close to the intersection the solution is influenced by the interface condition.

4.3.3 Conclusion

A flap or piston type wavemaker gives better results for the wave elevation compared with specifying a inlet velocity profile. The Piston type wavemaker gives closer crest and trough amplitudes compared with Stokes 2nd order wave theory which is more valid than linear wave theory in this case. Both Flap type wavemakers gives almost similar values as the Piston type wavemaker. All three wavemakers can therefore be used to produce free surface waves with reasonable wave amplitudes. By using a sub domain to limit the motion specified region, a *GGI* interface boundary condition can be used. The interface boundary influence the fluid flow locally around the intersection, but does not affect the fluid flow further downstream or the wave elevation worth mentioning.

4.4 Case 3: Comparison with a Validation Case

The article by Silva et al. (2010) did similar analysis of a two dimensional numerical wave tank with ANSYS CFX. In order to achieve similar results a equivalent case study was done with almost similar mesh, boundary conditions and numerical settings. From the article by Silva et al. (2010) the case with the best results was chosen to be validated. The domain used in the present case is shown in figure 4.20. The domain length was set to $L = 35m$, water depth $h = 1.5m$ and a extruded length was $0.1m$. At the inlet wall a flap wavemaker was modeled by a moving wall. At the end of the domain a beach with slope $1 : 3$ was used. With $1.0m$ height of air, the actual length of the initial free surface was $33.5m$. A total of 6 runs was performed with different settings in order to achieve similar results as the selected result from Silva et al. (2010).
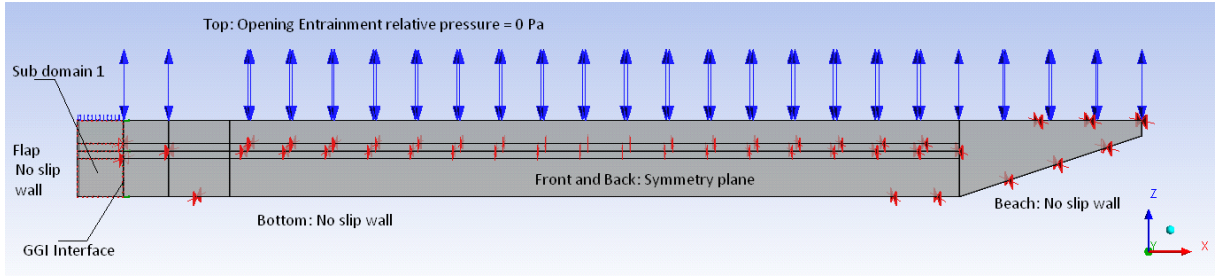
Figure 4.20: Domain for case 3

The mesh was made equivalent with the finest mesh used by Silva et al. (2010). The mesh parameters are given in table 4.11. Similar as in section 4.2 the Δx and Δz represents the element size in the uniform area close to the free surface. Air_z and $Water_z$ represents number of elements in the above air phase and the below water phase respectively. There was used more elements in the below water phase than in the above air phase since shallow water wave parameters was studied and the water motion more interesting than the air motion. The mesh at the domain end was made parallel with the beach slope towards a normal wall at the top end in run $1-5$. In run 6 the mesh over the beach was made normal to the free surface, which also was the case in the chosen validation case by Silva et al. (2010). A figure of the used mesh in run $1-5$ can be seen in figure 4.14 in the previous section 4.3. The mesh over the beach in run 6 can be seen in figure 4.27(c).

Parameter	Setting
Domain length	$35m$
Water depth	$1.25m + 0.25m$
Air height	$0.75m + 0.25m$
Extruded width	$0.1m$
Number of Elements	107680
Δx	0.05
Δz	0.005
$\Delta x/\Delta z$	10
Air_z	20
$Water_z$	40

Table 4.11: Mesh details for case 3.

4.4.1 Boundary conditions and numerical settings

The domain and boundary conditions used in case 2 in section 4.3 for the different wavemakers was similar to the validation case and was also used here. A short summary of conditions in section 4.3.1 is given. Two sub domains with a *GGI* interface was used. The flap was hinged $0.5m$ above the bottom and set as a moving no slip wall. The bottom and the beach boundary was set to a no slip wall, $U_{wall} = 0$. The top boundary was set to a entrainment opening with zero static pressure. The front and back boundaries was set to symmetry planes. The numerical settings used is given in table 4.12.

In table 4.13 settings used in each run is given. Six runs was performed with constant input to the flap motion. The flap wavemaker was given a oscillation period of $T = 2.0s$ and a stroke lenght $S = 0.2m$ at the free surface. The wave period will be the same as the flap period and from the wavemaker theory the wave amplitude becomes $\zeta_A = 0.645m$. The initial condition in table 4.13 means a linear wave profile defined at the initial time step along the tank. In run 2 and 3 a initial linear wave was used in the first $6m$ and $15m$ along the tank respectively, similar as shown previously in figure 4.6. Number of convergence loops in each transient time step will in practice always be the maximum value due to

Parameter	Setting
Version	CFX 13.0
Model	Transient
Turbulence	Laminar and $K - \epsilon$
Advection Discretization Scheme	Specified blend, blend factor =1
Time Discretization Scheme	Second order Backward Euler
Convergence criteria	$RMS < 1E - 5$
Precision	Single
Total time	$25s$
Time step	$\Delta t = 0.01s$

Table 4.12: Numerical settings for the validation case.

the hard convergence criteria. Regarding the turbulence setting, the article by Silva et al. (2010) used a laminar model and therefore similar model is used in all runs except run 3 which used a $K - \epsilon$ model.

Run	Wave Amplitude $\zeta_A[m]$	Wave Period $T_p[s]$	Initial surf. $[m]$	Conv. loops	Turbulence
1	0.0645	2.0	$-$	$3 - 6$	*Laminar*
2	0.0645	2.0	$0 - 6$	$3 - 6$	*Laminar*
3	0.0645	2.0	$0 - 15$	$3 - 6$	$K - \epsilon$
4	0.0645	2.0	$-$	$10 - 15$	*Laminar*
5	0.0645	2.0	$-$	$1 - 3$	*Laminar*
6	0.0645	2.0	$-$	$1 - 3$	*Laminar*

Table 4.13: Numerical settings for each run.

From the selected wave period, the wave length becomes $\lambda = 5.79m$ and the wave number $k = 2\pi/\lambda = 1.085m^{-1}$ by use of linear wave theory. With constant mesh parameters, non dimensional mesh values becomes $\lambda/\Delta x = 115.8$ and $\zeta_A/\Delta z = 25.8$ which are reasonable values according to Silva et al. (2010). Shallow water is assumed since $h = 1.5m > \lambda/2 = 2.89m$ is not true. The linear wave theory criteria states that $kh = 1.63 << 1$ and $\zeta_A/h = 0.043 << 1$. The first criteria does not hold so consequently the waves are not linear. The Ursell number, $Ur = \frac{k\zeta_A}{(kh)^2} = 0.0162$, is higher than in the first section 4.2 indicating larger nonlinearity. In Stokes 2nd order theory the maximum amplitude criteria $\zeta_A/h = 0.043 < 0.26$ holds and the Ursell criteria $U_r = 0.0162 < 1/3$ holds. Stokes 2nd order waves will therefore be more comparable with the numerical results.

In table 4.14 the critical depth z_{crit} and the depth based Froude number Fn is given. A explanation of the critical depth and the wave amplitude base Reynolds number was given in section 4.2. The critical depth indicate a large mixing layer almost to the bottom. The maximal Froude number based on linear wave theory indicate subcritical flow.

Critical depth: z_{crit} $(Re_A <= 3000)$	$-1.11m$
Maximal Froude number Fn	0.0570

Table 4.14: Critical depth where the amplitude based Reynolds number is less og equal to the critical value 3000, and the depth based Froude number. Origo located at the free surface gives negative z values towards the bottom.

4.4.2   Results

Wave elevation run 1

In figure 4.21 the wave elevation along the tank length at different time steps for run 1 is shown. The same issues obtained in section 4.3 was also seen here. The flap wavemaker will have a transient start before steady waves are produced. In the first sub figure at $t = 5s$, the first transient waves can be seen. A larger wave is produced at the start which also can be seen in the front of the wave train in all the other sub figures in figure 4.21. After the transient first wave the wave profile is more regular and closer to the input wave parameters. Still a variation in crest and trough amplitude is obtained along the tank. At the end of the domain the mesh over the beach obviously disturbs the mean free surface with some irregularities as seen around $30m$ downstream at $t = 15s$ and $t = 20s$. The reason will be the mesh over the beach which was not made normal to the free surface. This could be one reason for the variation of the steady wave profile along the tank. Also the sudden start of the flap wavemaker can have affected the surface wave elevation. Similar figures for run $1-6$ can be found in appendix C.2.
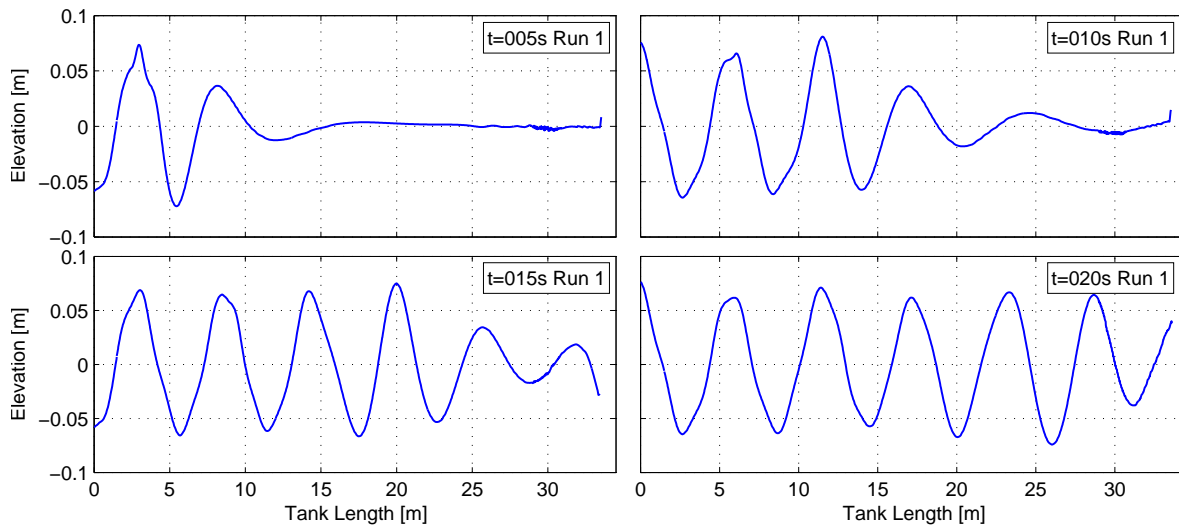
Figure 4.21: Wave Elevation along the tank length for run 1 at $t = 5s$, $t = 10s$, $t = 15s$ and $t = 20s$.

In figure 4.22 the time series from run 1 at four sections along the tank is plotted. Similar to the wave elevation along the tank length in figure 4.21, a larger transient wave is obtained in the front of the wave train. The time series at the given sections shows a more steady wave profile with almost a sinusoidal shape. By comparing the time series from the four sections it looks like the wave profile is inclined with a small angle. At section $x = 1.5m$ and $x = 5m$ the wave profile is inclined a small angle to the right. At section $x = 3m$ it is opposite with a small inclined angle to the left. The different small inclination angles can be due to the discretization of elements along the tank length. The variation in wave amplitude along the tank length will also influence time time series and the inclination can be due to the variation in the wave amplitude along the tank length. In the time series both the wave crest and wave trough amplitudes are steady with similar values. Similar time series for run $1-6$ is given in appendix C.2.
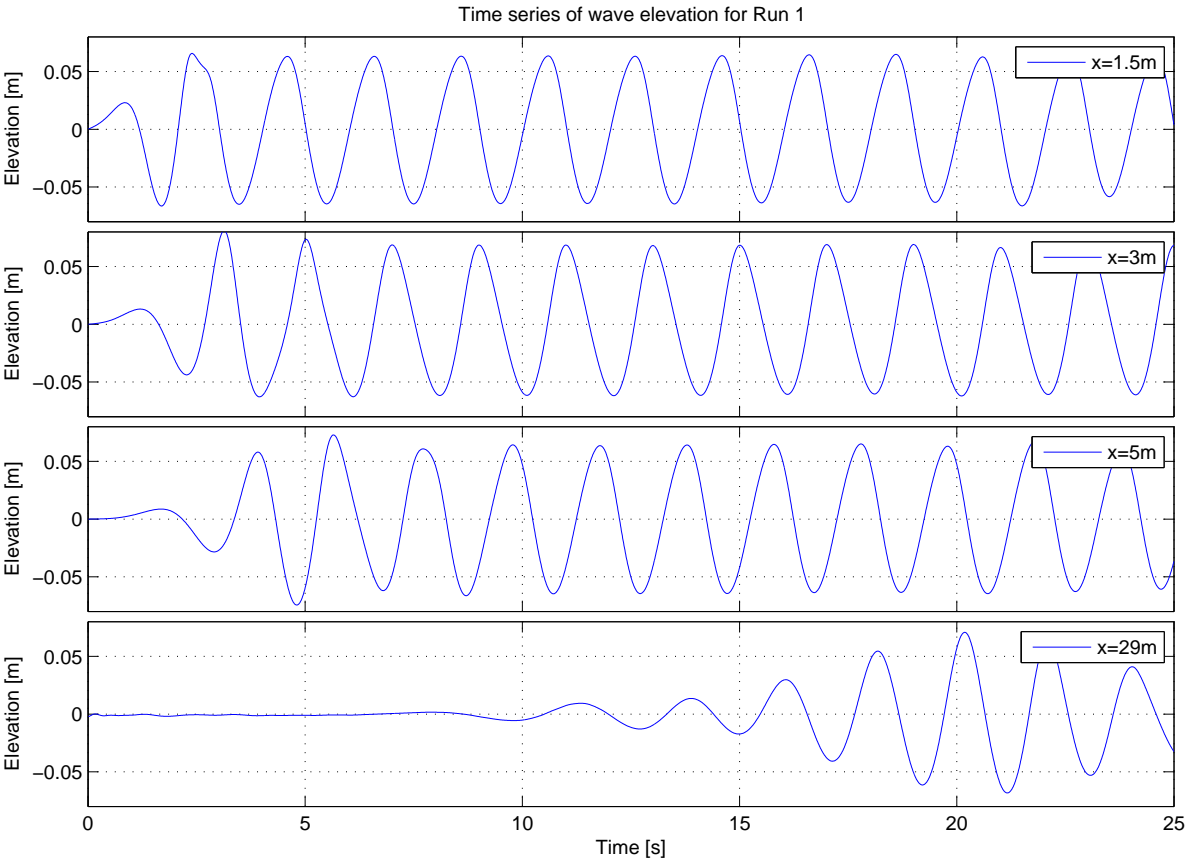
Figure 4.22: Time series of wave elevation for run 1 at section $x1.5m$, $x = 3m$, $x = 5$ and $x = 29m$.

In figure 4.23 the peak values from the timeserie of the wave elevation in run 1 at a section at $x = 1.5m$ is plotted. The total wave height H equal the wave crest amplitude plus the wave trough amplitude, $H = \zeta_C + |\zeta_T|$. The crest amplitudes and trough amplitudes shows similar values and both are close to the input wave amplitude from the wavemaker theory of $\zeta_A = 0.0645m$.
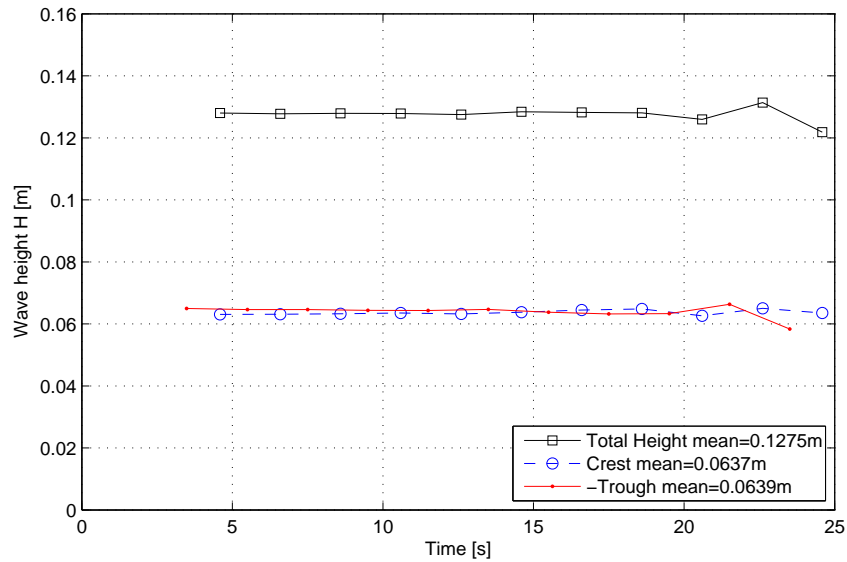
Figure 4.23: Peak values from time serie of wave elevation at $x = 1.5m$ in run 1. The total wave height equal the wave crest amplitude plus the wave trough amplitude.

Figure 4.24 shows the timeserie at $x = 1.5m$ for run 1 compared with linear and stokes 2nd order wave theory. In figure 4.24(a) the wave elevation from CFD agrees well with both linear and stokes 2nd order wave theory. The difference is due to the small inclination of the wave profile from CFD. In figure 4.24(b) the difference compared with stokes 2nd order wave theory is shown.
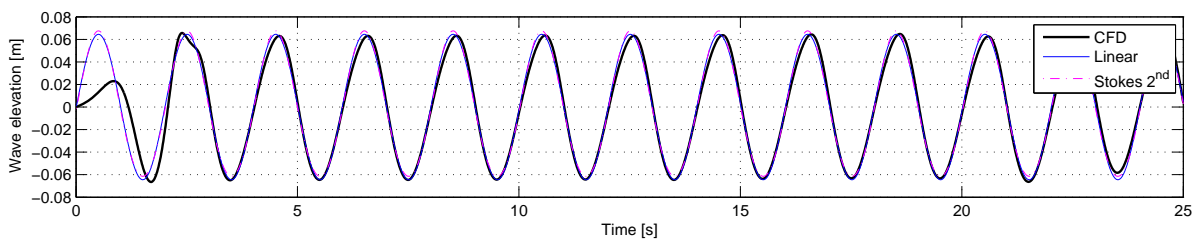
(a) Comparison between timeserie of wave elevation at section $x = 1.5m$ in run 1, linear wave theory and stokes 2nd order wave theory.
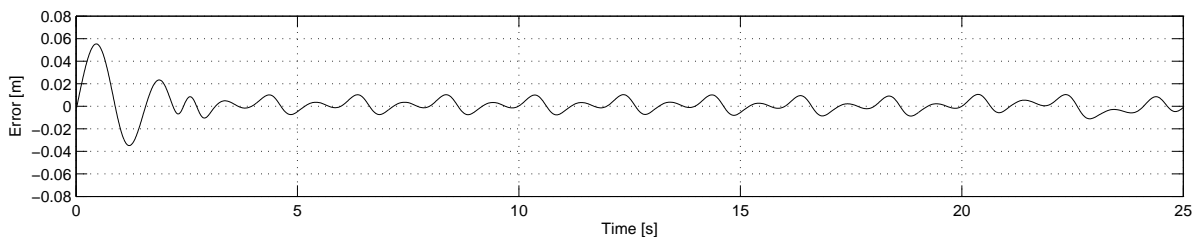
(b) Error between wave elevation at $x = 1.5m$ in run 1 and stokes 2nd order wave theory.

Figure 4.24: Timeserie of wave elevation at $x = 1.5m$ compared with wave theory.

Number of Coefficient loops

In figure 4.25 the wave elevation along the tank at $t = 20s$ is shown for run 1, 4 and 5. All with similar settings except number of coefficient loops in each time step. run 1 with minimal 3 and maximal 6 coefficient loops, run 4 with minimal 10 and maximal 15 coefficient loops and run 5 with minimal 1 and maximal 3 coefficient loops. The coefficient loops is dependent of the convergence criteria. If the criteria is reached before maximum number of coefficient loops, the solver will jump out and continue to the next time step. The solver will always use the minimal number of coefficient loops. With a hard convergence criteria the maximum number of coefficient loops will in practice always be used which was the case here. The difference between 3 to 15 maximal number of coefficient loops is small especially in the first waves close to the wavemaker. Further downstream there can be seen a small deviation where the run with the most number of coefficient loops have the largest amplitude. Regarding the computation time, increasing the number of coefficient loops is crucial. The time will almost be doubled if number of coefficient loops is doubled. Therefore a maximum of 15 coefficient loops will not be suggested. Due to the small deviation between 3 and 6 maximal coefficient loops, 3 coefficient loops can be used if the computation time is critical. Mininum 3 to maximum 6 coefficient loops will be suggested in combination with a achievable convergence criteria. If the solution do not converge within $3 - 6$ coefficient loops it is recommended to reduce the time step instead of increasing the number of coefficient loops in each time step. The same suggestion is given in the user manual ANSYS (2010).
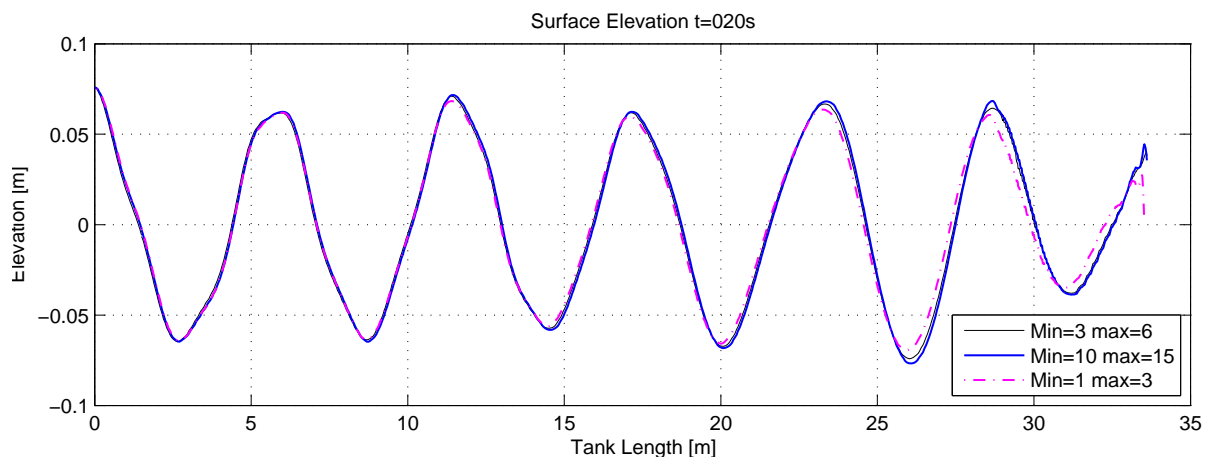
Figure 4.25: Comparison of wave elevation with different coefficient loops. Run 1 with min 3 and max 6 coefficient loops, Run 4 with min 10 and max 15 coefficient loops and Run 5 with min 1 and max 3 coefficient loops.

Initial wave condition

In figure 4.26 the wave elevation along the tank for run 3 is shown. In run 3 the initial condition was specified with a linear wave elevation in the first 15 meters of the tank length. With a given wave elevation at the initial time, convergence will be improved due to smaller transient effects in the start. The wave profile will also be improved and will keep the initial shape downstream the tank length which can be seen at $t = 5s$ and $t = 10s$. A more correct wave profile would be achieved by use of Stokes 2nd order wave theory, since it is more valid with the given wave parameters. After $t = 15s$ the waves have reached the beach and reflected back into the domain. At $t = 20s$ the wave amplitude is reduced which indicates that the beach will give reflections. The computation time should therefore not be longer than the time used by the waves to reach the end of the domain.
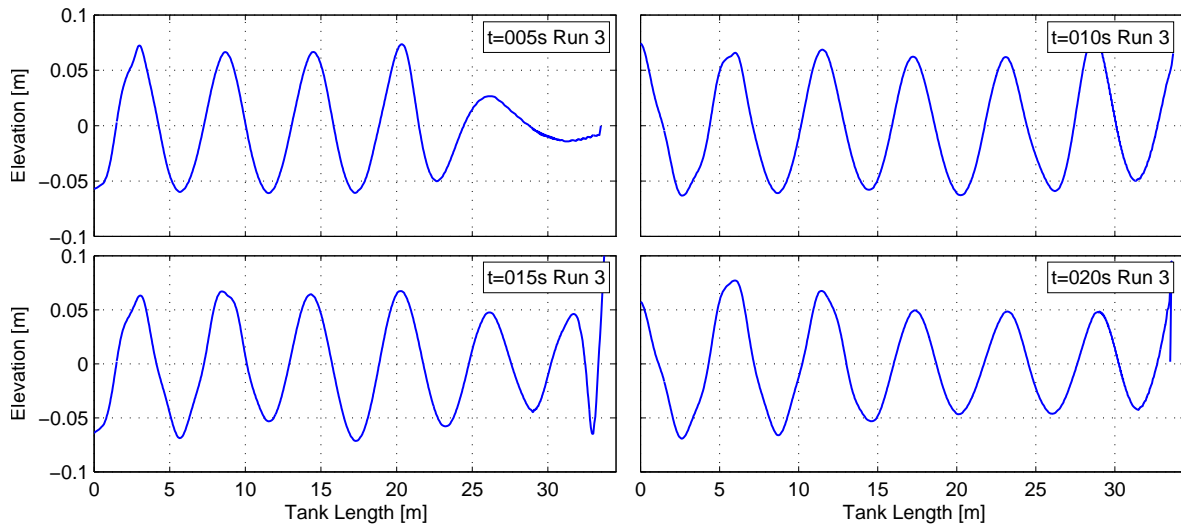
Figure 4.26: Wave Elevation along the tank length for run 3.

Mesh over the beach

Figure 4.27 shows a contour plot of the superficial water velocity for run 1 at $t = 15s$ and a closer view of the beach for run 1 and 6 at $t = 15s$. In figure 4.27(a) it can be seen that the shallow water assumption is valid since the waves reach the bottom of the domain. The water particle oscillation following the orbital path can be seen from the regular periodic variation along the tank. The pattern deviates from the wave theory on the free surface with some irregularities. Notice the change in velocity at the end of the domain over the beach. The mesh clearly affect the fluid motion and give some unnatural velocities. In figure 4.27(b) and 4.27(c) a close view of the superficial water velocity over the beach is shown for run 1 and 6. In run $1 - 5$ the mesh over the beach was stretched towards the upper end wall of the domain. In run 6 the mesh was improved and made normal to the mean free surface. From the contour plot of the superficial velocity a unnatural velocity increase is obtained by use of the first mesh. The unnatural velocity increase is absent with a mesh normal to the free surface, as seen for run 6. Therefore the mesh will be recommended to be normal to the free surface.
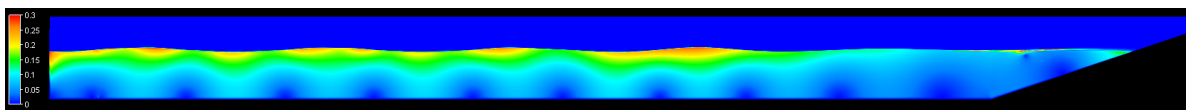
(a) Contour plot of superficial water velocity for run 1 at $t = 15s$.
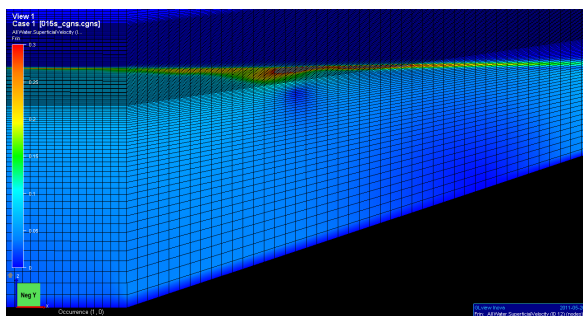
(b) Close view of contour plot of superficial velocity and mesh over beach in run 1 at $t = 15s$.
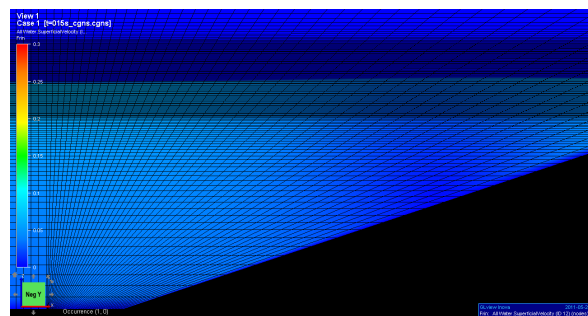
(c) Close view of contour plot of superficial velocity and mesh over beach in run 6 at $t = 15s$.

Figure 4.27: Close view of contour plot of superficial velocity and mesh over the domain beach in run 1 and 6.

Compare with Validation case

In run 6 the mesh over the beach was similar to the mesh used in the validation case and run 6 was chosen in order to compare the wave elevation. In addition the results from run 6 gave best results of the studied runs. In figure 4.28 the wave elevation along the tank from run 6 at $t = 20s$ and the chosen validation case from Silva et al. (2010) at $t = 19.4s$ is shown. Both results is in addition compared with linear and Stokes 2nd order wave theory.
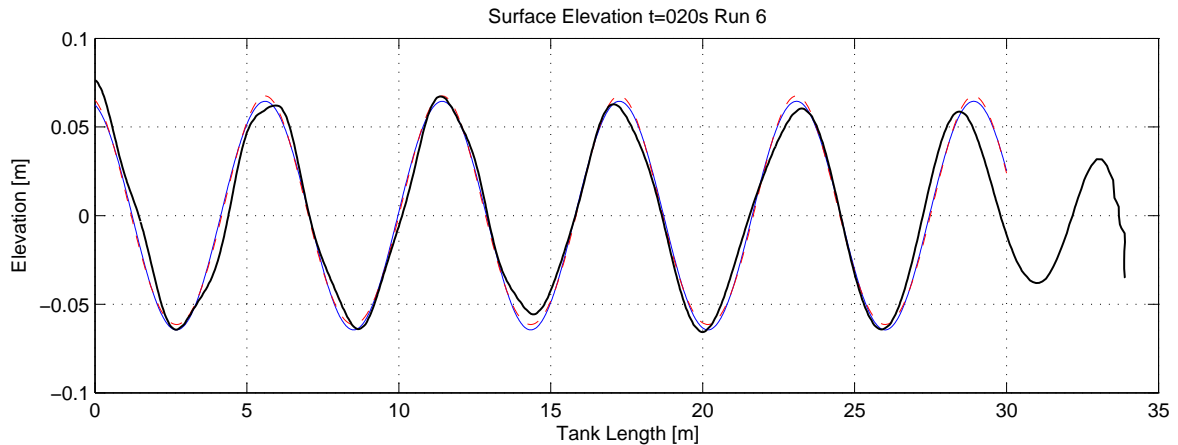
(a) Present results. Wave elevation along the tank length from run 6 at $t = 20s$ from present work compared with Linear and Stokes 2nd order wave theory. Legend given in 4.28(b) where blue line indicate linear theory, red dotted line indicate Stokes 2nd order theory and black line results from run 6.
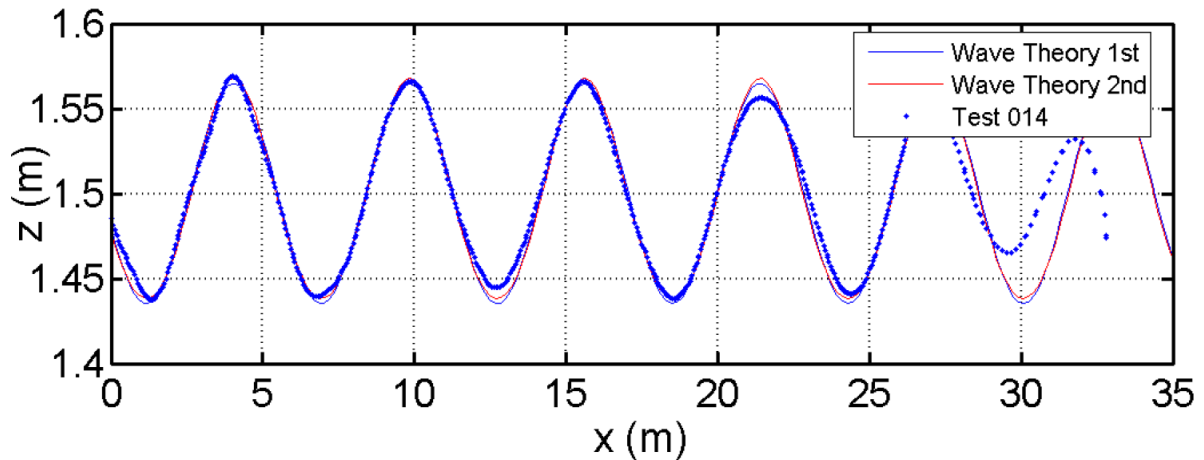
(b) Results from Silva et al. (2010).Wave elevation along the tank length at $t = 19.4s$. Regarding the difference in z coordinate at the free surface, Silva et al. (2010) used origo on bottom giving mean free surface at $1.5m$.

Figure 4.28: Wave elevation along the tank length run 6 at $t = 20s$ and the validation case at $t = 19.4s$. Both results compared with linear and Stokes 2nd order wave theory.

From the assumptions regarding the wave parameters the 2nd order Stokes theory should be the most correct wave elevation. Due to the variation in amplitude the wave elevation in figure 4.28(a) shows similar values, with some variance, to both the linear and the 2nd order wave theory. Notice also the small difference between linear and stokes 2nd order wave theory. The results from the validation case in figure 4.28(b) shows a more steady profile and also gives almost similar values as the wave theory. A direct comparison with the validation case was not performed since results from only each second was saved to avoid large data amount in the present work. Why Silva et al. (2010) presented results at $t = 19.4s$ can be questionable. The phase between the results in figure 4.28(a) and 4.28(b) is reasonable with a time deviation of $0.6s$. A closer look shows that the obtained deviation from wave theory can be seen from both the present results in run 6 and the validation case results. The deviation at the wave

trough around $x = 14m$ in run 6 is almost similar to the deviation seen in wave trough from the validation case around $x = 13m$. Also similar, the deviation at the wave crest at around $x = 23m$ in run 6 is almost similar to the deviation seen in the wave crest from the validation case around $x = 22m$. With the time difference between $t = 20s$ in run 6 and $t = 19.4s$ in the validation case in mind, the results is almost similar. One reason for Silva et al. (2010) have a more steady result can be use of a smoother start of the flap wavemaker. By giving the flap wavemaker a slower start for the first cycle, large water accelerations and unnatural numerical effects can be avoided. Notice also that the observed larger transient first wave in run $1 - 5$ is almost absent in run 6 with the mesh normal to the free surface over the beach as only difference.

4.4.3 Conclusion

From the wave elevation along the tank length a variation in wave amplitude is obtained. The reason for the variation along the tank length can be the mesh quality, boundary conditions, first cycle flap motion or the numerical settings. Time series of the wave elevation at given sections gives almost similar results as linear and Stokes 2nd order wave theory and it was obtained small difference between linear and 2nd order wave theory with the used wave parameters. A small inclination of the wave profile in the time series was obtained. The reason can be the element discretization combined with the free surface discrete position. Also the obtained variation in wave amplitude along the tank length will affect the time series. Compared with the chosen validation case published by Silva et al. (2010), they achieved to produce steady and more regular waves than in the present work. The reasons can be unmentioned numerical parameters in the article or smoothing of the wave elevation results. One case which not was mentioned, can be the use of a slower first cycle start of the flap wavemaker. By a slower start of the wavemaker, unnatural large water accelerations and numerical initial effects can be avoided. Also convergence can be improved by a slower wavemaker start. Overall a flap wavemaker can be used in a numerical wave tank to produce reasonable free surface waves. Initial wave elevation and velocities in part of the domain gives better convergence in the start of the numerical computation. The wave profile is also more stable along the tank length when a initial wave elevation along the tank is used. Regarding number of coefficient loops in each time step, $3 - 6$ coefficient loops will be suggested in combination with a achievable convergence criteria. The mesh is suggested to be normal to the free surface all over the domain.

4.5 Case 4: Modeling of The Student Wave Tank

The student wave tank at the department of Marine Technology in Trondheim was used for the experiments which will be presented in chapter 7. In order to do a similar study the wave basin was modeled with similar dimensions in ANSYS CFX. The dimensions of the physical wave tank is given in table 4.15. A amplitude study was performed with three different amplitudes combined with constant wave period, domain, mesh and numerical settings. Double precision was in addition tested in a single run to see if there was any improvement.

Parameter	*Dimensions*
Length	$25m$
Width	$2.8m$
Depth	$1.0m$
Wavemaker	Single Flap

Table 4.15: Dimensions of Student Wave Tank at department of Marine Technology.

The domain used in the numerical computation is shown in figure 4.29. Similar dimensions given for the physical tank was used. The total length was set to $L_t = 28m$ which gave a free surface of $25m$ for a beach with slope $1 : 3$ at the domain end. The water depth was set to $1.0m$ and similar the modeled air height to $1.0m$. A two dimensional analysis was performed with an extruded length of $0.1m$. In the performed experiments in chapter 7, two wave probes was mounted at $x = 7.3m$ and $x = 8.7m$. In order to compare the wave elevation, four sections measuring the wave elevation was placed at $x = 2.0m$, $x = 7.3m$, $x = 8.7m$ and $x = 21.5m$. The sections can be seen in figure 4.29. In figure 4.29 the yellow mark indicate a monitor point where selected data from the solver was logged.
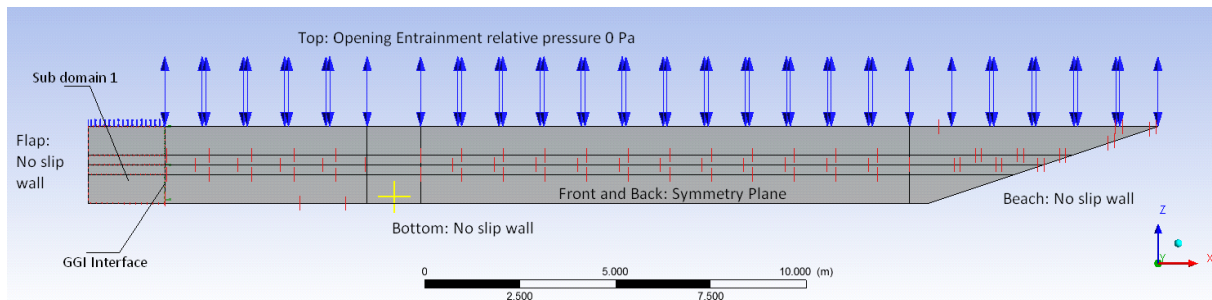
Figure 4.29: Domain used for modeling a similar wave tank as the student tank at department of Marine Technology.

In table 4.16 the specific mesh parameters is given and in figure 4.30 the mesh is shown. Similar as earlier noted the Δx and Δz represents the element size in the uniform area around the free surface. Air_z and $Water_z$ represents number of elements in the above air phase and below water phase respectively. The same settings for Δx and Δz used in the validation case in section 4.4 was used also here. With a smaller tank length and tank depth compared with the validation case in section 4.4, the number of elements was reduced. The mesh over the beach was made normal to the free surface similar as in run 6 in the validation case in section 4.4.

Parameter	Setting
Domain length	$28m$
Water depth	$0.75m + 0.25m$
Air height	$0.75m + 0.25m$
Extruded width	$0.1m$
Number of Elements	67200
Δx	0.05
Δz	0.005
$\Delta x/\Delta z$	10
Air_z	20
$Water_z$	20

Table 4.16: Mesh details in studied Wave Tank

4.5.1 Boundary conditions and numerical settings

Same boundary conditions used for the wavemaker method in section 4.3.1 was used and a short summary is given. The domain was divided at $x = 2m$ in two sub domains with a *GGI* interface connection. The bottom and the beach boundary was set to a no slip wall, $U_{wall} = 0$. The top boundary was set to a entrainment opening with zero static pressure. The front and back boundaries was set to symmetry planes. The bottom hinged flap was set as a moving no slip wall. The numerical settings used is given in table 4.17.

(a) Mesh upstream   (b) Mesh downstream with the beach
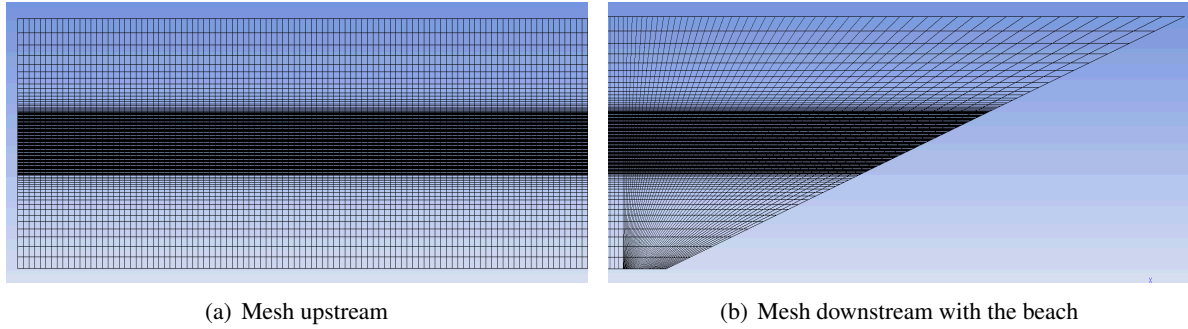
Figure 4.30: Mesh used in studied Wave Tank

Parameter	*Setting*
Version	CFX 13.0
Model	Transient
Turbulence	SST
Advection Discretization Scheme	Specified blend, blend factor =1
Time Discretization Scheme	Second order Backward Euler
Convergence criteria	$RMS < 1E - 3$
Convergence loops	$3 - 6$
Precision	Single and double
Total time	$25s$
Time step	$\Delta t = 0.01s$

Table 4.17: Numerical settings for the validation case.

A *SST* turbulence model was used since later on the same domain was used with a submerged structure in chapter 6. In this case only free surface waves was studied and a laminar turbulence model could have been used. In table 4.18 settings used in each run is given. Three runs was performed with constant period T and increasing wave amplitude ζ_A. The density was changed from the previous cases to $\rho = 1000kg/m^3$, since the physical student tank contained fresh water. In table 4.18 the three runs for the amplitude study is given.

Run	Stroke S $[m]$	T $[s]$	ζ_A $[m]$	λ $[m]$	$\lambda/\Delta x$	$\zeta_A/\Delta z$	ζ_A/h	$k = \frac{2\pi}{\lambda}$ $[1/m]$	H/λ	$U_r = \frac{k\zeta_A}{(kh)^2}$
1	0.101	1.5	0.05	3.3515	67	10	0.01	1.875	1/33.5	0.0267
2	0.152	1.5	0.075	3.3515	67	15	0.075	1.875	1/22.34	0.0400
3	0.203	1.5	0.1	3.3515	67	20	0.1	1.875	1/16.76	0.0533
4	Run 1 with Double precision enabled									

Table 4.18: Numerical settings for each run. S is the flap stroke at the surface, T is the wave period, ζ_A is the wave amplitude,$H = 2\zeta_A$ is the wave height, k is the wave number and U_r is the Ursell number.

Shallow water is assumed since $h = 1.0m > \lambda/2 = 1.67m$ is not true. The linear wave theory criteria's in shallow water states that $kh = 1.875 << 1$ and $\zeta_A/h << 1$. The first criteria does not hold so consequently the waves are not linear. The Ursell number increase as the wave amplitude increases, indicating larger unlinearities. In Stokes 2nd order theory the maximum amplitude criteria $\zeta_A/h < 0.26$ holds and the Ursell criteria $U_r =< 1/3$ holds. Stokes 2nd order waves will therefore be more comparable with the numerical results. Notice the number of elements in a wave length ($\lambda/\Delta x = 67$) which is below the recommended value in the article by Silva et al. (2010). The reason was the change in period from the validation case in section 4.4 which will change the wave length. The reduction in the $\lambda/\Delta x$ value was obtained during the analysis. About the time step the non dimensional value

$T/\Delta t = 150$ which is in accordance with the suggested value from Silva et al. (2010).

In table 4.19 the critical depth z_{crit} and the depth based Froude number Fn is given from linear wave theory. A explanation of the values was given in section 4.2. The critical depth indicate a large mixing layer. For the largest amplitude the amplitude based Reynolds number never gets below the critical value. The maximal Froude number based on linear wave theory indicate sub critical flow for all three amplitudes.

Run	1	2	3
Wave amplitude ζ_A	$0.05m$	$0.075m$	$0.1m$
Critical depth: z_{crit} ($Re_A <= 3000$)	$-0.45m$	$-0.82m$	$-$
Maximal Froude number Fn	0.071	0.105	0.140

Table 4.19: Critical depth where the amplitude based Reynolds number is less or equal to the critical value of 3000, and the depth based Froude number. Origo located at the free surface gives negative z values towards the bottom.

In addition a single test with double precision was performed. The same amplitude used in run 1 with similar settings except enabled double precision, was used in run 4. The double precision will be important if small scale relative differences becomes significant. If there is large difference between element sizes or large pressure or velocity variations the double precision can improve the accuracy of the solution. Regarding free surface flows it is often hard to achieve convergence based on residuals and the ANSYS Solver manual ANSYS (2010) suggests double precision to improve convergence in some cases. Especially when surface tension model is used the double precision will be required to avoid round off errors in the curvature calculation. In the present case both surface tension and the viscous shear stress force on the surface is neglected. The drawback of using double precision is increased computation time.

4.5.2 Results

Wave Elevation

In figure 4.31 the wave elevation along the tank length for the three runs are compared. In front of the wave train a larger unsteady wave is created similar as shown in figure 4.21 in section 4.4. In the steady part the wave crest amplitudes give reasonable values close to the input values. The wave trough amplitudes shows larger difference especially when the wave height increases which is in accordance with the second order wave theory. Notice the small phase difference between the runs. After some distance downstream the tank the wave length reduces especially for the smallest wave amplitude. The reason for the wave length reduction could be the mesh fineness along the tank. The wave amplitude also shows a small reduction along the tank length in the steady part. The reason for the crest amplitude reduction can be the mesh fineness vertically around the free surface or influence from the boundaries. Similar wave elevation along the tank given for each run can be seen in appendix C.3.

In figure 4.32 the time series of the surface elevation at the studied sections in the tank is shown. Also here a small phase difference can be seen at the sections downstream. The wave crest amplitudes gives steady values in accordance with the input values. From the different sections a small variation in both the crest amplitude and the trough amplitude can be obtained similar as for the elevation along the tank length.

Differences can more easily be obtained by plotting the crest and trough amplitude values of the waves instead of the total time series. In figure 4.33, 4.34 and 4.35 the wave crest amplitudes and the wave trough amplitudes are shown for run 1, 2 and 3 respectively. The wave height is defined as $H = \zeta_C + |\zeta_T|$. In both linear and Stokes 2nd order wave theory the total wave height will be similar.
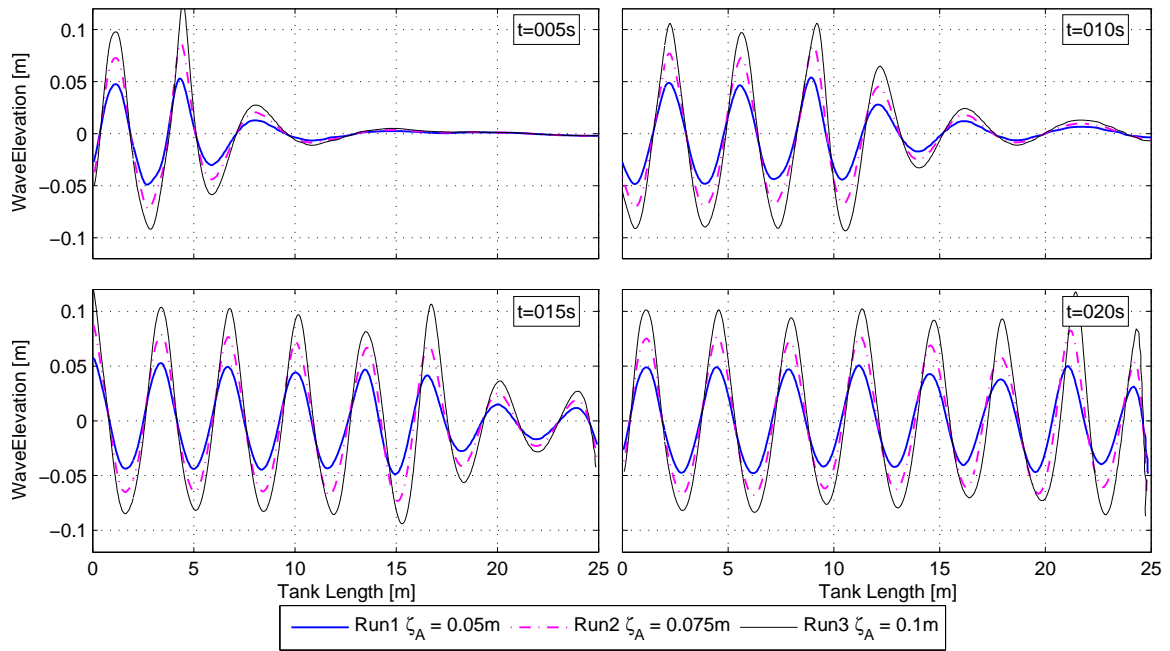
Figure 4.31: Comparison of wave elevation along the tank length for run 1, 2 and 3 at time step $t = 5s$, $t = 10s$, $t = 15s$ and $t = 20s$.
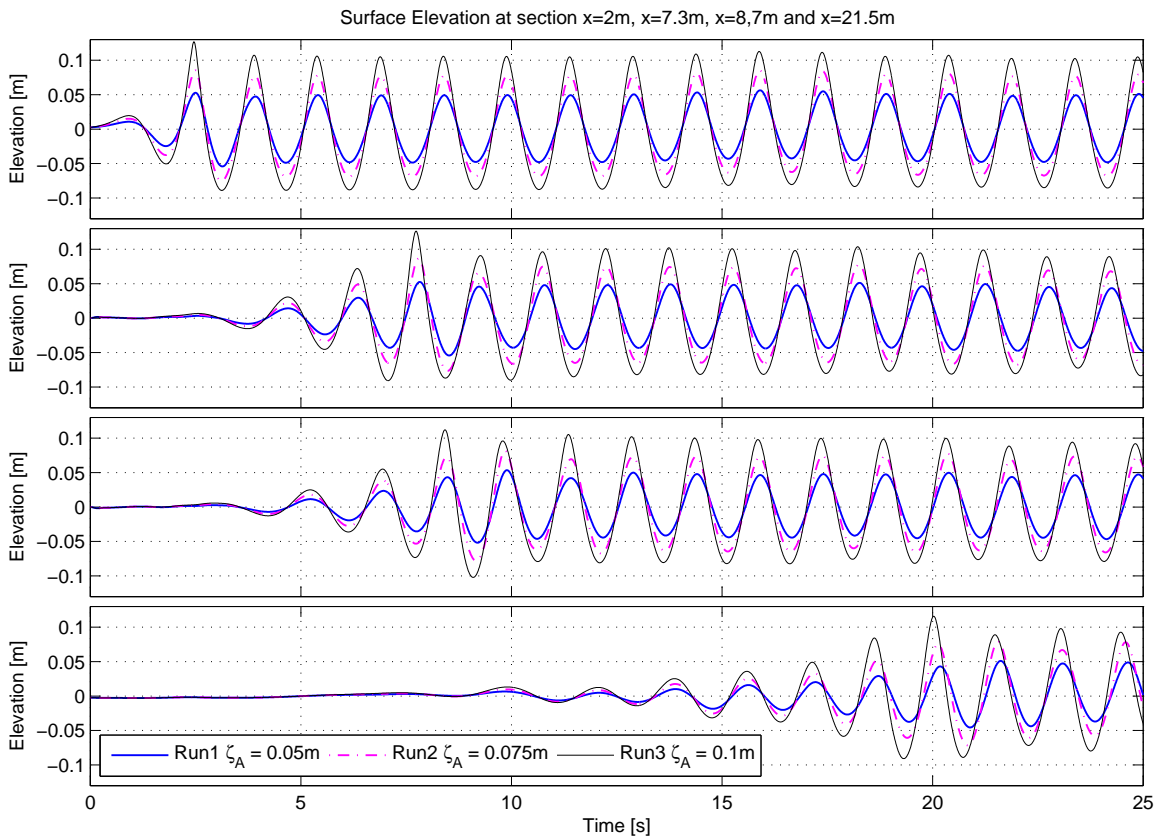
Figure 4.32: Timeseries of wave elevation for all runs at section $x = 2.0m$, $x = 7.3m$, $x = 8.7m$ and $x = 21.5m$.
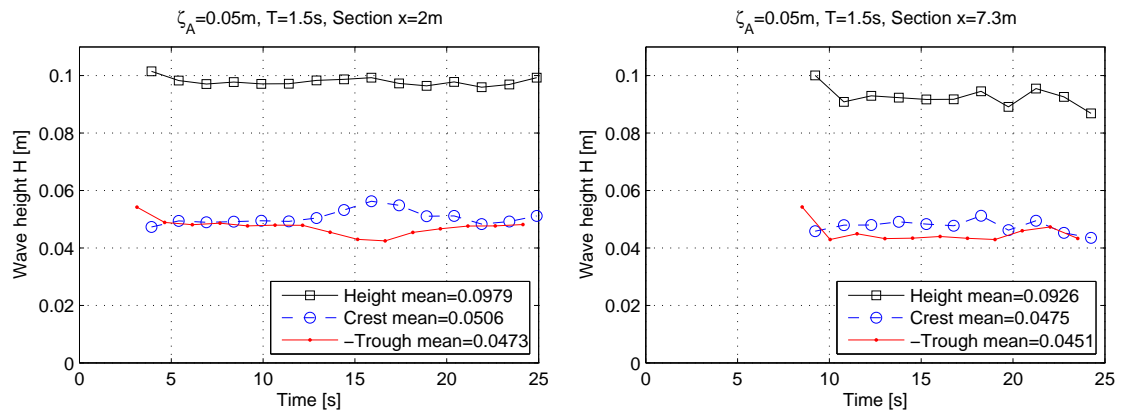
(a) Wave crest and trough amplitude Run 1 at $x = 2.0m$. (b) Wave crest and trough amplitude Run 1 at $x = 7.3m$.

Figure 4.33: Wave crest, wave trough and wave height for run 1 with $\zeta_A = 0.05m$ at section $x = 2.0m$ and $x = 7.3m$.
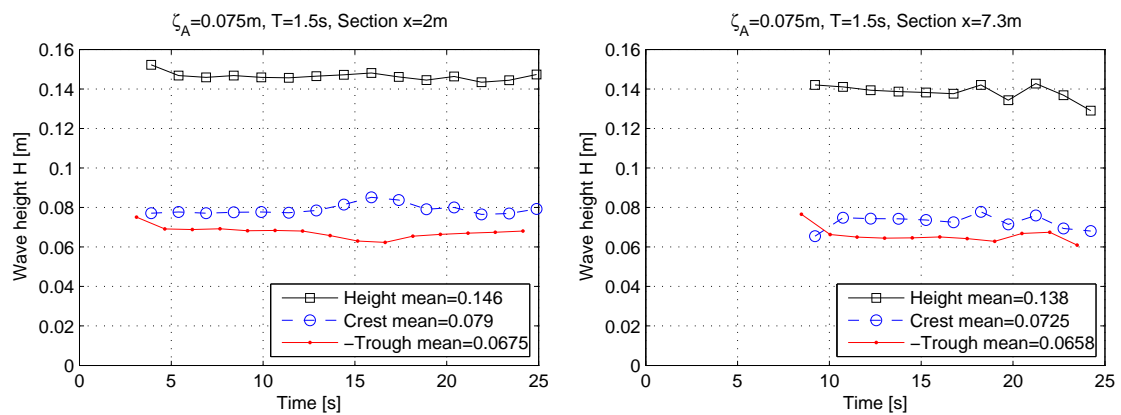
(a) Wave crest and trough amplitude Run 2 at $x = 2.0m$. (b) Wave crest and trough amplitude Run 2 at $x = 7.3m$.

Figure 4.34: Wave crest, wave trough and wave height for run 2 with $\zeta_A = 0.075m$ at section $x = 2.0m$ and $x = 7.3m$.
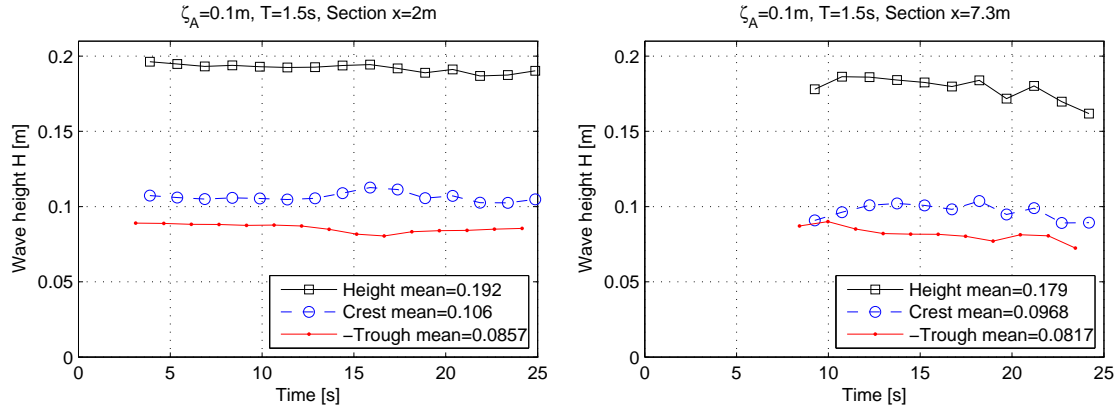
(a) Wave crest and trough amplitude Run 3 at $x = 2.0m$. (b) Wave crest and trough amplitude Run 3 at $x = 7.3m$.

Figure 4.35: Wave crest, wave trough and wave height for run 3 with $\zeta_A = 0.1m$ at section $x = 2.0m$ and $x = 7.3m$.

In Stokes 2nd order theory the wave elevation will be overall a little higher compared to linear theory. The wave height at the first section at $x = 2.0m$ for the three runs shown in figure 4.33(a), 4.34(a) and 4.35(a) gives close values compared with the input wave height. At the next section at $x = 7.3m$ a reduction in wave height can be seen for all three runs. The reduction in wave height along the tank length is small and difficult to see from the time series.

In table 4.20 and 4.21 the Stokes 2nd order wave amplitudes is compared with the measured mean wave amplitudes at section $x = 2.0m$ and $x = 7.3m$ respectively. The deviation shows that the crest amplitude differ more than the trough amplitude and the largest deviation is found for the largest wave amplitude. The deviation increases between the two studied sections at $x = 2.0m$ and $x = 7.3m$ indicating that the waves are damped along the tank length. Largest damping obtained for the largest amplitude. Reasons for the damping along the tank can be the mesh fineness along the tank and the element aspect ratio. Also the boundary conditions could affect the wave elevation along the tank length.

Run	CFD_{mean} ζ_C [m]	$Stokes2^{nd}$ ζ_C [m]	$Deviation$ ζ_C [%]	CFD_{mean} ζ_T [m]	$Stokes2^{nd}$ ζ_T [m]	$Deviation$ ζ_T [%]
1	0.0506	0.0528	**4.2**	0.0473	0.0472	**−0.2**
2	0.079	0.0813	**2.8**	0.0675	0.0687	**1.7**
3	0.106	0.1113	**4.8**	0.0857	0.0887	**3.4**

Table 4.20: Wave crest, ζ_C, and wave trough, ζ_T, amplitudes at section $x = 2.0m$ compared with theory.

Run	CFD_{mean} ζ_C [m]	$Stokes2^{nd}$ ζ_C [m]	$Deviation$ ζ_C [%]	CFD_{mean} ζ_T [m]	$Stokes2^{nd}$ ζ_T [m]	$Deviation$ ζ_T [%]
1	0.0475	0.0528	**10.04**	0.0451	0.0472	**4.45**
2	0.0725	0.0813	**10.82**	0.0658	0.0687	**4.22**
3	0.0968	0.1113	**14.33**	0.0817	0.0887	**7.89**

Table 4.21: Wave crest, ζ_C, and wave trough, ζ_T, amplitudes at section $x = 7.3m$ compared with theory.

In table 4.22 the wave height at $x = 7.3m$ is compared with the input wave height. In addition the deviation divided by the length from the wavemaker is given in %. The deviation per meter tank length gives the numerical damping in the total wave height along the tank lenght.

Run	Input $2\zeta_A\ [m]$	$CFD_{mean,7.3m}$ $\zeta_C + |\zeta_T|\ [m]$	$Deviation$ $[\%/m]$
1	0.1	0.0926	**1.01**
2	0.15	0.1383	**1.04**
3	0.2	0.1785	**1.47**

Table 4.22: Wave height at $x = 7.3m$ compared with input wave height. In addition deviation given in $[\%/m]$.

Wave Velocity

In figure 4.36 the total superficial water velocity at $t = 20s$ is shown. The total velocity is the magnitude of the velocity vector, and therefore zero velocity is the minimal velocity. The maximum velocity is located at the wave crest and at the zero up- and down crossing the minimum velocity can bee obtained from the almost regular blue areas underneath the crossings. The fact that the blue low velocity areas not are totally regular indicates that the wave crest is not symmetric with the wave trough and the waves are nonlinear. The wave velocities propagates to the bottom indicating shallow water. Close to the bottom the velocity tends to be zero, which will be true exactly at the bottom due to the no slip condition. The reason for the blue zone close to the bottom, indicating zero velocity, will be due to the large mesh size where the grid element next to the bottom will have zero constant velocity.
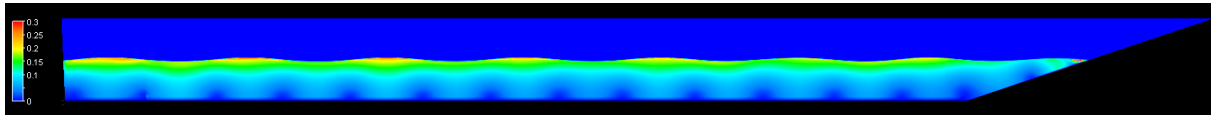
Figure 4.36: Superficial water velocity at $t = 20s$. Red indicate maximum $0.3m/s$ and blue indicate minimum $0m/s$.

In figure 4.37 the superficial water velocity in x-direction along the tank length is shown together with three studied sections. One section at the wave crest, one section at the zero-crossing and one section at the wave trough. In figure 4.38 the velocity profile at the three sections is compared with linear theory velocities. The actual mean wave elevation at the studied sections was measured to be $\zeta_A = 0.045m$ and was used for calculating the linear horizontal velocity. At the wave trough the velocity profile gives good agreement compared with linear horizontal x-velocity. At the zero-crossing the horizontal x-velocity is almost zero as expected. A small velocity increase is seen close to the free surface. The reason could be the manually selected section which might not was located exactly on the zero crossing line due to the mesh discretization. The horizontal x-velocity below the wave crest has the same shape as from linear theory but give slightly lower values. Close to the free surface the velocity below the wave crest seems to increase faster than the theoretical velocity. The reason for the deviation under the wave crest was found to be the use of a mean measured wave amplitude at the studied sections. With a increase of $5mm$ to the crest amplitude the theoretical velocity become similar to the measured velocity under the wave crest. Notice the almost linear velocity reduction close to the bottom wall from the CFD results. From the boundary conditions a no slip wall was used giving zero horizontal x-velocity at the wall. In addition the mesh was extruded with few and larger elements towards the bottom. Therefore the boundary layer close to the bottom will be coarse and show a linear reduction toward zero velocity at the wall. In the potential theory the bottom boundary condition only states no flow trough the wall, $\partial \mathbf{V}/\partial n = 0$, which aloud a horizontal x-velocity component at the wall.

The difference between Linear and Stokes 2nd order horizontal velocity is shown in figure 4.39 with a wave amplitude $\zeta_A = 0.1m$ similar as in run 3. There is a small difference close to the free surface, but overall the linear velocity gives almost similar values. This indicates that a linear wave potential can be used as a first prediction with reasonable accuracy even if the linearity assumptions not are fulfilled as in
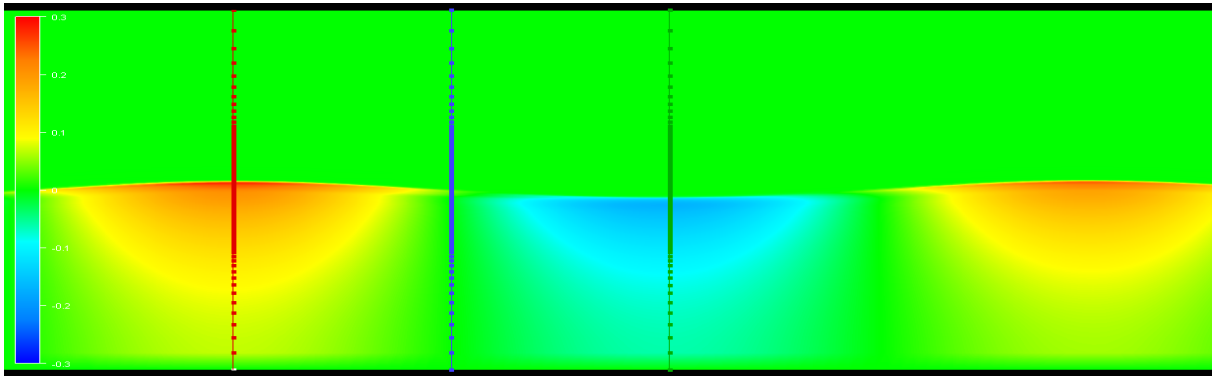
Figure 4.37: Superficial water velocity in x-direction along the tank length with $\zeta_A = 0.05m$. Red indicate maximum $0.3m/s$, green indicate zero water velocity and blue indicate minimum $-0.3m/s$.
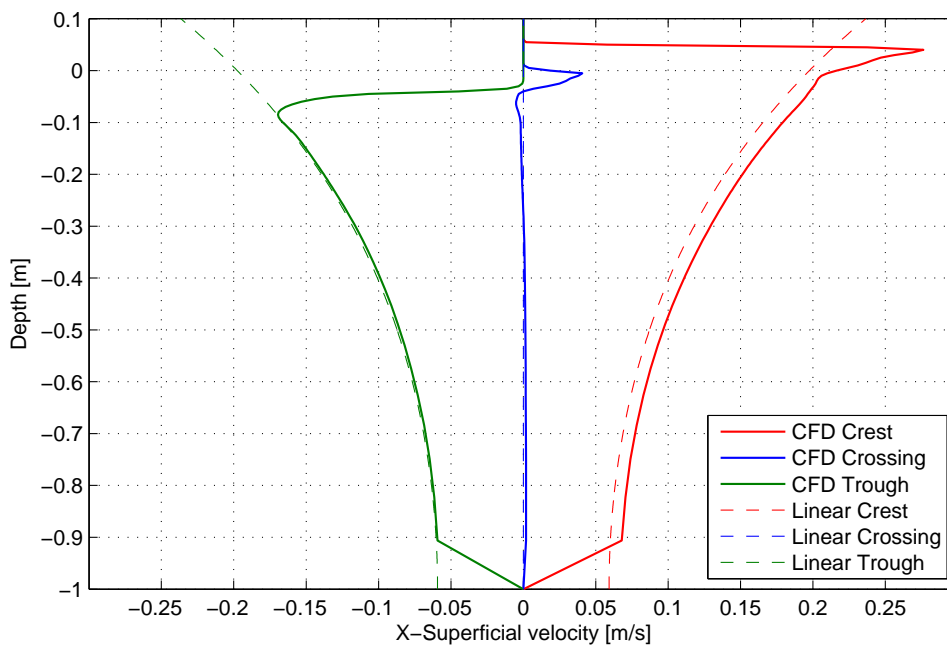
Figure 4.38: Comparison of horisontal water velocity with $\zeta_A = 0.05m$ and $h = 1.0m$ between CFD results and Stokes 2nd order. The maximum x-velocity located at the wave crest, zero x-velocity at the crossing ($z = 0.0m$) and minimum x-velocity at wave trough.

this case.
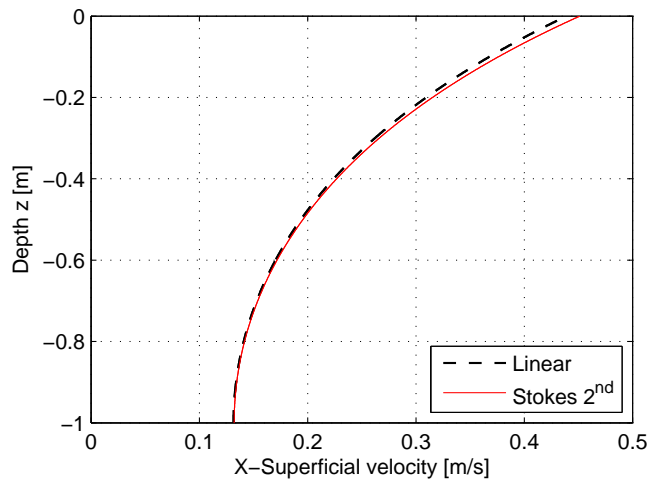
Figure 4.39: Comparison of horisontal water velocity under a wave crest with $\zeta_A = 0.1m$ and $h = 1.0m$ between Linear and Stokes 2nd order wave theory.

Wave Pressure

At the same studied sections given in figure 4.37 the total pressure can be evaluated. By subtracting the static pressure from the total pressure the dynamic wave pressure can be found. The static pressure is defined as $p_{static} = -\rho g z$, where ρ is the density, g is the gravity and z is the vertical coordinate positive upwards with origo at the mean free surface level. In figure 4.40 from Dean & Dalrymple (1984) the pressure variation under a wave crest and wave trough from linear theory can be seen. In linear theory the static pressure is defined up to the actual water level, $z = \zeta_C$, under a wave crest and up to mean surface level, $z = 0m$ under a wave trough. The dynamic wave pressure is the consequence of the orbital water particle motion in the fluid. In order to keep atmospheric pressure at the free surface, surface waves will balance the dynamic pressure.
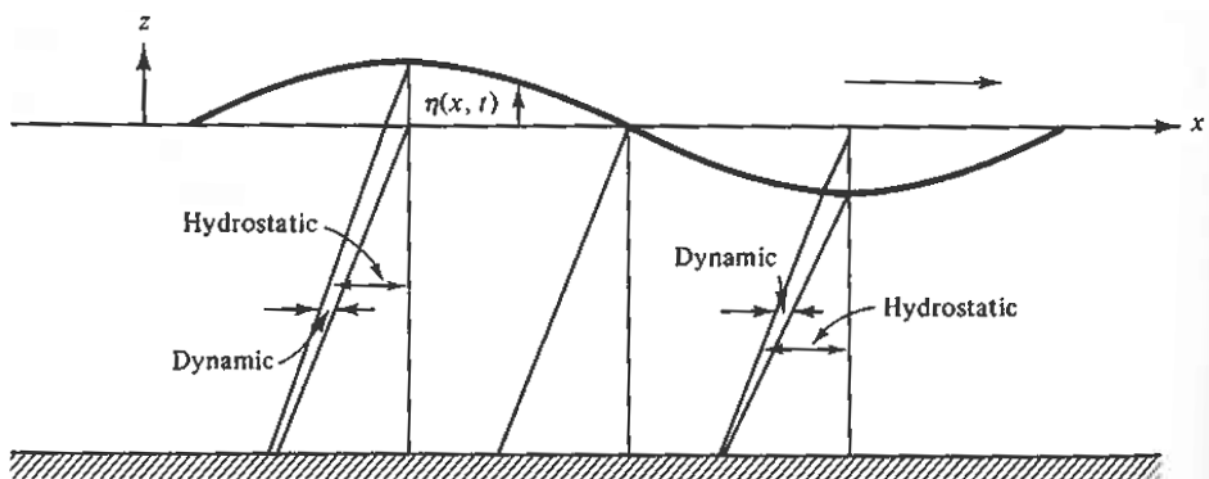
Figure 4.40: Pressure variation under a wave crest and a wave trough according to linear wave theory (Fig 4.4 in Dean & Dalrymple (1984)).

In figure 4.41 the dynamic wave pressure from the sections in figure 4.37 is compared with the dynamic pressure from linear wave theory under a wave crest, at zero-crossing and under a wave trough. The actual mean wave amplitude was measured to $\zeta_A = 0.045m$ at the studied sections and this value was

used to calculate the dynamic wave pressure with linear theory. Under the wave trough the dynamic wave pressure gives coincident values with the theoretical dynamic pressure. At the zero-crossing the dynamic pressure is almost zero. Under the wave crest the dynamic pressure follows the same shape from linear theory, but deviates with a small lower value. The small deviation was found to be around $30Pa$. A static pressure difference of $30Pa$ indicate a elevation difference of $3mm(z_{diff} = 30Pa/(\rho g)$. The difference can therefore be of reasons that the actual wave crest amplitude might be around $3mm$ higher than the used mean wave amplitude, which also was observed when studying the horizontal x-velocity under the wave crest. Overall the dynamic wave pressure under a wave period from CFD gives satisfactorily results compared with linear wave theory.
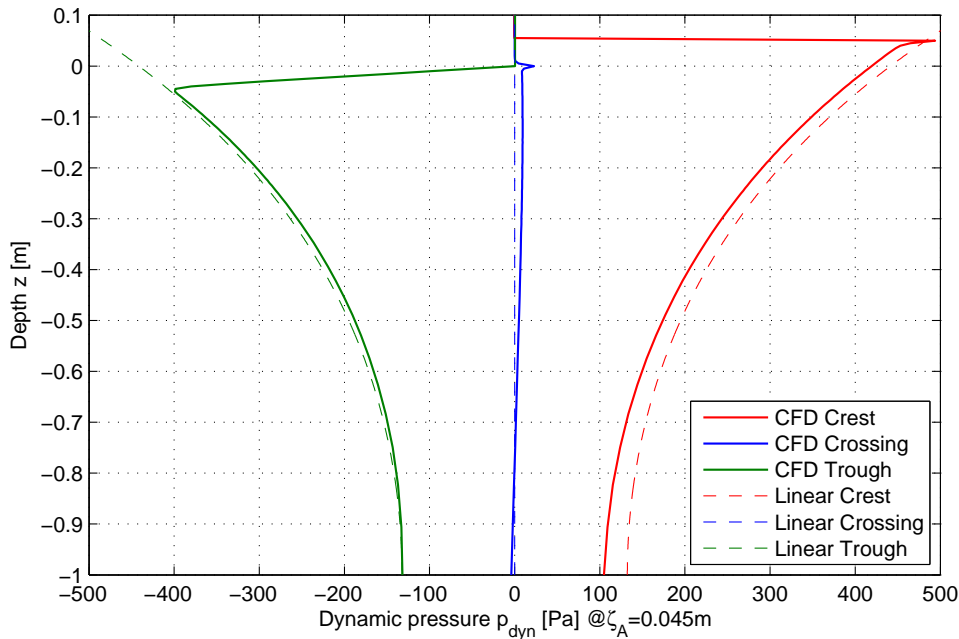
Figure 4.41: Comparison of dynamic wave pressure p_{dyn} under a wave crest, at the zero crossing and under a wave trough with linear dynamic wave pressure.

In figure 4.42 the dynamic pressure under a wave crest, zero crossing and wave trough is compared between linear theory and Stokes 2nd order theory. Small difference is obtained and the linear theory can be used as a first approximation.
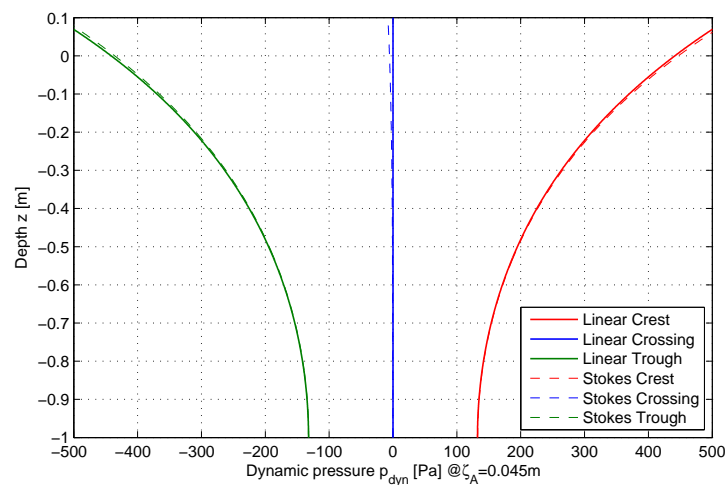
Figure 4.42: Comparison of dynamic wave pressure p_{dyn} under a wave crest, at the zero crossing and under a wave trough between Linear and Stokes 2nd order dynamic wave pressure.

Double precision

One single test, run 4, was performed similar as run 1 with double precision enabled as only difference. In figure 4.43 the wave crest and wave trough amplitudes from run 1 and 4 is compared at section $x = 2.0m$ and $x = 7.3m$. The amplitudes shows exactly similar results indicating no difference by using double precision in this specific case. The reason can be the simplification regarding the free surface model and that the mesh and time discretization give reasonable convergence with single precision.
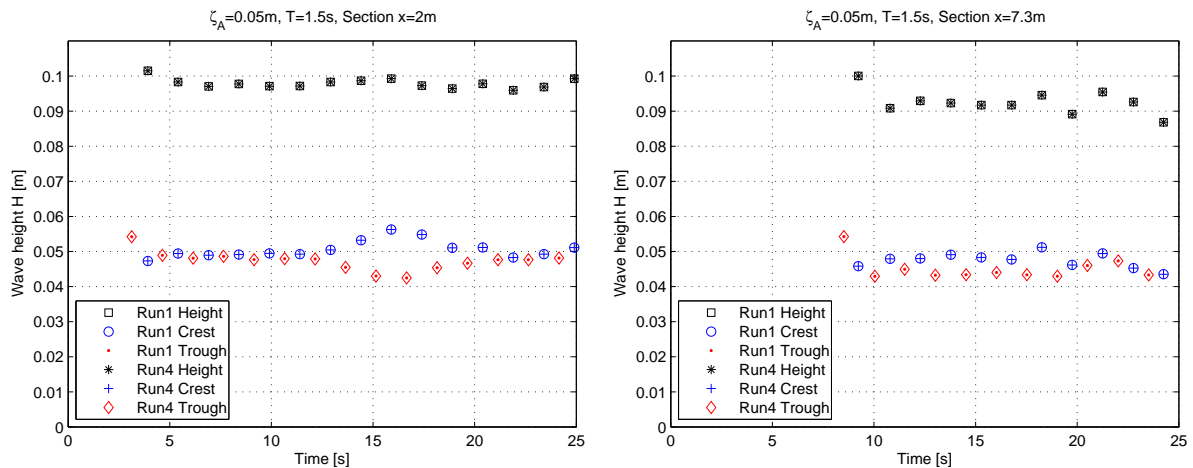
(a) Wave crest and trough amplitude Run 1 and 4 at $x = 2.0m$. (b) Wave crest and trough amplitude Run 1 and 4 at $x = 7.3m$.

Figure 4.43: Comparison with and without Double precision enabled. Wave crest, wave trough and wave height for run 1 and 4 with $\zeta_A = 0,05m$ at section $x = 2.0m$ and $x = 7.3m$. No difference obtained by using Double Precision.

4.5.3 Conclusion

The bottom hinged flap gives satisfactorily waves in shallow water. A small damping and some variation in wave amplitude along the tank length was obtained. The reason could be the mesh fineness along the tank length which was not in accordance with the suggested value given by Silva et al. (2010). The $\lambda/\Delta x$ value is therefore recommended to be larger than 66. Also the element aspect ratio can be of importance. A aspect ratio of $\Delta x/\Delta z = 10$ was used. With finer mesh along the tank length the element aspect ratio will decrease. In free surface flows the aspect ratio is of importance and a value larger than $O(10^1)$ will often result in instability or poor convergence given by Godderidge et al. (2008). From the time series of the wave elevation at given sections a steady wave profile was obtained. From the studied superficial horizontal water velocity good agreement was obtained under a wave crest, at the zero-crossing and under a wave trough compared with linear wave theory. Correct velocity profiles indicate correct oscillation of the water particles following the orbital path. The dynamic wave pressure also showed good agreement with linear wave theory. From comparison between linear theory and Stokes 2nd order theory for the velocity and pressure profile, small differences was obtained. Linear theory can therefore be used as a first approximation with good accuracy even though the linear assumptions not are totally fulfilled. In a CFD analysis the fundamental parameters is the velocity, pressure and temperature. With isothermal assumptions the results from CFD showed good agreement and can be used to perform free surface wave studies with acceptable accuracy. Regarding double precision no difference was obtained with double precision enabled. The solver converges well with single precision in the present cases. The reason can be the simplifications in the free surface model and that the used mesh and time discretization gives good convergence with only single precision. Double precision will therefore not be necessary to achieve a fully converged solution, which can save computation time.

4.6   Conclusion

A numerical wave tank can be a effective tool to reduce analysis time and costs compared to physical experiments. A first approach will be to validate a numerical method to produce satisfying numerical waves compared with wave theory. In section 4.2 the first method, a inlet velocity profile from linear wave theory was used to produce numerical waves. The inlet velocity profile can be used to produce numerical waves, but the static water pressure outlet condition will not be recommended. The advantage with the velocity profile method is that the studied wave theory can be implemented directly to the initial conditions. In similar way of using linear wave theory, higher order Stokes wave theory can be implemented to the initial conditions. A time discretization study was performed and a value of $\Delta t = 0.01$ gave reasonable convergence for the wave crest amplitude. With a wave period of $T = 0.98s$ the non dimensional parameter $T/\Delta t = 98$. In the article by Silva et al. (2010) $T/\Delta t >= 100$ was suggested and will be recommended.

In section 4.3 three different wavemakers was studied. A hinged flap, a bottom hinged flap and a piston. The same domain used by Silva et al. (2010) was used. The method with a moving piston or flap is similar to a mechanical wavemaker in a wave basin. In a numerical implementation the wavemaker was defined with a oscillated boundary wall at the start of the domain. All three modeled wavemakers produced almost similar results. The piston wavemaker gave closest results compared with Stokes 2nd order wave theory. The flap wavemakers gave similar results close to the piston wavemaker results, so all three wavemakers will be suggested in a numerical wave tank.

In section 4.4 a validation case from Silva et al. (2010) was chosen in order to try to achieve similar results. A hinged flap was used to produce numerical waves with a beach at the domain end. In the sub domain covering the wavemaker a motion specified mesh was used. Numerical disturbance was seen at the intersection between the motion specified and the rigid sub domain. Some variations and damping along the tank length was obtained in all cases. The reason could be the boundary conditions or the mesh fineness selected. From studied time series at given sections the surface elevation gave steady results. A small inclination of the wave profile was obtained for the time series which could be due to the variation in wave elevation along the tank length or the element discretization. The mesh is suggested to be normal to the free surface in all parts of the domain. The validation case published by Silva et al. (2010) gave a small value more steady results than the present work, although the same numerical settings was used. The reason could be some unmentioned numerical settings in the published article by Silva et al. (2010). One possible case could be the initial start of the flap wavemaker. A slower first cycle start of the flap wavemaker can avoid large unnatural water accelerations and numerical effects. A slow started wavemaker will be suggested.

In section 4.5 a bottom hinged flap was used in three cases with different wave amplitude. Similar as earlier, a small tendency with a variation in amplitude along the tank length was obtained also here. The time series gave steady results at the given sections. A closer look at the crest and trough amplitudes showed a small damping along the tank. The damping increased with increased wave amplitude. The reason can be the mesh fineness along the tank and the aspect ratio of the elements. Damping along the tank can also be obtained in a physical wave tank. $\lambda/\Delta x >= 100$ and $\Delta x/\Delta z < 10$ will be suggested values to reduce the numerical damping along the tank. Regarding the fluid particle motion the superficial horizontal water velocity showed good agreement with wave theory under a wave crest, wave trough and at zero crossing. A correct wave velocity profile indicate correct oscillation of the water particles following the orbital path. Also the dynamic wave pressure at the same studied sections gave good agreement with wave theory. The fact that the velocity and pressure showed good results states that the wavemaker method can be used to produce numerical waves with good accuracy.

The suggested values regarding numerical waves for mesh parameters and time step is given in table 4.23.

Parameter	Setting
Elements per wave length	$\lambda/\Delta x >= 100$
Elements per wave amplitude	$\zeta_A/\Delta x > 10$
Mesh aspect ratio	$\Delta x/\Delta z < 10$
Timestep per wave period	$T/\Delta t > 100$

Table 4.23: Summary of suggested values for a numerical wave tank.

4.7 Discussion and further work

A numerical wave tank can be modeled and simulated with CFD. A model of a physical wave basin can be implemented and perform similar analysis as a physical test. The advantage will be reduced time and costs. Also the fact that similarity in Reynolds number can be achieved and direct comparison since the numerical model can be modeled in both full scale and model scale. A preferred method would be to use the selected wave theory directly to the input parameters. The velocity specified input method will therefore be more attractive if it could produce better results than in the present work. A closer study on the velocity specified input method is therefore suggested. A slower start of the input velocity is also suggested for further work. The use of wave elevation and velocity field from wave theory as initial condition along the tank length gave improved convergence. When using pre-made waves at the initial condition, the time before the waves hit the domain end will be reduced. The static pressure outlet condition will force the elevation to the mean level and give wave reflections. If the actual water elevation at the domain end was known the actual static pressure could be defined. Then a dynamic pressure outlet could be implemented with a opening boundary condition at the domain end. The dynamic pressure outlet will be suggested for further work.

Another approach in order to avoid reflections at the domain end will be to add a damping zone to the domain. In a damping zone the waves will gradually be damped out to the mean water level and the velocity field damped out to zero velocities. A damping zone can be modeled in different ways. The most simplest would be to only increase the element size both horizontal and vertical. This will lead to a large numerical damping. In the present work a increase in element size was tested out but small disturbances was obtained in the damping zone. Also harder convergence was obtained when large aspect ratios of the elements was introduced due to the increased element size. Another method can be to add sources in the momentum equation which will damp out the waves. A isotropic momentum loss model was tried out, but appropriate loss coefficients was not investigated. The momentum loss model gave reflections and was not used in the present work. Introducing a damping zone will therefore be suggested to further work. The advantage with a damping zone will be a reduced domain size resulting in faster computation time and longer analysis can be performed. With a longer analysis time also irregular sea states can be investigated. With a flap or piston wavemaker one only need to add a time dependent stroke length to produce a irregular sea. A numerical wave tank for irregular sea will be suggested for further work.

In order to reduce computation time, running in parallel will be suggested. Issues regarding convergence and instability in the solver was obtained when running in parallel. In the user manual of ANSYS (2010) some advices is given for free surface flows in parallel. When a larger domain is modeled, for example a three dimensional analysis, reduced computation time will be important. A study on free surface flows performed in parallel will therefore be suggested for further work.

Chapter 5

Theoretical approach

In the design phase of offshore structures an important part is to calculate the wave forces. Chakrabarti (1987) lists up three methods to calculate the wave forces.

1. Morison equation
2. Froude-Kriloff theory
3. Diffraction theory

Both the Morison equation and the Froude-kriloff method can be used when the structure is small compared with the wave length. The Morison equation is based on a inertia force and a drag force. When the drag forces, or viscous forces, are significant the Morison equation can be used. The Froude-kriloff theory uses the undisturbed wave pressure to calculate a force on the structure surface. When the drag forces are negligible and inertia forces dominate the Froude-Kriloff method can be used. If the structure is large compared with the wave length the structure will affect the wave field and the diffraction theory should be taken into account. The diffraction theory gives theoretical values of the added mass force due to the fluid flow affection by the structure. In our case the structure is assumed small compared to the wave length and relatively short wave periods are studied resulting in small KC numbers. The Froude-Kriloff method has therefore been used with assumed and empirical based added mass coefficients in order to have a first approach on the wave forces. In this section the linear wave velocity potential will be used to calculate the Froude-Kriloff pressure force on each protection cover.

5.1 Froude Kriloff Pressure Force

The pressure force from a undisturbed wave is called the *Froude-Kriloff force*. A undisturbed wave means that the body does not affect the pressure field under the wave. In fact, when calculating the pressure, we just assume the structure to be there and use the dynamic wave pressure at the positions of the assumed structure walls. The assumption that the body will not affect the pressure field is a simplification and will not be true in a real fluid flow. The use of potential theory also simplifies the problem by assuming no viscous contributions. Still, due to the assumptions, the Froude-Kriloff force can be used when we assume a small structure compared to the wave length and small drag forces. The undisturbed pressure force can be found by integrate the pressure over the body surface, shown in equation 5.1.

$$F^{FK} = - \iint_S p \cdot \vec{n} ds \tag{5.1}$$

In equation 5.1 p is the pressure, $\vec{n}$ is the unit vector normal to the body surface pointing into the fluid

and S is the body surface. The dynamic wave pressure can be found by replacing the pressure, p, by the dynamic wave pressure p_{dyn}.

5.1.1   Froude Kriloff force on rectangular cover

The horizontal Froude-Kriloff force on the rectangular cover can be found by integrating the dynamic wave pressure over the side walls shown in equation 5.2. In figure 5.1 the normal vectors and position of $x1$, $x2$, $z1$ and $z2$ are shown.
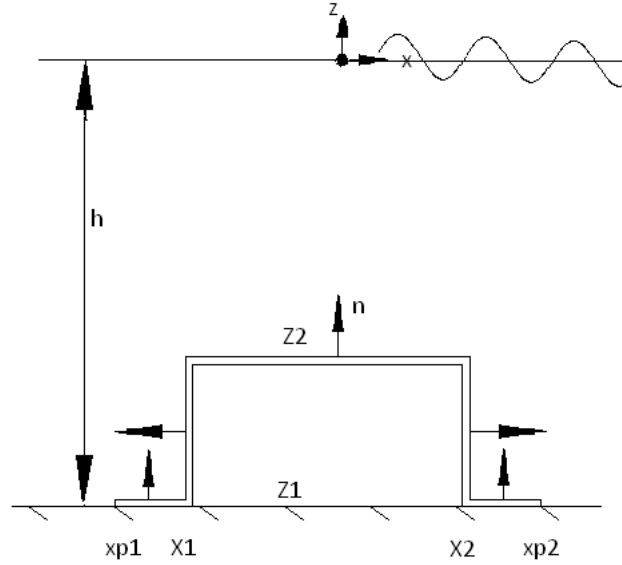
Figure 5.1: Normal vectors and wall coordinates on rectangular cover.

$$F_x^{FK} = -\int\limits_{z_1}^{z_2} p_{dyn,x1}(-1)bdz - \int\limits_{z_1}^{z_2} p_{dyn,x_2}(1)bdz \tag{5.2}$$

By inserting the dynamic pressure we get equation 5.3.

$$F_x^{FK} = -\frac{\rho g \zeta_A b}{cosh(kh)} \int\limits_{z_1}^{z_2} coshk(z+h)dz \left[(-1)cos(kx_1 - \omega t) + (1)cos(kx_2 - \omega t)\right] \tag{5.3}$$

Further solving the integral and use some trigonometric relations we get equation 5.4.

$$F_x^{FK} = -\frac{\rho g \zeta_A b}{cosh(kh)} \left[\frac{1}{k}2sinh(kd/2)cosh(kd/2)\right] \left[-2sin(kl/2)sin(k(x_1+l/2) - \omega t)\right] \tag{5.4}$$

The expression in 5.4 can be rearranged to equation 5.5.

$$F_x^{FK} = \rho lbd \frac{sinh(kd/2)}{kd/2}\frac{sin(kl/2)}{kl/2}\left[kg\zeta_A\frac{cosh(kd/2}{cosh(kh)}sin(k(x_1+l/2) - \omega t)\right] \tag{5.5}$$

By introduce the volume inside the cover, $V = lbd$, and the horisontal water acceleration at the center of the cover section, $\frac{\partial u}{\partial t} = kg\zeta_A \frac{\cosh(kd/2)}{\cosh(kh)}\sin(k(x_1 + l/2) - \omega t)$, we get the final expression for the horizontal Froude-Kriloff force on the rectangular cover given in equation 5.6.

$$F_x^{FK} = \rho V \frac{\sinh(kd/2)}{kd/2} \frac{\sin(kl/2)}{kl/2} \frac{\partial u}{\partial t} \tag{5.6}$$

Equation 5.6 is similar to the horizontal Froude-Kriloff force for a fully submerged rectangular object presented by Dean & Dalrymple (1984). We see that the pressure force can be expressed as a force proportional with the acceleration, similar as a mass force. The non dimensional coefficients, $\frac{\sinh(kd/2)}{kd/2}$ and $\frac{\sin(kl/2)}{kl/2}$, accounts for the vertical and horizontal pressure variation respectively. When the dimensions l and d becomes small compared with the wave length $\lambda = 2\pi/k$, these coefficients will go towards 1. In figure 5.2 the non dimensional pressure coefficient is plotted against increasing wave length λ with constant dimensional length l.
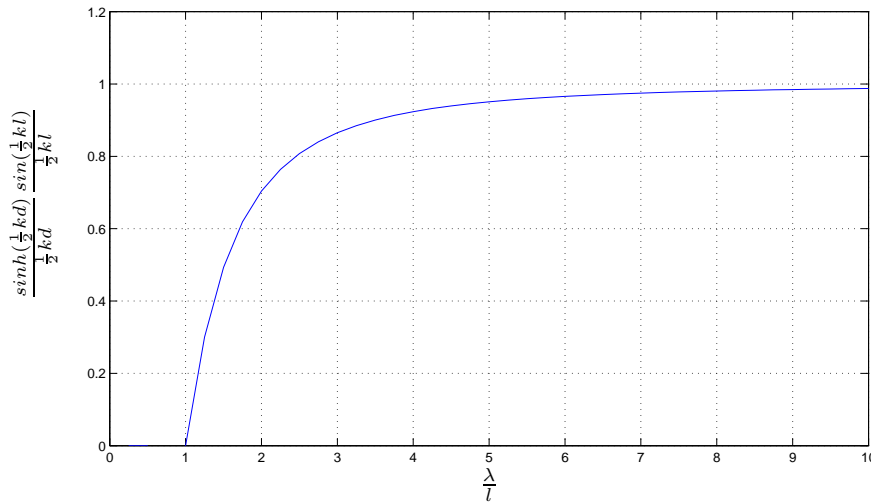
Figure 5.2: Non dimensional pressure coefficient for increasing wave length λ by structure length l.

Structures can be classified into *large volume structures* and *small volume structures* dependent of their ability to affect the wave field. When λ/l becomes smaller than 5 the structure is classified as a large volume structure. In figure 5.2 the non dimensional pressure coefficient is almost close to 1 for $\lambda/l > 5$. In our case, with $l = 0.2m$, the wave length must be $\lambda < 1m$ in order to be classified as a large volume structure. In the present work the smallest wave length was $\lambda_{min} = 1.56m$, which gives $\lambda/l = 7.8$ and a small volume structure is assumed. The result shows that for fully submerged small volume structure the Froude-Kriloff force can be evaluated as $F_i^{FK} = \rho V \frac{\partial u_i}{\partial t}$ where $\frac{\partial u_i}{\partial t}$ is the water particle acceleration in the force direction.

The vertical pressure force can be calculated in similar manner as the horizontal force. Since the protection cover is situated on the bottom, only the top side of the cover and the two horizontal side plates will give contribution to the vertical force. The vertical force equation is given in equation 5.7.

$$F_z^{FK} = -\int_{x_1}^{x_2} p_{dyn,z_2}(1)bdx - \int_{xp_1}^{x_1} p_{dyn,z_1}(1)bdx - \int_{x_2}^{xp_2} p_{dyn,z_1}(1)bdx \tag{5.7}$$

The vertical pressure force on the top of the protection cover is given in equation 5.8. The non dimensional terms distribute the pressure and relate the force to the acceleration at centre of the cover at

$x = x_1 + l/2$ and $z = -h + d/2$.

$$F_{z,cover1}^{FK} = \rho V \frac{cosh(kd)}{kd} \frac{1}{sinh(kd/2)} \frac{sin(kl/2)}{kl/2} \frac{\partial w}{\partial t} \qquad (5.8)$$

Notice the non dimensional term $\frac{cosh(kd)}{kd} \frac{1}{sinh(kd/2)}$ in equation 5.8 which not goes towards unity for small volume structures. Since we only get contribution from the top side of the structure the vertical force can not be given equivalent to a Morison inertia term. Still the vertical force is proportional to the vertical water particle acceleration. The pressure force on the two side plates can be found in similar manner and is given in equation 5.9. A similar non dimensional term relates the force to the acceleration in center. $A_p = l_p b$ is the area over one side plate.

$$F_{z,plates}^{FK} = 2\rho A_p \frac{cos(k(l+l_p)/2)}{k} \frac{1}{sinh(kd/2)} \frac{sin(kl_p/2)}{kl_p/2} \frac{\partial w}{\partial t} \qquad (5.9)$$

The total vertical Froude Kriloff force on the rectangular protection cover is given in equation 5.10.

$$\begin{aligned} F_z^{FK} = &\rho V \frac{cosh(kd)}{kd} \frac{1}{sinh(kd/2)} \frac{sin(kl/2)}{kl/2} \frac{\partial w}{\partial t} \\ &+ 2\rho A_p \frac{cos(k(l+l_p)/2)}{k} \frac{1}{sinh(kd/2)} \frac{sin(kl_p/2)}{kl_p/2} \frac{\partial w}{\partial t} \end{aligned} \qquad (5.10)$$

5.1.2   Froude-Kriloff force on half circular cover

In similar manner as outlined for the rectangular cover, the Froude-Kriloff force on the half circular cover can be found. Due to the half circular shape the integral over the surface become more difficult to solve analytically. The force equation 5.1 is therefore given with cylindrical coordinates in equation 5.11 where $x = rcos\theta$, $z = -h + rsin\theta$, $ds = brd\theta$ and $\vec{n} = [n_x, n_z] = [cos\theta, sin\theta]$.

Figure 5.3: Normal vectors and wall coordinates on rectangular cover.

$$F^{FK} = -\int_\theta p \cdot \vec{n} br d\theta \qquad (5.11)$$
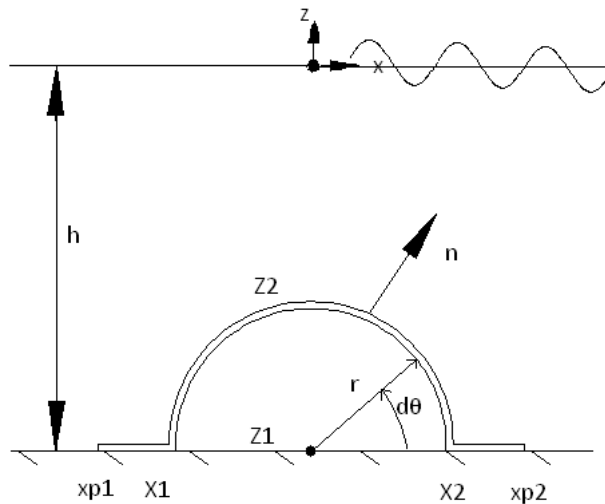
By rewrite the dynamic wave pressure to cylindrical coordinates and insert it into equation 5.11 we get equation 5.12.

$$F^{FK} = -\int\limits_0^\pi \rho g \zeta_A \frac{cosh k(h - h + r sin\theta)}{cosh(kh)} cos(kr cos\theta - \omega t)\vec{n}br d\theta \qquad (5.12)$$

The horizontal force is given in equation 5.13 with $\vec{n} = cos\theta$ and rearranged.

$$F_x^{FK} = \frac{\rho g \zeta_A br}{cosh(kh)} - \int\limits_0^\pi cosh k(h - h + r sin\theta)cos(kr cos\theta - \omega t)cos\theta d\theta \qquad (5.13)$$

The integral can be solved by series expansion of the trigonometric functions and only use the first expansion term due to linearity assumptions. The resulting horizontal force is given in equation 5.14 where $V = (\pi r^2 b)/2$ and $\frac{\partial u}{\partial t}$ is the horizontal water acceleration at the origin of the cross section ($x = 0$ and $z = -h$). Equation 5.14 is similar to the simplified Froude-Kriloff force on a fully submerged small volume structure. A similar study with more details can be found in Chakrabarti (1987).

$$F_x^{FK} = \rho V \frac{\partial u}{\partial t} \qquad (5.14)$$

Similar the vertical force on the half circular surface can be found by the same equation 5.11 only replacing the normal vector with $\vec{n} = sin\theta$. For the total vertical force, the additional contribution from the two side plates has to be taken into account. The total vertical force is given in equation 5.15 where u is the horizontal water velocity at the origin of the cross section ($x = 0$ and $z = -h$). A more detailed study can be found in Chakrabarti (1987). The second term in equation 5.15 is the vertical pressure force over the two side plates, similar as in equation 5.9.

$$\begin{aligned} F_z^{FK} = &-\rho V \frac{2}{\pi} \left[\frac{cos(kr)}{kr} + \frac{sin(kr)}{(kr)^2} + \int\limits_0^{kr} \frac{sin\theta}{\theta} d\theta \right] \omega u \\ &+ 2\rho A_p \frac{cos(k(l + l_p)/2)}{k} \frac{1}{sinh(kd/2)} \frac{sin(kl_p/2)}{kl_p/2} \frac{\partial w}{\partial t} \end{aligned} \qquad (5.15)$$

5.1.3 Total force

The total hydrodynamic force can be found by use of the Morison equation method or diffraction theory. The Morison equation given in equation 5.16 is valid for wave forces on a vertical cylinder from the bottom to a point above the wave crest. The well known, and often abused, equation can be used to study submerged structures in waves. The first term represents the mass force which is proportional with the undisturbed fluid acceleration $\frac{\partial u_i}{\partial t}$ and the second term is the drag force proportional with the undisturbed fluid velocity u_i squared. i denote the force direction $[x, y, z]$. The mass coefficient C_M and the drag coefficient C_D has to be empirically determined. The mass coefficient is often written as $C_M = 1 + C_a$ where C_a is the added mass coefficient. In the present work the Morison method can only be used for the horizontal force component, since the studied structures are bottom mounted and the vertical forces only will work on the top side without any contribution from the bottom side.

$$F_i = \rho V C_M \frac{\partial u_i}{\partial t} + \frac{1}{2}\rho C_D l|u_i|u_i \qquad (5.16)$$

In our case with wave loads the fluid velocity will exponentially decay towards the bottom giving low fluid velocities over the studied protection cover. In the quadratic drag term the fluid velocity is in addition squared which will indicate very small drag forces. Therefore the mass force is assumed to dominate and drag forces will be neglected. In appendix A, figure A.1 gives a schematic overview of the different force regimes valid for large volume structures. The inertia forces will dominate for wave heights smaller than $H < 0.2m$ with $l = 0.2m$ which was the case for most of the studied parameters. The total mass force will not only have contribution from the pressure force. The fluid will be affected by the structure and give diffraction forces. The total force can therefore be assumed to be the Froude kriloff pressure force and in addition a empirically added mass force due to the diffraction. In appendix A in figure A.1 the diffraction forces can be assumed to be small for wave lengths larger than $\lambda > 1.25m$ with $l = 0.2m$, which was the case for all the studied parameters. The horizontal Froude kriloff pressure force for both the rectangular and half circular protection cover was found to be proportional with the horizontal fluid acceleration. The total horizontal force for both protection covers can therefore be written as in equation 5.17, where A_x is the horizontal added mass. As also shown in equation 5.17 the total force can be written equivalent to the mass term in the Morison equation with the added mass term related to the displaced water volume ρV by a added mass coefficient C_a.

$$F_x = (\rho V + A_x)\frac{\partial u}{\partial t} = \rho V (1 + C_a)\frac{\partial u}{\partial t} \tag{5.17}$$

The horizontal two dimensional added mass coefficient can be found empirically or by diffraction theory. From DNV-RP-C205 (2010) two dimensional added mass coefficients for regular two dimensional geometries can be found. For the rectangular protection cover, a two dimensional rectangle with aspect ratio $l/d = 2$, the two dimensional added mass in infinitely fluid can be found to be $m_a = 1.7\rho A_R$. $A_R = \pi a^2$ is a reference area given for a circular cross section with radius $a = d/2$. In our case the structure is located on the bottom which will affect the fluid flow and consequently the added mass. From DNV-RP-C205 (2010) a two dimensional added mass coefficient for a circular two dimensional cylinder close to a wall can be found. At the wall the two dimensional added mass for the circular cylinder is given as $C_a^{2d} = \pi^2/3 - 1 = 2.29$. If the same increase in added mass at a wall is assumed for our rectangular cylinder, the two dimensional added mass becomes $m_a^{2d} = 1.7 \cdot 2.29\rho A_R = 3.893\rho A_R$. The horizontal added mass coefficient for the rectangular protection cover will then be $C_a^{2d} = 3.893 \cdot A_R/A$ where $A = ld$. With the given cross sectional dimensions of $l = 0.2m$ and $d = 0.1m$, the two dimensional added mass coefficient becomes $C_{a,1}^{2d} = \mathbf{1.53}$. For the half circular protection cover the added mass coefficient used for a full circular cylinder at a wall can be used, and only adjust the reference area with the actual area. The horizontal added mass coefficient for the half circular protection cover will then be $C_{a2}^{2d} = 2.29 \cdot A_R/A$, where $A = (\pi(d^2))/2 = A_R/2$. With cross sectional dimension $d = 0.1$, the two dimensional added mass coefficient becomes $C_{a,2}^{2d} = \mathbf{1.145}$. Chakrabarti (1987) gives a solution for the diffraction forces on a large volume structure half circular cylinder mounted on the bottom. The total horizontal force from Chakrabarti (1987) is given as $F_x = 2\rho V \frac{\partial u}{\partial t}$. Which indicate a total mass coefficient of $C_m = 2 = 1 + C_a$. The added mass coefficient then becomes $C_a = 1$ for the half circular protection cover, which is close to the assumed value.

Vertically we can not use a similar approach since the structure is situated on the bottom and only the top side and the two additional flat side plates give contribution to the vertical force. The total vertical force on the two flat plates on each side will be assumed to be the vertical Froude-Kriloff pressure force without any affection on the surrounding water. Similar if the wave length is long compared to the structure length the top side will only feel the additional water underneath the waves and the diffraction will be negligible. The vertical water particle motion is assumed small since in linear wave theory the vertical water velocity and acceleration is a order of magnitude lower than the horizontal water velocity and acceleration. The vertical force will therefore be assumed to be dominated by the Froude-Kriloff force. In a design phase the Froude-Kriloff force can be assumed to give the total vertical force as a first approach.

In table 5.1 the used horizontal added mass coefficients is given. The result of the theoretical forces can be seen in chapter 6 in comparison with the numerical forces from the CFD analysis.

Rectangular cover 1	$C_a = 1.53$
Half Circular cover 2	$C_a = 1.145$

Table 5.1: Horizontal added mass coefficient.

5.1.4   Discussion and Further work

The outlined Froude-Kriloff forces in this chapter is based on a undisturbed linear wave velocity potential. Since we assume a small volume structure the forces will mostly be mass dominated. Drag forces will be of minor importance since the horizontal and vertical fluid velocities is assumed small for the studied wave parameters. The presence of the of the structure will affect the fluid accelerations which can be accounted for by empirical added mass coefficients. The actual forces will be dependent of many parameters as Reynolds number, Keulegan-Carpenter number and affection from bottom and the free surface. In addition the added mass coefficients will be frequency dependent. Therefore the chosen added mass coefficients does not necessarily give the correct force contribution as in a real fluid flow.

In a real fluid flow in the environment for the full scale protection covers, there is usually also current in combination with the free surface waves. A combination of current and waves will be necessary to investigate in order to get the total force contribution. A current force will addition induce a lift force on the protection covers. The drag forces will be of more importance and the horizontal forces will be much larger. A theoretical approach of a wave- current combination will be suggested for further work in order to investigate the total force contribution and possible displacement or overturning of the protection cover.

Chapter 6

CFD Analysis on Protection Covers

In this chapter the numerical wave tank delevoped in section 4.5 in chapter 4 has been used to perform a two dimensional analysis of wave forces on two simplified protection covers. Similar wave amplitudes and wave periods used in the three first runs in section 4.5 was used to produce external wave forces on the submerged protection covers. Only difference compared to the three first runs in section 4.5 was the implementation of the two protection covers in each seperate domain. The numerical analysis was done in connection with the experimental tests presented in chapter 7. The physical experiments was performed in the student wave tank similar to the modeled domain in section 4.5 in chapter 4. Three runs was performed for each protection cover, giving in total 6 runs.

6.1 Definitions and Numerical settings

The additional installation frame used in the experiments was modeled together with the protection cover in the numerical domain in order to achieve similarity with the physical experiments. In figure 6.1 the dimensions for the modeled frame and the two protection covers is shown. The rectangular cross section will be referred to as cover 1 and the circular protection cover as cover 2. For simplification the frame with the protection cover was only implemented by changing the bottom boundary geometry and modeled as no slip walls. The boundaries around the protection cover with the two flat side panels was isolated as a seperate region in order to only make measurements from the actual boundaries defining the protection covers.
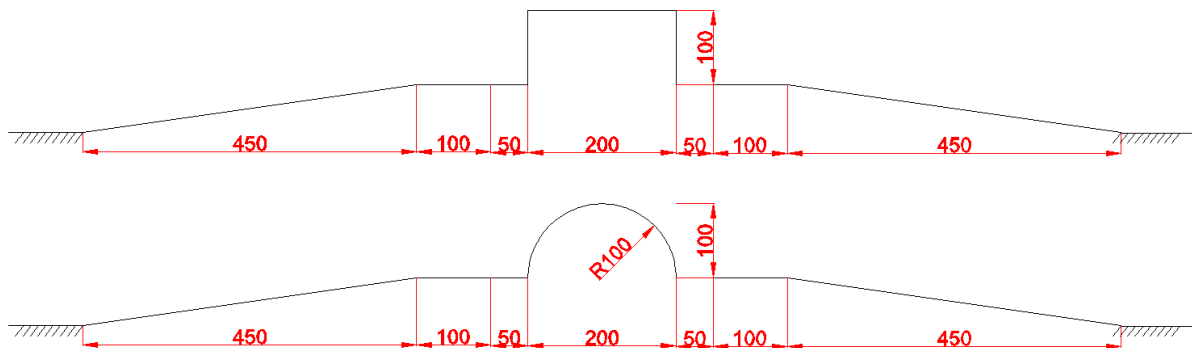

Figure 6.1: Dimensions used for the protection covers in the domain. All dimensions in millimeters [mm].

The domain used for the rectangular cover is shown in figure 6.2. Same domain was used for the half circular protection cover. Similar as in section 4.5 the domain length was set to $L_t = 28m$ which gave a

free surface of $25m$ with a beach with slope $1 : 3$ at the domain end. The water depth was set to $1.0m$ and $1.0m$ air was modeled above. A two dimensional analysis was performed with an extruded length of $0.1m$. Four sections was defined to measure the wave elevation at $x = 2.0m$, $x = 7.3m$, $x = 8.7m$ and $x = 21.5m$. The sections can be seen as vertical lines in the domain in figure 6.2. The protection covers was modeled with cover center at $x = 8.0m$, similar as in the physical experiments.
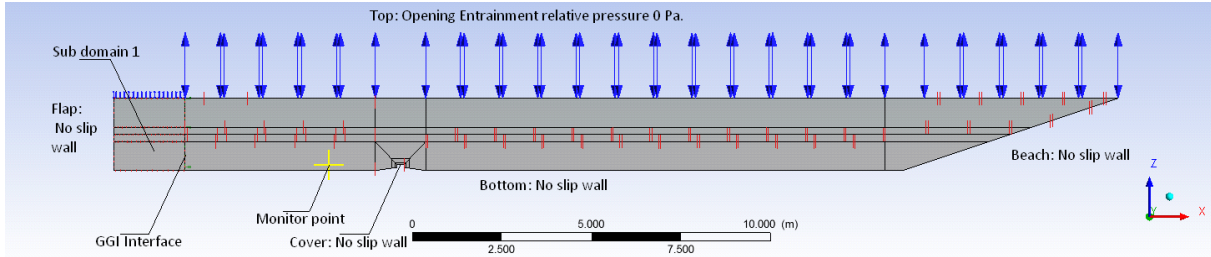

Figure 6.2: Domain used with rectangular cover. Similar domain was used for the circular domain.

The mesh parameters used is given in table 6.1. Close to the free surface there was used 120 elements vertically between $z = \pm 0.25m$, giving $\Delta z = 0.0042$, instead of 100 elements as earlier used in the studied wave tank in 4.5 in chapter 4. The reason was to try to achieve less variation in wave amplitude along the wave tank. As commented earlier in the conclusion in section 4.6 the horizontal number of elements should be increased rather than the vertical number of elements around the free surface due to the suggested values by Silva et al. (2010) and to keep a low element aspect ratio. The numerical study on the protection covers was performed at the same time as the numerical wave tank study and the suggestions given for a numerical wave tank was developed afterwards. For further work the mesh will be recommended to be modified in accordance with the suggested values. In figure 6.3 a closer view of the mesh around the two protection covers is shown. On the top side of the rectangular cover the mesh density was $\Delta x_{cover} = 0.004$ and on the vertical sides the mesh density was $\Delta z_{cover} = 0.005$.

Parameter	Setting
Domain length	$28m$
Water depth	$0.75m + 0.25m$
Air height	$0.75m + 0.25m$
Extruded width	$0.1m$
Number of Elements	91920
Δx	0.05
Δz	0.0042
$\Delta x / \Delta z$	12
Air_z	20
$Water_z$	20

Table 6.1: Mesh details in studied Wave Tank

Similar numerical settings and boundary conditions used in section 4.5 in chapter 4 was used. A short summary is given. The domain was divided at $x = 2m$ in two sub domains with a *GGI* interface connection. The bottom and the beach boundary was set to a no slip wall, $U_{wall} = 0$. The protection cover was also set to a no slip wall. The top boundary was set to a entrainment opening with zero static pressure. The front and back boundaries was set to symmetry planes. The bottom hinged flap was set as a moving no slip wall. The numerical settings used is given in table 6.2.

A monitor point was defined at $x = 6m$ and $z = -0.832m$, two meters in front of the cover center. The vertical position was chosen similar to the top position of the cover. In the numerical analysis the cover top was located at $z = -0.835m$. In the physical experiments there was in addition extra $3mm$ due to plate thickness of the inclined side panels which gave a top location at $z = -0.0832m$. The modeled
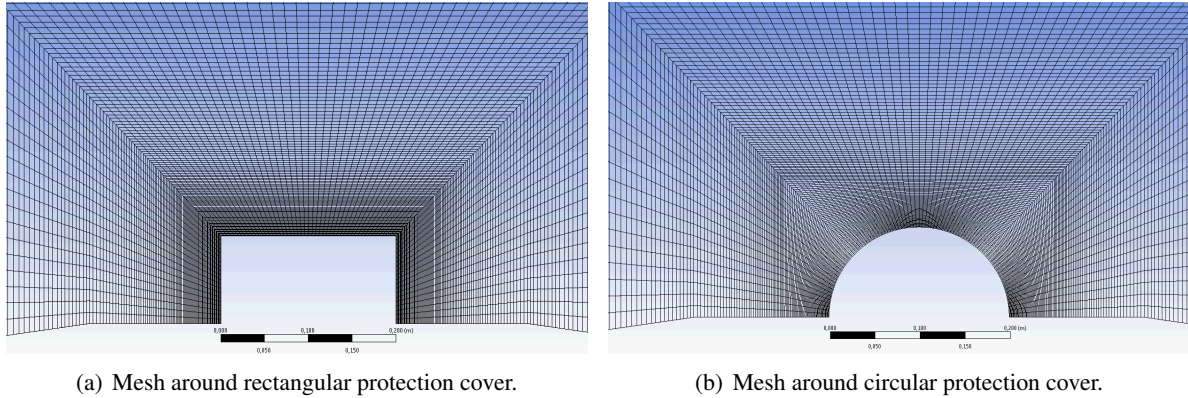
(a) Mesh around rectangular protection cover.

(b) Mesh around circular protection cover.

Figure 6.3: Close view of mesh for the two protection covers.

Parameter	*Setting*
Version	CFX 13.0
Model	Transient
Turbulence	SST
Advection Discretization Scheme	Specified blend, blend factor =1
Time Discretization Scheme	Second order Backward Euler
Convergence criteria	$RMS < 1E - 3$
Convergence loops	$3 - 6$
Precision	Single
Mode	Serial
Total time	$25s$
Time step	$\Delta t = 0.01s$

Table 6.2: Numerical settings for the validation case.

protection cover did not take the plate thickness into account. $3mm$ difference was seen as a small deviation and new analysis was not performed. At the monitor point water velocity in both horizontal and vertical direction and the pressure was logged. On the protection cover the walls and the two side panels was isolated in order to measure forces. Both pressure forces and viscous forces was logged on the isolated walls. In addition also the torque around the y-axis was logged. Due to use of global axis instead of local axis the overturning moment is not shown in the present work.

In table 6.3 the 6 performed runs with the related wave input parameters is given.

Run	Cover type	T [s]	ζ_A [m]	λ [m]	$\lambda/\Delta x$	$\zeta_A/\Delta z$	ζ_A/h	$k = \frac{2\pi}{\lambda}$ [1/m]	H/λ	$U_r = \frac{k\zeta_A}{(kh)^2}$
1	1	1.5	0.05	3.3515	67	12	0.01	1.875	1/33.5	0.0267
2	1	1.5	0.075	3.3515	67	18	0.075	1.875	1/22.34	0.0400
3	1	1.5	0.1	3.3515	67	24	0.1	1.875	1/16.76	0.0533
4	2	1.5	0.05	3.3515	67	12	0.01	1.875	1/33.5	0.0267
5	2	1.5	0.075	3.3515	67	18	0.075	1.875	1/22.34	0.0400
6	2	1.5	0.1	3.3515	67	24	0.1	1.875	1/16.76	0.0533

Table 6.3: Numerical settings for each run. S is the flap stroke at the surface, T is the wave period, ζ_A is the wave amplitude, $H = 2\zeta_A$ is the wave height, k is the wave number and U_r is the Ursell number.

The non dimensional parameters are almost similar as in 4.5 in chapter 4 and the same assumptions can be used. Shallow water is assumed since $h = 1.0m > \lambda/2 = 1.67m$ is not true. The linear

criteria $kh = 1.875 << 1$ is not fulfilled and indicate nonlinear waves. Both Stokes 2nd order criteria, $\zeta_A/h < 0.26$ and $U_r =< 1/3$, holds and Stokes 2nd order waves will be more comparable than linear theory. Regarding the mesh the same issue obtained in section 4.5 regarding to few horizontal elements compared with the wave length was obtained. The non dimensional time step value was $T/\Delta t = 150$. In table 6.4 non dimensional parameters regarding the fluid flow is given.

Run	ζ_A [m]	z_{crit} [m]	R_e [−]	F_n [−]	KC [−]
1 and 4	0.050	−0.45	15920	0.071	0.52
2 and 5	0.075	−0.82	23880	0.105	0.78
3 and 6	0.100	−	31840	0.140	1.04

Table 6.4: Fluid flow parameters for the three different wave amplitudes ζ_A. z_{crit} is the critical depth when $Re_A >= 3000$), R_e is the Reynolds number over the protection cover, F_n is the tank depth based Froude number and KC is the Keulegan Carpenter number over the protection cover.

The critical depth indicate a large turbulent mixing layer from the definition of the amplitude based Reynolds number which exceed 3000 above z_{crit}. For the largest wave amplitude the whole tank depth will have $Re_A > 3000$. The Reynolds number based on the length of the protection cover indicate a turbulent flow and that a turbulence model should be used in the analysis. The tank depth based Froude number is similar as in the wave tank without the protection cover and indicate sub critical flow. The Keulegan Carpenter number is low indicating that inertia forces will dominate and drag forces of minor importance. Both the Reynolds number and the Keulegan Carpenter number is calculated from the maximal horizontal fluid velocity at the top of the protection cover from linear wave theory.

6.2 Results and Discussion

All six numerical analysis in this section was performed in serial on a local $64 - bit$ computer with a Intel Xeon $X5680@3.33GHz$ processor and $32GB$ installed memory. In table 6.5 the computation time of each run is listed.

Run	Computation time [h]
1	64.52
2	66.47
3	51.42
4	55.80
5	55.56
6	55.57

Table 6.5: Compitation time for each run.

6.2.1 Wave Elevation

In figure 6.4 the surface elevation at $x = 7.3m$ and $x = 8.7m$ is compared with Stokes 2nd order wave elevation for run 1 with $\zeta_A = 0.05m$. A very well agreement is obtained indicating that the assumptions for using Stokes $2^n d$ order wave theory was reasonable. Note that by using linear wave theory just a small deviation is found around the crest and trough of the wave, but similar wave height will be obtained. The used wave amplitude in the theoretical wave elevation is taken from the actual measured wave amplitude from the CFD analysis at $x = 7.3m$. For the elevation at $x = 8.7m$ only a change in the kx value in

the theoretical surface elevation expression was done. By comparing the elevation at the two sections at $x = 7.3m$ and $x = 8.7m$ in figure 6.4 small or no disturbance from the submerged protection cover can be assumed.
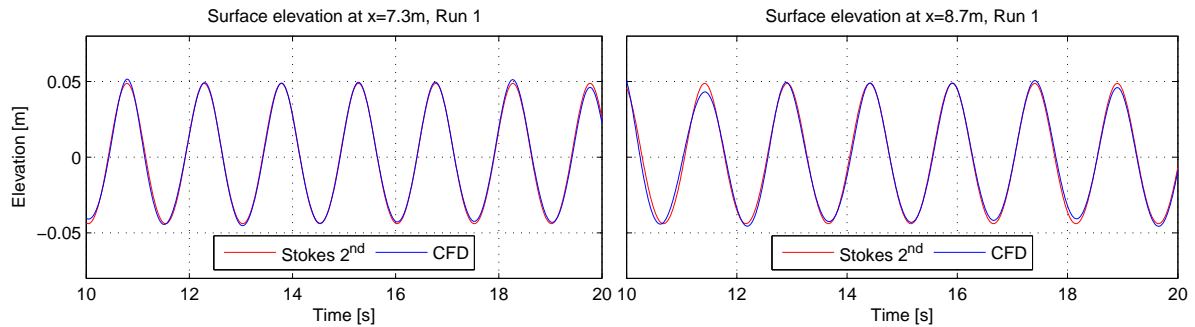

Figure 6.4: Wave elevation at $x = 7.3m$ and $x = 8.7m$ compared with Stokes 2nd order wave elevation.

6.2.2   Comparison at studied monitor point

At the studied point, $2m$ upstreams of the center of the protection cover and $z = -0.832m$, the water was assumed unaffected by the protection cover. The horizontal and vertical water velocities and the total pressure was logged as function of time during the analysis. In figure 6.5 the horizontal and vertical water velocity is compared with Stokes 2nd order wave velocities. The studied time was selected between $t = 10s - 20s$ with steady wave elevation. For the horizontal water velocity a variation in time was obtained. Also the mean horizontal velocity from the studied time section was obtained a small value lower than the mean horizontal Stokes 2nd velocity. From the Stokes theory a mean net mass flow in the propagation direction will be assumed due to the open orbital path. From the actual wave parameters the net mass flow will be very small and the mean horizontal Stokes 2nd velocity will be close to $0m/s$. The mean horizontal velocity from the studied time was in fact a small value negative indicating a small negative mass flow which not will be natural. Regarding the vertical water velocity, good agreement with Stokes 2nd order wave velocity. Small deviation was found at both the maximal and minimal with smaller values from CFD. The reason could be the actual water elevation at the studied point. Overall the velocities gave good agreement.
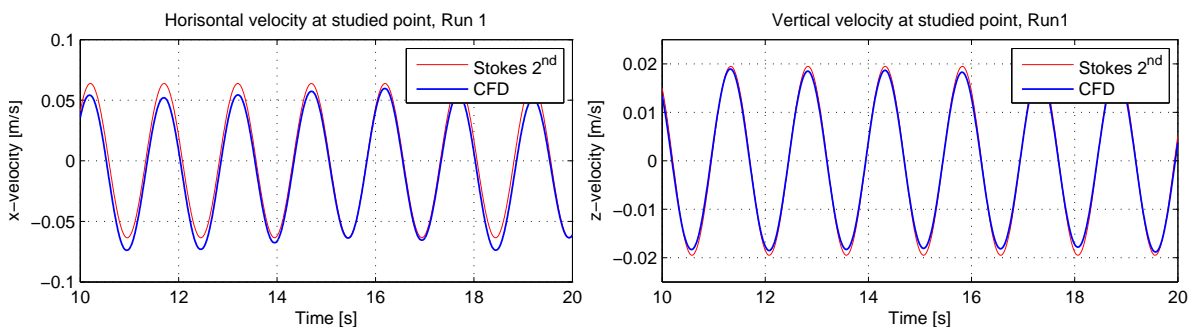

Figure 6.5: Horisontal and vertical water velocity at studied point ($x = 6m$, $z = -0.832m$) compared with Stokes 2nd order wave velocity.

In figure 6.6 the dynamic wave pressure from the measured point is compared with Stokes 2nd order wave theory. The total pressure was logged. The dynamic pressure was found by subtracting the initial pressure value from the total pressure measured at the studied point. The initial pressure from a mean free surface will be the static water pressure, $p_{static} = -\rho g z$, and the atmosphere pressure p_0. From the comparison the magnitude of the measured dynamic pressure gives good agreement with Stokes 2nd

order wave theory. Note that linear dynamic wave pressure will almost be coincident with the Stokes 2nd order dynamic pressure. A overall lower value and some variation in the studied time period is obtained from the measured dynamic pressure. The reason will mostly be the variation in water velocity since the actual measured wave elevation in the studied time period was steady.
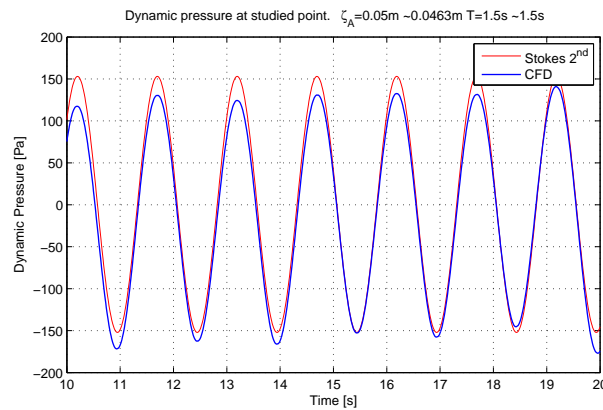

Figure 6.6: Dynamic wave pressure from studied point ($x = 6m$ and $z = -0.832m$) compared with Stokes 2nd order wave theory.

6.2.3 Force measurement

In ANSYS CFX there is several methods to make force measurements. The CFX Expression Language (CEL) has several built in functions for force measurements. The *force* function can be used to find the total hydrodynamic force acting on a region. The *force* function calculate both pressure forces and viscous forces. Another approach is to use the *areaInt* function. The pressure force can be found by integrate the pressure over the area of the studied region. Similar the viscous friction forces can be found by integrate the shear stress over the area of the studied region. Also a *torque* function is given in the built in CEL expressions. Note that only the dynamic forces has been studied. In vertical direction the pressure force will have a static contribution which has been subtracted from the total vertical force in order to only study the dynamic wave forces. In figure 6.7 the different CEL expressions used to calculate force and is shown.

Figure 6.7: CEL expressions used to calculate total force, pressure force, viscous force and torque on a given region in ANSYS CFX.

In figure 6.8 the total horizontal and vertical dynamic force on the rectangular cover from run 1 is compared between CFD and theoretical force. Similar in figure 6.9 the horizontal and vertical dynamic force on the half circular cover from run 4 is compared between CFD and theoretical force.

The numerical forces gives good agreement with theory. In the horizontal direction the total linear calculated force was based on the Froude-Kriloff force together with a added mass force. The suggested added mass coefficients gave a conservative horizontal force for the rectangular cover. The measured horizontal added mass coefficients from the CFD analysis was found from curve fitting to be $C_{a,1}^{CFD} = 1.4$ for the
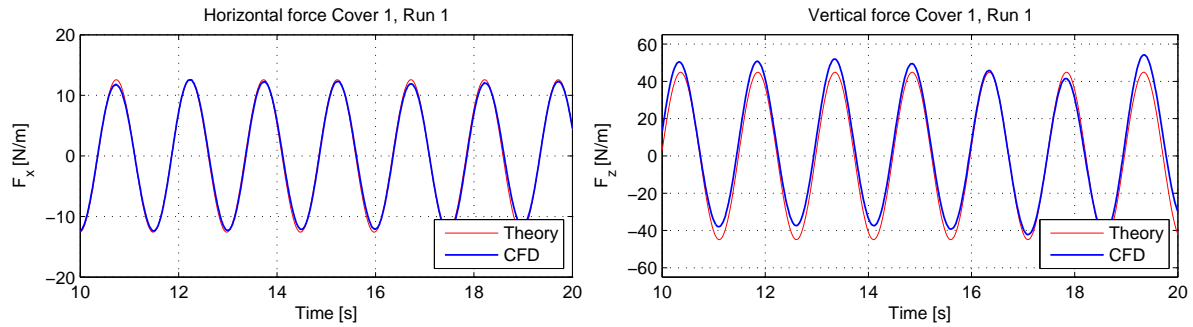
Figure 6.8: Comparison of horizontal and vertical dynamic force on rectangular cover for run 1 between CFD and Theoretical approach. Vertical theoretical force calculated as Froude Kriloff pressure force without added mass contribution. Horizontal theoretical force calculated as Froude Kriloff pressure force with contribution from a added mass force with $C_a = 1.53$.
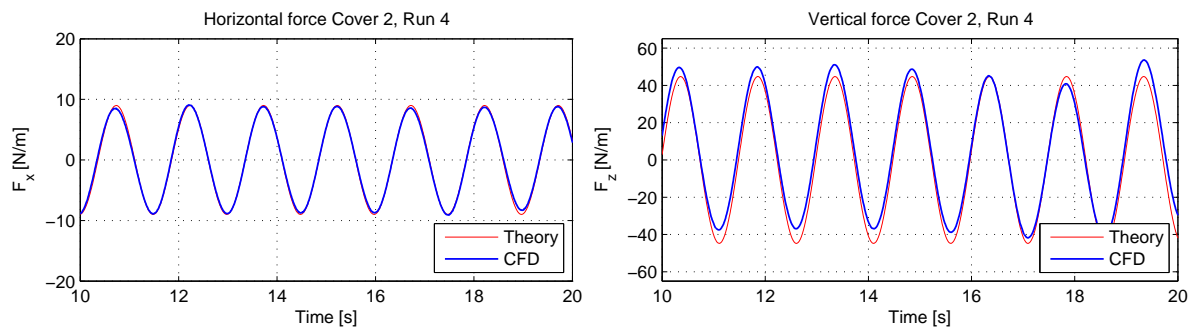

Figure 6.9: Comparison of horizontal and vertical dynamic force on half circular cover for run 4 between CFD and Theoretical approach. Vertical theoretical force calculated as Froude Kriloff pressure force without added mass contribution. Horizontal theoretical force calculated as Froude Kriloff pressure force with contribution from a added mass force with $C_a = 1.145$.

rectangular protection cover and $C_{a,2}^{CFD} = 1.18$ for the half circular protection cover. The numerical added mass coefficients is close to the suggested coefficients which was based on the assumption given for a circular cylinder close to a wall and corrected to the actual geometry. The numerical vertical forces was a small value larger than the calculated Froude-Kriloff pressure force. The vertical fluid motion will be affected by the protection cover and give rise to a added mass force. In a theoretical approach one should therefore account for the vertical added mass contribution in order to have a conservative vertical force. On the other hand the vertical Froude-Kriloff pressure force can be used as a first value to get the order of magnitude of the vertical force. In order to check the contribution of viscous forces to the total force, the shear stress was integrated over the walls of the protection covers. In figure 6.10 vertical and horizontal viscous forces from run 1 is shown.
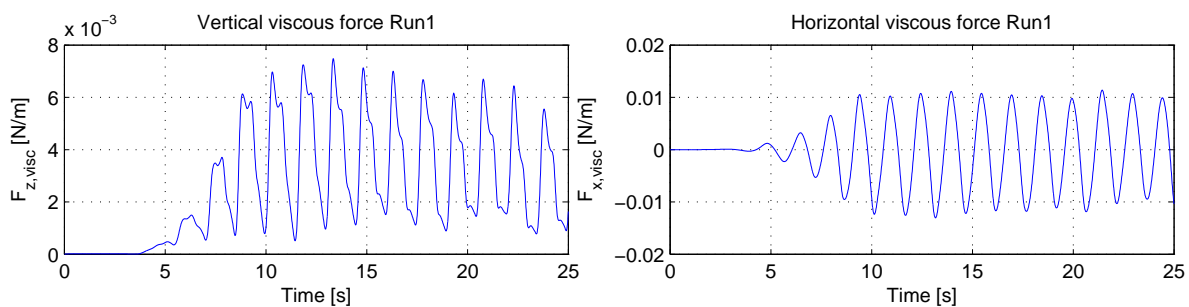

Figure 6.10: Vertical and horizontal viscous forces from run 1.

From figure 6.10 the viscous forces can be assumed small compared to the total force and hence neglected. Especially in the vertical direction with very small fluid velocities, the viscous forces was assumed to be small which was shown to be correct.

The numerical forces can be made non dimensional by the equation 6.1, where ρ is the density, g gravity, V volume of cover, ζ_A wave amplitude and h the water depth. The wave amplitude ζ_A is taken from the actual measured wave amplitude at $x = 7.3m$ in the CFD analysis. In figure 6.11 the non dimensional horizontal and vertical force for both the rectangular and the halfcircular protection cover is shown. Here cover 1 represents the rectangular cover and cover 2 represents the half circular cover.

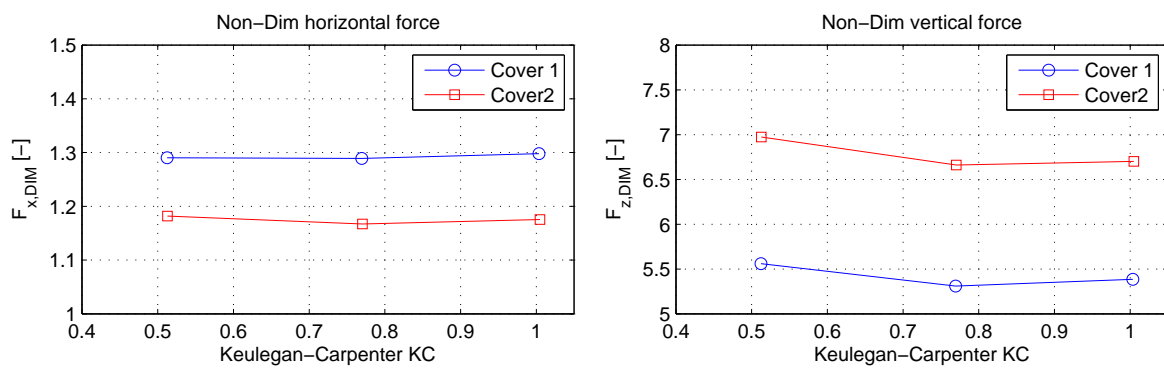$$F_{DIM} = \frac{F_{max}}{\rho g V \frac{\zeta_A}{h}} \tag{6.1}$$

Figure 6.11: Non dimensional forces on both rectangular and half circular protection cover.

The non dimensional horizontal force is larger for the rectangular protection cover which is reasonable due to the vertical walls instead of a smooth surface as over the half circular protection cover. The non dimensional vertical force is larger for the half circular protection cover. The projected area of the top side is equal for both the rectangular and half circular cover, but the total top surface of the half circular cover is slightly larger due to the curvature. The small amount larger top surface will give larger contribution to the vertical force. In addition the closed volume is smaller for the half circular cover which is represented in the denominator for the non dimensional force. Notice also the large difference between the horizontal and vertical force. The horizontal force has contribution from both sides of the cover and cancellation effects arise. Especially with long wave lengths compared to the cover length the horizontal force will be low. The general trend for both covers shows a almost constant non dimensional force with increasing KC number. In the experimental results in chapter 7 similar results can be seen and the same trend with a mean constant vertical force was obtained above $KC = 0.25$. For the numerical non dimensional force it could therefore be interesting to study non dimensional vertical forces below $KC = 0.25$ in order to obtain similar trend as in the experiments.

6.2.4 Contour plots and vector plots

In a numerical CFD analysis, fluid properties is calculated for each discretized element resulting in a powerful tool in order to investigate the fluid dynamics. The main governing physical parameters is the velocity, pressure and temperature. Further parameters can be evaluated from the physical quantities together with the actual studied domain. In figure 6.12 the Y^+ value over the half circular cover from run 4 at $t = 15s$ is shown.

The Y^+ value is the non dimensional wall distance described in chapter 3. In figure 6.12 the largest value of $Y^+ = 25$ is found on the side plates due to coarser elements there. In waves the velocities, following
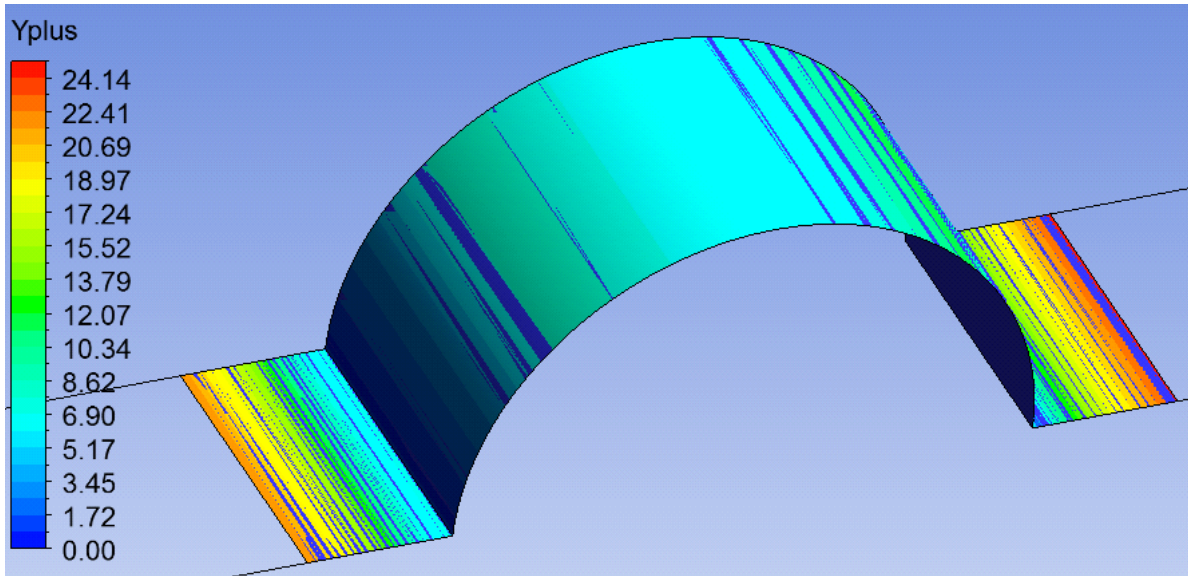
Figure 6.12: Y^+ value over the half circular protection cover from run 4.

the orbital paths, variates dynamically and also give a dynamic variation in the Y^+ value. A further investigation shows that the overall Y^+ values was low and in accordance with the suggested values for the chosen SST turbulence model.

in figure 6.13 a superficial water velocity vectors from run 4 at $t = 14s$ is shown. The oscillatory motion of the fluid particles can be seen from the direction of the vectors. The color scale represents the velocity magnitude and a decrease towards the bottom can be seen. The protection cover will have a small influence on the wave particle motion close to the bottom. Similar figure for $t = 15s$ and $t = 16s$ can be found in appendix D.
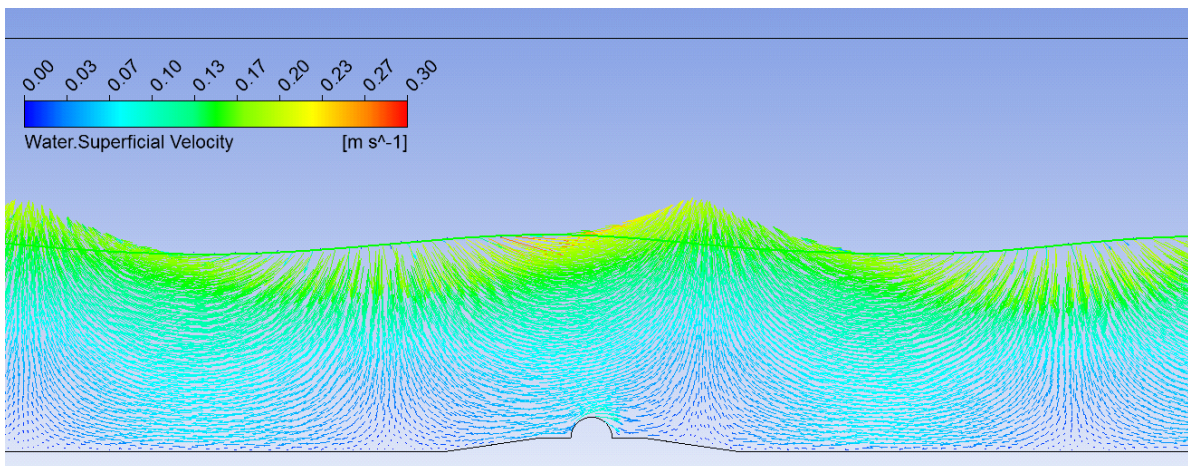

Figure 6.13: Superficial water velocity vectors over half circular protection cover in run 4 at $t = 14s$.

In figure 6.14 a contour plot of the superficial velocity from run 4 at $t = 20s$ is shown. Here the steady wave propagation along the tank can be seen.

In figure 6.15 a closer view of the superficial water velocity in x direction, in z direction and total direction from run 4 at $t = 20s$ is shown for the surface waves. The horizontal superficial water velocity is maximal positive under the wave crest and minimal negative under the wave through. The vertical superficial water velocity is maximal positive at the zero-down-crossing and minimal negative at the zero-up-crossing. Notice the same legend scale on the horizontal and vertical water velocity, where the
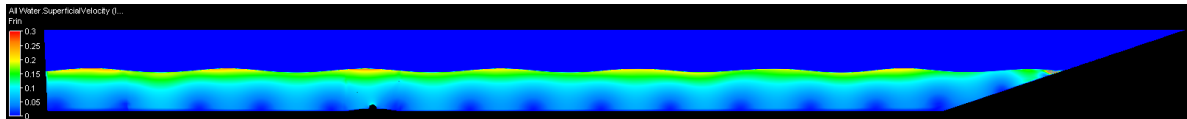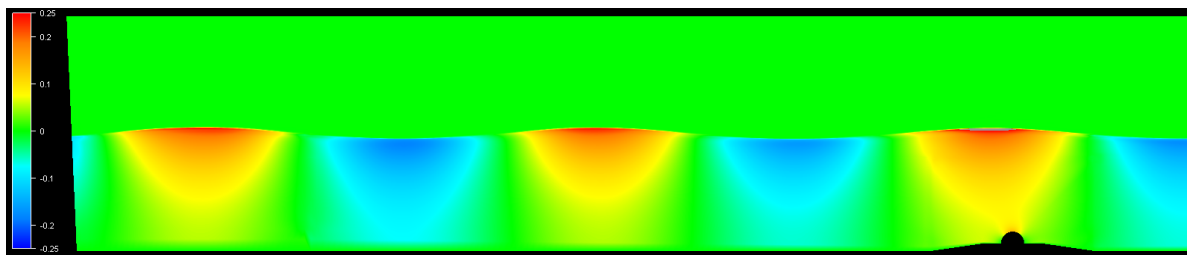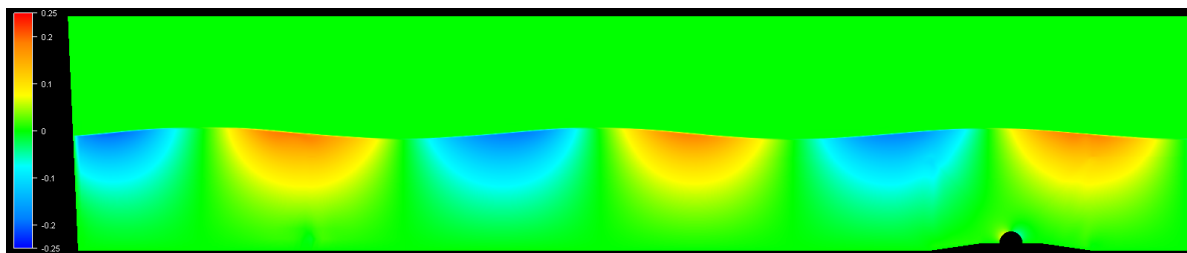
Figure 6.14: Superficial water velocity over half circular protection cover in run 4 at $t = 20$. Legend in [m/s].

vertical velocity is more damped out towards the bottom than the horizontal velocity. Above the half circular protection cover it can be seen that the horizontal water velocity propagates further down due to the influence of the protection cover.

(a) Superficial water velocity in x direction. Legend from $\pm 0.25 m/s$, red is maximal, green is zero, blue is minimal.

(b) Superficial water velocity in z direction. Legend from $\pm 0.25 m/s$, red is maximal, green is zero, blue is minimal.
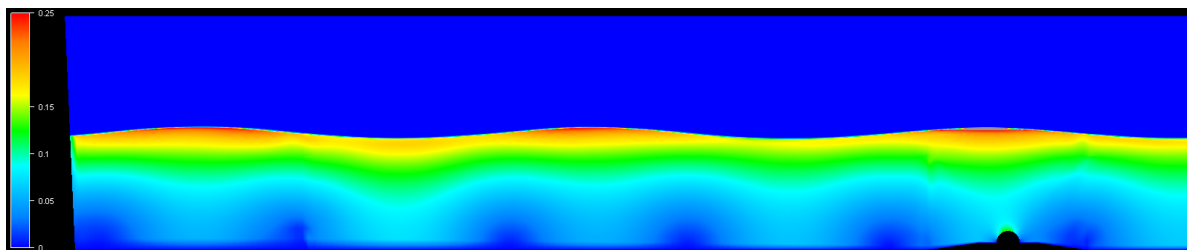
(c) Total superficial water velocity. Legend from $0.25 - 0m/s$, red is maximal, blue is zero.

Figure 6.15: Superficial water velocity from run 4 at $t = 20s$.

In figure 6.16 a closer view of the total superficial water velocity for run 1 and 4 at $t = 20s$ over the two protection covers is shown. In addition in sub figure 6.16(c) and 6.16(d) the mesh lines is shown. At the sharp edges on the rectangular cover, clear vortex shedding can be seen. For the half circular cover at the same time step, the vortex shedding is absent. The reason will be the low Keulegan-Carpenter number and the small velocities. Similar figures for time step $t = 19s$ and $t = 21s$ can be found in appendix D.

6.3   Conclusion

The modeled numerical wave tank from section 4.5 has been used to study wave forces on two different submerged protection covers. A similar setup as the performed experimental test was used in order to compare the results. A total of six runs was performed with three different wave amplitudes ζ_A and

(a) Total superficial water velocity for run 1 at $t = 20s$.

(b) Total superficial water velocity for run 4 at $t = 20s$.

(c) Total superficial water velocity for run 1 at $t = 20s$ with mesh.

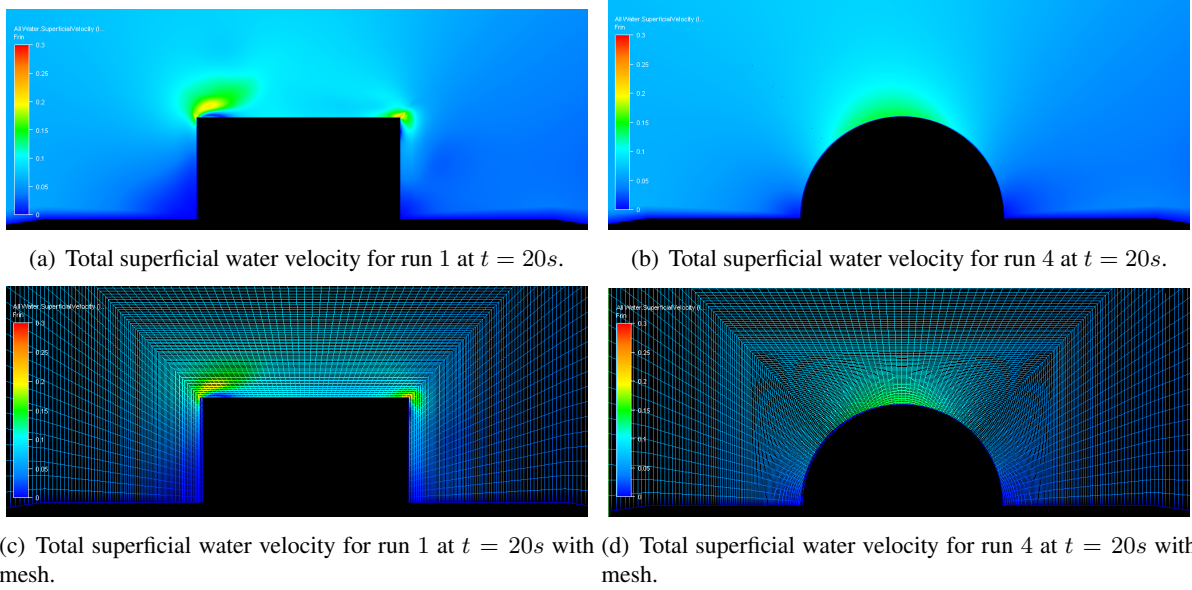(d) Total superficial water velocity for run 4 at $t = 20s$ with mesh.

Figure 6.16: Superficial water velocity from run 4 at $t = 20s$. Legend from $0.3 - 0m/s$.

constant wave period T for both the rectangular and half circular protection cover. The wave elevation at $x = 7.3m$ and $x = 8.7m$ gave good results compared with Stokes 2nd order wave theory. The number of horizontal elements compared with the wave length was smaller than the suggested value by Silva et al. (2010) and could be one reason for a obtained small variation in the wave elevation along the tank. The largest studied wave amplitude of $\zeta_A = 0.1m$ gave a non linear wave profile due to both shallow water and large wave steepness. At a studied point, water velocity and pressure was monitored and logged. The time series of the horizontal and vertical water velocities gave good results compared with Stokes 2nd order theory. The dynamic pressure was found from the total pressure corrected by the initial static pressure and gave good results compared with Stokes 2nd order wave theory. Horizontal and vertical forces was calculated from the isolated sides of the studied protection cover. Both the total force, pressure force and viscous force was found. The Viscous forces was obtained to be very small and was neglected. The horizontal force gave good results compared with the calculated theoretical force based on a Froude-Kriloff pressure force with a additional added mass contribution. In the theoretical approach, a horizontal added mass coefficient of $C_a = 1.53$ was used for the rectangular protection cover and $C_a = 1.145$ for the half circular cover. The CFD results gave a horizontal added mass coefficient of $C_a^{CFD} = 1.4$ for the rectangular protection cover and $C_a^{CFD} = 1.18$ for the half circular protection cover. The horizontal added mass coefficients from theory and CFD shows good agreement. Vertical forces was assumed to only be the Froude-Kriloff pressure force in the theoretical approach since the structure was assumed small compared with the wave length. The vertical forces from CFD was a small value larger than the theoretical Froude-Kriloff force for both the rectangular and half circular cover, indicating a influence from the structure on the surrounding water. A vertical added mass should therefore be assumed in the theoretical approach in order to have a conservative theoretical vertical force.

Chapter 7

Experimental tests

The main purpose of performing experiments can be divided into two parts. First wave forces on simplified protection covers in shallow water are of interest. Secondly the experiments can be used to validate a numerical CFD method, both a numerical wave tank and numerical force measurements.

7.1 Experimental setup

The experiments was performed in the student tank in one of the laboratory of MARINTEK located at the Department of Marine Technology at NTNU in Trondheim. The experiments was carried out in week 14 and 15 of 2011 with Torgeir Waal at MARINTEK as supervisor for the experiments. The wave tank is $25m$ long, $2.8m$ wide and $1.0m$ deep. A bottom hinged flap wavemaker is installed at the upstream end wall of the tank driven by a cylinder piston. At the downstream wall of the tank a curved beach type wave absorber is installed. In figure 7.1 a sketch of the tank cross section, the wave absorber and the wavemaker is shown.

(a) Cross section of Student Tank.
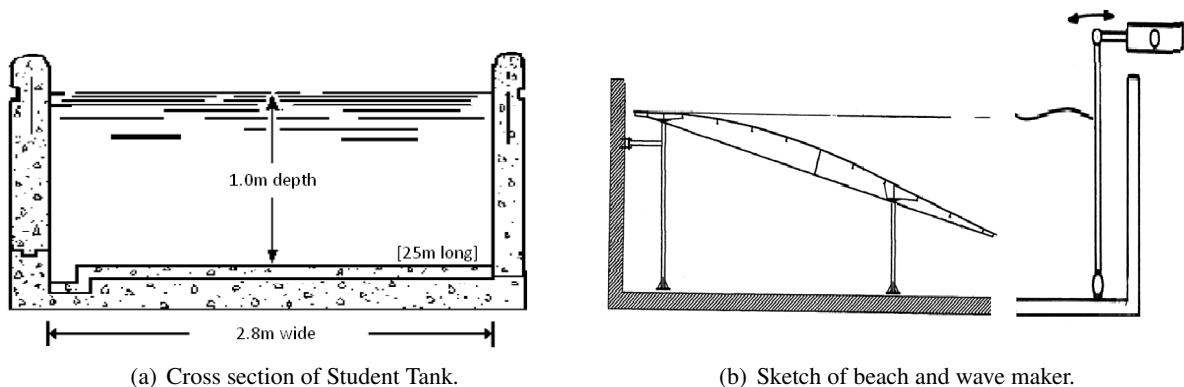
(b) Sketch of beach and wave maker.

Figure 7.1: Student Tank at the Department of Marine Technology at NTNU in Trondheim.

There was made two simplified protection covers by the engineering workshop at MARINTEK. One cover with a rectangular cross section and one cover with a half circular cross section. The covers was made of aluminum with cross sectional length of $0.2m$ along the tank, width of $2.0m$ across the tank and a height of $0.1m$ vertically. Both the rectangular and half circular protection cover was made with similar dimensions, where the circular diameter corresponds to the length of the rectangular protection cover. Both covers had two side plates of $0.05m$ width on each side. All aluminum plates which was used to make the models was $5mm$ thick. A detailed view of the two simplified protection covers can be seen in chapter 2. In order to make force measurements the protection covers had to be mounted on a

solid frame. The frame was made of aluminum and top side was lifted up $60mm$ to make room for force transducers. In figure 7.2 the rectangular cover model with the first used frame can be seen.
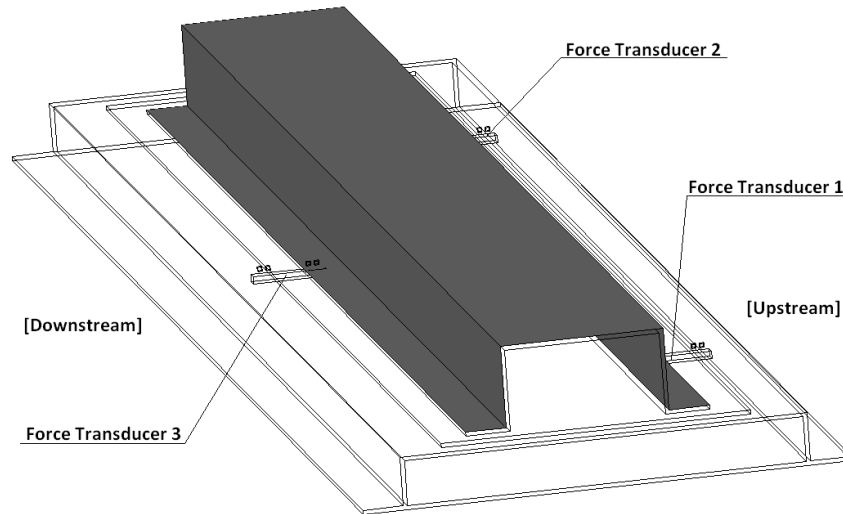

Figure 7.2: Model of rectangular protection cover in first used frame.

7.1.1 Instrumentation

In table 7.1 the used channels is given with the used transducers.

Channel nr.	Measurement	Unit	Description
1	Time	$t\,[s]$	Time of measurement
2	Force	$f1\,[N]$	Force 1 upstream
3	Force	$f2\,[N]$	Force 2 upstream
4	Force	$f3\,[N]$	Force 3 downstream
5	Elevation	$wp01\,[m]$	Wave Elevation 1 upstream
6	Elevation	$wp02\,[m]$	Wave Elevation 2 downstream

Table 7.1: Channels with the transducers used in the experimental measurements.

A total of five transducers was used, three force transducers and two wave probes. The force transducers was used to measure the vertical forces on the protection cover, two mounted upstreams and one mounted downstream. The reason for three force transducers instead of two was to make the cover more stable in the transverse direction. The plan was to use four transducers, two on each side, but to make it simpler only three force transducers was used. In figure 7.3 a illustration of a Omega load cell is shown, almost similar to the force transducer used in the experiments.

The used force transducers was limited to $70kg$ load and was based on a tension type load cell. A tension type load cell works similar as a strain gauge with thin electrical wires with varying resistance when elongated. The force will then be measured from the shear force over the load cell given from the varying resistance in the thin electrical wires. Full bridge strain gauges was used. One end of the force transducers was mounted horizontally underneath the cover side plates and the second end was mounted underneath the frame edge. In addition to the force measurements the wave elevation was measured at two positions by a wave probe at each position. A conductive type wave probe was used. In a conductive type wave probe the resistance in two parallel electrical wires half submerged is measured. The resistance will be dependent of the actual wetted length of the electrical wires. The surface elevation, the wet length of the wires, can directly be determined by measuring the current in the wires from a

Figure 7.3: Illustration of a Omega load cell.

known voltage across the wires. The signal from the transducers was connected to a $\pm 10 volt$ amplifier. A low pass digital butterworth filter was used with $f_g = 5Hz$ in order to remove high frequency noise from the measurements. Via a analog-digital converter the measured data was logged by the *Catman* logging software with a sampling frequency of $\Delta t = 20ms = 50Hz$.

7.1.2   Calibration

Before doing any measurements both the wave probes and force transducers had to be calibrated. The wave probes was calibrated by physically moving the wave probe some known distances and measure the actual resistance. By a translation factor, indicating the slope, the measured resistance was transformed to water elevation in meters [m] by assuming a linear relation. The force transducers was calibrated after they were mounted on the frame but before mounting the model cover. Three small weights with known mass was lied on each force transducer separately one by one with some time delay in order to make steady measurements. The measured force from each force transducer was compared with the known weights transformed to a force by the gravity constant $g = 9.81m/s^2$ and the translation factor for measured resistance to force was tuned. In figure 7.4 a picture of the calibration procedure with a $0.5kg$ weight is shown.
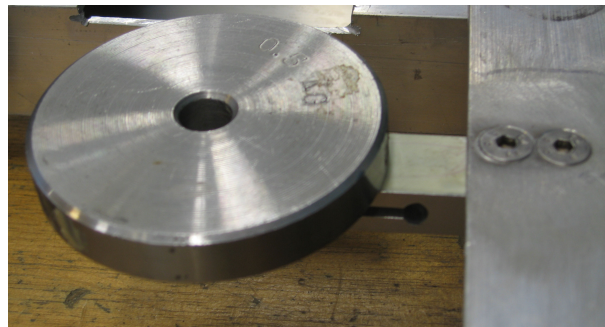

Figure 7.4: Calibration of a force transducer with a $0.5kg$ weight.

The calibration for the force transducers was done twice in order to see any deviation in the force transducers. The performed measurements was done with reference to calm water by zeroing in $10s$ before each measurement. The reason was to reduce temperature drift in the transducers. Strain transducers will in general emit a large amount of heat in comparison to the area which will affect the resistance and give drift in the measurements. After connection to the amplifier the force transducers must usually have some time to stabilize the temperature. Especially when the transducers are immersed in water the temperature drift can be significant before the temperature in the transducer stabilizes. Therefore the transducers was connected a long time before measurements started and zeroing before each measurement was performed. In addition $20s$ was logged before the wavemaker was enabled in order to measure a reference level for each measurement with calm water. During the experiments some of the

force transducers was obtained with drifting values even after a long time. The reason could be lack in the watertight sealing of the transducers. The force transducers was then changed and replaced with similar force transducers. The new transducers was calibrated similar to the original used transducers. In addition, when the structure was out of the tank, both the new and the old transducers was calibrated. The earlier calibrated force transducers showed small or no deviation from the reference calibration load. In this way the calibration was performed both before and after some performed measurements for some of the transducers.

7.1.3 Model dimensions

In the first test experiments a large influence from the sharp edges of the frame was obtained. The sharp edges gives strong separation points and vortex shedding at the edges would definitely be induced and affect the fluid flow towards the model of the protection cover. To avoid the sharp edges on the frame, the frame was modified with two inclined side panels made of aluminum and placed on both sides. The inclined side panels was also bended with a horizontal part mounted over the force transducers close the the protection cover. The screws fastening the inclined side panels and the force transducers was in addition flush mounted to reduce flow affection. With the two inclined side panels the fluid flow will almost be unaffected before reaching the model cover. The new frame with the inclined side panels can be seen in figure 7.5 for both models of the protection covers. The two dimensional dimensions of the two models mounted on the frame with the inclined side panels is given in figure 7.6. The total breath of the model covers was $b = 2m$.
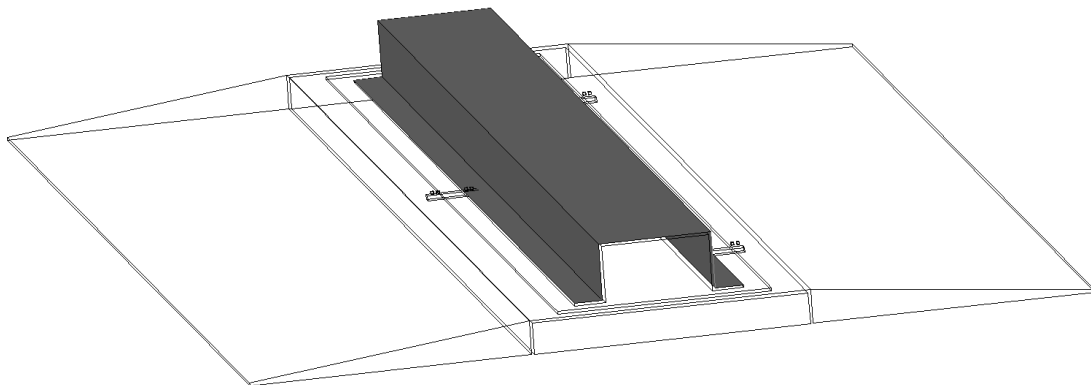
(a) Model of rectangular protection cover.
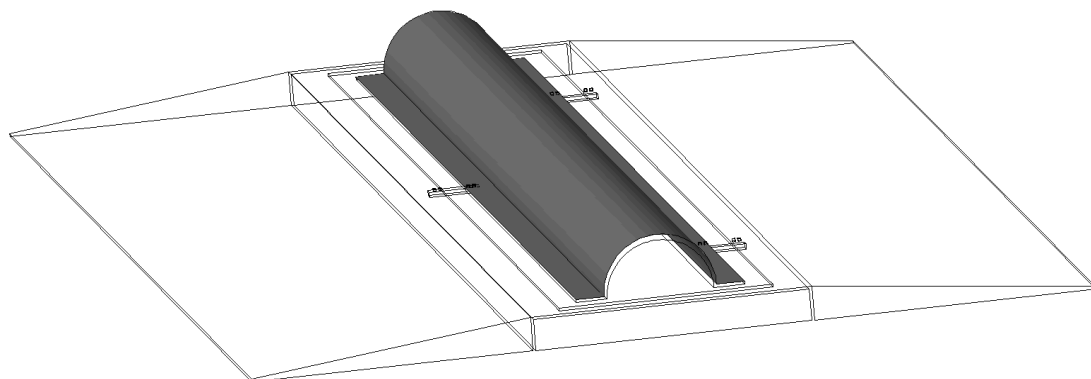
(b) Model of half circular protection cover.

Figure 7.5: Model of protection covers mounted on the frame with inclined side panels.

(a) Two dimensional dimensions of the rectanguler protection cover model.

(b) Two dimensional dimensions of the half circular protection cover model.
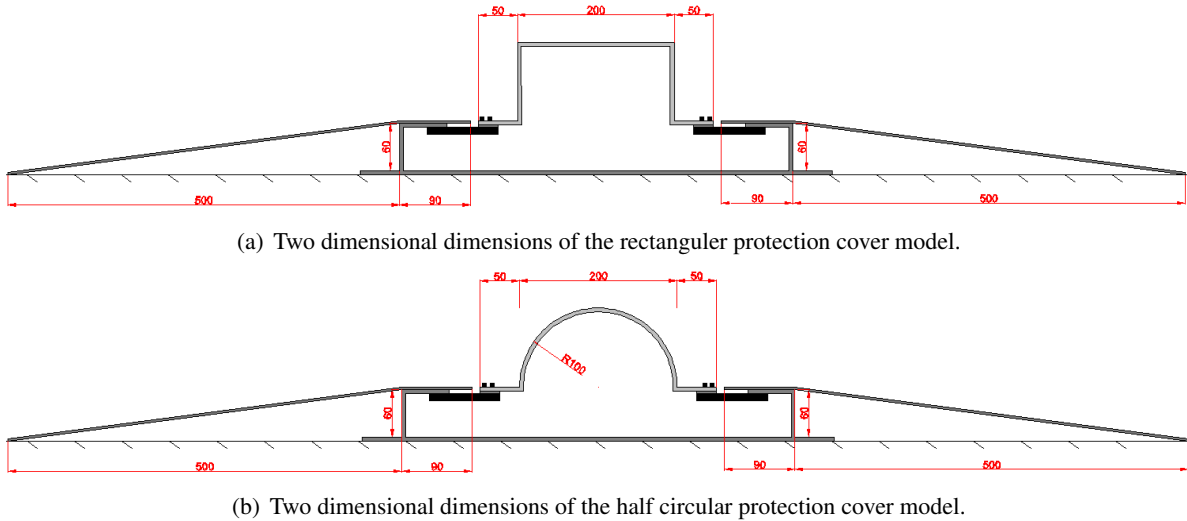
Figure 7.6: Two dimensional section of the two protection cover models with given dimensions in millimeters [mm].

The model of the protection cover was mounted on the frame and placed on the tank bottom with the center of the cover at $x = 8m$ downstream of the wavemaker. On each side of the frame, close to the tank walls, extra stabilizing weights of $10kg$ was placed to make sure that the frame was fixed during the experiments. The two wave probes was mounted on each side of the cover model, $0.7m$ from the center. With origin on the free surface at the wavemaker the wave probes was located at $x_1 = 7.3m$ and $x_2 = 8.7m$. The experimental setup which was used in the experiments is shown in figure 7.7.
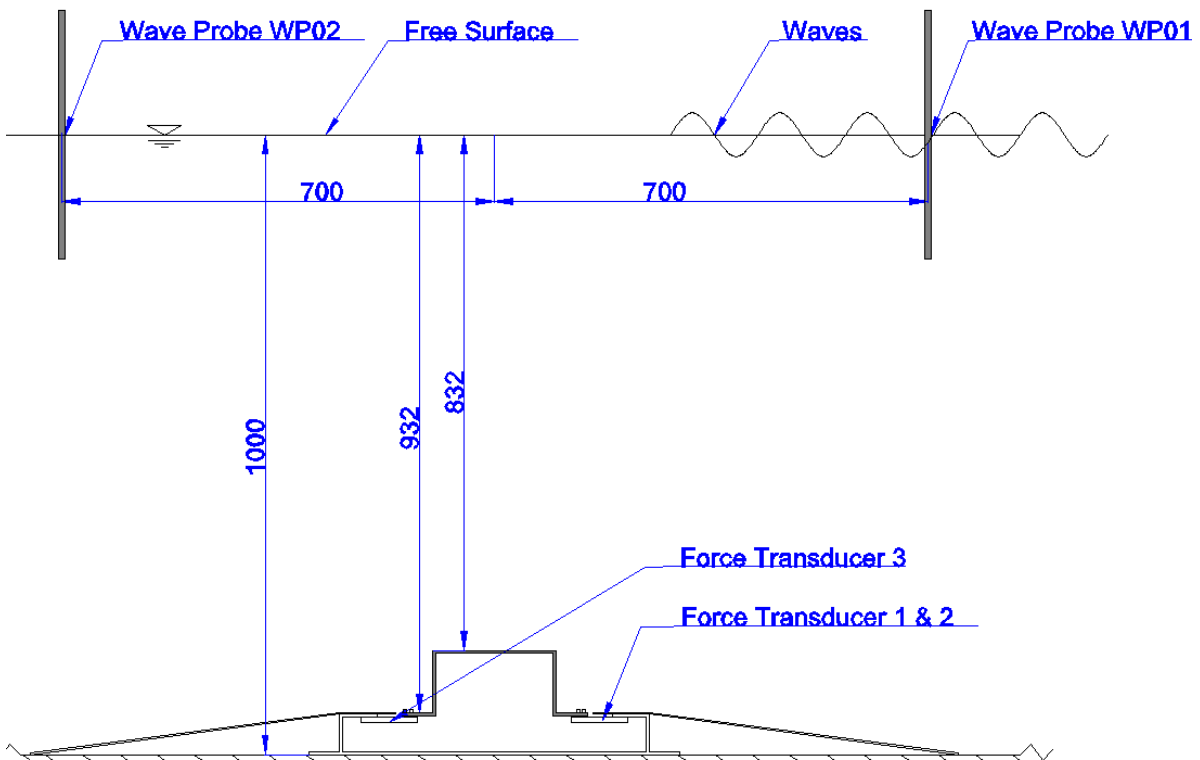

Figure 7.7: Experimental setup. All measurements in millimeters [mm].

In addition to the inclined panels the cross-sectional openings on the protection covers was covered with tape. The unattainable aim for the experimental setup was to avoid movement of the water particles inside the frame and protection cover. With only static pressure inside the cover, the force transducers will measure the dynamic force from the waves. If the water particles inside the protection cover starts to move, the pressure inside the cover will be dynamic and the wave induced dynamic pressure will tend to be canceled out giving a reduction in the pressure force measurements. The isolation of the water inside of the frame and protection cover will be improved with the additional tape on the cross sectional ends. At the top of the cross-section a small opening was kept in order to be sure that no air will be trapped inside the model. In addition tape was used at the frame end sides as well, leaving only a small gap opening of about $1cm$ along the mud mats. This small gap will be the main opening for the water particles to move freely to the inside of the cover. In figure 7.8(a) a picture of the rectangular protection cover model with tape on the cross-section is shown. In figure 7.8(b) the frame with the inclined side panels and the rectangular protection cover mounted is shown.
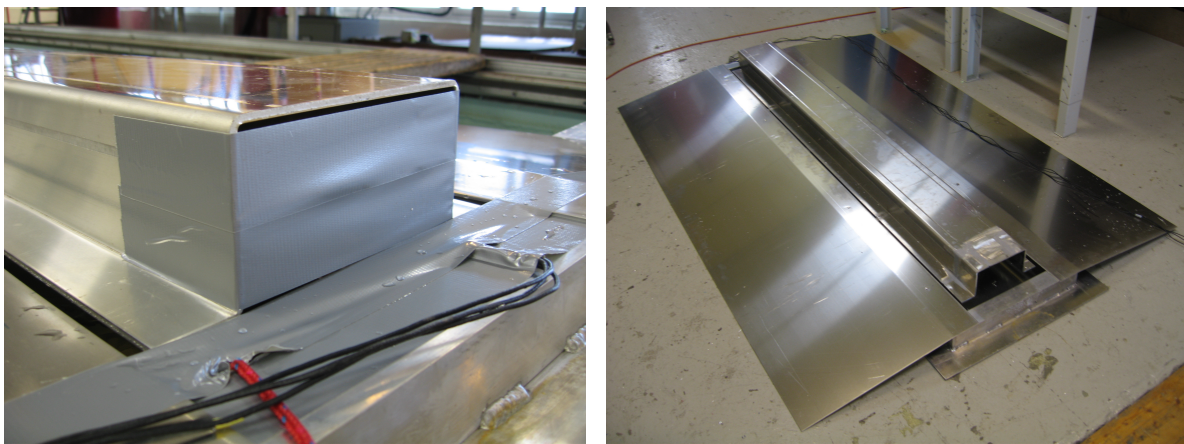
(a) Model of the rectangular protection cover with tape on the cross sections and at the frame end openings.

(b) Frame with inclined side panels and rectangular protection cover mounted.

Figure 7.8: Picture of taped cross section and mounted frame with inclinded side panels and the rectangular cross section mounted.

7.1.4 Input Wave Parameters

The bottom hinged flap was programmed by the same wavemaker theory given by Dean & Dalrymple (1984) and presented in section 3.5 in chapter 3. Four different wave periods was studied combined with six different wave amplitudes. For the lowest wave period of $T = 1.00s$ only the three lowest wave amplitudes was used due to breaking wave. A total of 21 measurements was therefore performed for each protection cover. The wave parameters used as input to the wavemaker for all the 21 measurements is given in table 7.2 together with some non dimensional wave parameters.

Experiment	ζ_A [m]	T [s]	k [1/m]	λ [m]	H/λ [$-$]	$2h/\lambda$ [$-$]	$U_r = \frac{k\zeta_A}{(kh)^2}$
1	0.025	1.00	4.027	1.560	1/31.25	1.28	0.0015
2	0.025	1.25	2.604	2.413	1/48.26	0.83	0.0037
3	0.025	1.50	1.875	3.351	1/67.03	0.60	0.0071
4	0.025	1.75	1.463	4.295	1/85.90	0.47	0.0117
5	0.050	1.00	4.027	1.560	1/15.60	1.28	0.0031
6	0.050	1.25	2.604	2.413	1/24.13	0.83	0.0074
7	0.050	1.50	1.875	3.351	1/33.51	0.60	0.0142
8	0.050	1.75	1.463	4.295	1/42.95	0.47	0.0234
9	0.075	1.00	4.027	1.560	1/10.40	1.28	0.0046
10	0.075	1.25	2.604	2.413	1/16.09	0.83	0.0111
11	0.075	1.50	1.875	3.351	1/22.34	0.60	0.0213
12	0.075	1.75	1.463	4.295	1/28.63	0.47	0.0350
13	0.100	1.25	2.604	2.413	1/12.06	0.83	0.0147
14	0.100	1.50	1.875	3.351	1/16.76	0.60	0.0285
15	0.100	1.75	1.463	4.295	1/21.47	0.47	0.0467
16	0.125	1.25	2.604	2.413	1/9.65	0.83	0.0184
17	0.125	1.50	1.875	3.351	1/13.41	0.60	0.0356
18	0.125	1.75	1.463	4.295	1/17.18	0.47	0.0584
19	0.150	1.25	2.604	2.413	1/8.04	0.83	0.0221
20	0.150	1.50	1.875	3.351	1/11.17	0.60	0.0427
21	0.150	1.75	1.463	4.295	1/14.32	0.47	0.0701

Table 7.2: Table of wave input parameters to the wavemaker. ζ_A is the wave amplitude, T is the wave period, λ is the wave length, k is the wave number, $H = 2\zeta_A$ is the wave height, l is cover length and U_r is the Ursell number.

From table 7.2 the wave steepness, $s = H/\lambda$, give small values when the amplitude is low and the wave length is large which indicate linear waves. In addition the Ursell number is also low for small amplitudes indicating linearity. For large wave amplitudes combined with relatively short wave lengths, the wave steepness increases and becomes close to the breaking criteria of $S_{crit} = 1/7$. Therefore only wave amplitudes up to $\zeta_A = 0.075m$ was combined with the lowest wave period of $T = 1.00s$. The Ursell number was largest for the largest wave amplitude of $\zeta_A = 0.150m$ indicating non linear waves mostly due to the shallow water. The shallow water approximation can be assumed when $2h/\lambda < 1.0$. Only the lowest wave period of $T = 1.00s$ can be assumed in deep water.

7.2 Error Sources

Physical experiments will always be dependent of the choice of modeling, the assumed simplifications and uncertainties in the instrumentation and the modeling of environmental loads. Some important error sources given In Steen & V.Aarsnes (2010) will be:

1. Scale effects
2. Incorrect modeling of structures
3. Incorrect modeling of environment
4. Instrumentation and measurement errors
5. Error in analysis and interpretation of results

In the performed experiments scale effects and incorrect modeling of the structure can be important

when scaling to full scale due to difference in Reynolds number and simplifications in the model design. When comparing with numerical CFD results this will not be the case since similar fluid properties between experiments and numerical settings can be achieved and the actual structure geometry can be modeled. Incorrect modeling of environment will in this case be the generation of the free surface waves, limitations in the water tank and the isolation of the water inside the models. The accuracy of the wavemaker and the wave reflections from the tank walls will be an issue, see section 7.2.1. The water inside the covers will be affected and give influence on the force measurements. Instrumentation and measurement errors will be dependent of the accuracy of the used transducers and the calibration of the transducers. Wave probes normally have $\pm 1 mm$ accuracy and force transducers normally have $1 - 5\%$ deviation from measured value given from Steen & V.Aarsnes (2010). The interpretation of the results can be due to round of errors or human errors. The human error source will be represented in all procedures in a experiment. A uncertainty analysis is often recommended for novel experiments with less earlier gained experience. In the present experiments a uncertainty analysis has not been performed.

7.2.1 Tank Wall Effects

The physical tank give space limitations dependent of the size of the water tank. The most important effect will be the wave reflections from the tank walls. The end wall downstream of the wavemaker will give limitations on the measurement time since the generated waves will be reflected normally towards the wavemaker after some time dependent of the wave celerity. The side walls will give interference effects. In experimental measurements on fixed submerged structures in waves the tank wall interference effects can be significant and give large effects on the experimental results. J.Xia & J.R.Krokstad (2001) studied the interaction of gravitational water waves with stationary ocean structures in a wave channel. In figure 7.9 results from 1st order vertical force measurements from J.Xia & J.R.Krokstad (2001) is shown. At some frequencies corresponding to the transverse resonance frequencies of the water channel, the measured vertical forces dropped a value a order of magnitude lower than the predicted values without wall reflections.
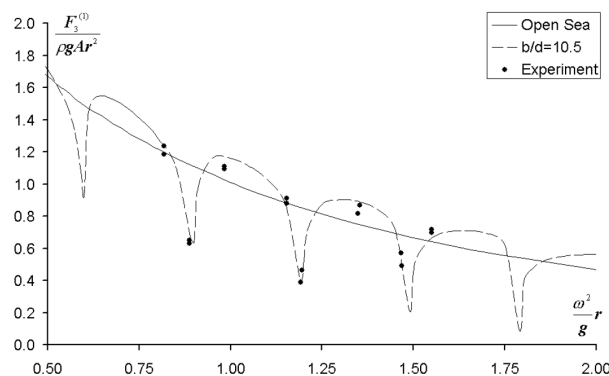

Figure 7.9: Tank wall interference effect on 1st order vertical force measurement performed by J.Xia & J.R.Krokstad (2001) at frequencies corresponding to the transverse resonance frequencies of the water channel, the vertical force drops a order of magnitude lower than the predicted values without wall reflections.

The resonance periods from the transverse wave system in the student wave tank can be found by assuming a multiply of a standing half wave transverse of the tank. The wavelength relation becomes $\frac{n\lambda}{2} = B$, where B is the tank breadth and λ the transverse wave length. By assuming shallow water and using the dispersion relation $\omega^2 = kgtanh(kh)$, where g is the gravity constant, $k = 2\pi/\lambda$ is the wave number and h the water depth, the resonance period can be found. The resulting equation for the transverse resonance periods is given in equation 7.1, where n is a integer.

$$T_n = \sqrt{\frac{2\pi B}{ngtanh\left(\frac{n\pi h}{B}\right)}} \qquad (7.1)$$

The effect of a standing transverse wave in a basin is called seiching. The period of seiching equals the resonance period of the transverse wave. By assuming shallow water $tanh(kh) \approx kh$ and the period of seiching becomes $T = \frac{2B}{n\sqrt{gh}}$ known as the Merian formula, Dean & Dalrymple (1984).

In table 7.3 the four first transverse resonance periods is compared with the input wave periods given to the wavemaker.

n	Resonance period [s]	Wave Period, T [s]
1.	2.106	1.75
2.	1.354	1.50
3.	1.122	1.25
4.	0.947	1.00

Table 7.3: Transverse resonance periods calculated from equation 7.1 with $B = 2.8m$, $g = 9.81m/s^2$ and $n = 1 - 4$. In addition the used wave periods is given for comparison.

The four first transverse resonance periods in the student tank is in the same area as the used wave periods indicating that the wall interference effect will have some influence on the results. The third and fourth eigenperiod of the transverse wave system is almost similar to the lowest wave periods of $T = 1.25s$ and $T = 1.00s$. During the experimental measurements observation of the wave generation should be done in order to see if any transverse waves becomes large. The transverse waves will mostly be obtained after the measurements when the longitudinal waves are damped out at the downstream beach wave absorber. A transverse wave system can in some cases be going for a long time with low damping indicating a long time before calm water will be achieved in the tank. The tank wall interference effects can be avoided by using a larger wave basin with wave absorbers at the two boundary sides. In a numerical wave tank a $3D$ analysis with no slip side wall boundary conditions should be used in order to account for the tank wall effects.

7.3   Scaling

Experimental tests are in most cases performed with a model of the actual size of the studied geometry. Normally the size of the test facility is the limiting condition but also to have similar relations regarding water depth. The experimental results in model scale can be scaled to full scale by demand geometric, kinematic and dynamic similarity. The geometric similarity states proportional local dimensions in geometry for model and full scale. The kinematic similarity states similar velocity relations in model and full scale. As a consequence of the kinematic similarity the velocity vectors should have same directions and the streamlines becomes geometrically similar in model and full scale. The dynamic similarity states similar force relations. The forces of importance is the inertia force, viscous force, and the gravitational force. Similarity between inertia and viscous forces indicate similar Reynolds number. By similar Reynolds number the viscous forces will be correctly scaled between model and full scale. Similar Reynolds number is in practice often hard to achieve and not practically impossible in most cases. Similarity between inertia forces and gravity forces indicate similar Froude number. By similar Froude number gravity forces will be correctly scaled. Since free surface waves is gravity driven, similarity in Froude number combined with geometric and kinematic similarity gives similar wave pattern between model and full scale. In the present case, Froude scaling with geometric and kinematic similarity will

be assumed. In equation 7.2 the scaling ratio for some physical quantities is given based on similarity in Froud number $F_n = \frac{U}{\sqrt{(gL)}}$ and a scaling ratio $\lambda = L_S/L_M$.

$$\text{Force } F_S = \frac{\rho_s}{\rho_m}\lambda^3 F_M$$

$$\text{Moment } M_S = \frac{\rho_s}{\rho_m}\lambda^4 M_M$$

$$\text{Time } t_S = \sqrt{\lambda} t_M \qquad (7.2)$$

$$\text{Pressure } p_S = \frac{\rho_s}{\rho_m}\lambda p_M$$

In equation 7.2, Sub text $_S$ indicate full scale and $_M$ indicate model scale. A common size of a full scale protection cover can be a length of $15m$ along the pipe, cross sectional width of $6m$ and a height of $2m$. Compared with the used model scale dimensions of the simplified protection covers, the scaling factor becomes $\lambda = 20$. From $h_M = 1m$ water depth in the tank, the full scale depth will be $h_S = 20m$. The proper scaling of the experimental measurements has not been done since the related CFD analysis was carried out with similar dimensions and fluid properties as the model scale. As a comment, in a CFD analysis a correct scaling of viscous forces can be achieved due to similarity in Reynolds number by using similar dimensions and fluid properties as the studied case.

7.4   Results and Discussions

All the 21 measurements listed in table 7.2 was performed for both the rectangular and the half circular model of the protection covers, resulting in total 42 performed measurements. Between each measurement calm water was required. Dependent of the wave period a transverse wave with low damping was observed which gave long time before calm water was achieved. In some cases it lasted over $30min$. before calm water was achieved. The measured time duration was in the order of a minute, but due to the slow wave damping the experiments was time consuming. In table 7.4 some fluid properties from the performed experiments is given.

Parameter	Variable	Value
Density of Fresh Water	ρ	$1000kg/m^3$
Dynamic viscosity, $T = 15\deg C$	μ	$1.4e-3Ns/m$
Reynolds number (max)	Re	$1070.5 - 30722$
Keulegan-Carpenter (max)	KC	$0.038 - 1.88$

Table 7.4: Fluid properties in the performed experiments.

As a comment, the Reynolds number and the Keulegan Carpenter number given in table 7.4 is calculated from the maximum horizontal fluid velocity at the top of the protection cover taken from linear wave theory. The wave theory was tuned with phase and wave amplitude from the actual measured wave elevation at the upstream wave probe $wp01$. The smallest maximum value for both the Reynolds number and the Keulegan-Carpenter number was obtained in experiment 1 with the lowest wave amplitude and shortest wave period. Similar the largest maximum values for the Reynolds number and the Keulegan-Carpenter number was obtained in experiment 21 with the largest wave amplitude and longest wave period. The variation in maximum Reynolds number indicate large variation in the horizontal fluid velocity on the top of the protection cover. The Keulegan Carpenter number is low indicating dominating inertia forces and minor drag forces. The oscillation period will disturb the flow from getting stable and vortex shedding will be absent on smooth surfaces. On the rectangular protection cover the sharp edges

will definitely give vortex shedding, but on the half circular protection cover the vortex shedding will most probably be absent. As reference , in a fluid flow around a circular cylinder in a infinitely fluid the vortex shedding will be absent for $KC < 4$ Pettersen (2007).

7.4.1 Logging of Measurements

In figure 7.10 the measured data from the two wave probes and the three force transducers from experiment 7. with $\zeta_A = 0.05m$ and $T = 1.50s$ is shown.
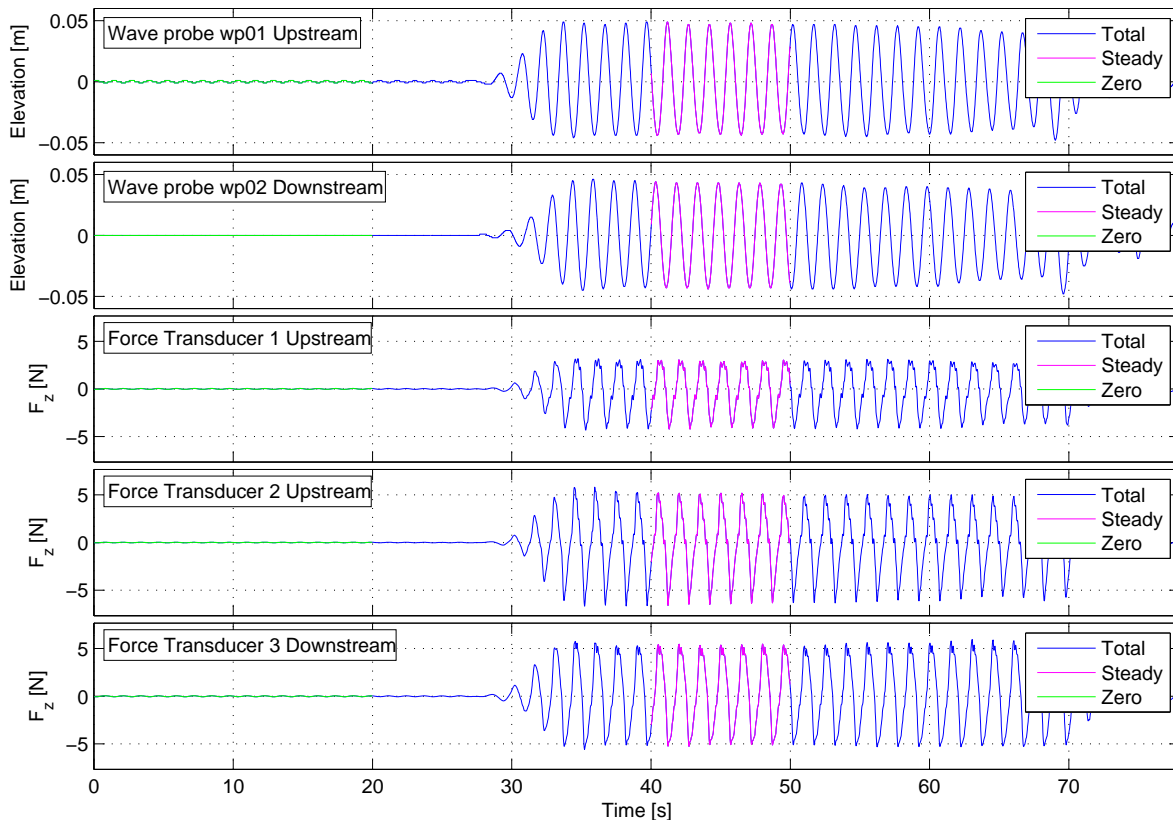

Figure 7.10: Wave elevation from experiment 7 on rectangular protection cover with $\zeta_A = 0.05m$ and $T = 1.5s$. Blue indicate total measurement, green indicate zero part and red indicate steady part.

The logging of measurement data started some seconds before the wavemaker was enabled. The first part of measurement with calm water, marked green, shows that the force transducers are stable around zero. When waves are generated and becomes stable the force measurements shows steady measurements with almost constant amplitudes. The selected steady part of the measurements, marked red, was corrected with the mean value of the first zero measurement,marked green, in order to only get the dynamic contribution from the surface waves.

7.4.2 Wave Measurements

In figure 7.11 the steady part from the two wave probes from experiment 7. with $\zeta_A = 0.05m$ and $T = 1.50s$ is shown.

The wave elevation in figure 7.11 is steady with almost constant crest and trough amplitudes. The crest amplitude is a small value larger than the trough amplitude indicating a nonlinear wave profile. From
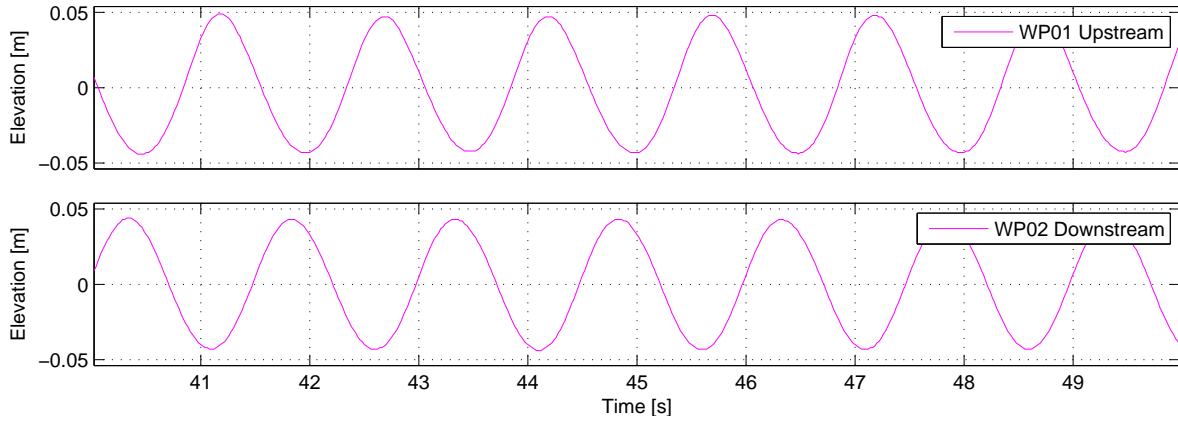
Figure 7.11: Steady part of wave elevation from experiment 7 on rectangular protection cover with $\zeta_A = 0.05m$ and $T = 1.5s$.

comparing the elevation from the two wave probes, a reduction is obtained for the downstream wave probe $wp02$. The reason can be damping along the tank length and in addition a small affection from the submerged structure. In figure 7.12 the steady part of the measured wave elevation at the two wave probes with $\zeta_A = 0.05m$ and $T = 1.5s$ is compared with linear wave theory.
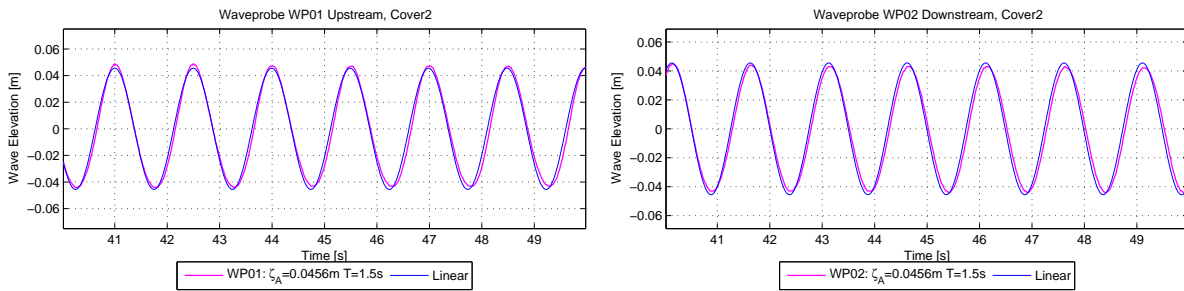
(a) Wave elevation at $wp01$ upstream compared with linear wave theory.

(b) Wave elevation at $wp02$ upstream compared with linear wave theory.

Figure 7.12: Steady part of wave elevation from experiment 7 on circular protection cover with $\zeta_A = 0.05m$ and $T = 1.5s$ compared with linear wave theory.

In figure 7.12 there is small difference between the measured elevation and linear wave theory. With the given input wave amplitude $\zeta_A = 0.05m$ and wave period $T = 1.5s$ there was seen small difference between linear and Stokes 2nd order wave theory. By a comparison between the two wave probes, a small reduction in crest amplitude can be seen. The reason will mostly be the damping along the tank. A small, but almost constant, phase deviation can also be seen in figure 7.12. The linear wave elevation was tuned to match the first measured crest value at $wp01$ upstream. There can be some inaccuracy in the selected crest peak value which will give a small phase deviation. For the comparison with the downstream wave probe $wp02$, a distance of $x = 1.4m$ was added to the kx term in the $sin(kx - \omega t - phase)$ term in the expression for the linear wave elevation. No large phase difference is seen between the two positions from the wave theory, indicating that the physical distance between the two wave probes was correct measured to $1.4m$. A larger difference between linear and Stokes 2nd order wave elevation can be obtained by studying a more non linear wave. In figure 7.13 the measured wave elevation at $wp01$ upstream from experiment number 19 with $\zeta_A = 0.175m$ and $T = 1.25s$ is compared with linear and Stokes 2nd order wave elevation.

In figure 7.13(b) the Stokes 2nd order wave elevation gives a very good match with the measured wave elevation. The linear wave elevation in figure 7.13(a) suffers with describing the non linear effects and gives lower crest and trough amplitude values. From this result the Stokes 2nd order wave theory will be
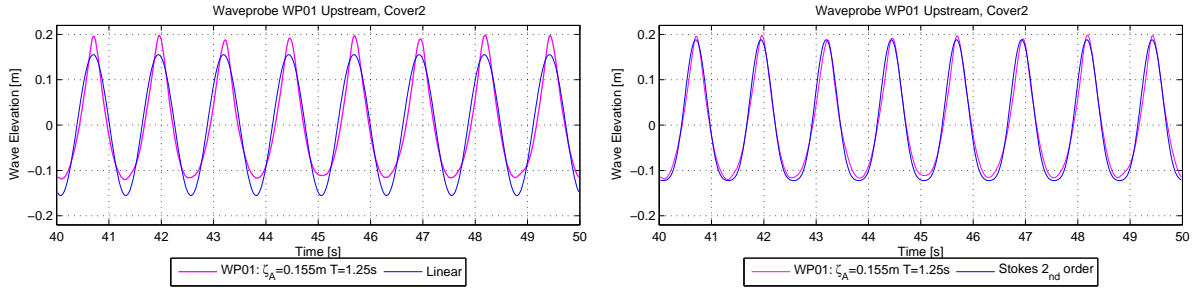
(a) Wave elevation at $wp01$ upstream compared with linear wave theory.

(b) Wave elevation at $wp01$ downstream compared with Stokes 2nd order wave theory.

Figure 7.13: Steady part of wave elevation from experiment 19 on circular protection cover with $zeta_A = 0.175m$ and $T = 1.25s$ compared with linear and Stokes 2nd order wave theory.
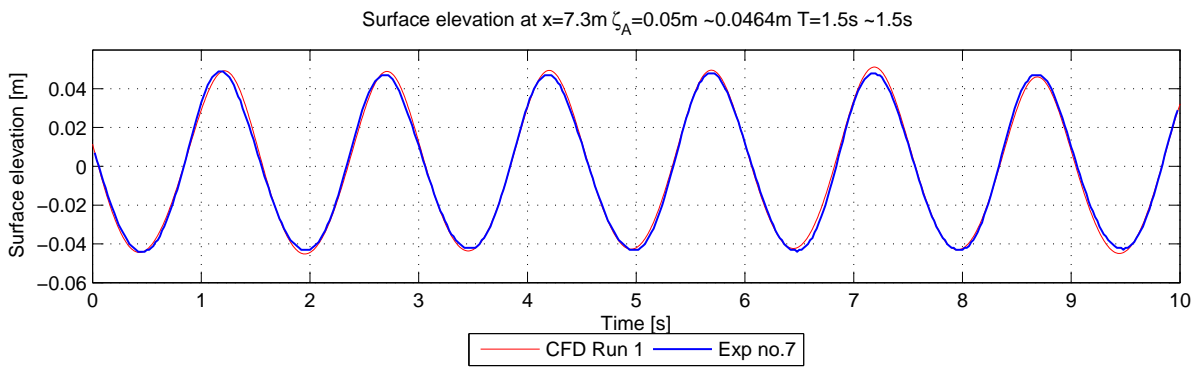

Figure 7.14: Comparison of wave elevation from CFD and Experiment. CFD analyis run 1 and experiment 7, both with input $\zeta_A = 0.05m$ and $T = 1.5s$.

the suggested theory for comparison with the experiments and for calculation of fluid particle velocities over the protection cover.

In section 4.5 in chapter 4 a numerical wave tank with similar dimensions as used in the experiments was modeled. In the numerical analysis three different wave amplitudes of $\zeta_A = [0.05m, 0.075m, 0.100m]$ was used with a wave period of $T = 1.5s$. In the numerical wave tank a section at the same position of $x = 7.3m$ as the first upstream wave probe $wp01$ was modeled and time series of the wave elevation was measured. In figure 7.14 the wave elevation from run 1 in the CFD analysis is compared with the wave elevation measured at $wp01$ in experiment 7 , both with similar input of $\zeta_A = 0.05m$ and $T = 1.5s$.

The comparison in figure 7.14 shows good agreement between numerical and experimental wave elevation. The studied time from the CFD analysis is taken from the steady part between $t = 10s$ and $t = 20s$. The studied time from the experimental measurement is between $t = 40s$ and $t = 50s$. The time series is tuned to match at the first wave crest peak. The observed damping along the tank in the numerical analysis in section 4.5 in chapter 4 shows to be similar to the damping in a physical wave tank.

From the total 42 performed experiments, with 6 different wave amplitudes and 4 different wave periods, a mean wave height and a mean period can be calculated from the two wave probes. The total wave height is defined from the trough to the crest, $H = \zeta_C + |\zeta_T|$. In table 7.5 the calculated mean wave height from both wave probes is given together with the input wave height. In both linear and Stokes 2nd order wave theory the wave height will be equal to $H = 2\zeta_A$.

The deviation shown in table 7.5 shows that the reduction in wave elevation increases with increasing wave amplitude. The reason will mostly be the input to the flap wavemaker which is based on linear potential theory. The wavemaker was not calibrated in connection with the performed experiments. The

$2\zeta_A$	Wave Probe Upstream $wp01$		Wave Probe Downstream $wp02$		
	H_{mean}^{exp}	Deviation	H_{mean}^{exp}	Deviation	Deviation per m.
$[m]$	$[m]$	$[\%]$	$[m]$	$[\%]$	$(wp01/7.3m)[\%/m]$
0.050	0.051	-2.20	0.047	6.00	-0.30
0.100	0.100	0.00	0.093	7.00	0.00
0.150	0.149	0.67	0.137	8.67	0.09
0.200	0.184	7.80	0.173	13.50	1.07
0.250	0.231	7.78	0.216	13.60	1.07
0.300	0.279	6.95	0.252	16.00	0.95

Table 7.5: Calculated mean wave height from measured wave elevation at $wp01$ upstream and $wp02$ downstream.

earlier calibration of the wavemaker was assumed to still be valid since no differences was done to the flap wavemaker system. The deviation in wave elevation is also larger further downstream given by the second wave probe $wp02$. The reduction between the two wave probes will mostly be due to the damping along the tank, but can also be from disturbances of the submerged structure. In addition in table 7.5 the deviation in wave height for the first wave probe at $x = 7.3m$ is given in $[\%/m]$, which gives the damping per meter along the tank length. The damping per meter tank lenght is very small for wave heigths below $H = 0.15m$. For larger wave heights a damping of around $1\%/m$ is obtained and is similar to the obtained numerical damping at the same position in the numerical wave tanke given in section 4.5. Similar the calculated mean period from both wave probes is given in table 7.6 together with the input wave period.

T	Wave Probe Upstream $wp01$		Wave Probe Downstream $wp02$	
	T_{mean}^{exp}	Deviation	T_{mean}^{exp}	Deviation
$[s]$	$[s]$	$[\%]$	$[s]$	$[\%]$
1.00	1.000	0.00	1.001	-0.10
1.25	1.249	0.08	1.250	0.00
1.50	1.498	0.13	1.497	0.20
1.75	1.748	0.11	1.750	0.00

Table 7.6: Calculated mean wave period from measured wave elevation at $wp01$ upstream and $wp02$ downstream.

In table 7.6 a very small deviation in the wave period is found. The wave period will be similar in both linear and Stokes 2nd order wave theory. The reason for the small deviation can be that the wave period is similar to the flap oscillation period directly. As long as the accumulator system for the piston which moves the flap wavemaker is steady and continuously, the oscillation period will be reasonable steady. From studying each separate experiment it was obtained larger deviation in the produced wave height when the wave period increased. In figure 7.15 the measured wave height from the upstream wave probe $wp01$ is plotted for the actual studied wave periods.

In figure 7.15 it can clearly be seen that the wavemaker system is strongly dependent of the oscillation period. For low periods the wave height is larger than the input value, and for higher periods the wave height is lower than the input value. Around $T = 1.4s$ the produced wave heights is almost similar to the input wave heights. The wave probe $wp01$ was located $7.3m$ from the wavemaker flap and a small damping along the tank length must be assumed. Larger periods than $T = 1.50s$ combined with wave heights larger than $H = 2\zeta_A = 0.20m$ gives large deviation in actual wave height which must be accounted for. In figure 7.16 the same data as in figure 7.16, the measured wave height at $wp01$ upstream, is plotted against the input wave height along lines with constant period. Notice the red dotted line which indicate a ratio of 1 between the input wave height and the measured wave height. Remember also that
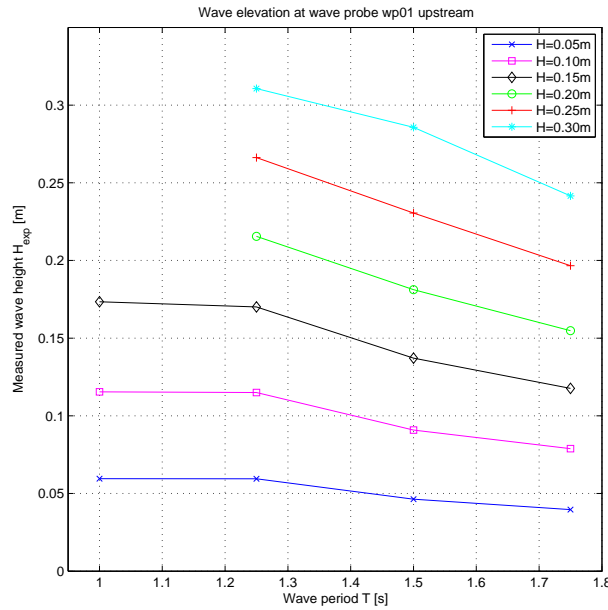
Wave elevation at wave probe wp01 upstream

Figure 7.15: The measured wave height, $H = \zeta_C + |\zeta_T|$, at the upstream wave probe $wp01$ $7.3m$ from the wavemaker is given for the studied wave periods T.

the measurements at $wp01$ was $7.3m$ from the wavemaker and some damping along the tank would be reasonable to assume. The input wave height will therefore be assumed to be slightly larger than the measured wave height if the damping is taken into account. In figure 7.16 the correct constant period line should therefore be just above the red dotted median line. The lowest wave period of $T = 1.00s$ seems to give good results for all the tested wave heights. The wave period of $T = 1.25s$ gives good results up to $H = 2\zeta_A = 0.150m$. Increasing wave period gives increased wave height. Especially above $H = 0.150m$ and $T = 1.00s$ the wavemaker tends to produce higher waves than the input values.
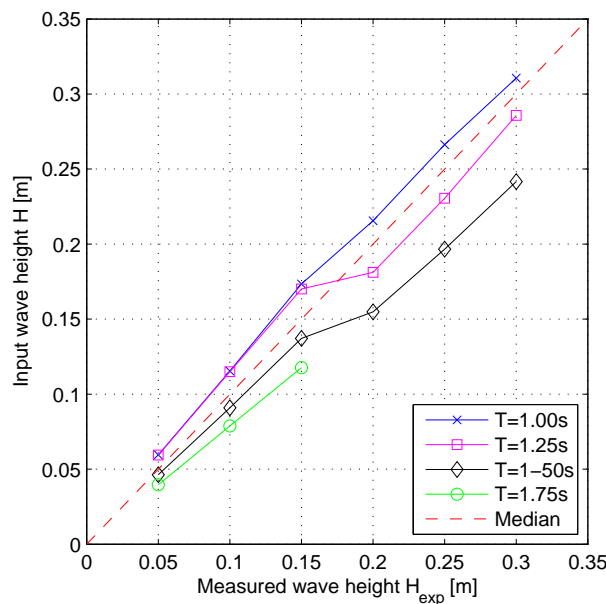
Figure 7.16: The measured wave height, $H = \zeta_C + |\zeta_T|$, at the upstream wave probe $wp01$ $7.3m$ plotted against input wave height to the wavemaker along lines with constant period.

7.4.3 Force Measurements

In figure 7.17 the steady part from the three force transducers from experiment 7. with $\zeta_A = 0.05m$ and $T = 1.50s$ is shown.
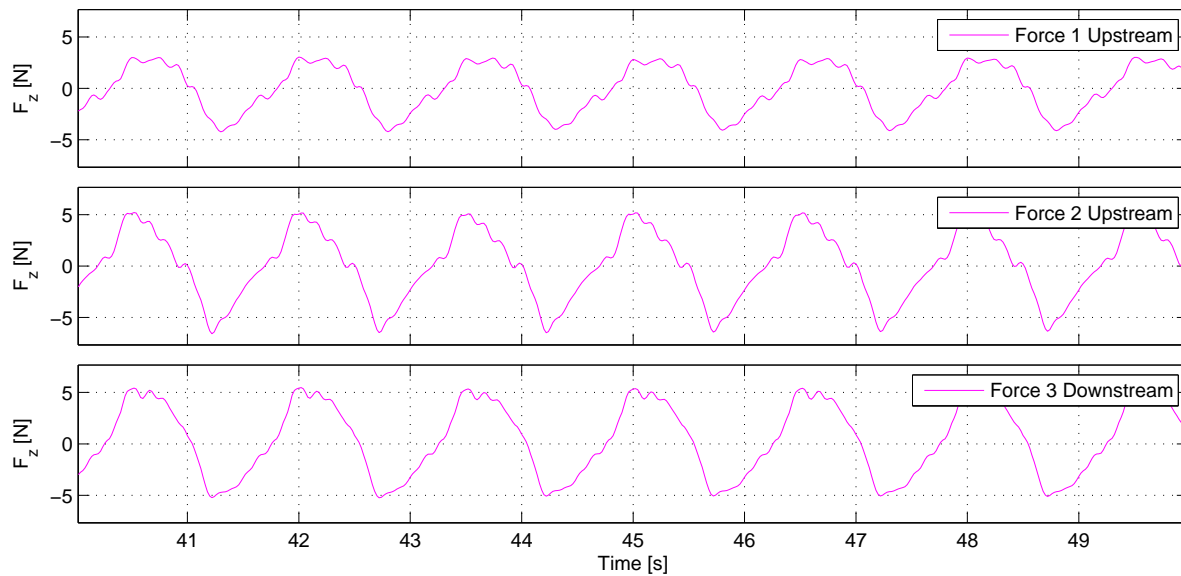
Figure 7.17: Steady part of force measurements from experiment 7 on rectangular protection cover with $\zeta_A = 0.05m$ and $T = 1.5s$.

The steady part of the force measurements in figure 7.17 shows a regular trend following the wave period for all three force transducers. A small overlying frequency is observed and can be due to small vibrations in the mounted frame. A force transducer has a larger sensitivity to vibrations than a wave probe. When small forces are measured the transducer will in addition capture small vibrations. A difference in force amplitude is obtained from the three different force transducers. The reason for the different amplitude values will be due to the placements of the force transducers. Since two force transducers was mounted upstream and only one transducer downstream a asymmetry in the measurements will be reasonable. In addition a small deviation in placement from the actual mass center of the protection cover will also give asymmetry in the measurements. A small phase difference between the upstream and downstream mounted force transducers can also be seen. The phase difference will be due to the variation in wave elevation over the protection cover sides where the forces are measured. The structure is assumed small in comparison with the wave length and the small phase will be negligible. The total vertical force will be the sum of the three force transducers. In figure 7.18 the total vertical force from experiment 7 with $\zeta_A = 0.05m$ and $T = 1.5s$ is shown. The force is given in $[N/m]$ by dividing the total measured force with the length of the protection cover of $b = 2.0m$.
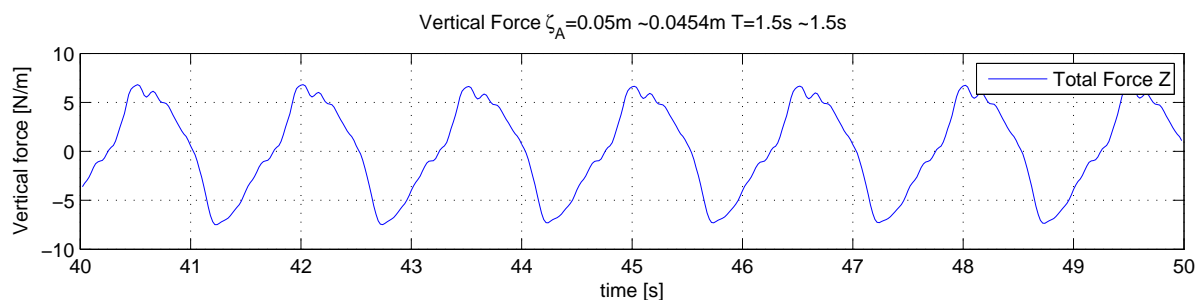
Figure 7.18: Total vertical force from experiment 7 with $\zeta_A = 0.05m$ and $T = 1.5s$.
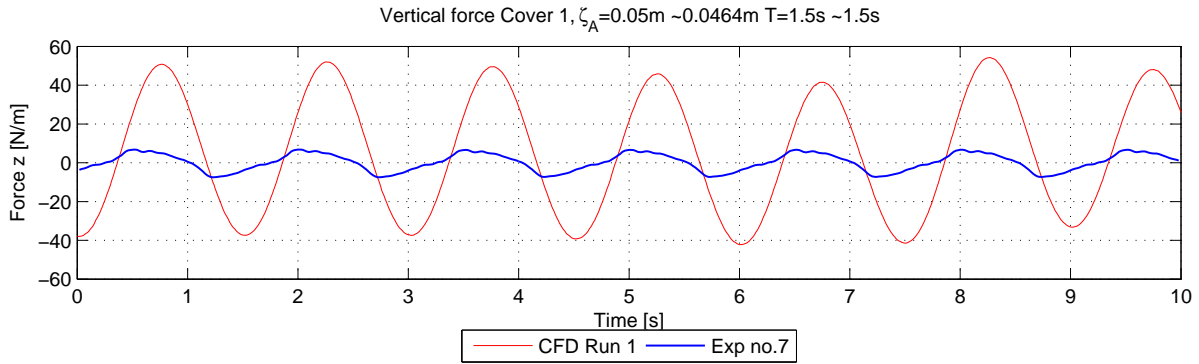
Figure 7.19: Total vertical force from experiment 7 and CFD run 1 with $\zeta_A = 0.05m$ and $T = 1.5s$.

In section 6.2 in chapter 6 the results from similar numerical analysis compared with theoretical vertical forces with the same wave amplitude, $\zeta_A = 0.05m$, and wave period, $T = 1.5s$, indicate a vertical force amplitude of $F_{z,max}^{num} \pm 45N/m$. In figure 7.19 the total vertical force from experiment 7 is compared with vertical force from CFD analysis run 1 in section 6.2 in chapter 6.

In section 6.2 in chapter 6 the vertical force from CFD also was in accordance with the theoretical vertical Froude-Kriloff pressure force. The experimental measurements give a total vertical force $6.5 - 8.5$ times lower than both the numerical CFD force and the theoretical Froude-Kriloff pressure force. The same factor between the measured and numerical vertical forces was also seen for the other experiments with similar settings as the numerical analysis. Obviously the experimental force measurements has been affected by some effects which not was taken into account by the CFD analysis and the theoretical approach.

Some difference between experimental and numerical results would be reasonable due to difference in the model setup and between experimental and numerical environmental conditions. In the present case the largest difference between the experiments and the numerical analysis was the water underneath the protection cover. In the CFD analysis a simplification was implemented by only changing the bottom curvature and isolate the surfaces of the protection cover in order to only measure forces on the protection cover walls. In the experimental setup the frame, which the protection cover was mounted on, was filled with water due to small openings. The water underneath the protection cover would only cancel the static pressure force if the water underneath was at rest. If the water inside the cover could be assumed to be at rest the dynamic pressure from the waves would not be present under the protection cover. Due to shallow water in the experiments the waves induced particle motions all the way to the bottom. During the experiments there was obtained oscillation of the water around the bottom mounted frame. The water inside the protection cover would therefore also have some dynamic oscillation. The tape used at the cross sections would prevent some motion but a totally isolation was impossible with the used experimental setup. A oscillation of the water underneath the protection cover could give unwanted pressure effects. The dynamic water motion inside the protection cover can be one factor in order to explain the lower experimental measured vertical forces. A pressure gauge inside the protection cover would therefore be strongly recommended in order to study the pressure variation inside the protection cover compared with the outer dynamic wave pressure.

Another factor affecting the measurement can be the calibration and the experimental setup. The calibration was performed several times and in some cases also after some of the measurements in order to see if the force transducers was drifting from the calibrated value. The data acquisition system from the transducers, via the amplifier, digital filter, A/D converter and in to the logging software was set up together with Torger Waal from MARINTEK. He also checked the settings regarding the data acquisition system afterwards. During the first experiments some of the force transducers was replaced due to unnatural oscillations in calm water after long stabilizing time. The reason was assumed to be bad water sealing

in the transducers. The measurements with the first used transducers was not used. Regarding the installation on the frame, internal stresses could appear when tighten the force transducers between the frame and the protection cover. A calibration check was performed after the protection cover was mounted before the total system was submerged. In addition some flexibility was seen in the force transducers when loaded.

From the environmental conditions, tank wall effects in the tank can have affected the measurements by setting up a transverse wave system. From the observations by J.Xia & J.R.Krokstad (2001) the measured vertical force was a order of magnitude lower at the resonance periods of the transverse wave system in the tank. In the present experiments the input wave periods was around, and some times close to, the resonance periods of the transverse wave system. The tank walls would therefore have some influence on the vertical force measurements. During the experiments the transverse waves was observed in a small scale and was much smaller than the longitudinal waves. After the wavemaker was turned off and the longitudinal waves was damped out at the end beach, the transverse oscillations was clearly seen. After some of the experiments the time to achieve calm water was long due to the transverse wave system with small damping.

Further results and discussion regarding the measured forces will focus on differences between the two selected geometries due to the large deviation between numerical CFD analysis and theoretical calculations compared with the experimental force measurements. In figure 7.20 the mean maximal vertical force from the steady part of the vertical force measurement for each experiment is given for both protection covers. The lines corresponds to constant wave period with increasing wave amplitude. Similar figure with constant amplitude lines can be found in appendix E.
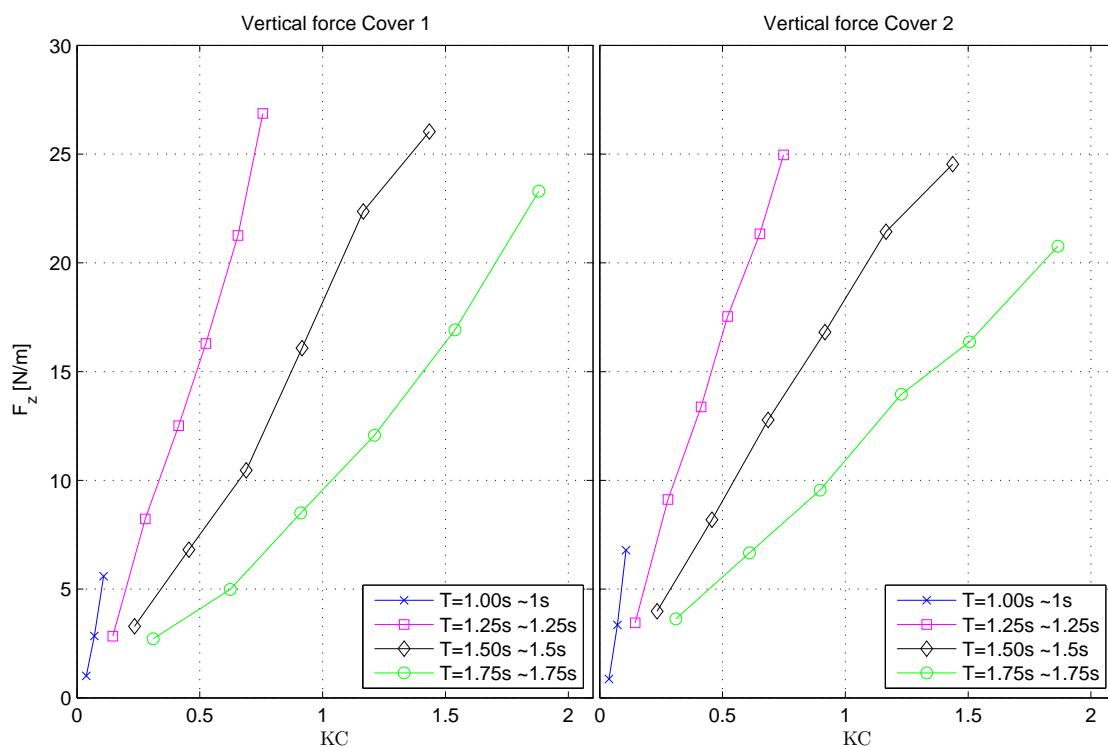
Figure 7.20: Maximal vertical force on rectangular protection cover.

In figure 7.20 almost similar results is obtained for the two covers. The rectangular cover, 1, gives a small value larger vertical forces compared with the half circular cover. The KC number increase with increasing wave period which is reasonable due to proportionality. The slope of the constant period lines is reduced with increasing wave period. For the largest wave period of $T = 1.75s$ the vertical forces shows a reduced tendency. For the half circular cover the constant period lines almost have a constant slope giving linear relationship between vertical forces and KC number. For the rectangular

cover a increased slope is obtained especially for the largest wave period, which indicate a higher order relationship between vertical forces and KC number.

The experimental forces can be made non dimensional similar as the numerical forces, by the equation 7.3, where ρ is the density, g gravity, V volume of cover, ζ_A wave amplitude and h the water depth. The wave amplitude ζ_A is taken from the actual measured wave amplitude from $wp01$ at $x = 7.3m$. In figure 7.21 the non dimensional vertical force for both the rectangular and the half circular protection cover is shown. Here cover 1 represents the rectangular cover and cover 2 represents the half circular cover. More figures of non dimensional vertical forces can be found in appendix E.

$$F_{DIM} = \frac{F}{\rho g V \frac{\zeta_A}{h}} \tag{7.3}$$
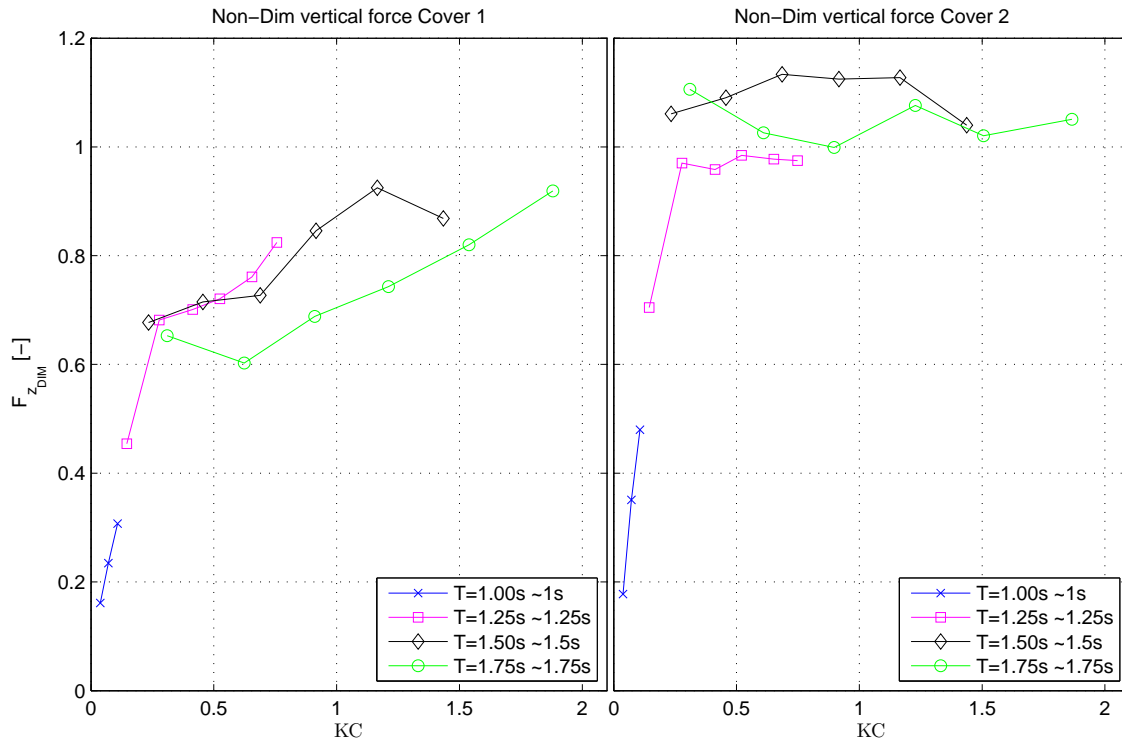
Figure 7.21: Non dimensional vertical force on cover 1 and 2 with constant period lines.

In figure 7.21 a larger non dimensional vertical force is obtained for the half circular cover. The same difference was obtained in the numerical vertical force but with different non dimensional values. A trend for all the points shows a large increase for low KC below $KC = 0.25$. Above $KC = 0.25$ the non dimensional vertical force is flattened out with a smaller increase for larger KC numbers. Especially for the half circular cover the mean non dimensional vertical force seems to become constant above $KC = 0.25$ for constant wave periods. For the rectangular cover a transition can be seen around $KC = 0.25$ but still the non dimensional vertical force increase above $KC = 0.25$.

7.4.4 Overturning Moment

The overturning moment of the protection cover can be calculated from the measured vertical forces by multiplying each force with the normal length to the rotation axis. A overturning moment means that the protection cover will be tilted around a axis on the side plate ends, (mud mat). For simplicity the rotation axis was set at the center of the downstream force transducer, such that only the upstream force transducers gave contribution to the overturning moment. The arm length was measured to $l_{arm} = 0.26m$

from the center mounting of the upstream force transducers to the center mounting of the downstream force transducer. The vertical forces was positive upwards. In figure 7.22 the steady part of the calculated overturning moment for run 7 is shown.
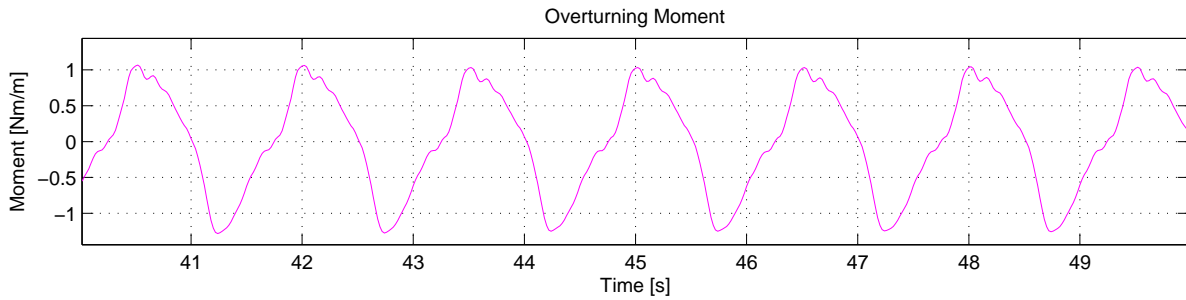
Figure 7.22: Overturning moment from run 7.

The moment can be made dimensionless in similar manner as the force, by dividing with a length scale. The characteristic length of the cover, $l = 0.2m$ is used as length scale and the non dimensional moment equation is given in equation 7.4. In figure 7.23 the maximal non dimensional overturning moment for both the rectangular and half circular protection cover is shown. In appendix E the overturning moment with constant amplitude lines can be found.

$$M_{DIM} = \frac{M_{max}}{\rho g V l \frac{\zeta_A}{h}} \tag{7.4}$$
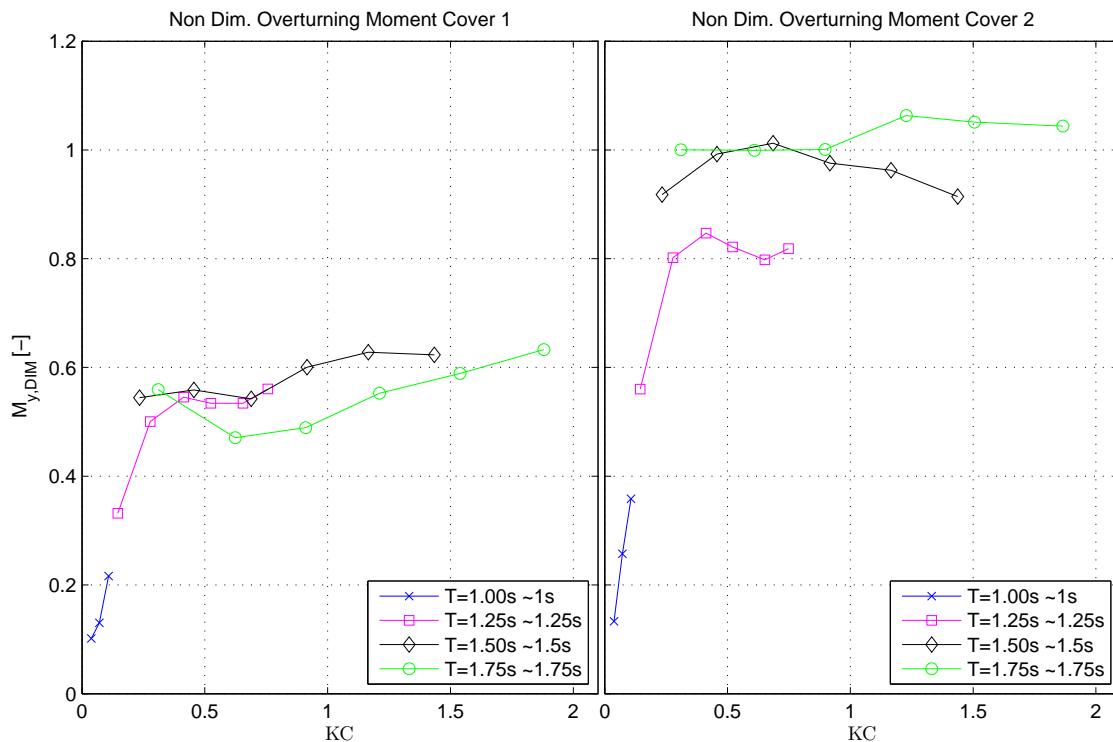
Figure 7.23: Non dimensional overturning moment.

In figure 7.23 the non dimensional overturning moment is larger for the half circular cover compared with the rectangular cover. The reason will be due to larger non dimensional vertical force on the half circular cover. A general trend is that the non dimensional overturning moment has a large increase for low KC numbers and with decreasing slope for larger KC numbers. Over a certain KC value, dependent of the

wave period, the non dimensional overturning moment becomes constant for increasing KC numbers. For the rectangular cover the non dimensional moment shows a transition above $KC = 0.25$ with minor increase above. The half circular cover also shows a transition around $KC = 0.25$ but a larger dependency of the wave period can be seen. The same data points with constant amplitude lines given in appendix E shows a better coherence where the non dimensional moment tends towards a constant value of 0.6 for the rectangular cover and 1 for the half circular cover.

7.5   Conclusion

A parameter study was done on both the rectangular and half circular protection cover models with variation in both wave period T and wave amplitude ζ_A. A total of 21 measurements was performed for each model where vertical force on the protection cover from three force transducers and wave elevation from two wave probes was measured. Shallow water was assumed except for the lowest wave period where deep water could be assumed. The Experiments was originally planned as a validation for the numerical CFD calculations and to investigate the shallow water wave forces on simplified protection covers. Due to the difference in modeling, a proper validation for the measured forces with the CFD analysis was not achievable.

The numerical wave elevation at similar sections was compared with experimental results. A direct comparison of the wave elevation between experiments and CFD gave good agreement. The experimental wave elevation gave also good agreement with Stokes 2nd order wave theory. Especially the cases with large wave amplitude and steepness, as in experiment 19, the wave elevation was highly non linear and Stokes 2nd order theory gave much better agreement than linear wave theory. The flap wavemaker gave similar wave parameters as the input parameters for low periods below $1.25s$. Increased period gave increased wave height. Above $H = 0.15m$ and $T = 1.0s$ the wavemaker tends to produce higher waves than the input values.

The vertical forces was not comparable with the CFD computations. The reason will mostly be the difference in modeling and experimental setup. In the performed experiments there was openings between the protection cover and the frame and the cover was filled with water on the inside. During the experiments the wave orbital motion was observed around the protection cover and also for the water inside the cover. The water motion inside the cover will give a dynamic contribution to the original static water pressure inside the cover. The dynamic pressure contribution can give cancellation effects to the measured vertical forces. Cancellation effects of the measured forces can also be due to affection of the tank walls. A transverse wave system can be established in the tank due to wave reflections. The selected wave periods was found to be around and close to the natural periods of the transverse wave system. The transverse waves was only observed after the longitudinal waves from the wavemaker was damped out, but the tank walls will have some influence on the force measurements. Other factors which can affect the vertical force measurements can be measurement errors in the force transducers and errors in the acquisition system. In all experiments, also the human error factor will be representative. Regarding the two different geometries of the studied covers, a similar trend in the measured forces was observed. The rectangular cover gave a small value larger forces. For the non dimensional forces the half circular cover gave largest values. The non dimensional overturning moment was also largest for the the half circular cover.

7.6   Further work

Regarding the experimental setup, the modeled frame could be made better in order to achieve a undisturbed water flow towards the studied cover. The openings between the frame and the studied cover should be made smaller or sealed with a a elastic sealing in order to avoid water to flow inside the cover.

A pressure gauge should be used inside the studied cover in order to obtain the dynamic movement of the water inside. To avoid tank wall effects, a larger basin could be used. A larger test facility indicate larger costs. The wave periods could also be selected with the transverse periods in mind.

In order to study the possibility of horizontal movement of a protection cover, the horizontal forces would be of more interest than the vertical forces. Horizontal force measurements was found more difficult to achieve due to unbalance in the mountings. The horizontal force measurements is suggested for further work.

Only regular waves has been studied in the present experiments. Irregular sea states will be of interest in order to have a more realistic sea state and will be suggested for further work. The limitation in wave height and water depth in the student tank also limit the parameter study. A deeper wave tank combined with larger wave heights will be suggested in order to perform a extreme wave criteria. The protection covers can in some cases be lying on the bottom during a winter without stabilizing rock dumping. Therefore a wave height with one year return period is recommended for further work.

The force measurements are presented as non dimensional forces. A scaling to full scale has not been done and is suggested to further work. Also a statistical uncertainty analysis is suggested for further work.

Chapter 8

3D CFD Analysis

A simple three dimensional analysis was established in order to study some three dimensional effects and investigate the additional computation time.

8.1 Domain and Settings

The two dimensional domain in figure 6.1 in chapter 6 was extruded $2.0m$ and shorten to a total length of $20m$ in order to establish a simple three dimensional analysis. Two runs was performed with wave amplitude $\zeta_A = 0.05m$ and wave period $T = 1.5s$, one for each cover type similar to run 1 and 4 for the two dimensional analysis in chapter 6. The used three dimensional domain is shown in figure 8.1.
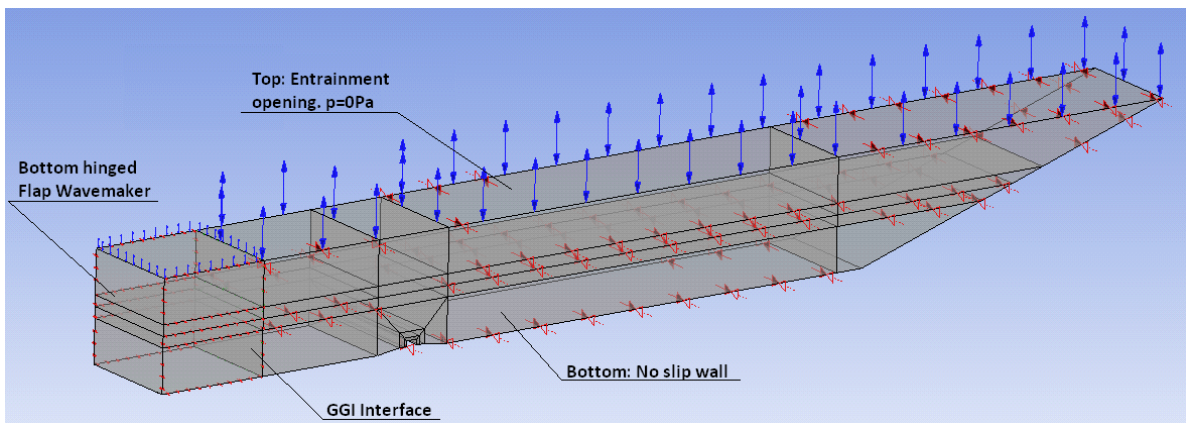
Figure 8.1: Three dimensional domain.

The total length of the domain was $20m$. Due to the beach with slope $1 : 3$ the mean free surface was $17m$. The water depth was $1.0m$ and similar $1.0m$ of air was modeled. The extruded length was $2.0m$. Wave elevation was measured at four sections along the tank, at $x = 2m$, $x = 4.3m$, $x = 5.7m$ and $x = 13.5m$. The same numerical settings as given in table 6.2 in chapter 6, and similar boundary conditions as for the two dimensional analysis was used. As a comment similar as the two dimensional analysis, symmetry planes was used on the tank wall sides. In order to compare with a physical wave tank, the tank walls should have been set to a wall with no slip condition. In table 8.1 the mesh details is given.

Notice only 20 elements in the extruded y direction, which not will be suggested but was chosen in order to limit the computation time. The total number of elements was large and a smaller domain will be

Parameter	Setting
Domain length	$20m$
Water depth	$0.75m + 0.25m$
Air height	$0.75m + 0.25m$
Extruded width	$2m$
Number of Elements	1326400
Δx	0.05
Δy	10
Δz	0.0042
$\Delta x/\Delta z$	12
Air_z	20
$Water_z$	20

Table 8.1: Mesh details in 3D Wave Tank.

suggested. The performed runs is given in table 8.2. See more detailed parameters for run 1 and 4 in table 6.3 and 6.4 in chapter 6.

Run	Cover	ζ_A $[m]$	T $[s]$
1	Rectangular	$0.05m$	1.5
2	Half circular	$0.05m$	1.5

Table 8.2: Performed runs in 3D analysis.

The analysis was performed in serial with single precision. The total computation time was around $10h$ for $1s$ simulation time, giving around $200h = 8.3days$ for $20s$ simulation time. In a numerical wave tank, a transient analysis is necessary. A three dimensional analysis should definitely be performed in parallel in order to reduce computation time. Due to some convergence errors regarding free surface flows in combination with running in parallel, a serial analysis was performed. For further use, a proper set up of the parallel environment must be established to reduce the computation time.

8.2 Results

Similar as is chapter 6 the wave elevation and forces was measured. In figure 8.2 the wave elevation along the tank length at $t = 5s$, $t = 10s$, $t = 15s$ and $t = 20s$ for the rectangular cover in run 1 is shown. Similar results for the half circular cover can be found in appendix F.

In figure 8.3 the time series of the wave elevation from four section along the tank at $x = 2m$, $x = 4.3m$, $x = 5.7m$ and $x = 13.5m$ is shown for the rectangular cover in run 1. Similar results for the half circular cover can be found in appendix F.
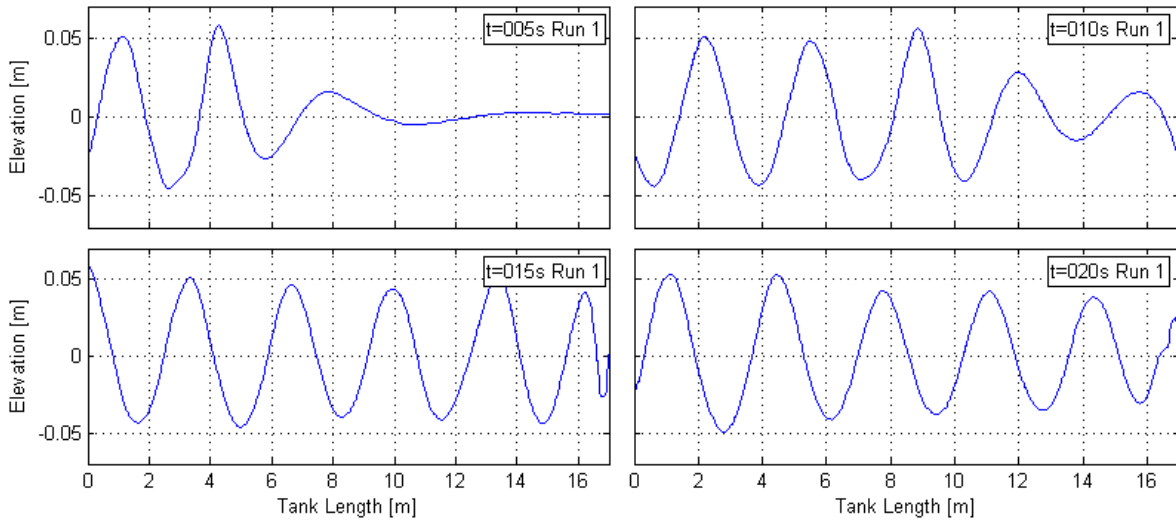
Figure 8.2: Wave elevation along the tank length at $t = 5s$, $t = 10s$, $t = 15s$ and $t = 20s$ for the rectangular protection cover from the 3D analysis.
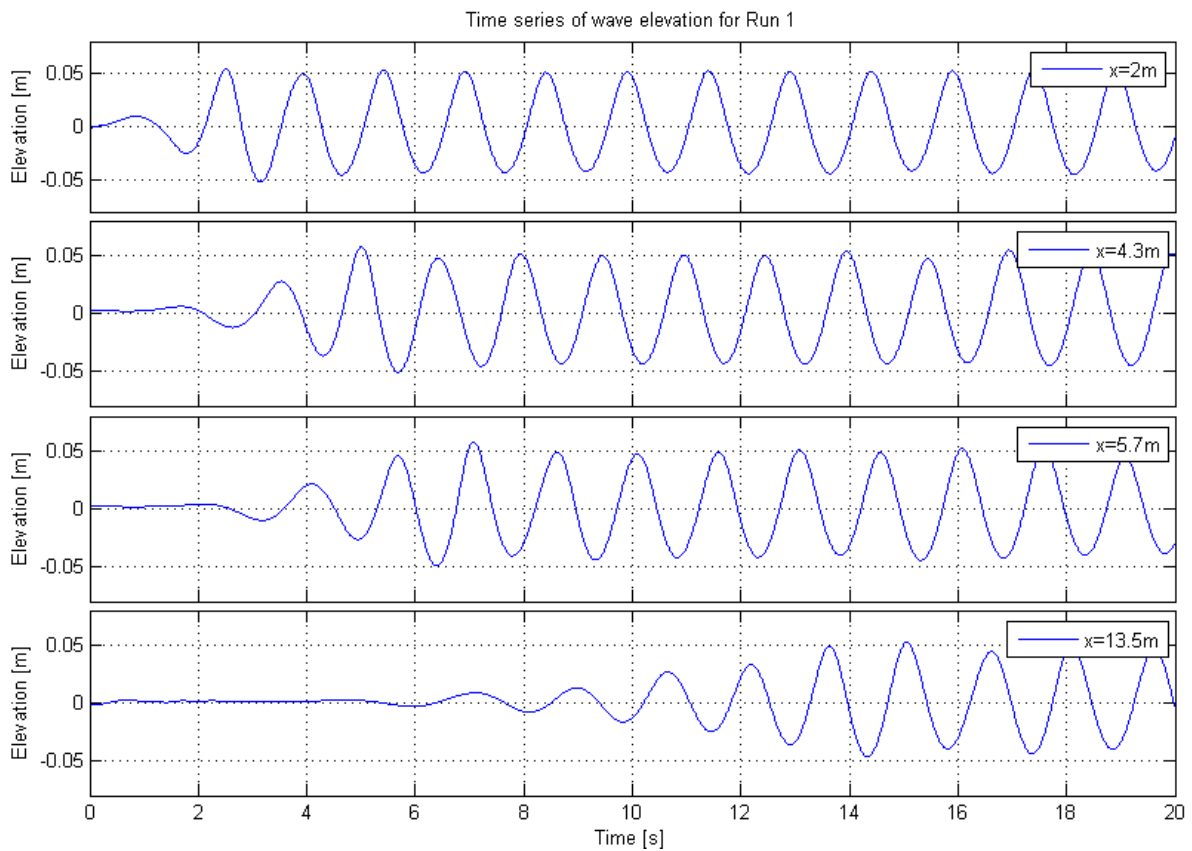
Figure 8.3: Time series of wave elevation along the tank length at $x = 2m$, $x = 4.3m$, $x = 5.7m$ and $x = 13.5$ for the rectangular protection cover from the 3D analysis.

In figure 8.4 the steady part of the horizontal and vertical dynamic forces from run 1 and 2 is shown.

(a) Horizontal and vertical dynamic forces on the rectangular protection cover in run 1.

(b) Horizontal and vertical dynamic forces on the half circular protection cover in run 2.
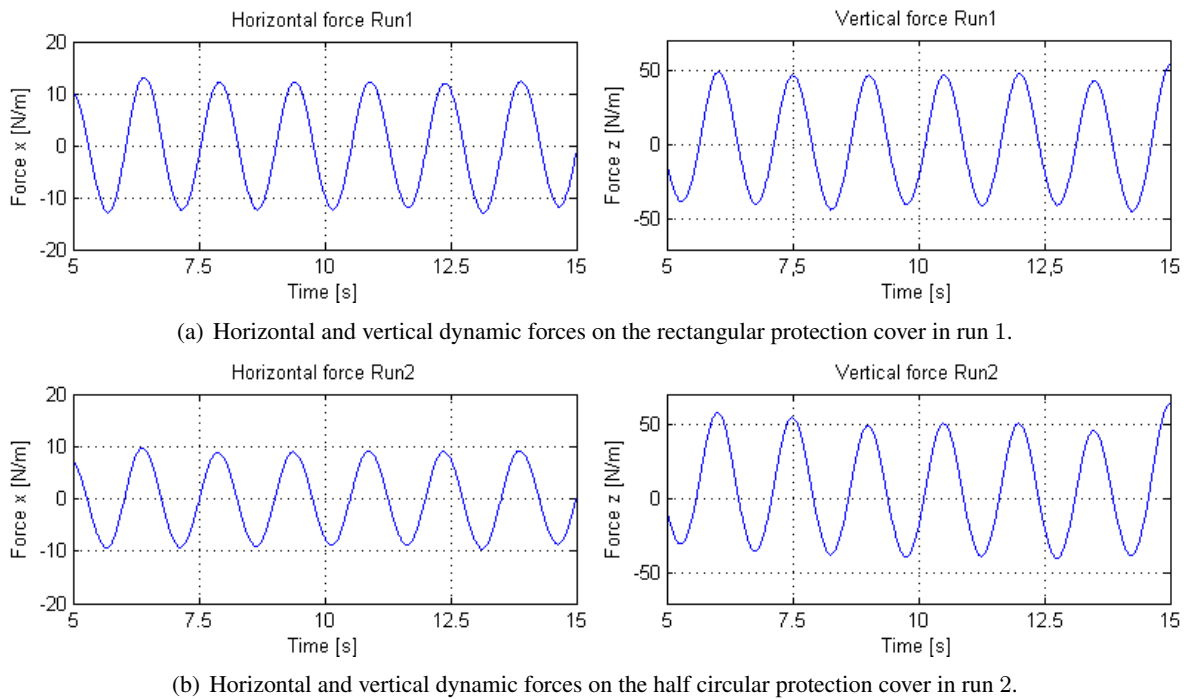
Figure 8.4: Steady horizontal and vertical dynamic wave forces on the studied protection covers in run 1 and 2.

8.3   Conclusion and discussion

A three dimensional analysis is time consuming and demand larger computer memory and storage. The present simple analysis with only 20 elements in the extruded length of $2.0m$ gave a indication on the computation time and the request for running in parallel. Establish a proper parallel environment is suggested for further work. Number of elements should be set larger in the extruded length in order to study three dimensional effects. The extension of the total domain should be reduced to be able to have more elements in the extruded length. In combination with a smaller domain, a damping zone will be suggested for further work. The wave elevation and force measurements gave similar results as the two dimensional numerical wave tank. The tank side walls should be modeled as a no slip wall in order to be able to compare the results with a physical wave tank. Also the tank wall effects regarding the transverse wave system could be accounted for with no slip wall boundaries.

References

A.Bhinder, M., G.Mingham, C., M.Causon, D., T.Rahmati, M., A.Aggidis, G., & V.Chaplin, R. (2009). A joint numerical and experimental study of a surging point absorbing wave energy converter (wraspa). *ASME* $28th$ *International Conference on Ocean, Offshore and Arctic Engineering, May* $31-$ *june* 4, *Honolulu, Hawaii, USA.*

A.E.Maguire, & D.M.Ingram (2009). Hydrodynamics and absorption efficiencies of wavemakers. $8th$ *European Wave and Tidal Energy Conference, Uppsala, Sweden..*

Andersson, H. I. (1988). *Introduction to Turbulence Modeling.*

ANSYS (2010). *ANSYS CFX-Solver User Manual and Modeling guide release 13.0.*

Babanin, A. V. (2006). On a wave-induced turbulence and wave-mixed upper ocean layer. *Geophysical Research Letters, VOL. 33..*

Burrows, R., Tickell, R. G., Hames, D., & Najafian, G. (1997). Morison wave force coefficients for application to random seas. *Applied Ocean Research* 19, $183-199..$

Chakrabarti, S. (1987). *Hydrodynamics of offshore structures.* Computational Mechanics Publications.

Chakrabarti, S. K., & Naftzger, R. A. (1989). Wave forces on hemicylinders. *Ocean Engineering, Vol. 16, No.* 1. pp $49-69..$

C.M.Dong, & C.J.Huang (2001). On a $2-d$ numerical wave tank in viscous fluid. *Eleventh International offshore and Polar Engineering Conference Stavanger, Norway, June* $17-22..$

Dean, R. G., & Dalrymple, R. A. (1984). *Water Wave Mechanics for Engineers and Scientists.* Prentice Hall, Inc.

DNV-RP-C205 (2010). *DNV Recommended Practice, Environmental Conditions and Environmental Loads.*

Elangovan, M., & Sahoo, G. (2010). Generation of irregular wave for marine application by piston type wave maker. *International Offshore and Polar Engineering Conference Beijing China June* $20-25..$

Faltinsen, O. M. (1990). *Sea Loads on Ships and Offshore Structures.* Cambridge University Press.

Godderidge, B., Phillips, A., Lewis, S., Turnock, S., Hudson, D., & Tan, M. (2008). The simulation of free surface flows with computational fluid dynamics. In *ANSYS UK User Conference.*

Gran, S. (1973). Wave forces on submerged cylinders. *Fifth Offshore Technology Conference, Houston, Texas, April* $29-May$ $2..$

Havn, J. (2010). *Project Thesis, Hydrodynamic Calculations with ANSYS CFX.*

Herbich, J. B., & Shank, G. E. (1970). Wave forces on submerged structures theory and experiment. *Second Offshore Technology Conference, Houston, Texas, April* $22-24..$

J.C.Park, Y.Uno, T.Sato, H.Miayata, & H.H.Chun (2004). Numerical reproduction of fully nonlinear multi-directional waves by a viscous $3d$ numerical wave tank. *Ocean Engineering* 31, $1549 - 1565.$.

J.H.Ferziger, & M.Peric (2002). *Computational Methods for Fluid Dynamics*. Springer.

J.Xia, & J.R.Krokstad (2001). Wave forces on a body in confined waters. 14th *Australasian Fluid Mechanics Conference, Adelaide, Australia, December* $10 - 14.$.

Koo, W., & Choi, K. (2010). Bragg reflection of numerical waves by a $2d$ numerical wave tank. *Twentieth International Offshore and Polar Engineering Conference, Beijing, CHina, June* $20 - 25.$.

Mei, C. C., & L.Black, J. (1968). Scattering of surface waves by rectangular obstacles in water of finite depth. *Journal of Fluid Mechanics, vol.*38*, part* 3*, pp.*$499 - 511.$.

Menter, F. (1994). Two-equation eddy-viscosity turbulence models for engineering applications. *AIAA-Journal , 32(8), pp. 269-289.*.

Miche, M. (1951). Le pouvoir reflechissant des ouvrages maritimes exposes a l'action de la houle. *Annals des Ponts et Chausses, 121e Annee, 285-319.* (translated by Lincoln and Chevron, University of California, Berkeley, Wave Research Laboratory, Series 3, Issue 363, June 1954).

M.N.Gomes, C.R.Olinto, L.A.O.Rocha, J.A.Souza, & L-A-Isoldi (2009). Computational modeling of a regular wave tank. *Engenharia Tèrmica (Thermal Engineering) Vol.*8 *No.*1 *June, pp.*$44 - 50.$

Myrhaug, D. (2006). *Oceanography, Wind and Waves Lecture notes in TMR4230*.

Park, J.-C., & Kim, K.-S. (2009). Numerical simulations of fully nonlinear wave motions in a digital wave tank. $5th$ *WSEAS International Conference on System Science and Simulation Engineering, Tenerife, Canari Islands, Spain, December* $16 - 18.$.

Park, Y.-S., Chen, X.-S., & Kim, W.-J. (2010). Cfd application tothe evaluation of wave and current loads on cylindrical platform model for ocean wind turbine. *Ninth International Society of Offshore and Polar Engineerings (ISOPE), Pacific/Asia Offshore Mechanics Symposium, Busan, Korea, November* $14 - 17.$.

Pettersen, B. (2007). *Hydrodynamic, Lecture notes in Marin Teknikk 3 TMR4247*.

Pleskachevsky, A., Dobrynin, M., Babanin, A. V., Günther, H., & Stanev, E. (2010). Turbulent mixing due to surface waves indicated by remote sensing of suspended particulate matter and its implementation into coupled modeling of waves, turbulence, and circulation. *Journal of Physical Oceanography, American Meteorological Society, April* 2011*, Vol.* 41*.*.

Silva, M. C., de Araújo Vitola, M., Pinto, W. T., & Levi, C. A. (2010). Numerical simulation of monochromatic wave generated in laboratory: Validation of a cfd code. In 23° *Congresso Nacional de Transporte Aquaviário, Construcão Naval e Offshore*.

Sinai, Y. (2010). Approximate boundary conditions for cfd simulations involving ambient surface (gravity) waves. *ANSYS Europe Ltd. UK.*.

Steen, S., & V.Aarsnes, J. (2010). *Experimental Methods in Marine Hydrodynamics, Lecture notes in TMR7*.

Åström, K. J., & Wittenmark, B. (1997). *Computer Controlled Systems, Theory and Design, Third Edition*. Prentice Hall Inc.

Venugopal, V., Varyani, K. S., & Westlake, P. C. (2008). Drag and inertia coefficients for horizontally submerged rectangular cylinder in waves and currents. *Engineering for the Maritime Environment, IMechE. Vol.* 223*, Part M.*.

Versowsky, P. E., & Herbich, J. B. (1974). Wave forces on submerged model structures. *Sixth Offshore Technology Conference, Houston, Texas, May* 6 − 8..

White, F. M. (2006). *Viscous fluid flow*. McGRaw Hill.

White, F. M. (2008). *Fluid Mechanics*. McGRaw Hill.

Williams, A. N. (1994). Froude-krylov force coefficients for bodies of rectangular section in the vicinity of the free-surface and sea-bed. *Ocean Engineering, Vol.* 21, *No.* 7, *pp.* 663 − 682..

Wilson, J. F. (1984). *Dynamics of Offshore Structures*. John Wiley and Sons Inc. Wiley Interscience publication.

Wu, G., & Jr., O. H. (2009). Cfd modeling of fully nonlinear water wave tank. *ASME* 28*th International Conference on Ocean, Offshore and Arctic Engineering, May* 31− *june* 4, *Honolulu, Hawaii, USA*.

Y.Wu, T. (1981). Long waves in ocean and coastal waters.

Appendix A

Force regimes
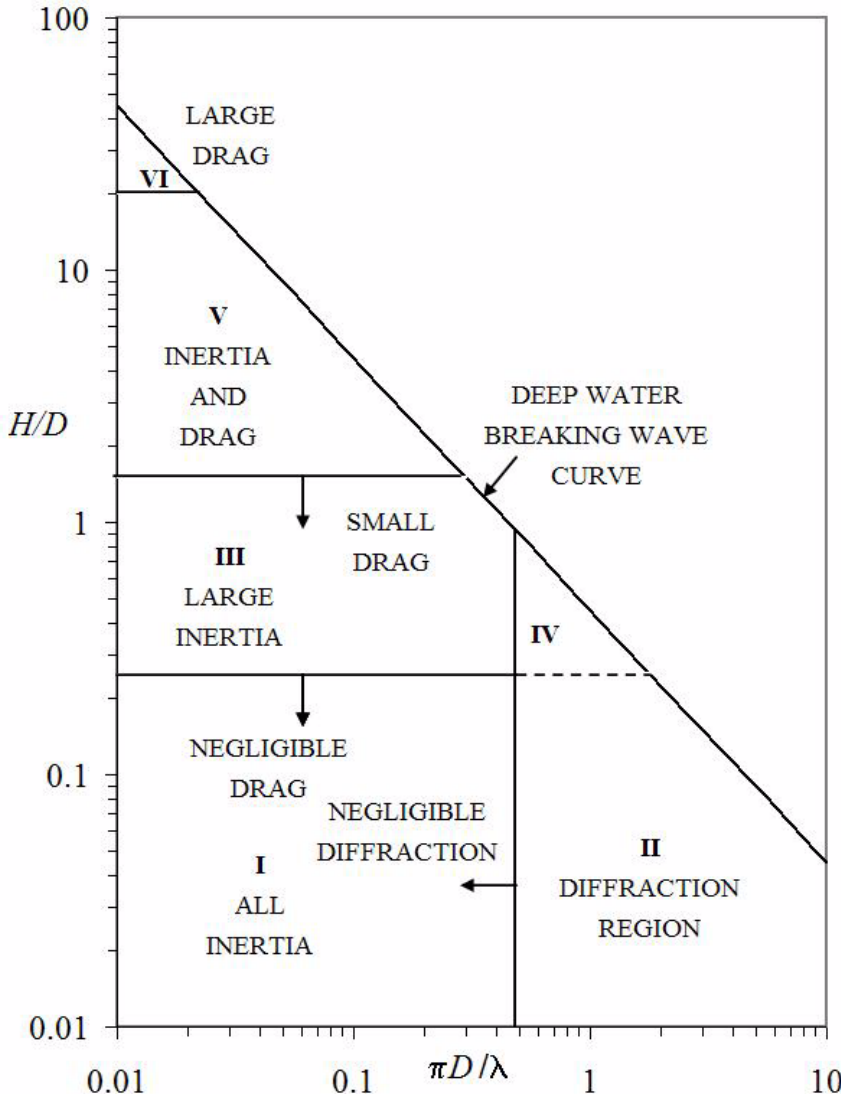
Figure A.1: Different wave force regimes from Chakrabarti (1987) valid for large volume structures. D is characteristic length, $H = 2\zeta_A$ is the wave height and λ is the wave length. Taken from $DNV - RP - C205 - (2010)$.

Appendix B

Wave Theory validity
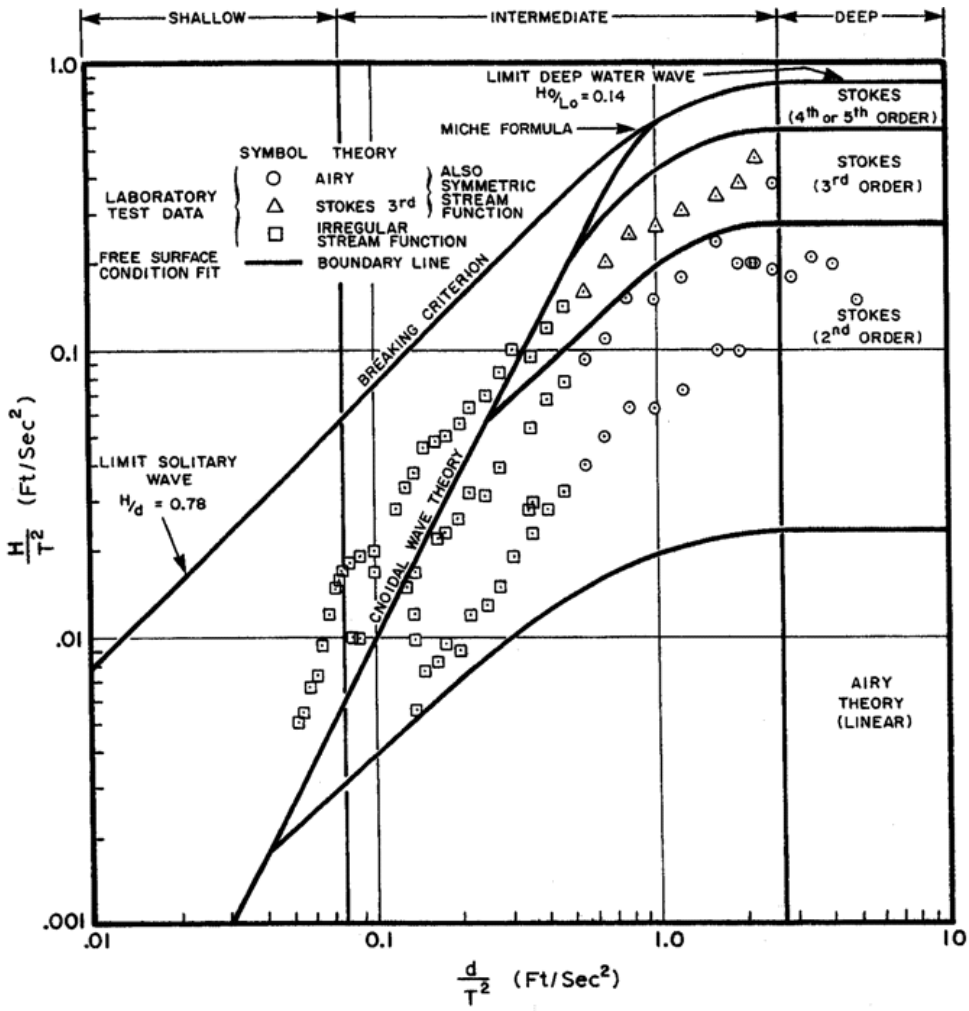
Figure B.1: Ranges of validity for various wave theories. The horizontal axis is a measure of shallowness while the vertical axis is a measure of steepness, Chakrabarti (1987). H is wave height, T is wave period and $d = h$ is water depth. Taken from $DNV - RP - C205 - (2010)$.

Appendix C

Figures from The Numerical Wave Tank

C.1 Case 1: Linear Wave Velocity Input

C.1.1 Surface elevation along the tank length

In figure C.1 to C.6 the surface elevation along the tank length for Case 1, the linear wave velocity input i shown for $t = 0s$ to $t = 25s$ respectively.
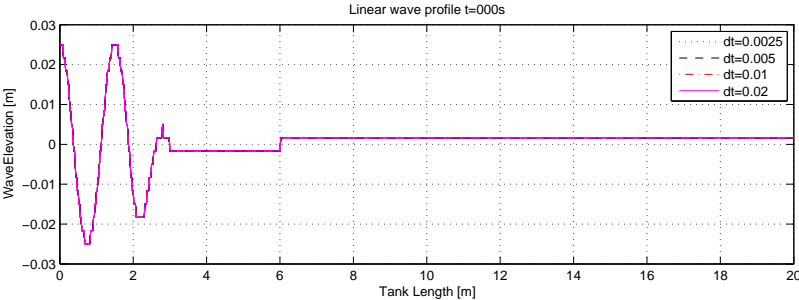
Figure C.1: Surface elevation along the tank length for all runs at $t = 0s$
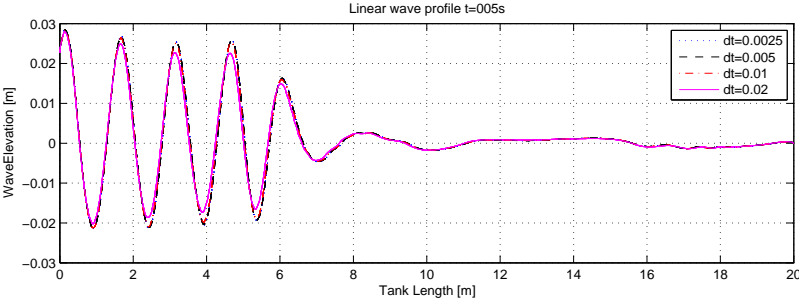
Figure C.2: Surface elevation along the tank length for all runs at $t = 5s$
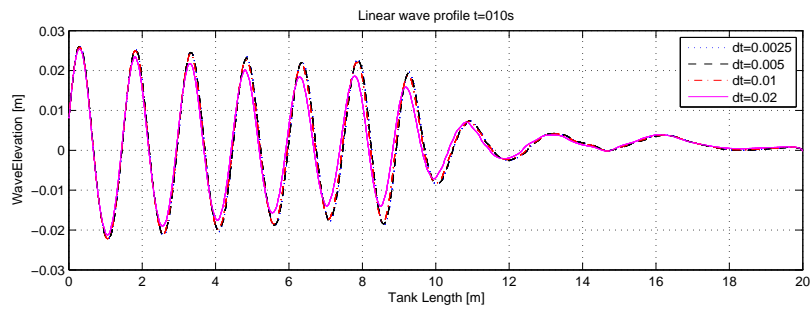
Figure C.3: Surface elevation along the tank length for all runs at $t = 10s$
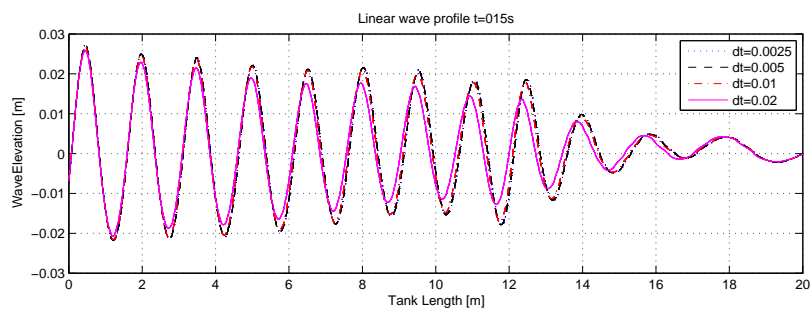
Figure C.4: Surface elevation along the tank length for all runs at $t = 15s$
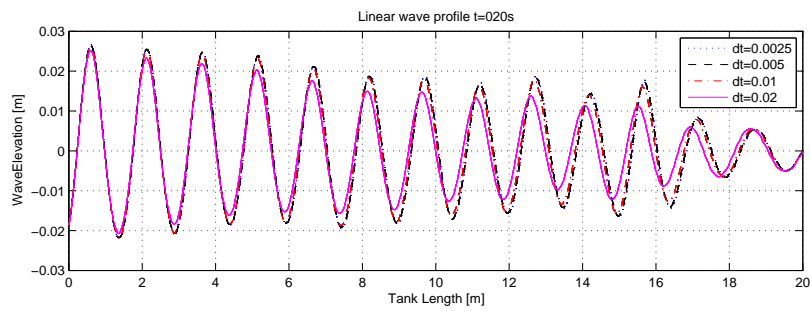
Figure C.5: Surface elevation along the tank length for all runs at $t = 20s$
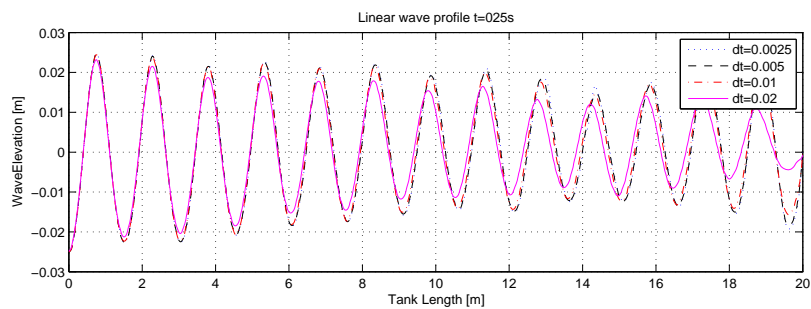
Figure C.6: Surface elevation along the tank length for all runs at $t = 25s$

C.1.2 Superficial Water Velocity for run 1

In figure C.7(a) to C.7(f) the contour plot of the superficial water velocity from run 1 i shown.
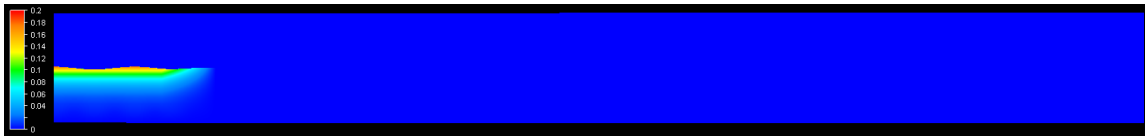
(a) Superficial water velocity for run 1 at $t = 0s$

(b) Superficial water velocity for run 1 at $t = 5s$
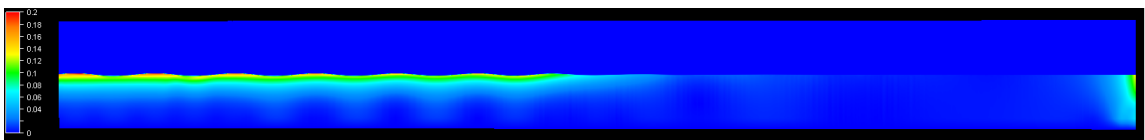
(c) Superficial water velocity for run 1 at $t = 10s$
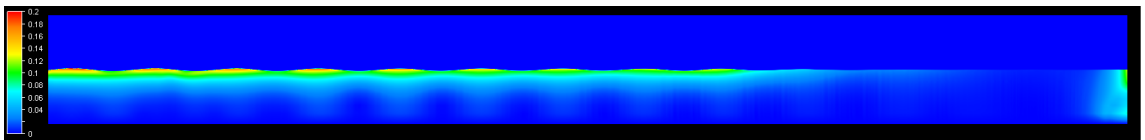
(d) Superficial water velocity for run 1 at $t = 15s$
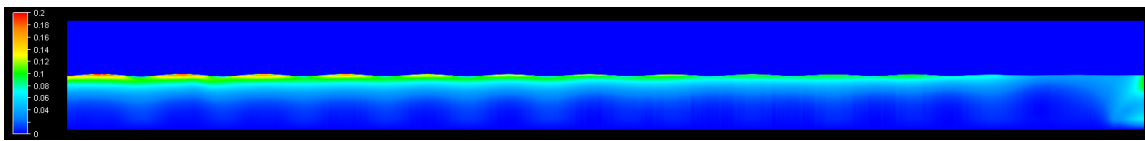
(e) Superficial water velocity for run 1 at $t = 20s$
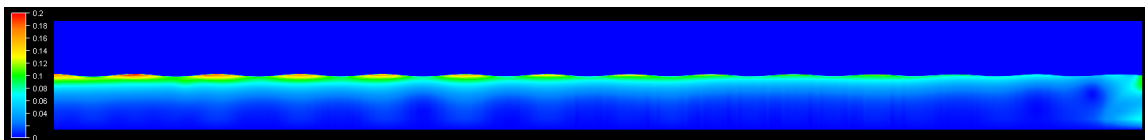
(f) Superficial water velocity for run 1 at $t = 25s$

Figure C.7: Superficial water velocity for run 1 at $t = 0s - 25s$

C.2 Case 3: Comparison with a Validation Case.

C.2.1 Wave Elevation along the Tank Lenght

In figure C.8 to figure C.13 the wave elevation along the tank lenght at $t = 5s$, $t = 10s$, $t = 15s$ and $t = 20s$ is shown.
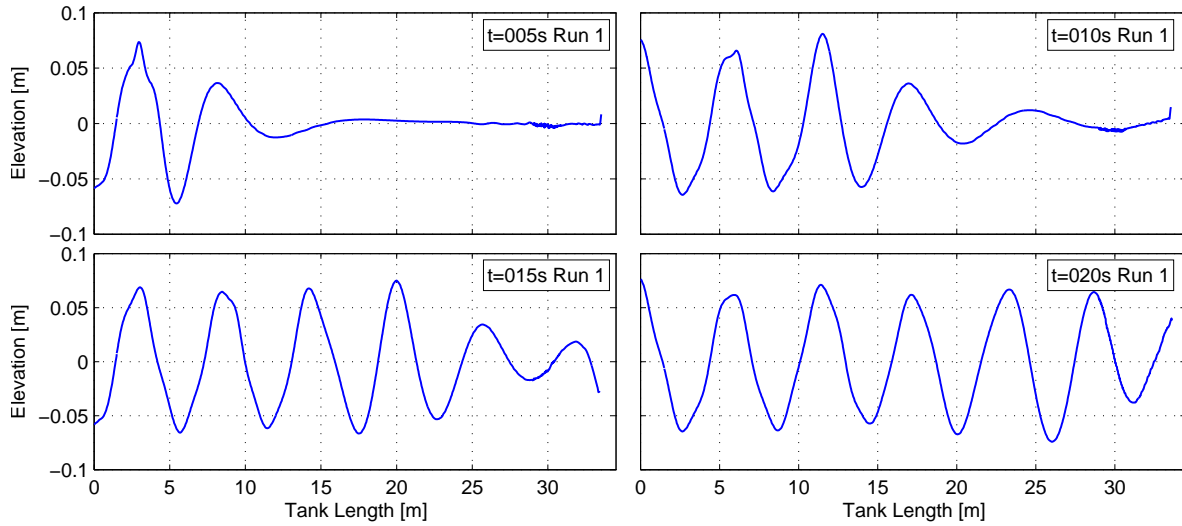
Figure C.8: Wave Elevation along the tank lenght for run 1
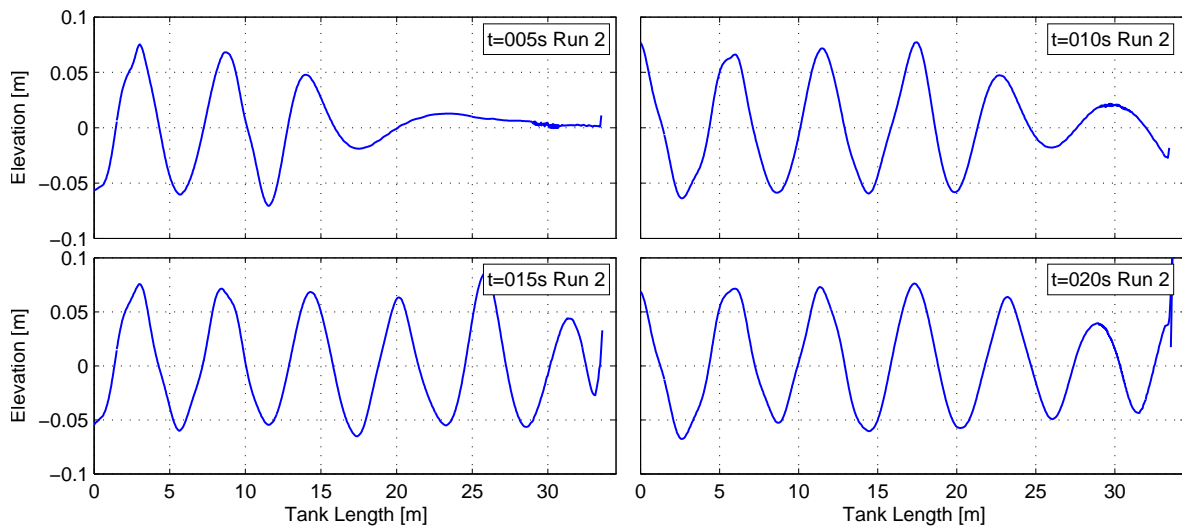
Figure C.9: Wave Elevation along the tank lenght for run 2
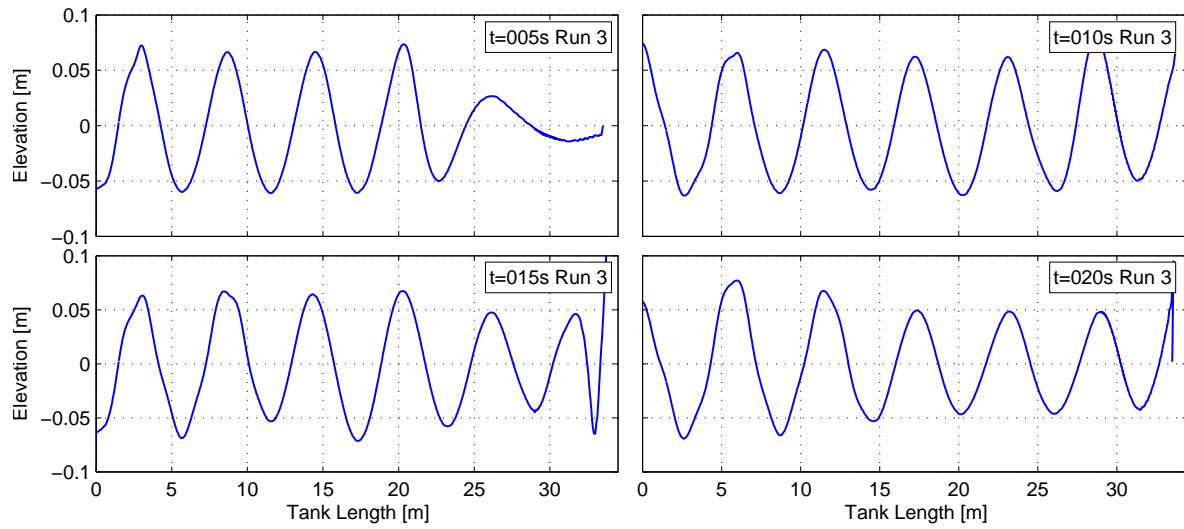
Figure C.10: Wave Elevation along the tank lenght for run 3
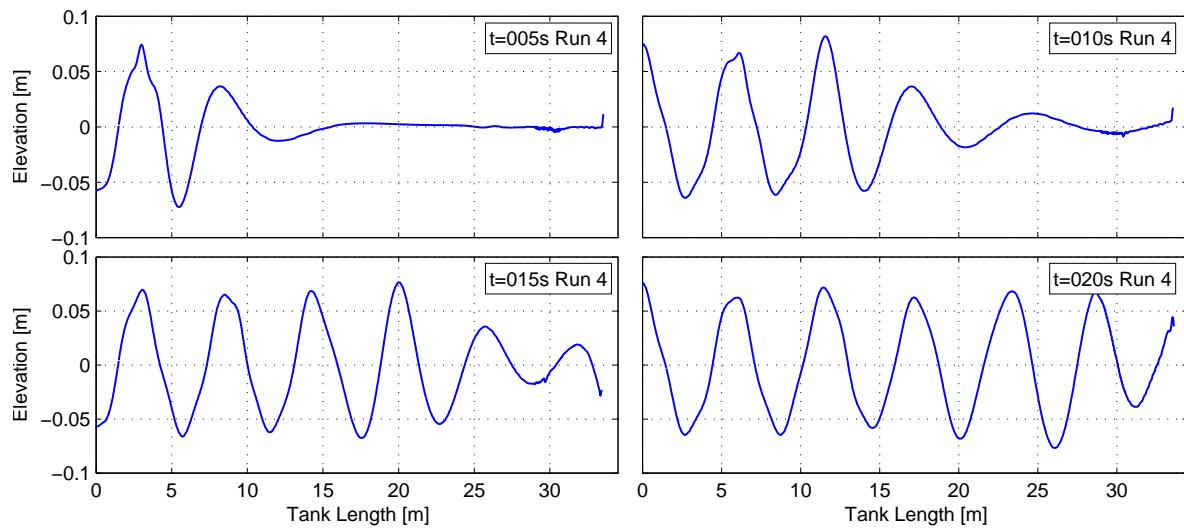
Figure C.11: Wave Elevation along the tank lenght for run 4
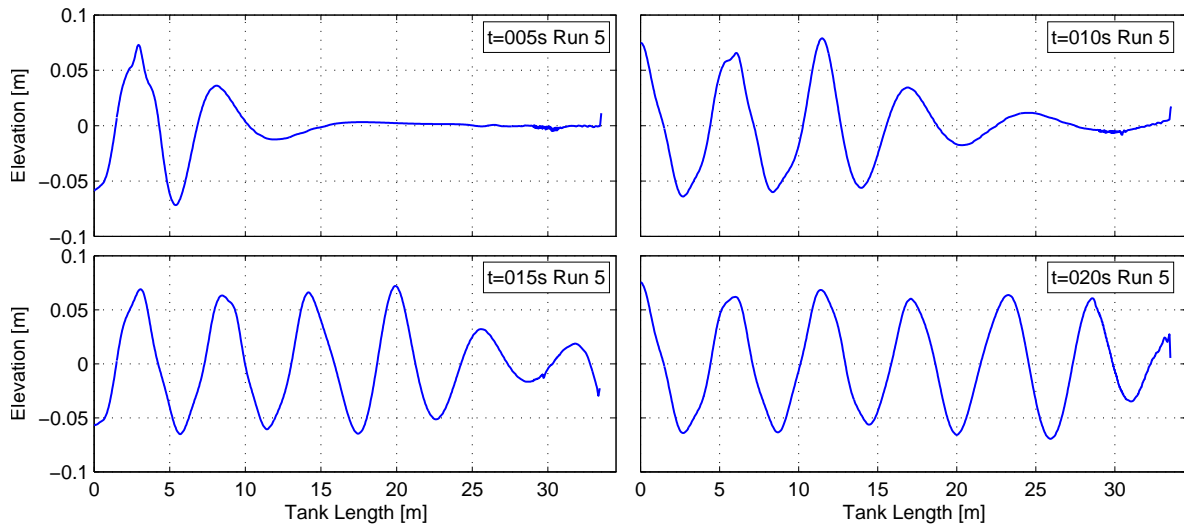
Figure C.12: Wave Elevation along the tank lenght for run 5
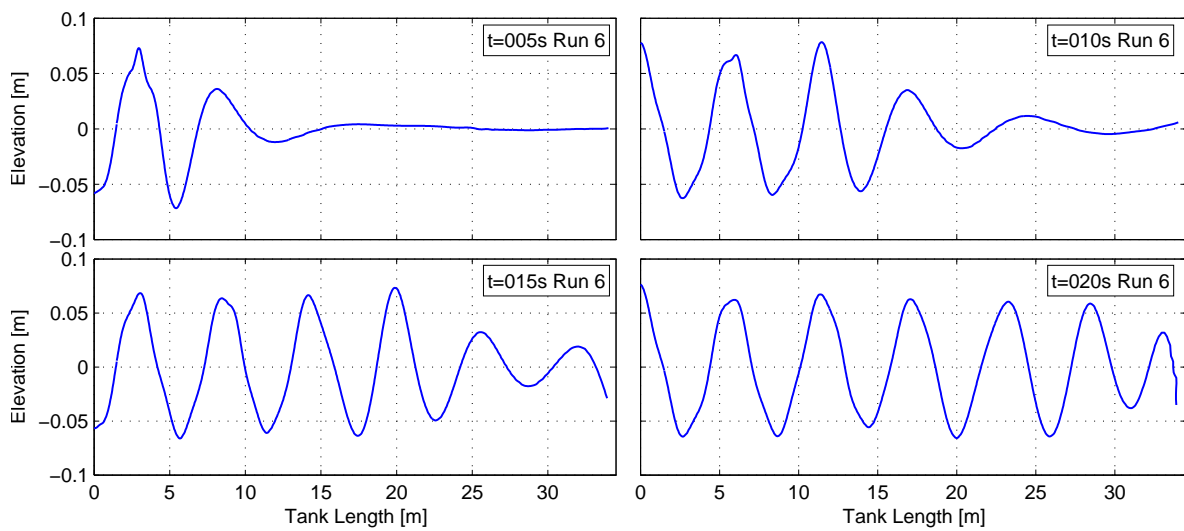
Figure C.13: Wave Elevation along the tank lenght for run 6

C.2.2 Timeseries of the Wave Elevation

In figure C.14 to figure C.19 timeseries of the wave elevation at section $x = 1.5m$, $x = 3m$, $x = 5m$ and $x = 29m$ is shown.
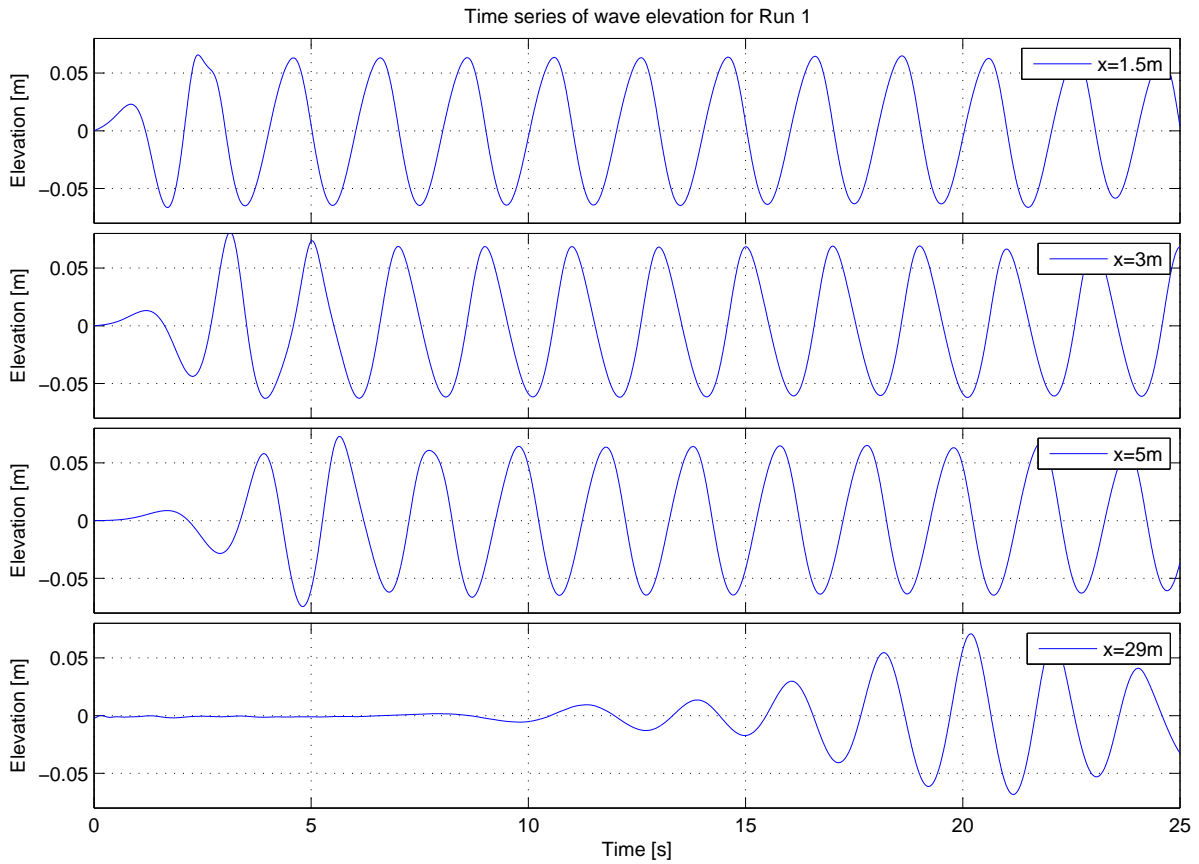
Figure C.14: Timeseries of wave elevation for run 1 at section ,$x = 1.5m$,$x = 3m$,$x = 5m$ and $x = 29m$.
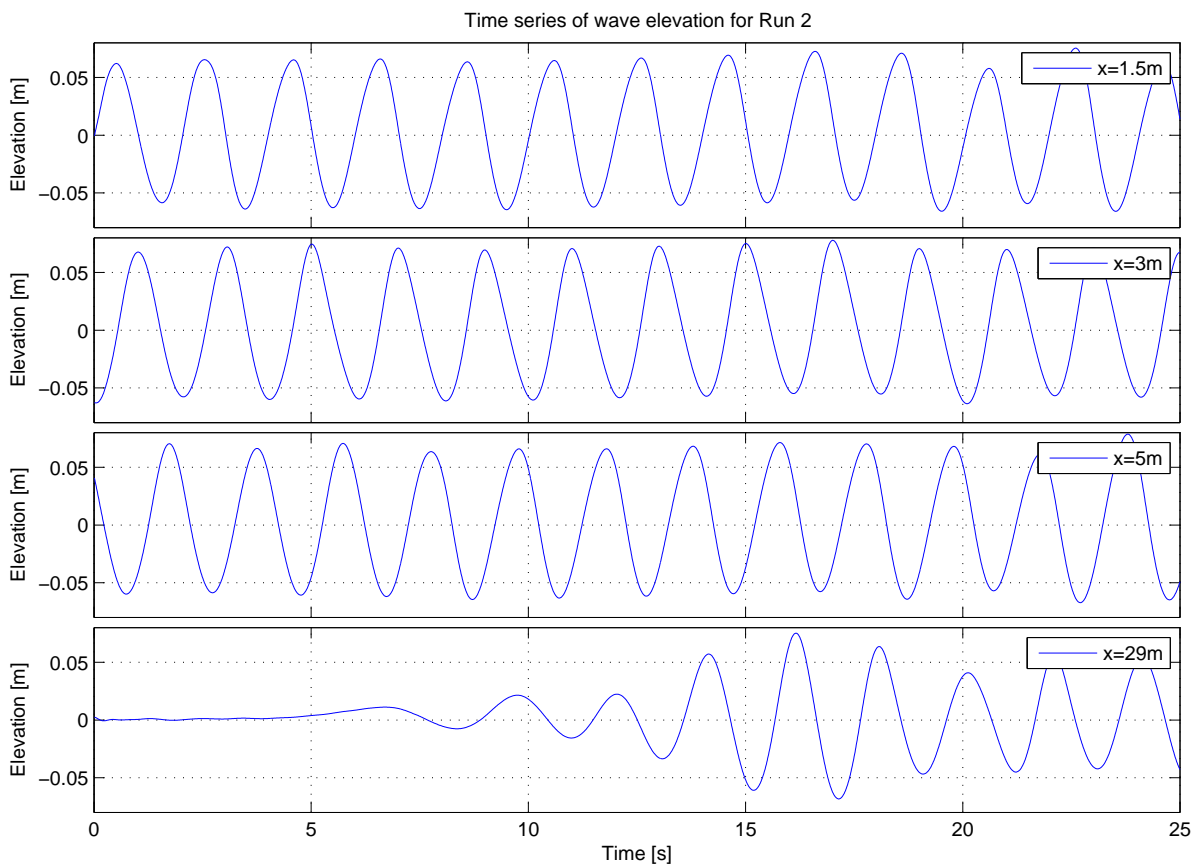
Figure C.15: Timeseries of wave elevation for run 2 at section ,$x = 1.5m$,$x = 3m$,$x = 5m$ and $x = 29m$.
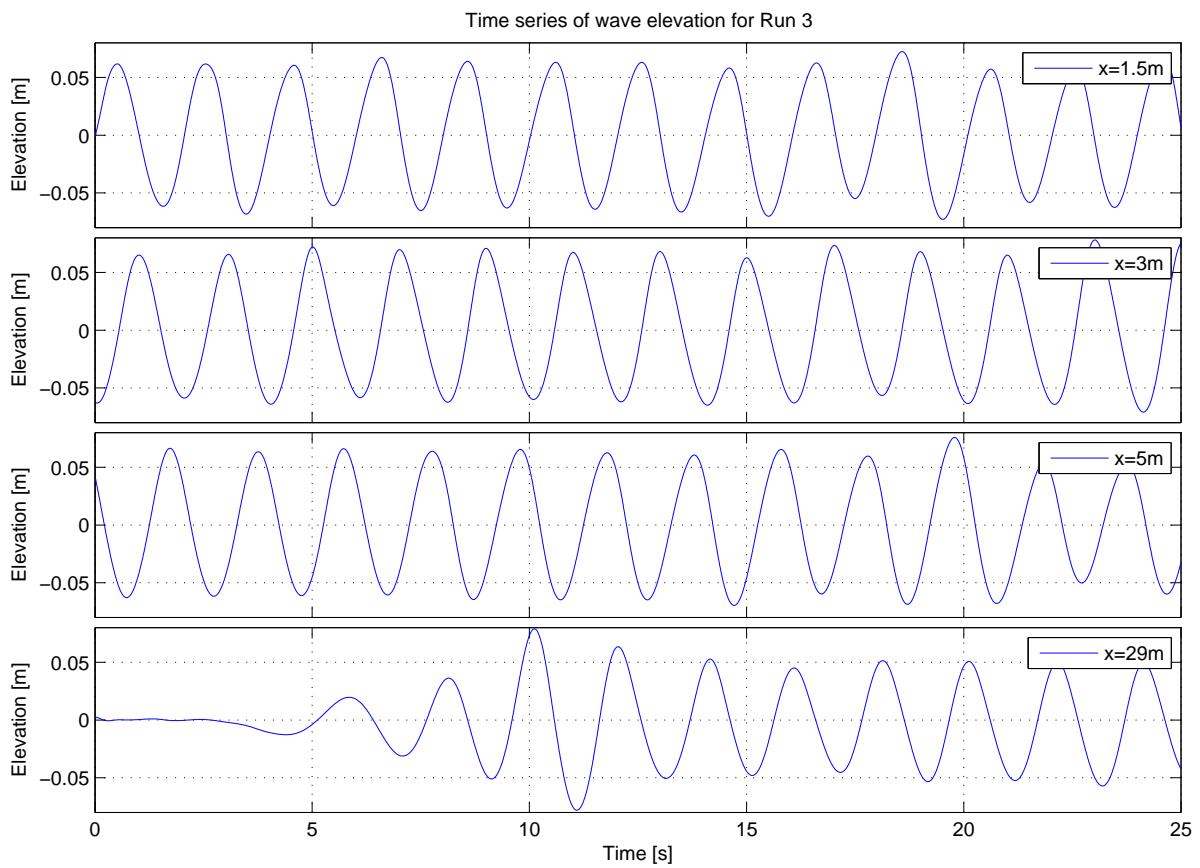
Figure C.16: Timeseries of wave elevation for run 3 at section ,$x = 1.5m$,$x = 3m$,$x = 5m$ and $x = 29m$.
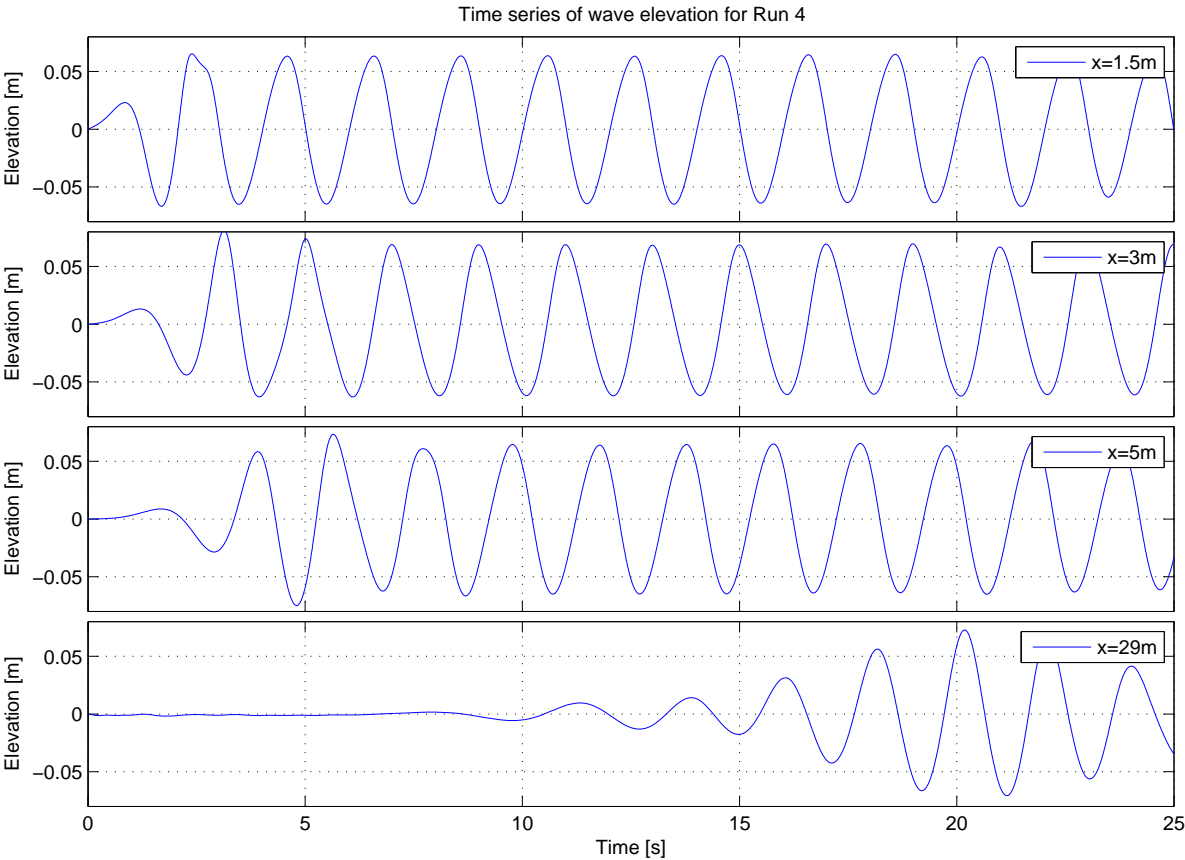
Figure C.17: Timeseries of wave elevation for run 4 at section $,x = 1.5m$,$x = 3m$,$x = 5m$ and $x = 29m$.
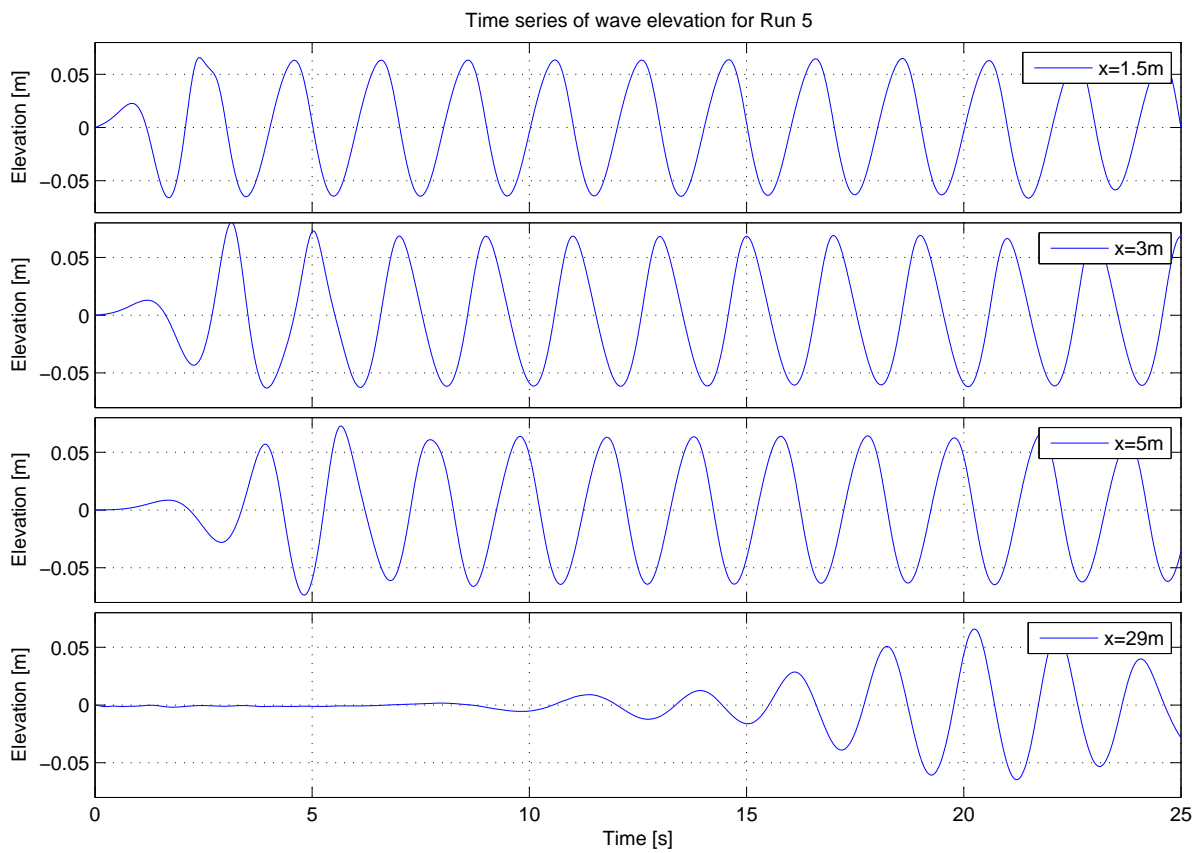
Figure C.18: Timeseries of wave elevation for run 5 at section ,$x = 1.5m$,$x = 3m$,$x = 5m$ and $x = 29m$.
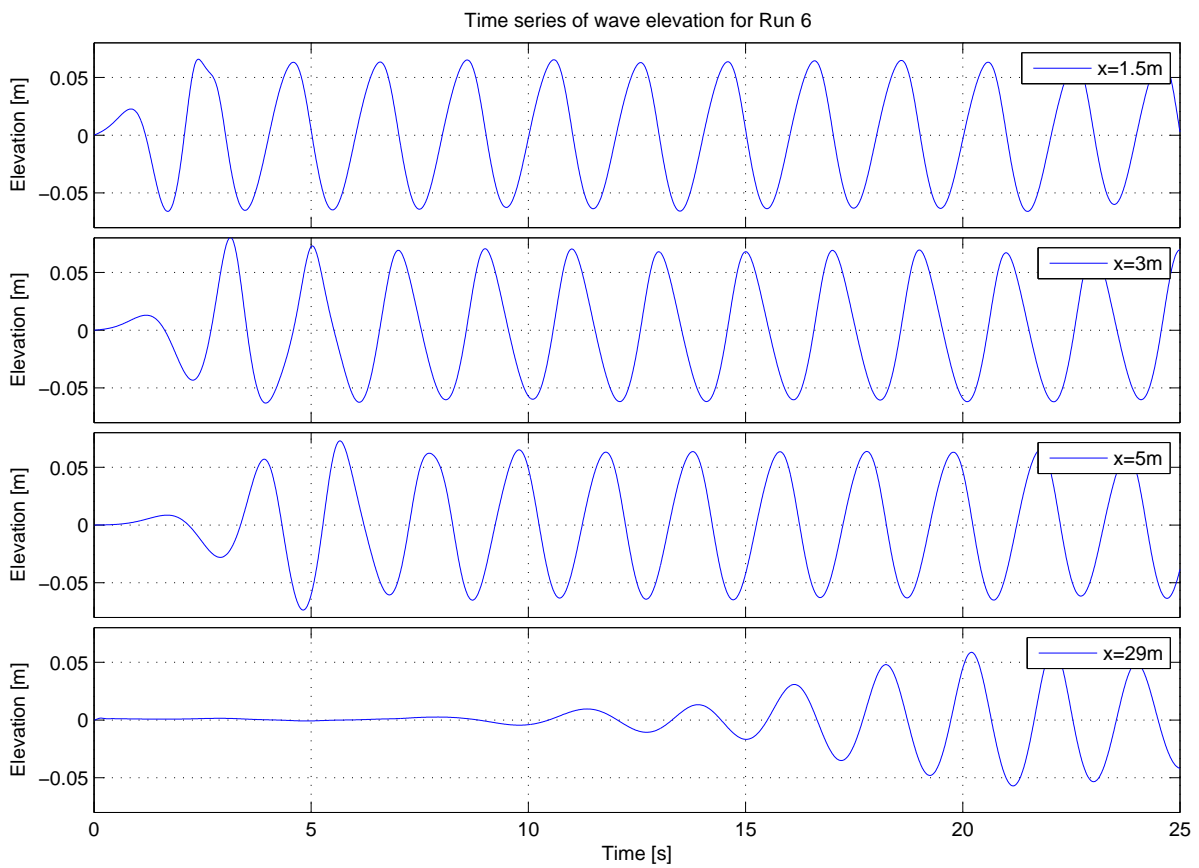
Figure C.19: Timeseries of wave elevation for run 6 at section ,$x = 1.5m$,$x = 3m$,$x = 5m$ and $x = 29m$.

C.3   Student Wave Tank

C.3.1   Wave elevation along the tank length for run $1 - 3$
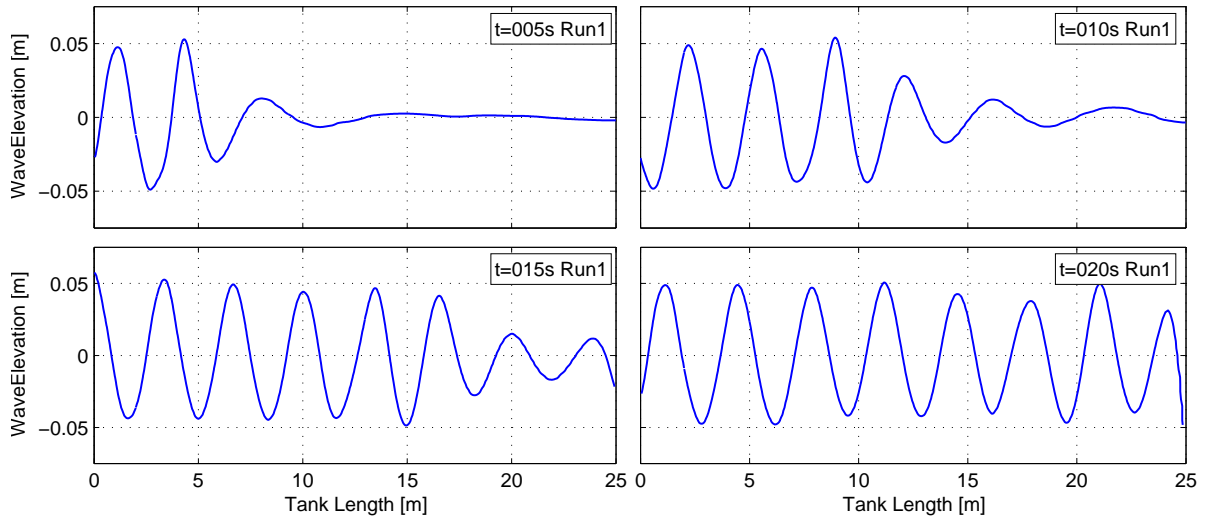
Figure C.20: Wave Elevation along the tank length for run 1
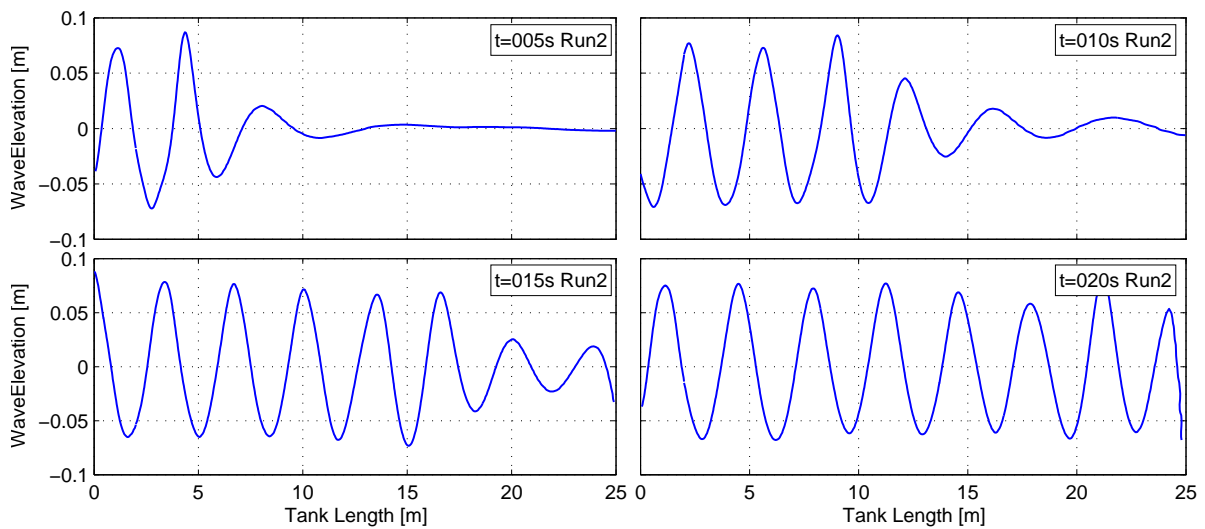
Figure C.21: Wave Elevation along the tank length for run 2
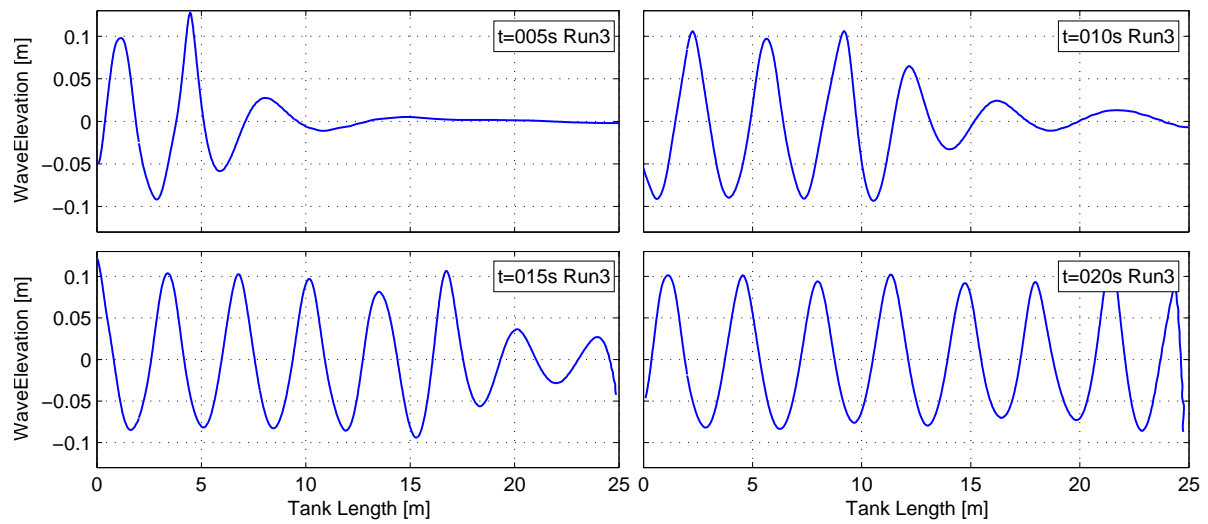
Figure C.22: Wave Elevation along the tank length for run 3

C.3.2   Time series of wave elevation for run $1 - 3$
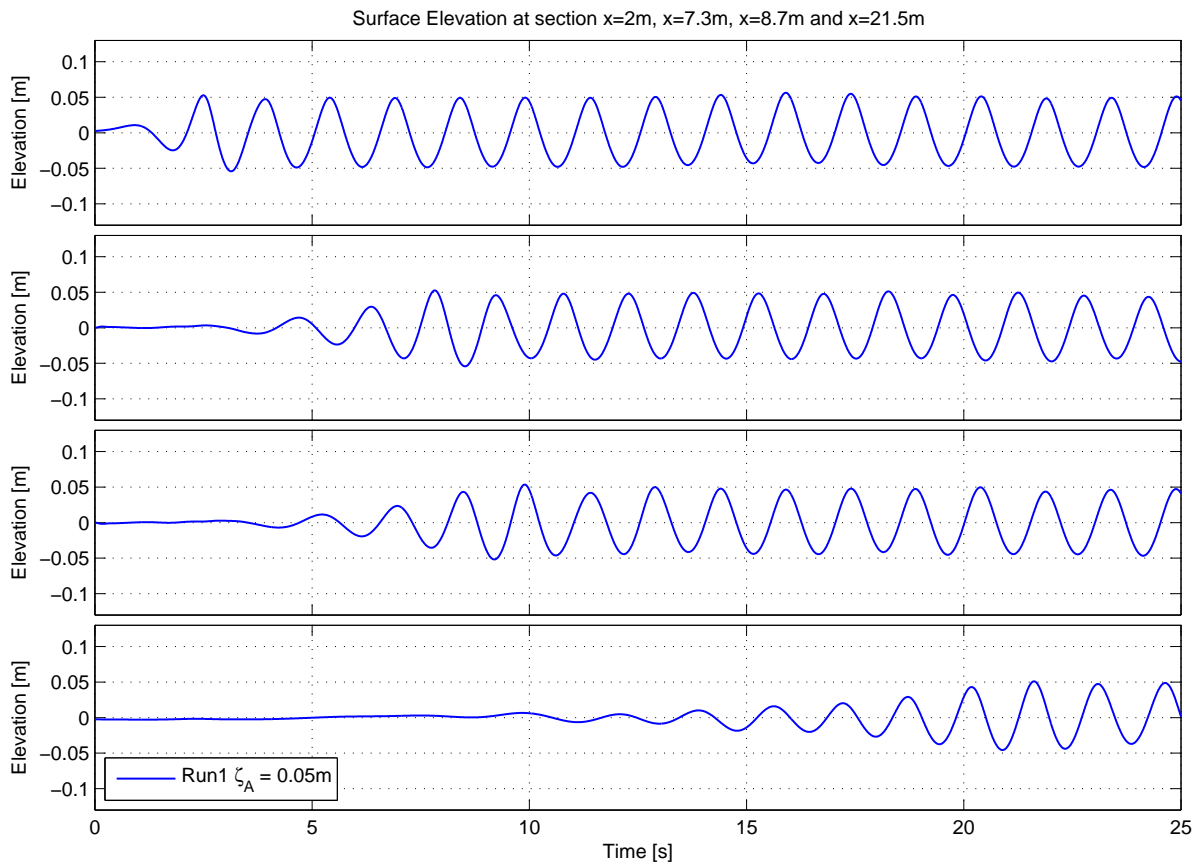
Figure C.23: Time series of wave Elevation for run 1.
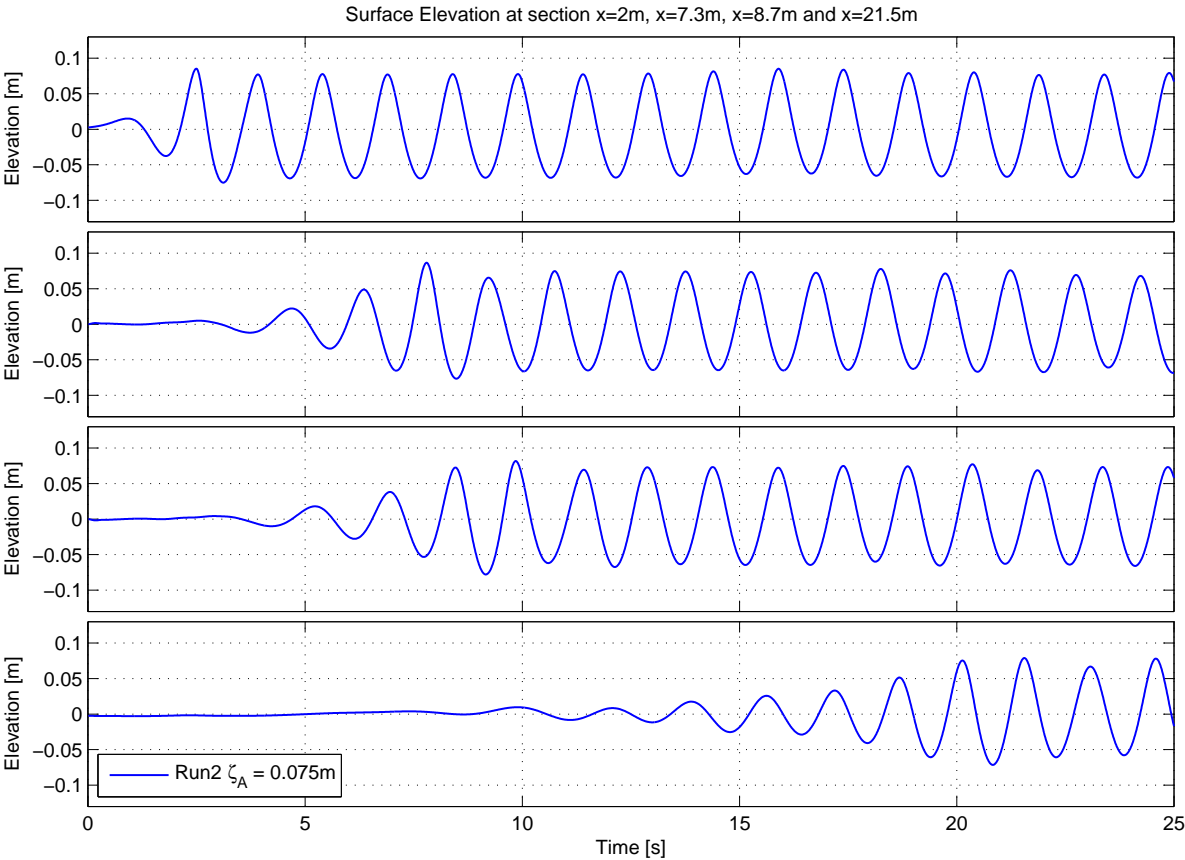
Figure C.24: Time series of wave Elevation for run 2.
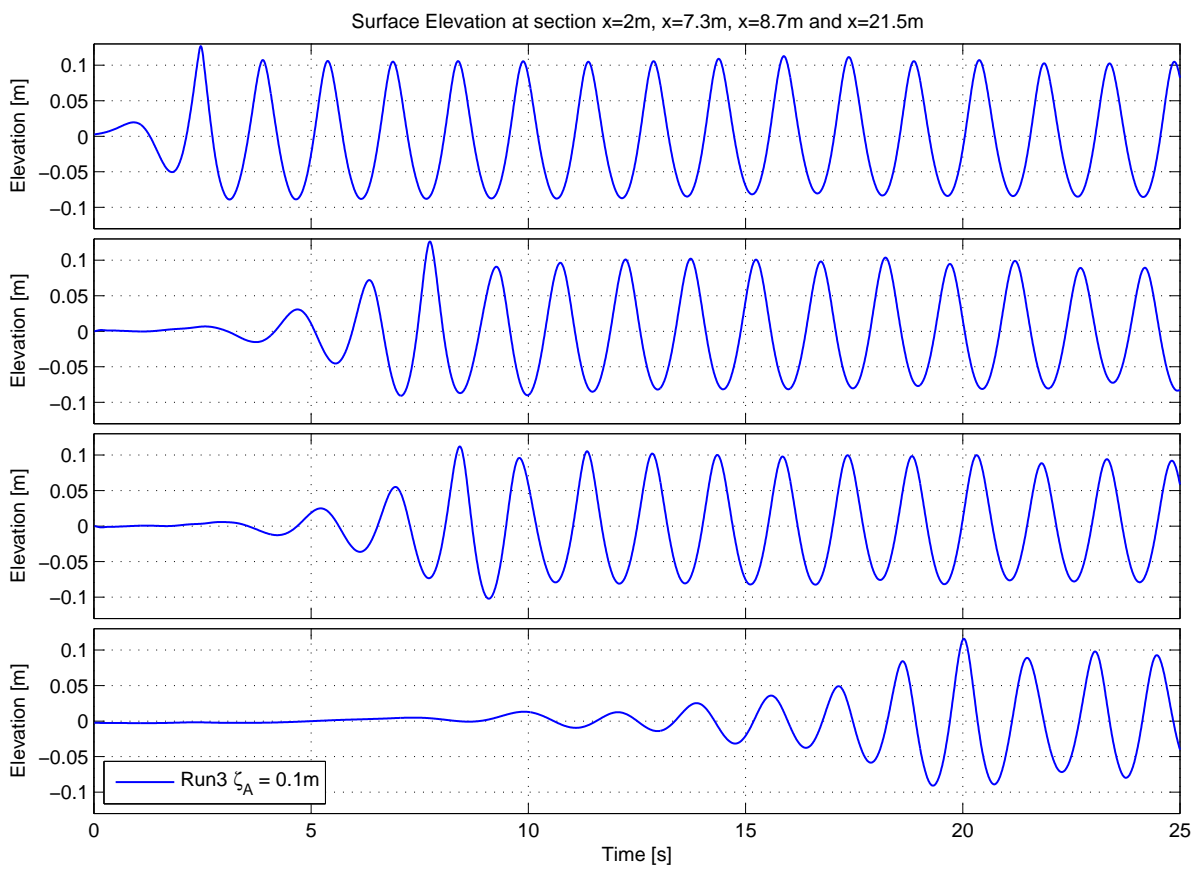
Figure C.25: Time series of wave Elevation for run 3.

Appendix D

Figures from CFD Analysis on Protection Covers

D.1 Wave Elevation at $x = 7.3m$ and $x = 8.7m$.

Numerical wave elevation at position $x = 7.3m$ and $x = 8.7m$ similar to the two wave probes $wp01$ and $wp02$ in the experimental setup compared with Stokes 2^n order wave elevation. Run $1 - 3$ is shown. Similar results were obtained for run $4 - 6$ with similar wave amplitude ζ_A and wave period T.
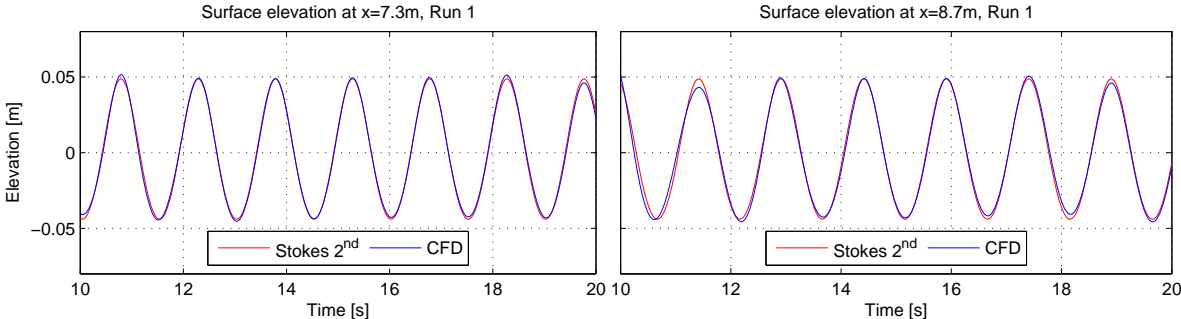
Figure D.1: Wave elevation at $x = 7.3m$ and $x = 8.7m$ compared with Stokes 2nd order wave elevation. Run 1
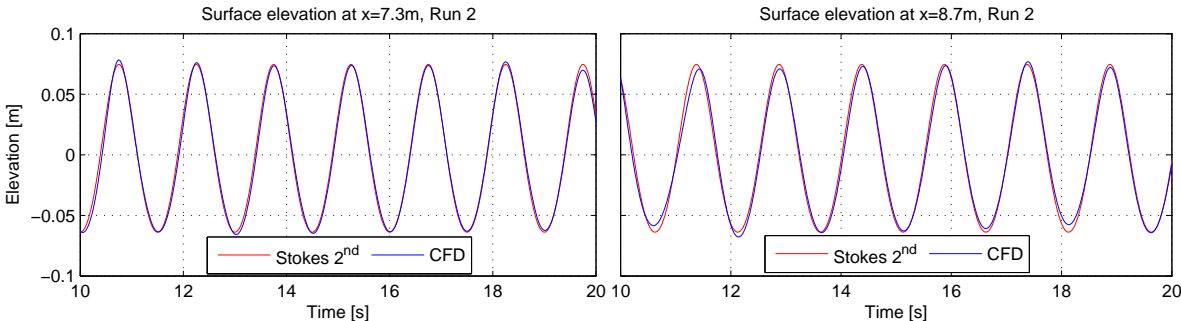
Figure D.2: Wave elevation at $x = 7.3m$ and $x = 8.7m$ compared with Stokes 2nd order wave elevation. Run 2
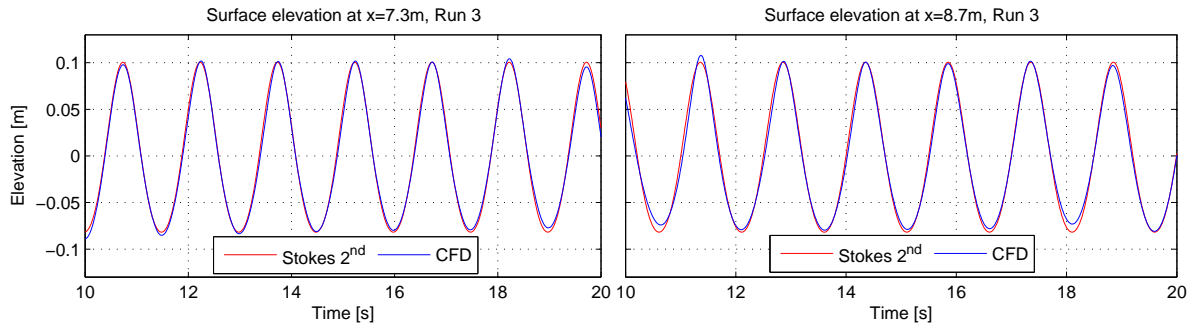
Figure D.3: Wave elevation at $x = 7.3m$ and $x = 8.7m$ compared with Stokes 2nd order wave elevation. Run 3

D.2 Horizontal and vertical forces on Protection Cover 1 and 2.

Numerical forces compared with theoretical calculations. Vertical theoretical force calculated as Froude Kriloff pressure force without added mass contribution. Horizontal theoretical force calculated as Froude-Kriloff pressure force with contribution from a added mass force with $C_{a,1} = 1.53$ for rectangular cover and $C_{a,2} = 1.145$ for the half circular cover.
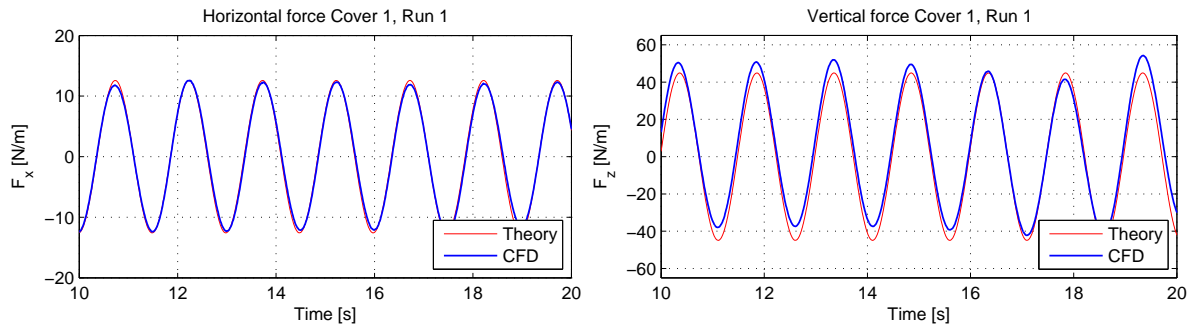
Figure D.4: Comparison of horizontal and vertical force on rectangular cover for run 1 between CFD and Theoretical approach.
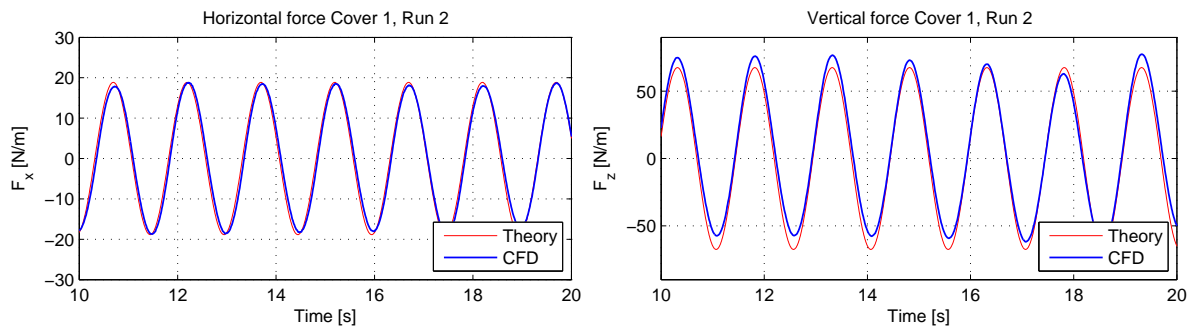
Figure D.5: Comparison of horizontal and vertical force on rectangular cover for run 2 between CFD and Theoretical approach.
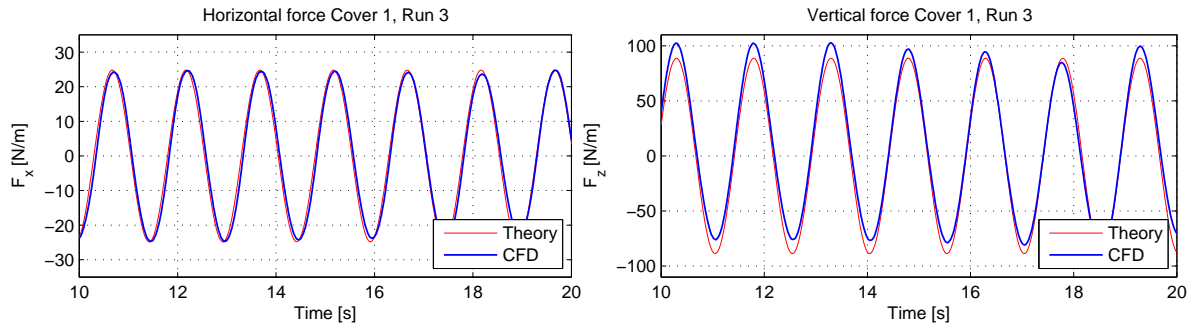
Figure D.6: Comparison of horizontal and vertical force on rectangular cover for run 3 between CFD and Theoretical approach.
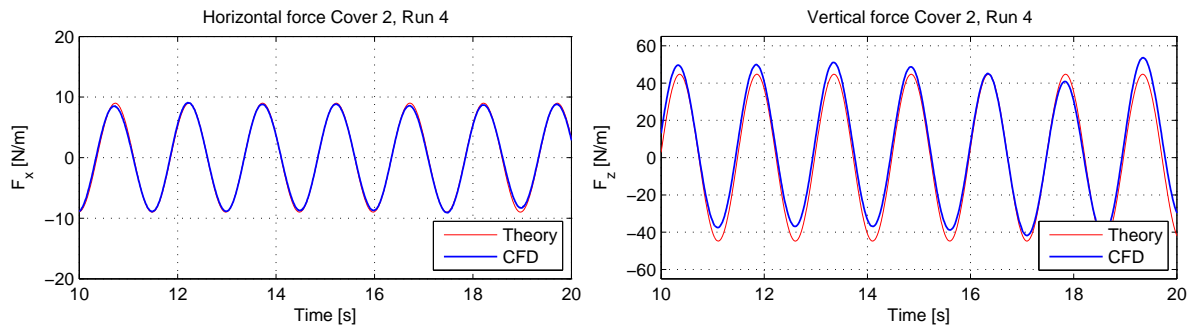
Figure D.7: Comparison of horizontal and vertical force on half circular cover for run 4 between CFD and Theoretical approach.
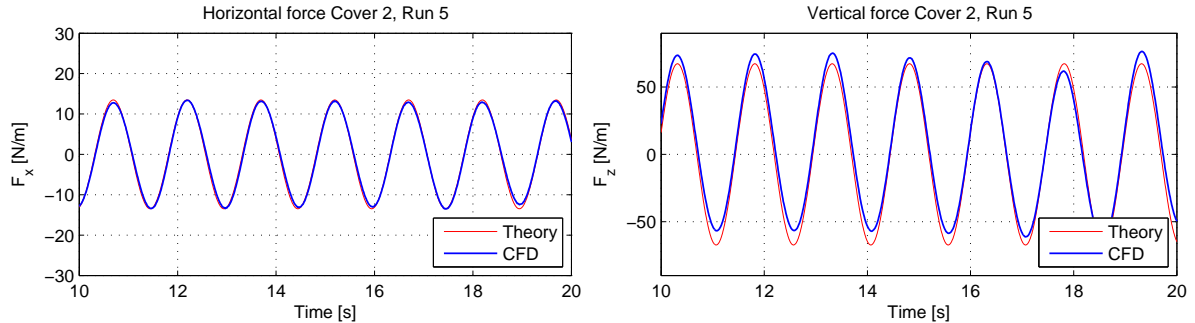

Figure D.8: Comparison of horizontal and vertical force on half circular cover for run 5 between CFD and Theoretical approach.
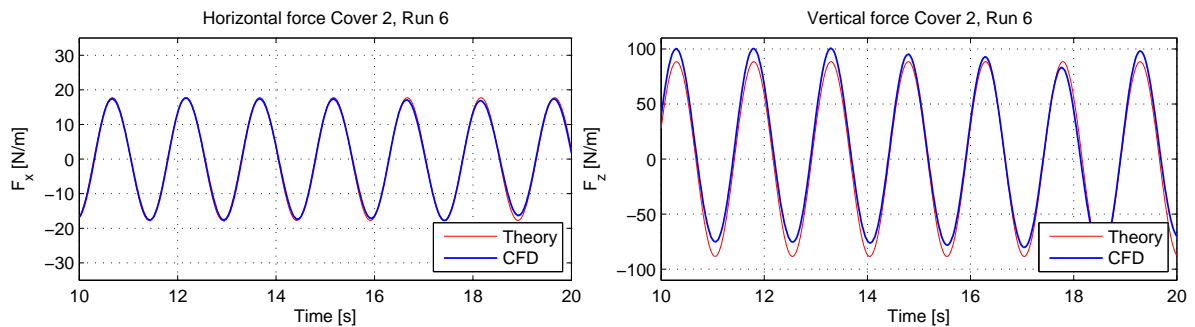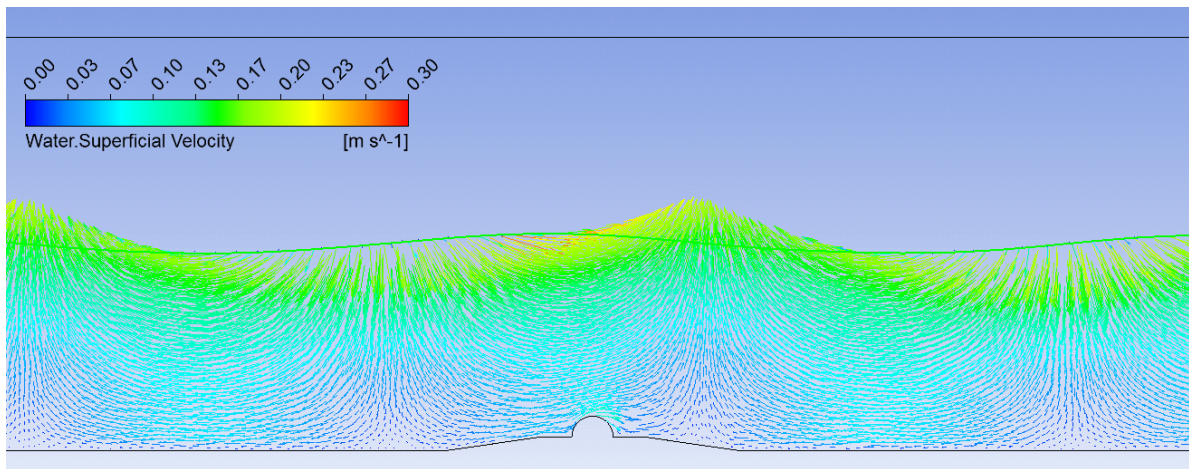

Figure D.9: Comparison of horizontal and vertical force on half circular cover for run 6 between CFD and Theoretical approach.

D.3 Superficial water velocity vectors

Figure D.10: Superficial water velocity vectors over half circular protection cover in run 4 at $t = 14s$.
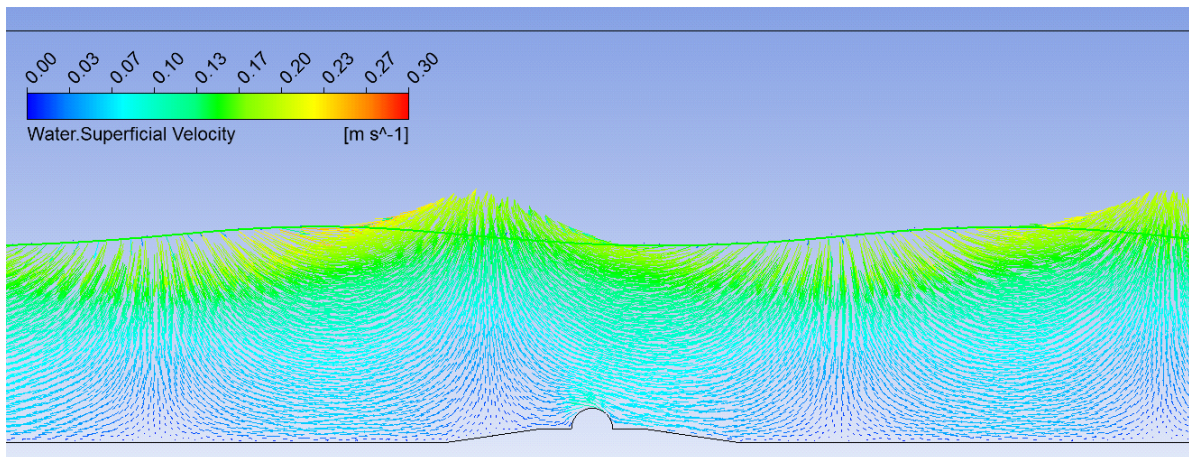

Figure D.11: Superficial water velocity vectors over half circular protection cover in run 4 at $t = 15s$.
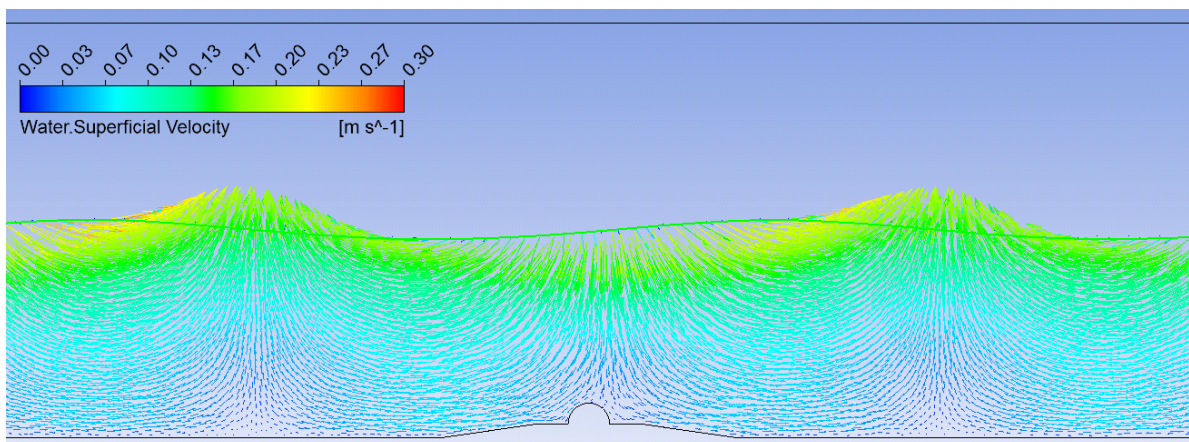

Figure D.12: Superficial water velocity vectors over half circular protection cover in run 4 at $t = 16s$.

D.4 Superficial water velocity over the protection covers

In figure D.13 the total superficial water velocity for the rectangular and half circular protection cover with the free surface wave from run 1 and 4 at $t = 20s$ can be seen. In figure D.14 the total superficial water velocity over the rectangular and half circular protection cover from run 1 and 4 at different time steps can be seen.
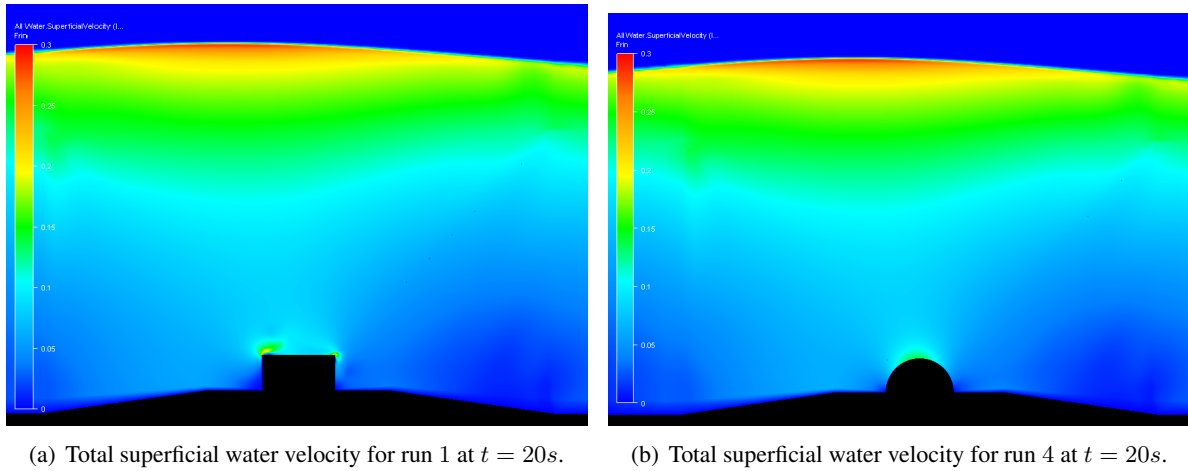

(a) Total superficial water velocity for run 1 at $t = 20s$.

(b) Total superficial water velocity for run 4 at $t = 20s$.

Figure D.13: Superficial water velocity from run 1 and 4 at $t = 20s$. Legend in $0.3 - 0m/s$.

(a) Total superficial water velocity for run 1 at $t = 19s$.

(b) Total superficial water velocity for run 4 at $t = 19s$.

(c) Total superficial water velocity for run 1 at $t = 20s$.

(d) Total superficial water velocity for run 4 at $t = 20s$.

(e) Total superficial water velocity for run 1 at $t = 21s$.

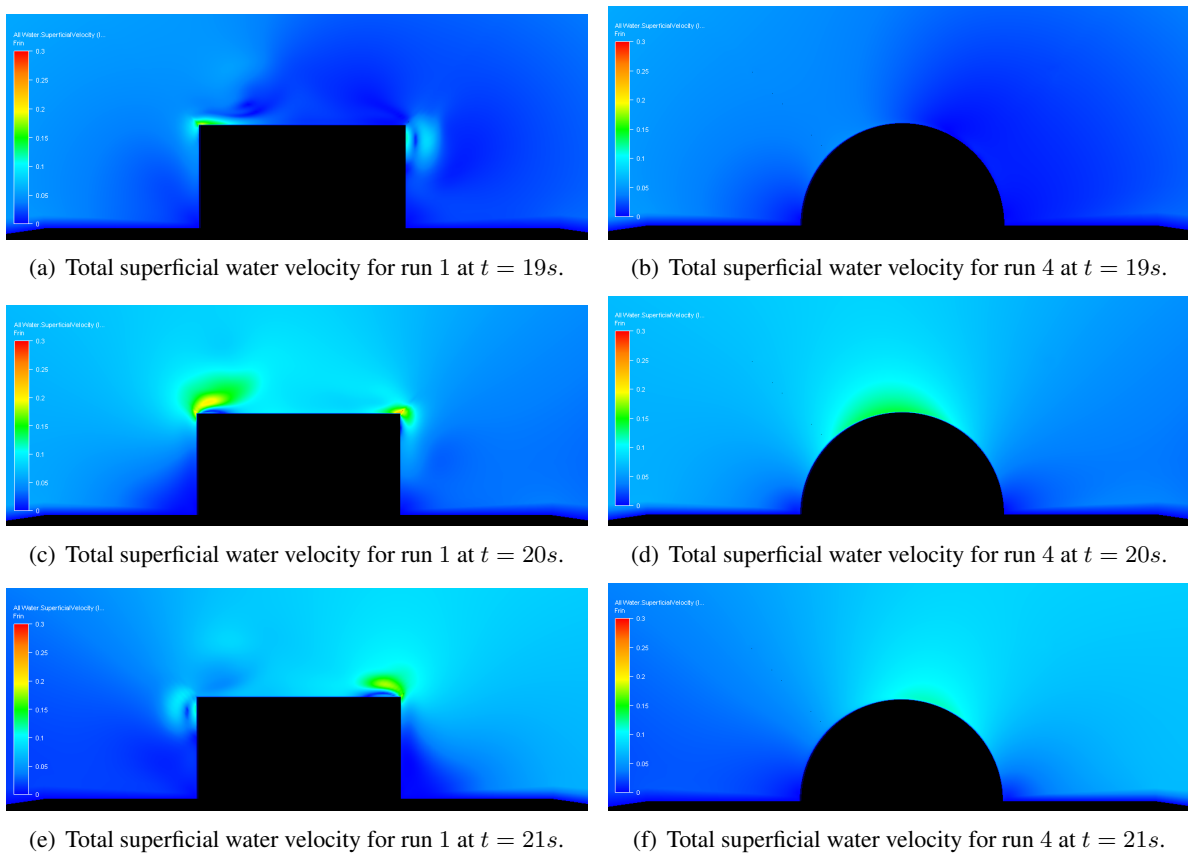(f) Total superficial water velocity for run 4 at $t = 21s$.

Figure D.14: Superficial water velocity from run 1 and 4 at $t = 19 - 21s$. Legend in $0.3 - 0m/s$.

Appendix E

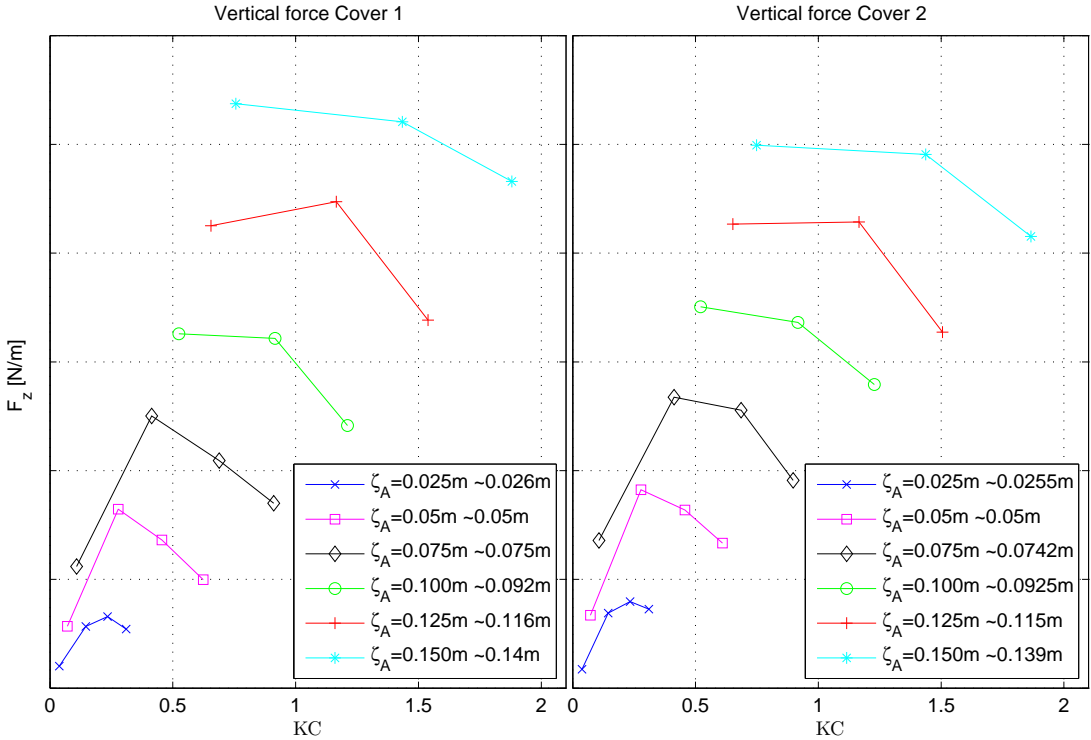# Figures from Experimental tests

E.1 Vertical forces

Figure E.1: Vertical force on cover 1 and 2.

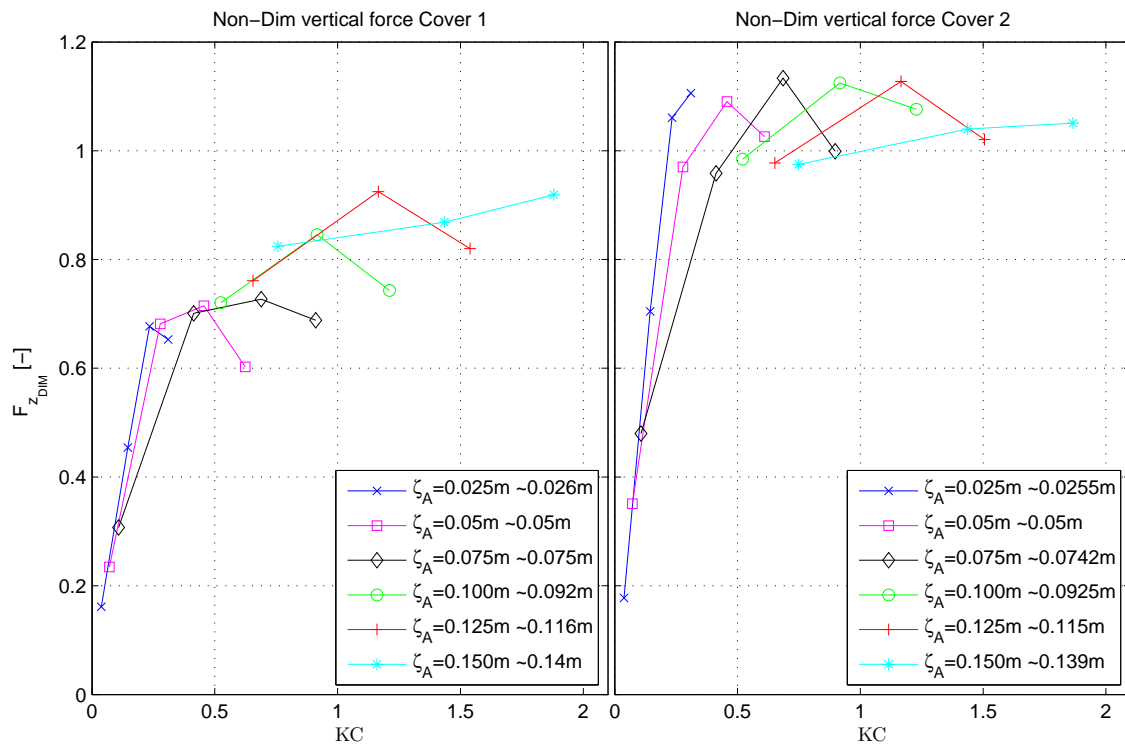## E.2 Non dimensional vertical forces

Figure E.2: Non dimensional vertical force on cover 1 and 2.
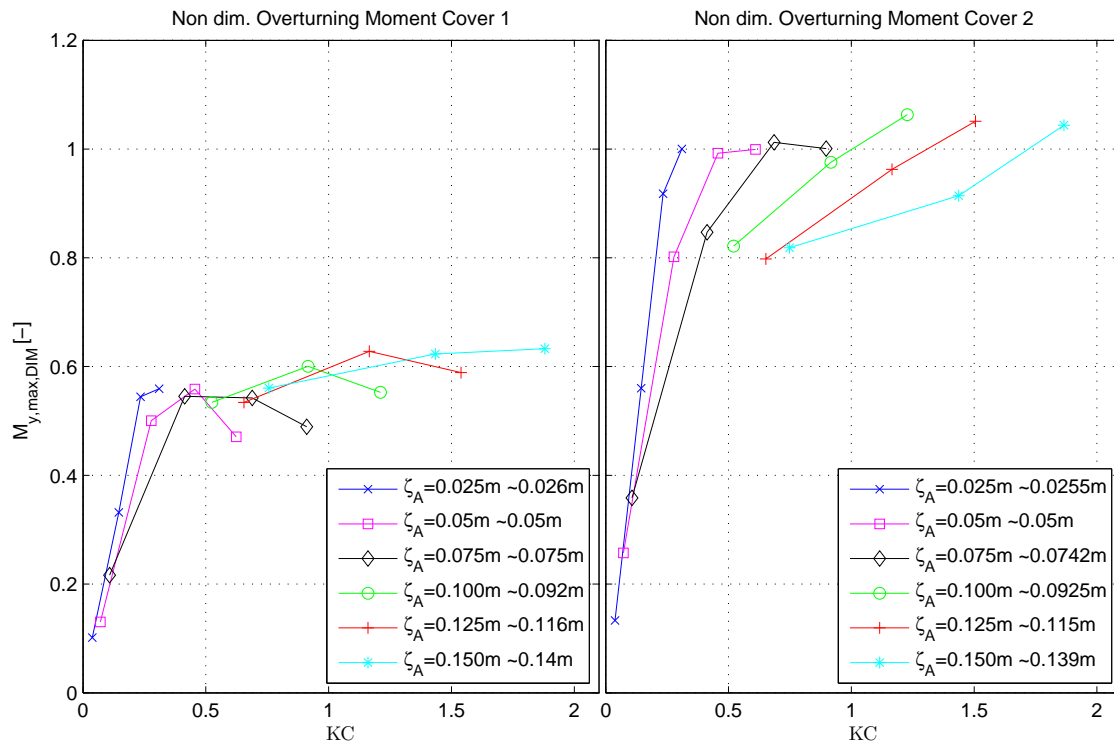
E.3 Non dimensional overturning moment

Figure E.3: Non dimensional overturning moment for cover 1and 2.

Appendix F

Figures from the 3D CFD analysis

F.1 Wave elevation from run 2.

In figure F.1 the wave elevation along the tank length for the half circular protection cover in run 2 is shown. In figure F.2 the time series of the wave elevation from four section along the tank at $x = 2m$, $x = 4.3m$, $x = 5.7m$ and $x = 13.5m$ is shown for the half circular cover in run 2.
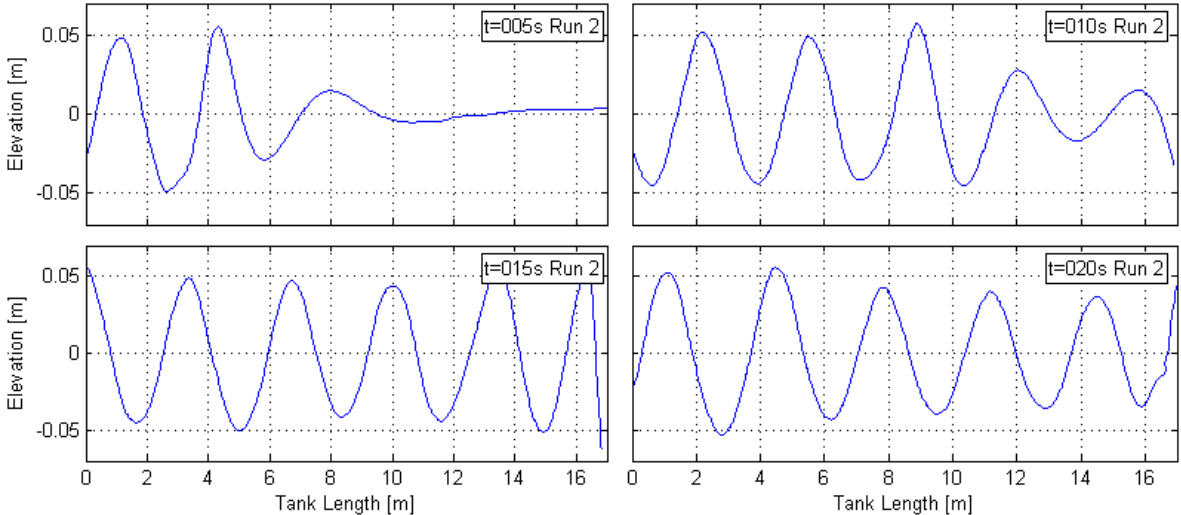

Figure F.1: Wave elevation along the tank length at $t = 5s$, $t = 10s$, $t = 15s$ and $t = 20s$ for the half circular protection cover from run 2 in the 3D analysis
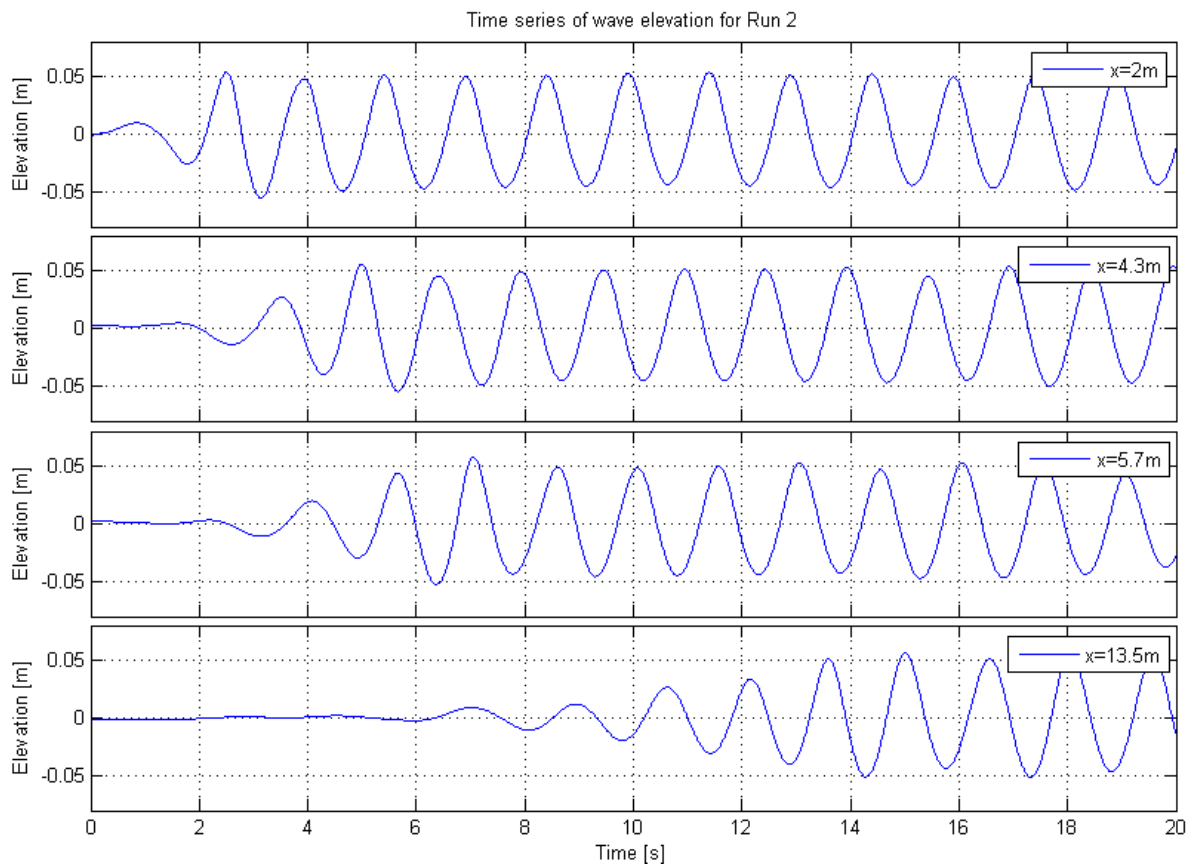
Figure F.2: Time series of wave elevation along the tank length at $x = 2m$, $x = 4.3m$, $x = 5.7m$ and $x = 13.5m$ for the half circular protection cover from run 2 in the 3D analysis.